

ISTANBUL TECHNICAL UNIVERSITY ★ GRADUATE SCHOOL

**CONSTITUTIVE FAILURE MODELLING AND ANALYSIS OF
STEEL WIRE ROPE STRUCTURES SUBJECTED TO IMPACT LOADING**

Ph.D. THESIS

Adem CANDAS

Department of Mechanical Engineering

Mechanical Engineering Programme

FEBRUARY 2021

ISTANBUL TECHNICAL UNIVERSITY ★ GRADUATE SCHOOL

**CONSTITUTIVE FAILURE MODELLING AND ANALYSIS OF
STEEL WIRE ROPE STRUCTURES SUBJECTED TO IMPACT LOADING**

Ph.D. THESIS

**Adem CANDAS
(503122011)**

Department of Mechanical Engineering

Mechanical Engineering Programme

Thesis Advisor: Prof. Dr. C. Erdem İMRAK

FEBRUARY 2021

İSTANBUL TEKNİK ÜNİVERSİTESİ ★ LİSANSÜSTÜ EĞİTİM ENSTİTÜSÜ

**ÇELİK TEL HALAT YAPILARININ DARBE YÜKÜ ALTINDA
HASAR MODELLENMESİ VE İNCELENMESİ**

DOKTORA TEZİ

**Adem CANDAS
(503122011)**

Makina Mühendisliği Anabilim Dalı

Makina Mühendisliği Programı

Tez Danışmanı: Prof. Dr. C. Erdem İMRAK

ŞUBAT 2021

Adem CANDAŞ, a Ph.D. student of ITU Graduate School 503122011 successfully defended the thesis entitled “CONSTITUTIVE FAILURE MODELLING AND ANALYSIS OF STEEL WIRE ROPE STRUCTURES SUBJECTED TO IMPACT LOADING”, which he prepared after fulfilling the requirements specified in the associated legislations, before the jury whose signatures are below.

Thesis Advisor : **Prof. Dr. C. Erdem İMRAK**
Istanbul Technical University

Jury Members : **Prof. Dr. Cemal BAYKARA**
Istanbul Technical University

Prof. Dr. Cüneyt FETVACI
Istanbul University-Cerrahpaşa

Prof. Dr. Ekrem TÜFEKÇİ
Istanbul Technical University

Prof. Dr. Erkan ÖTERKUŞ
University of Strathclyde

Date of Submission : **January 27, 2021**

Date of Defense : **February 23, 2021**

To my family,

FOREWORD

I would like to thank my advisor, Prof. İMRAK, for his countless assistance and unconditional help. I also would like to thank Prof. ÖTERKUŞ for his guidance and comments on Peridynamics. I will never forget his hospitality during my visit to Glasgow, UK. Their suggestions and comments on numerical modelling and applications were very helpful to the study. This work would not be come into being without their positive feedbacks and encouraged supports.

Many people have also provided valuable assistance and advice in completing this work. I owe great appreciation to Prof. SARIKAYA, who encouraged me and provided valuable guidance for my career in academy. I think it is essential that I thank my long term friends and companions, Salih GÜLŞEN and Tuğrul AYDEMİR for their help in preparing scripts used in this study. There were a multitude of individuals who helped me to arrive at this point. Thanks to colleagues in Material Handling Group and Hüseyin GÜNDÜZ who provided precious assistance during years in ITU.

My sincere thanks are due to the thesis committee members Prof. TÜFEKÇİ, Prof. BAYKARA, and Prof. FETVACI for their guidance, encouragement and support.

Finally, I must express my warmest appreciation to my family for their constant and continued support and patience.

February 2021

Adem CANDAŞ
(Mech. Eng., M.Sc.)

TABLE OF CONTENTS

	<u>Page</u>
FOREWORD	ix
TABLE OF CONTENTS	xi
ABBREVIATIONS	xiii
SYMBOLS	xv
LIST OF TABLES	xvii
LIST OF FIGURES	xix
SUMMARY	xxiii
ÖZET	xxv
1. INTRODUCTION	1
1.1 Dynamic Fracture Mechanics.....	1
1.1.1 Fracture modes	2
1.1.2 Wave propagation	3
1.1.3 Crack initiation and propagation	3
1.1.4 Micro-cracks and toughening mechanism.....	4
1.2 Modelling Approaches	5
1.2.1 Finite Element Method.....	5
1.2.2 Discrete Element Method.....	7
1.2.3 Molecular Dynamics	7
1.2.4 Boundary Element Method.....	7
1.2.5 Peridynamics	8
1.3 Motivation of the Thesis.....	9
1.4 Outline of the Thesis	11
2. METHODOLOGY	13
2.1 Peridynamic Formulation	13
2.2 Damage Model in Peridynamics	17
2.2.1 Fracture modes and crack propagation.....	20
2.2.2 Local damage for crack growth.....	21
2.2.3 Micro-crack definition	22
2.3 Impact Modelling	24
2.3.1 Rigid impactor	24
2.3.2 Flexible impactor.....	25
2.4 Numerical Solution Method	26
2.4.1 Discretization in peridynamics	26
2.4.2 Numerical convergence scheme	27
2.5 Test Suit and Model Validation	28
3. KALTHOFF WINKLER EXPERIMENT	33
3.1 Benchmark Problem.....	36

3.2 Stochastically Distributed Micro-Cracks.....	40
3.2.1 Micro-cracks with varying densities.....	40
3.2.2 Micro-cracks with various number.....	44
4. WIRE ROPES.....	49
4.1 Structure of Wire Ropes	52
4.2 Theory of Wire Ropes	55
4.2.1 Theoretical models	56
4.2.1.1 Purely tensile or fibre model.....	56
4.2.1.2 Orthotropic sheet model	56
4.2.1.3 Theory of thin rod.....	57
4.2.1.4 Helical rod model	57
4.3 Literature Review	57
4.3.1 Experimental studies	61
4.3.2 Recent studies on impact load and contacts in wire rope modelling.....	62
5. MODELLING OF WIRE ROPES USING PERIDYNAMIC THEORY	71
5.1 Codes and Software.....	71
5.1.1 Handling with Outputs	72
5.1.1.1 Outputs in Matlab	72
5.1.1.2 Outputs in Ovitto	74
5.1.2 Micro-Crack Code.....	76
5.2 Wire Rope Modelling Code.....	78
5.3 Modelling of Wire Ropes using Peridynamic Theory.....	79
5.3.1 Convergence tests: m-convergence	84
5.3.2 Convergence tests: δ -convergence	89
5.3.3 Convergence tests comparison.....	95
5.3.4 Wave propagation	96
6. CONCLUSIONS.....	99
REFERENCES.....	103
APPENDICES.....	121
APPENDIX A	123
APPENDIX B.....	125
APPENDIX C.....	127
APPENDIX D	129
APPENDIX D.1	132
APPENDIX E.....	133
APPENDIX F	135
APPENDIX G	139
CURRICULUM VITAE.....	145

ABBREVIATIONS

ADR	: Adaptive Dynamic Relaxation
BEM	: Boundary Element Method
CCM	: Classical Continuum Mechanics
CDM	: Continuum Damage Mechanics
DEM	: Discrete Element Method
EPFM	: Elastic-Plastic Fracture Mechanics
XFEM	: Extended Finite Element Method
FEM	: Finite Element Method
IWRC	: Independent Wire Rope Core
LFEM	: Linear Elastic Fracture Mechanics
MD	: Molecular Dynamics
NDT	: Non-destructive Testing
OVITO	: Open Visualization Tool
PD	: Peridynamics

SYMBOLS

\mathbf{b}	: Body load
c	: Bond constant
κ	: Bulk modulus
r_{sh}	: Critical distance
G_c	: Critical energy release rate
ρ	: Density
WD	: Diameter of a wire section
\mathbf{u}	: Displacement vector
d	: Distance between notches
Δ	: Distance between two sequential material point
E	: Elastic modulus or Young modulus
\mathbf{x}'	: Family member of a material point
\mathbf{f}	: Force vector
μ	: History-dependent scalar-valued step function
\mathcal{H}_x	: Horizon
δ	: Horizon radius
L	: Length
φ	: Local damage
a	: Main crack length
\mathbf{x}	: Material point
n	: Notch thickness
n_{divx}	: Number of material points in x -axis
n_{divy}	: Number of material points in y -axis
n_{divz}	: Number of material points in z -axis
ξ	: Relative position vector
D	: Rigid impactor diameter
H	: Rigid impactor height
v	: Rigid impactor velocity
ν	: Poisson's ratio
μ	: Shear modulus
c_{sh}	: Short-range constant
w	: Strain energy density
s	: Stretch
s_c	: Stretch (critical)
h or t	: Thickness
t	: Time
Δt	: Time increment
W	: Width

LIST OF TABLES

	<u>Page</u>
Table 2.1 : PD model parameters of the isotropic plate under uni-axial tension. .	29
Table 3.1 : Dimensions and parameters in Kalthoff-Winkler simulations.	36
Table 3.2 : Material properties of maraging steel.....	36
Table 5.1 : Output *.m files of Fortran program of Kalthoff-Winkler problem. ...	73
Table 5.2 : Dimensions and mechanical properties of impactor and single wire model.....	82
Table 5.3 : m-Convergence test setup and parameters.	84
Table 5.4 : δ -Convergence test setup and parameters.	89
Table 5.5 : Average velocity data.	96

LIST OF FIGURES

	<u>Page</u>
Figure 1.1 : Three crack modes with regard to the loading conditions in fracture mechanics: Mode I (Opening), Mode II (In-Plane Shear), and Mode III (Out-of-Plane Shear).....	2
Figure 1.2 : Comparison of (a) Classical (local) continuum mechanics, (b) Peridynamics and (c) Molecular dynamics.....	8
Figure 2.1 : Position and force vectors of two material points.	14
Figure 2.2 : A material point \mathbf{x} can only interact with a family member \mathbf{x}' in the horizon with radius δ	15
Figure 2.3 : Linear relation between critical stretch and bond force.	18
Figure 2.4 : Fracture surface and integration domain for critical energy release rate.....	19
Figure 2.5 : Initial and damaged model.	20
Figure 2.6 : Peridynamic crack propagation and experimental results with various crack orientation angles.....	20
Figure 2.7 : Local damage in PD (a) on the crack plane, (b) in front of the crack tip, and (c) behind the crack tip. The green lines indicate unbroken PD interactions and dashed lines with dots indicate broken PD interactions.....	21
Figure 2.8 : Local damage and crack propagation.	22
Figure 2.9 : Micro-crack plane (thick continuous line). The broken bonds are shown with lines with arrows.....	23
Figure 2.10 : Representation of contact between a rigid impactor and deformable target subjected to impact load.	24
Figure 2.11 : A case study to examine the horizon size effect on the crack propagation and branching. The plate is subjected to $V_0 = 50$ m/s along vertical axis.	28
Figure 2.12 : Geometry of a plate subjected uni-axial tension.	29
Figure 2.13 : (a) Discretization in PD and (b) meshing in FEM.....	30
Figure 2.14 : Displacements (a) $u_x(x, y = 0)$ for PD, (b) $u_y(x = 0, y)$ for PD, (c) $u_x(x, y = 0)$ for FEM, and (d) $u_y(x = 0, y)$ for FEM.	30
Figure 2.15 : Displacement along the centre x -axis.	31
Figure 2.16 : Displacement along the centre y -axis.	32
Figure 3.1 : The Kalthoff–Winkler experimental setup.	33
Figure 3.2 : The Kalthoff–Winkler (a) experimental setup and (b) peridynamic discretization model.	35
Figure 3.3 : Geometric details of the benchmark study: crescent-like micro-crack pattern.	37

Figure 3.4 :	(a) Crack propagations in Kalthoff–Winkler experiment (without micro-crack case) and (b) in the benchmark problem at 91.4 μs	38
Figure 3.5 :	(a) Crack propagations in Kalthoff–Winkler experiment (without micro-crack case) and (b) in the benchmark problem at 95.7 μs	39
Figure 3.6 :	Geometric details of the micro-crack pattern in the reference zone A_0 with the reference density n_0	41
Figure 3.7 :	The crack path of the case (a) $n_0 \times 0.75$, (b) $n_0 \times 1$, and (c) $n_0 \times 1.25$ cases at 91.4 μs (1050th time-step).	42
Figure 3.8 :	The macro-crack propagation velocities of without micro-crack and with micro-crack cases with densities $n_0 \times \{0.75, 1, 1.25\}$ between 52.2 and 91.4 μs . The initial and maximum velocities are shown with black boxes.	43
Figure 3.9 :	Geometric details of the micro-crack pattern in A_0, A_1, A_2 regions with a micro-crack density of n_0	44
Figure 3.10 :	The crack path of cases (a) A_1 (b) A_0 , and (c) A_2 cases at 91.4 μs (1050th time-step).....	45
Figure 3.11 :	The macro-crack propagation velocities of without micro-cracks, A_1, A_0 , and A_2 cases between 52.2 and 91.4 μs . The initial and maximum velocities are shown with black boxes.....	46
Figure 4.1 :	A damaged wire rope.....	51
Figure 4.2 :	Brittle wire fracture with minimal necking.	51
Figure 4.3 :	Components of a wire rope.....	53
Figure 4.4 :	Wire rope lay types: (a) right regular lay (sZ), (b)left regular lay (zS), (c) right lang lay (zZ), (d) left lang lay wire (sS).....	53
Figure 4.5 :	Cross sectional view of 1x6 wire strand.....	54
Figure 4.6 :	Basic strand types.	54
Figure 4.7 :	6x36 Warrington-Seale (IWRC) type wire rope with a steel core.....	55
Figure 4.8 :	The schematic cross section description of the strands of rotating and non-rotating IWRC.....	55
Figure 4.9 :	The contact types between wires in a helical strand.....	63
Figure 4.10 :	Definition of contact modes in a cross section of view of a strand, (a) radial contact and (b) lateral contact. d and d_0 are diameters of the outer wire and core, respectively. α is the lay angle.....	64
Figure 4.11 :	Finite element mesh of a slice of 1/12 of a 7-wire strand (a) global view, (b) detailed view in contact region. R_c is the radius of the centre core.....	65
Figure 4.12 :	Finite element mesh of a mixing type contact. More dense mesh structures are applied to the contact regions.	65
Figure 4.13 :	Increased mesh number in the contact region.	66
Figure 4.14 :	Finite Element mesh of a Warrington-Seale (WS12+6/6+6+1) strand and the detail view of contact.....	67
Figure 4.15 :	Identification of the contact surfaces with four surface approach.	67
Figure 4.16 :	Dimensions and 2D mesh of a helical strand.	68
Figure 4.17 :	Contact force distribution on (a) simple straight strand and (b) centre wire with finer mesh.....	69

Figure 4.18: Meshing of (a) straight centre wire and (b) outer compacted wire. Comparison of contact force distribution along (c) classical and (d) compacted wire strand.....	70
Figure 4.19: Meshing of wire strand with a pre-crack.....	70
Figure 5.1 : A plot window in Matlab generated with the script in Appendix A..	73
Figure 5.2 : A preview window from Ovito. The input file is from Appendix B.	74
Figure 5.3 : The definitions of the physical properties of particles in Ovito.	75
Figure 5.4 : A preview window of particles as time-series in Ovito.....	76
Figure 5.5 : The flowchart used for the determination of broken bonds to define micro-cracks.....	77
Figure 5.6 : The damaged material points and the crack line in OVITO.....	78
Figure 5.7 : Wire sections generated with the script given in Appendix E. <i>ndivx</i> and <i>ndivy</i> are (a) 31, (b) 61, and (c) 91.	79
Figure 5.8 : 3D view of a 1x6 wire rope with 1/2 lay length and contacts.	80
Figure 5.9 : 3D view of a wire rope subjected to impact load.	80
Figure 5.10: Dimensions of a single wire subjected to impact load.	81
Figure 5.11: Convergence tests setup in 1-D for simplicity: (a) m-convergence (constant $\delta = 0.003$ m), (b) δ -convergence (constant $m = 3$).	83
Figure 5.12: The discretized wire section with two pre-cracks for horizon size $\delta = 0.003$ m at the initial state.	85
Figure 5.13: The crack propagation for horizon size $\delta = 0.003$ m at $47.9 \mu\text{s}$ (550th time step).	86
Figure 5.14: The crack propagation for horizon size $\delta = 0.003$ m at $60.9 \mu\text{s}$ (700th time step).	87
Figure 5.15: The crack propagation velocities of m-convergence test cases between 17.4 and $56.6 \mu\text{s}$	88
Figure 5.16: Displacement in the y-direction of m-convergence tests along the central x axis at $56.6 \mu\text{s}$	89
Figure 5.17: The discretized wire section with two pre-cracks for $m = 3$ at the initial state.....	91
Figure 5.18: The crack propagation for $m = 3$ at $47.9 \mu\text{s}$ (550th time step).....	92
Figure 5.19: The crack propagation for $m = 3$ at $60.9 \mu\text{s}$ (700th time step).....	93
Figure 5.20: The crack propagation velocities of δ -convergence test cases between 17.4 and $47.9 \mu\text{s}$	94
Figure 5.21: Displacement in the y-direction of δ -convergence tests along the central x axis at $47.9 \mu\text{s}$	95
Figure 5.22: The wave propagation on the case with $m = 3$ and $\delta = 0.003$ m.	97
Figure F.1 : The wave propagation on m-convergence tests with $\delta = 0.003$ m during between 0 - $13.1 \mu\text{s}$	135
Figure F.2 : The wave propagation on m-convergence tests with $\delta = 0.003$ m during between 17.4 - $30.5 \mu\text{s}$	136
Figure F.3 : The wave propagation on m-convergence tests with $\delta = 0.003$ m during between 34.8 - $47.9 \mu\text{s}$	137
Figure F.4 : The wave propagation on m-convergence tests with $\delta = 0.003$ m during between 52.2 - $60.9 \mu\text{s}$	138
Figure G.1 : The wave propagation on δ -convergence tests with $m = 3$ during between 0 - $13.1 \mu\text{s}$	139

Figure G.2 : The wave propagation on δ -convergence tests with $m = 3$ during
between 17.4-30.5 μs **140**

Figure G.3 : The wave propagation on δ -convergence tests with $m = 3$ during
between 34.8-47.9 μs **141**

Figure G.4 : The wave propagation on δ -convergence tests with $m = 3$ during
between 52.2-60.9 μs **142**

CONSTITUTIVE FAILURE MODELLING AND ANALYSIS OF STEEL WIRE ROPE STRUCTURES SUBJECTED TO IMPACT LOADING

SUMMARY

Dynamic fracture is an important research topic in the science of fracture mechanics. The crack initiation and propagation is a problem that has received considerable attention because of its technical consequences. In case of impact loading and related failure mechanism both in macro- and micro-level should be carefully investigated. An impact load may adversely affect the system's operation, especially in cases where brittle structural elements are subjected to this load. Besides, brittle materials have advantages such as hardness and wear resistance, their deficiencies in terms of toughness and brittleness significantly restrain their usage in practice. This is the main reason that the problem of crack propagation at both macro- and micro levels is a problem of frequent discussion in the recent literature.

The dynamic fracture behaviour of brittle materials that contain micro-level cracks were examined when material subjected to impact loading. The investigation on the effect of micro-cracks on the crack propagation was carried out in the first step. The macro-crack initiates from notch tips in the Kalthoff– Winkler experiment, a classical impact problem. A micro-crack cluster was designed to decelerate this crack propagation. To define pre-defined micro-cracks in three-dimensional space, a two-dimensional micro-crack plane definition was proposed in the bond-based Peridynamics (PD).

PD is a non-local form of classical continuum theory. Randomly distributed micro-cracks with different number densities in a constant area and number in expanding area models were examined to monitor the toughening of the material. The velocities of macro-crack propagation and the time required for completing fractures were considered in several pre-defined micro-cracks cases. It has been observed that toughening mechanism only initiates by exceeding a certain number of micro-cracks; therefore, it can be said that there is a positive correlation between the density of pre-defined micro-cracks and macro-crack propagation rate and, also, toughening mechanism.

The classical impact problem was explained in details and then, wire rope structures that one of the most important elements in material handling were examined. The complexity of material handling area needs to manage many different machine and equipment. Therefore, accidents can inevitably occur in these areas. However, in general, there are further factors that affect the failure of ropes in an accident. Wire ropes are designed for static axial loading owing to its nature of structure. In that manner, an impact load can result in an undetermined mechanical response of the rope. Moreover, corrosion, insufficient lubrication, porosities in the working area, and wear can decrease the strength of wire ropes. The lifetime prediction of a rope system is a very complicated task because of the complex structure of ropes and different

loading conditions. However, to determine the reliability of material handling require more specific information about each element. With the help of proposed methods and findings in Kalthoff-Winkler problem, a theoretical scheme of analysing cable systems and wire ropes subjected to impact load with peridynamics was handled. Numerical studies were carried out, and the simulation parameters were discussed. It can be estimated that the failure of a wire in a strand does not affect its neighbours, because crack propagation in a wire cross-section ends at the outer surface of that wire. The resulting stress concentration that will cause crack propagation in adjacent wires is not observed. However, of course, there is some local transition of the load should be taken into account because of inter-contact states between wires. With regard to this, the work presented in this study can be extended to examine the inter-contact interaction between wires.

As a consequence, the effect of micro-cracks on a macro-crack propagation was investigated in Kalthoff-Winkler problem. The one most obvious finding to emerge from this study is that the less than a certain number of randomly located micro-cracks around the crack tip has no positive effect on fracture toughening mechanism. Nevertheless, adding more amounts of pre-defined micro-cracks in the same region can decrease crack propagation velocity and significantly increase the toughness. The second major finding was that there needs a certain number of micro-cracks for occurring of toughening effect. This study has found that an insufficient number of micro-cracks cannot decelerate the propagation of cracks. A certain number of micro-cracks should be placed in the body in order to obtain the toughening effect. In general, therefore, it seems that the density of micro-cracks in a constant area and the number of micro-cracks in expanding areas are significant parameters on toughening mechanism in a brittle material subjected to impact load. The findings of this investigation complement those of earlier studies. These findings support the PD's competence as an alternative to classical continuum mechanics for modelling of fracture and thus, designing of strengthen geometries. Although the study has successfully demonstrated that crack propagation and fracture characteristics, it has certain limitations in terms of properties of micro-cracks.

Dynamic crack propagation and failure in a wire cross section were studied. The programs used in the study were evaluated. Developed scripts that can be useful for further researchers were provided. Compared with average velocities in m -convergence tests, velocities in δ -convergence tests differentiate much more. It can be inferred that the minimum value of m (as an indicator of material points within a horizon) should be 3 for the models with given parameters and dimensions. The average velocities of $m = 3, 4$, and 5 models are very close to each other. The data for $\delta = 0.00450$ test should be considered an outlier because the crack did not propagate in contrast to other models. This result indicated that the horizon value, $\delta = 0.00450$ is not applicable for the model with given parameters. With the understanding of wave progression and mode transition relation, the model $\delta = 0.0015$ can be considered as a better parameter choice for the given model. The Mode I crack opening transition in the reference model indicates a routing of the crack in horizontal direction. These findings are thought of as a basis for the simulation of fracture mechanisms in wire ropes with PD.

ÇELİK TEL HALAT YAPILARININ DARBE YÜKÜ ALTINDA HASAR MODELLENMESİ VE İNCELENMESİ

ÖZET

Dinamik kırılma, kırılma mekaniği biliminde önemli bir araştırma konusudur. Çatlak başlangıcı ve ilerlemesi, sonucunda meydana gelecek hasarlar ve neden olacağı kazalar nedeniyle incelenmesi gereken bir sorundur. Darbe yükü ve sonucunda meydana gelen hasarın mekaniği hem makro hem de mikro düzeyde araştırılmaya ihtiyaç duymaktadır. Özellikle kırılma yapı elemanları darbe yüküne maruz kaldıklarında meydana gelen ani hasarlar nedeniyle sistemin çalışması beklenmedik bir anda olumsuz etkilenebilir. Gevrek malzemeler sertlik ve aşınma direnci gibi avantajlara sahip olmalarına rağmen, tokluk ve kırılma açısından eksiklikleri, pratikte kullanımlarını önemli ölçüde kısıtlamaktadır. Bu nedenle hem makro hem de mikro düzeyde kırık oluşması ve ilerlemesi sorunu geçmiş ve güncel literatürde sıkça tartışılan bir konu olmuştur. Bu kapsamda, bu çalışmanın amacı, genel olarak kırılma malzemelerinde, özel olarak ise çeşitli çevresel koşullar ve etkiler nedeniyle gevrekleşen ve darbe yüküne maruz kalan halatların hem mikro hem de makro düzeyde malzeme içinde bulunan çatlakların da etkisiyle dinamik kırılma davranışlarının incelenmesi ve hasar modellenmesi için parametrelerin belirlenmesidir. İlk olarak klasik bir darbe deneyi olan Kalthoff-Winkler deneyi ile başlanmıştır. Ardından bu modelde kullanılan yöntemler ve elde edilen sonuçlar ile halat hasarı modelleri geliştirilmiştir.

Çalışmayı bölüm bazında incelemek gerekirse, 1. Bölümde kırılma mekaniği hakkında literatürde mevcut bilgiler taranmış ve bir özet sunulmuştur. Kırılma mekaniğinin incelenmesi ve problemlerinin çözülmesinde sunulan teorik yaklaşımlar ve malzeme modelleri anlatılmıştır. Ayrıca, kırılma modları, dalga yayılımı, çatlak başlangıcı ve ilerlemesi ve mikro-kırık toklaşma mekanizması incelenmiştir. Kırılma mekaniğinde ortaya konan modellerin analitik çözümlerinin oldukça zor olması nedeniyle kullanılması zaruri olan sayısal modeller özetlenmiştir. Bölüm sonunda çalışmanın amacını ve ana hatlarını içeren başlıkların kısa bir özeti sunulmuştur.

Metodolojinin açıklandığı 2. Bölümde, Peridinamik (Peridynamic) teorisi anlatılmıştır. Peridinamik kavramı bir noktanın civarındaki diğer noktalarla aralarında kuvvet bağı olduğu duruma ithafen, Yunanca *peri* (yakında, çevresinde) ve *dinamik* (kuvvet) kavramlarının birleştirilmesiyle oluşturulmuştur. Klasik sürekli ortamlar mekaniğinde malzemedeki herhangi bir noktaya etkiyen kuvvetler, ayrıklaştırmaya bağlı olarak, en yakınındaki diğer noktalardan kaynaklanmaktadır. Örneğin bir boyutlu uzayda bir noktanın iki adet komşusu bulunmaktayken, üç boyutlu uzayda etki kaynağı altı nokta bulunmaktadır. Bu anlamda klasik teori yerel (local) olarak tanımlanır. Peridinamik teori ise yalnızca en yakındaki noktaların değil, belirli bir hacim içindeki diğer noktaların da etkisini denkleme dahil eder. Bu, teorisinin yerel olmayan (non-local) olmasını sağlar. Hareket denkleminin yapısının hacimsel integral üzerine kurulmuş olması özellikle süreksizlik ortamlarında teoriyi klasik yöntemlere göre avantajlı konuma getirir. Bununla birlikte Peridinamik model, integrale dayanan

yerel olmayan yapısı sayesinde özellikle kırılma mekaniği problemlerinin çözümünde sonlu elemanlar ağının her adımda tekrar oluşturulma (remeshing) gerekliliğini ortadan kaldırmış olur. Çatlak ve kırık tanımlamak, oluşturmak ve ilerlemesini gözlemek malzeme noktaları arasındaki bağların ortadan kaldırılmasıyla kolayca mümkündür. Teori, günümüzde hem mikro hem de makro ölçekte yaygın bir kullanım alanı bulmuştur. Henüz beta sürümleri yayınlanmasına rağmen bazı ticari analiz programlarında kullanılmaya başlanmıştır. Bazı özel teknikler ile sonlu elemanlar için geliştirilmiş programların Peridinamik teori çerçevesinde çalıştırıldığı örnekler de bulunmaktadır. Özetle bu bölümde, teorinin temel hareket denklemi, hasar modeli, kırık tanımlama, incelenecek malzemenin malzeme noktalarına bölünmesi (ayrıklaştırma) ve yakınsama problemleri açıklanmıştır. Bu kapsamda Peridinamik teorisinin dinamik kırılma mekaniği problemlerinde uygulanabilirliği incelenmiştir. Teori kapsamında çatlak oluşturma için genel bir algoritma ve program sunulmuştur.

Yapılan literatür araştırmalarında, mikro-çatlakların, darbe yüküne maruz kalan bir malzemedeki çatlak ilerlemesi üzerindeki etkisinin araştırılmasının sınırlı kaldığı görülmüştür. Bu kapsamda 3. Bölümde, klasik bir darbe deneyi olan Kalthoff-Winkler problemi ele alınmıştır. Metodoloji bölümde tanıtılan Peridinamik teori, mikro çatlakların dinamik çatlak ilerlemesi üzerindeki etkisini anlamak için bu problemde kullanılmıştır. Bu bölüm özetle, rastlantısal olarak malzeme içinde bulunan kusurların (mikro-çatlaklar) Kalthoff-Winkler deneyi özelinde, toklaşma mekanizmasına etkisi incelemiştir. Bu amaçla, PD için geliştirilen iki boyutlu bir çatlak tanımı ile malzeme içinde çok sayıda mikro-çatlak oluşturulmuştur. Ardından, dinamik çatlak ilerlemesi ve basınç dalgalarının darbe yükü ile malzemedeki ilerlemesi birlikte değerlendirilmiş ve çatlak ilerleme hızı gösteren grafikler sunulmuştur. Bu bölümde elde edilen en önemli bulgulardan biri, çatlak ucunun çevresinde rastgele yerleştirilmiş mikro-çatlakların, belirli bir sayıdan az olması durumunda kırılma toklaşma mekanizması üzerinde olumlu bir etkisinin olmamasıdır. Bununla birlikte, aynı bölgeye daha fazla miktarda mikro-çatlak eklemenin, çatlak yayılma hızını azaltabildiği ve dolayısıyla tokluğu artırdığı görülmüştür. İkinci önemli bulgu, sertleştirme etkisinin meydana gelmesi için belirli sayıda mikro çatlaklara ihtiyaç olduğudur. Yetersiz sayıda mikro-çatlağın ana çatlakların yayılmasını yavaşlatamayacağı gözlenmiştir. Toklaşmayı sağlamak için malzeme içinde belirli sayıda mikro-çatlak yerleştirilmelidir. Genel olarak, bu nedenle, sabit bir alandaki mikro çatlak sayısının yoğunluğunun ve büyüyen alanlardaki mikro-çatlak sayısının, darbe yüküne maruz kalan kırılma malzemedeki sertleşme mekanizması üzerinde önemli parametreler olduğu görülmektedir. Bu bölümdeki bulguların önceki çalışmalarda yer alan bulgularla uyumlu olduğunu gösteren karşılaştırmalar bölüm sonunda verilmiştir.

4. Bölümde tel halat yapıları incelenmiştir. Çelik tel halatlar, kaldırma ve taşıma makinalarında kullanılan önemli elemanlardan biridir. Yük taşımaları nedeniyle düzenli bir bakım programıyla gözetim altında tutulmalarına ihtiyaç vardır. Genel olarak kaldırma ve taşıma yapılan alanlarında bulunan her makina ve ekipmanın düzenli ve organize bir yönetim altında bulunması gereklidir. Bu organizasyonun sağlıklı bir şekilde sağlanmadığı durumlarda kazaların meydana gelmesi kaçınılmazdır. Yine de genel olarak, bir kazada halatların hasar görmesini etkileyebilecek temel yapısal faktörlerden bahsetmek gerekir. Çelik halatlar, yapıları gereği statik eksenel yükleri taşımak için tasarlanmıştır. Bu nedenle darbe yükünün etkimesi halatın mekanik tepkisinde belirsizliğe yol açabilir. Ayrıca literatürdeki yayınlar ve saha koşullarında yapılan incelemelerde gözlemlendiği üzere, korozyon,

yetersiz yağlama, çalışma alanındaki kirlilik ve aşınma halatların mukavemetini düşüren ve dolayısıyla ömrünü önemli ölçüde azaltan faktörler olarak öne çıkmaktadır. Bir halat sisteminin ömür tayini, halatların karmaşık yapısı ve farklı yükleme koşullarına verdikleri farklı tepkiler nedeniyle çok karmaşık bir hal alabilir. Bununla birlikte, bir kaldırma/taşıma makinasının hem güvenliğini hem de güvenilirliğini sağlamak için sistemdeki her bir elemanın bakım ve olası hasar durumlarına ilişkin bilgilerin tam olması gerekir. Bu kapsamda, bu bölümde yapılan araştırmalar özetlenmiş ve problemin tanımı yapılmıştır.

Ardından gelen 5. Bölümün başında, kullanılan modellerin kodlanması ve analizi hakkında bilgi verilmiştir. Genel olarak çalışmada yer alan simülasyonların bilimsel olarak tekrarlanabilir olmasını sağlamak amacıyla kullanılan kodlar paylaşılmıştır. İlk olarak, Kalthoff-Winkler problemi için Madenci ve Oterkus'un Peridynamic Theory and Its Applications kitabında sundukları Fortran kodu ele alınmıştır. Peridinamik ve benzer diğer sayısal yöntemlerin çözümünde birçok programlama dili kullanılabilir. Fortran diline aşina olmayan kullanıcılar için Matlab kullanımı önerilebilir. Ancak aynı işi yapan bir Matlab kodunun, en azından bu örnekte, Fortran kodu kadar hızlı çalışmayacağı unutulmamalıdır. Matlab'ın kolay bir kullanım sunan paralel hesaplama yeteneği bu hızı arttırabilir ancak yine de Fortran, hızlı bir hesap makinası olarak öne çıkmaktadır. Matlab ise oldukça kullanıcı dostu bir ortam sunmaktadır. Bir yorumlayıcı (interpreter) olması nedeniyle, yazılan kodun derlenmesine (compiling) ihtiyaç duyulmamaktadır. Bu nedenle, hata ayıklama süreci yeni bir programcı için daha kolay olabilir. Dahası, Matlab'da bulunan görselleştirme araçları, kullanıcıların geometrileri ve model sonuçlarını kolay ve hızlı bir şekilde kontrol etmesini sağlar. Sayısal modelleme çalışmaları için farklı programlar ve programlama dilleri önerilebilir. Ancak ilk adımda, özellikle hızlı görüntüleme olanakları nedeniyle Matlab ile başlamak faydalı olabilir. Fortran ve Matlab kodlarının benzerliği ve kendi aralarında kolay dönüştürülebilir olmaları da büyük bir avantajdır. Bununla birlikte, Matlab'da kodun son haline getirilmesinin ardından, tüm komut dosyasının Fortran dilinde derlenmesi, hız amacıyla tavsiye edilir. Peridinamik model sonuçlarının görüntülenmesi için Matlab kullanılabileceği gibi Ovito adlı başka bir alternatif de bulunmaktadır. Bu bölümde Ovito ve Matlab ortamında sonuçların grafiğe dökülmesi ayrıntılı olarak açıklanmıştır. Yine bu bölümde açıklandığı üzere, eklerde tezde kullanılan ve sonuçları görüntüleme amaçlı bir Matlab kodu, koddan elde edilen Matlab kodlarını Ovito programına aktarmak için bir Matlab dönüştürücü kodu, model sonuçlarını zamana bağlı şekilde kaydetmek için bir Fortran kod parçacığı ve son olarak halat kesiti modellemesinde kullanılan bir Matlab kod parçacığı sunulmuştur. Paylaşılan kod parçacıklarının Peridinamik ve benzeri sayısal modeller kullanan araştırmacılar için faydalı olması amaçlanmıştır.

Bölümün ikinci kısmında 4. Bölümde yapılan araştırmalar neticesinde ortaya çıkan simülasyon modelleri ortaya konmuştur. 5. Bölümdeki çalışmalar, 3. Bölümde kullanılan yöntemin ve geliştirilen modellerin doğruluğunun test edilmesi ve yapılan çıkarımlar ile ilerlemiştir. Kalthoff-Winkler probleminde kullanılan yöntemler ve bulgular yardımıyla, darbe yüküne maruz kalan halat sistemleri ve tel halatların Peridinamik ile analiz edilmesine yönelik teorik bir altyapı çalışması yapılmıştır. Sayısal çalışmalar yapılmış ve simülasyon parametreleri tartışılmıştır. Burada, halat kırılma modelinde farklı durumlar için verilen ortalama çatlak ilerleme hız tablosu değerlendirilmiştir. Buna göre m-yakınsama çalışmalarından elde edilen sonuçlara göre, verilen ölçülerde bir halat kesiti için gelecek çalışmalarda $m = 2$ değerinin

kullanılmaz olduđu, ancak modelin $m = 3, 4$ ve 5 deęerlerinde daha iyi sonuçlar verdiđi, horizon yakınsama testlerinde $0,0045$ deęerinde çatlak ilerlemesi olmadıđı, ancak küçülen horizon deęerinin çatlak ilerlemesini farklı hızlarla da olsa sağladıđı görülmüştür.

Tezin son bölümü olan 6. Bölüm, yapılan çalışmaların bir özetini ve elde edilen sonuçların yorumlanmasını içermektedir. Çatlak ilerleme hızlarının malzeme içindeki dalga yayılımı ve kırılma modlarıyla olan ilişkileri tartışılmıştır. Son olarak, yapılan çalışmaların deęerlendirilmesi ile birlikte gelecek çalışmalar için tavsiyelerde bulunulmuştur.

1. INTRODUCTION

The study of strength of materials is used to determine the behaviour of a solid during material selection, analysis, and design processes. A design is assumed to be suitable if applied stress is under the yield or ultimate strength depending on failure criteria. Considering very small displacements and deformations in a body, the theory of elasticity is a convenient method for most of materials [1]. However, a crack or flaw in a solid increases stresses in the tip of crack and that may result in the classical approach unusable. Therefore, the relationship between applied stress, flaw size, and fracture toughness are used to determine the strength of a material in the fracture mechanics approach. Crack is a line or surface in a body which has split without breaking into separate parts. Fracture (or damage) is the local separation of a body into two or more pieces. If the stress intensity factor calculating with the applied stress, crack, and part dimensions, exceeds the material fracture toughness, the fracture grows suddenly, which causes damage in the material [2].

Material properties affect which fracture mechanics approach is applicable for a certain material. Linear Elastic Fracture Mechanics (LEFM) consider only elastic deformation for either quasistatic or time-dependent (dynamic fracture) conditions. On the other hand, plastic deformation under quasistatic conditions is analysed with Elastic-Plastic Fracture Mechanics (EPFM). Dynamic, visco-elastic, and visco-plastic fracture mechanics include time as a variable and they are expressed as a general heading of non-linear fracture mechanics [2].

1.1 Dynamic Fracture Mechanics

Dynamic fracture is an essential topic in the science of fracture mechanics. However, it is recognizable only by understanding of the relation between requiring energy for fracture and the material strength in the macroscopic world [3]. Rapid crack propagation with low energy release characterizes the dynamic brittle fracture. It also shows very little plastic and/or viscoelastic deformation before failure occurs [4].

An engineering material shows different damage and failure characteristics under various loading rates, such as crack curving, crack branching, fragmentation, spallation, and delamination [4]. In that manner, it has been widely studied with computer simulations and experiments for years. Inertial effects are principal when the speed of crack tip is lower than stress wave velocity during the propagation process [3]. Although the crack advances quasistatically at the macroscopic scale, separation of each atom from another must be determined in the atomic scale. This condition is a fundamental of crack propagation. There are various mechanisms of non-linear damage in dynamic fracture. In the microscopic scale, granulation, void growth and coalescence in the failure were spotted in the failure of ductile materials [3]. The dynamic fracture may be appropriately defined at the macroscopic scale if non-linear constitutive laws can be formed for these phenomena.

1.1.1 Fracture modes

Three different load modes can be defined in fracture mechanics, as shown in Figure 1.1 [2]. In the first mode (Mode I), the governing force is applied in the normal direction to the crack surface. The tensile stress causes an opening in the body. The second mode (Mode II) is the sliding mode and termed as in-plane shear. In this case, shear stress governs crack propagation. It is acting parallel to the crack plane and it is also perpendicular to the crack front. The last mode (Mode III) is the tearing mode and termed as the out-of-plane shear state. The stress is acting parallel to the crack plane and crack front.

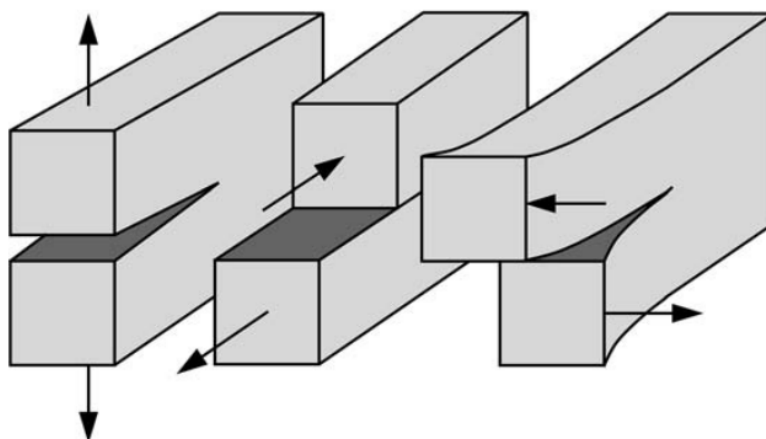


Figure 1.1 : Three crack modes with regard to the loading conditions in fracture mechanics: Mode I (Opening), Mode II (In-Plane Shear), and Mode III (Out-of-Plane Shear).

1.1.2 Wave propagation

One of the essential factors in the dynamic brittle fracture is wave propagation and interaction with cracks as they form the evolution of damage and fracture modes in brittle solids [4]. Various dynamic experiments were performed to understand the effect of stress wave during crack initiation and arrest, crack branching and curving [5]. Stress waves are reflected from the back surface, so this effect on cracks causes more spalling and fragmentation in brittle material under impact loading [6]. Advancing of crack front and transferring dynamic stress during crack propagation were modelled by a basic mathematical tool in [7,8]. Crack front waves were studied to develop a generic dynamic crack by these models in [9, 10]. It was shown that a localized disturbance of advancing of a crack front could propagate without delay along the crack front. Thus, the crack front wave was defined differently, except from classical longitudinal, shear, and Rayleigh wave modes [3]. Self-affine fracture surface roughness in both dynamic and static loading may be affected by crack front waves [11]. However, the observed exponent of scale dependence was not predicted in crack front wave theory [11]. In [12], it was stated that solitary waves could be evaluated as crack front waves. However, solitary waves may result from an interaction between shear waves and the crack front [13]. Guo and Gao [14] explained the crack propagation and dynamic failure according to the wave propagation.

1.1.3 Crack initiation and propagation

The crack propagation has been a question for fracture mechanics. In a single crack application, critical stress intensity factors and energy release rate are essential in practice. However, an energy condition may predict the wrong crack path in quasistatic loading and a controlling stress singularity is not a realistic view of crack tip state in these cases. A quasistatic fracture criterion was not agreeable with calculations of static behaviour but dynamic state, because of crack front waves and its possible effect on fracture surface roughness [3]. Kalthoff identified the failure mode transition state related to cracks in an experimental work [15]. A shear loaded crack may advance under local opening (Mode I) conditions by deviating through a kink angle or by forming a shear band along its initial direction (Mode II) depending on the impact

velocity. This transition means that velocity was effective in the failure criterion, which was observed for various metallic alloy [16] and polycarbonate [17,18]. Critical Mode II fracture toughness was proposed as a criterion [19]. Therefore, fracture surface roughness affects the Mode II toughness and there is a connection between crack front stability and crack front waves. It was stated in an early work that there was a strong relationship between the crack-tip stress intensity factor and the onset of crack propagation [5]. Thus, to determine the critical toughness as a material constant and measure it like fracture toughness, a standard experiment was suggested [20]. However, determining the time of initiation was a crucial difficulty. Because of placing a probe only on the surfaces, determining the moment of the submerged crack tip and stress state at a crack tip instantly were complicated. Initiation toughness is related to loading rate, but the effect of the material type is still unpredicted [3]. It was stated that initiation toughness increased with the loading rate for polymethylmethacrylate (plexiglass) material in [18].

1.1.4 Micro-cracks and toughening mechanism

Due to high stress concentrations, pre-existing micro-cracks appear in any type of materials [21]. Micro-cracks are significant dissipation mechanisms and they lead to the roughness of fracture surface [22–24], since they may act as nuclei for macro-cracks [3]. Therefore, the presence of micro-cracks around the tip of a macro-crack may lead to crack shielding or crack amplification and affect crack propagation significantly [25]. The amplification increases the stress intensity factors around the crack tip, whereas the shielding reduces them. Recent studies have stated that the micro-cracks and as a consequence, the shielding increases material toughness [26,27]. This phenomenon is mentioned as "micro-crack toughening" [28]. Location, orientation, and density of micro-cracks significantly alter the toughening mechanism and crack propagation due to changes in stress intensity around the main crack [29–31]. The formation of the damage zone was modelled [32,33] and spatial averaging was used to develop a cohesive law that reduced the non-linear material to a line of displacement discontinuity. Crack branching and the macro and micro-cracks interaction during crack growth was investigated in [34–37] and effects of crack closure were taken into account. In these studies, the relation between toughness and crack

velocity was explained with micro-cracking. An upper limit for the crack velocity was predicted as lies below the speed of Rayleigh wave. The earlier experimental and theoretical findings [38–40] were agreed with them. Examining the effect of non-uniformly arranged micro-cracks with analytical approaches is rather complicated due to complex mechanical behaviour [28]. Some analytical solutions were presented for uniformly distributed micro-cracks [41–45]. Several researchers investigated the effect of micro-cracks on the propagation of the main crack and obtained solutions with analytical approximations under certain restrictive assumptions [29, 41, 46, 47]. Tamuzs and Petrova [48] presented a review of studies that focus on problems and methods to investigate macro-crack growth in materials with micro-damages.

1.2 Modelling Approaches

There are different numerical approaches to simulate dynamic fracture such as, Finite Element Method (FEM), Discrete Element Method (DEM), Molecular Dynamics (MD), Boundary Element Method (BEM), and Peridynamics (PD). These methods have been used to model a mathematical representation of fracture modelling.

1.2.1 Finite Element Method

The equations of motion in continuum mechanics cannot be directly applied to the discontinuous field because the spatial derivatives in differential equations fail to exist when a discontinuity exists, such as a crack [4]. Thus, external criteria or special treatments are needed to introduce damage or cracks in such problems. Modifications on the classical models and FEM has been used to develop crack propagation and damage models to overcome those issues. FEM has been used with modifications such as cohesive-zone [49], element-erosion [50], and extended-FEM (XFEM) [51] to simulate crack propagation with a numerical approach.

XFEM resolves the mesh dependency problem [52]. Although XFEM was presented to analyse and simulate the dynamic crack propagation [52, 53], it increases the cost of simulations because of subdivision of cut elements for numerical integration [54]. Furthermore, branching criteria and artificial damage models are still required as input in this model. An interface damage model was studied to model the failure in matrix/fibre interfaces [55]. The crack needs to be tracked by using, for example,

level set [54]. The use of tracking of the crack path was studied in [56]. XFEM might not give a proper solution when fragmentation starts in the material. Although some researchers [57–64] stated that the XFEM is a useful method for simulating crack propagation, it is necessary to adjust the input fracture energy to precisely examine the dynamic fractures [65, 66]. Moreover, complexity and cost as a result of the sub-division of cut elements are other disadvantages of crack propagation modelling with XFEM [66].

The cohesive law implemented in finite elements was used in cohesive FEM. The cohesive zone model framework was first introduced by Dugdale [67] and Barenblatt [68]. Cohesive zone elements were developed to adapt the cohesive zone model in fracture mechanics [69, 70]. The cohesive zone elements usually placed between continuum elements can open to simulate crack initiation or crack propagation. However, the actual crack path should be defined first to place the cohesive zone elements. Pre-defining of the crack paths and damage modes are problematic due to the wave propagation and interaction with crack. Placing the cohesive zone elements as pre-defined is difficult because cascading branching or arresting the propagation of secondary branches can be formed in different material under the same loadings [71]. An additional problem is mesh dependency in cohesive zone finite element methods [72]. To allow a crack pass through the elements rather than along the element boundaries, enrichment functions (additional degrees of freedom) were added in discontinuous displacement field. The restriction of crack propagation path with element boundaries causes inaccurate results in element-erosion and the cohesive-zone techniques [65].

A stress-based continuum damage mechanics (CDM), the Sun-Khaleel model, was used to simulate fracture of glass impacted by solid particles [73]. The CDM model with a vanishing element technique explicitly took into account the strength degradation of glass. A large-scale classical molecular dynamics simulation was conducted to model the fracture of glass under hypervelocity impact load [74]. The initiation of fracture at the bottom of the plate was observed. Also, it was stated that fracture proceeded through the coalescence of nanopores or nanovoids created due to

the pressure wave emanating from impact. It was suggested that the FEM simulations could be used to extend such atomistic studies to macroscopic sizes.

1.2.2 Discrete Element Method

Rabczuk et al. [75] and Kostaski et al. [76] studied the dynamic crack propagation with Discrete Element Method (DEM). Braun and Fernández-Sáez [77] suggested a 2D discrete model and applied it to the benchmark problem in [19], though crack paths were lattice dependent for coarse meshes. Therefore, a more comprehensive and robust approach is a considerable requisite to determine crack nucleation, propagation, and interactions [28].

1.2.3 Molecular Dynamics

Another approach to dynamic fracture is atomistic modelling, such as Molecular Dynamics (MD) simulations. Dynamic fractures based on atomistic simulations were described briefly in [78]. The large-scale (exceeding one billion atoms) atomistic modelling of dynamic fracture was widely studied [79, 80]. However, it is difficult to model the original geometry because MD simulations can be applicable on only small scales bodies in a relatively short time. Using very high loading rate to accelerate simulations causes unrealistic results. Although MD can provide necessary information about the process of dynamic fracture, it still cannot achieve predictive capabilities for dynamic fracture [3]. On the other hand, MD simulations can predict dynamic fracture of the entire structure precisely, to obtain stress wave reflections from boundaries [54]. A sufficient high loading can lead to unstable crack path and cracks cannot branch with a certain criterion [54, 81]. However, the speed of crack propagation and the angle of crack branching were not captured correctly. For instance, the crack propagation of only one of the two branches and the other being blocked causes instabilities in MD simulations [54].

1.2.4 Boundary Element Method

Boundary element methods were used to analyse an arbitrary crack path and micro-crack formation, crack branching, crack closure and friction for the macroscopic problems [82, 83].

1.2.5 Peridynamics

Silling and Askari [84] presented Peridynamics (PD) method, which naturally involves crack modelling, nucleation, and progression in a continuum, thus overcoming the deficiencies of classical numerical approaches. Silling [85] established PD as a non-local form of continuum mechanics. PD is a non-local formulation in an integral form in contrast to the local differential form of classical continuum mechanics [86]. Figure 1.2 [87] shows a comparison of classical continuum mechanics (CCM) as a local form, peridynamics (PD) as a non-local form and molecular dynamics (MD). In Figure 1.2(a), a material point can only interact with the near neighbours. This is why the classical continuum model is defined as "local". In contrast to local theory, the material point can interact with the points within a certain range in non-local theory. Figure 1.2(b) represents Peridynamics as a non-local model. From this perspective, the non-local theory is a kind of molecular dynamics model. When the radius that limits the interaction between material points, is determined as infinitely large, the non-local theory can be called a continuous version of MD model (Figure 1.2(c)) In general, therefore, it seems that the non-local theory in a continuous body can be defined as a bridge between CMM and MD models.

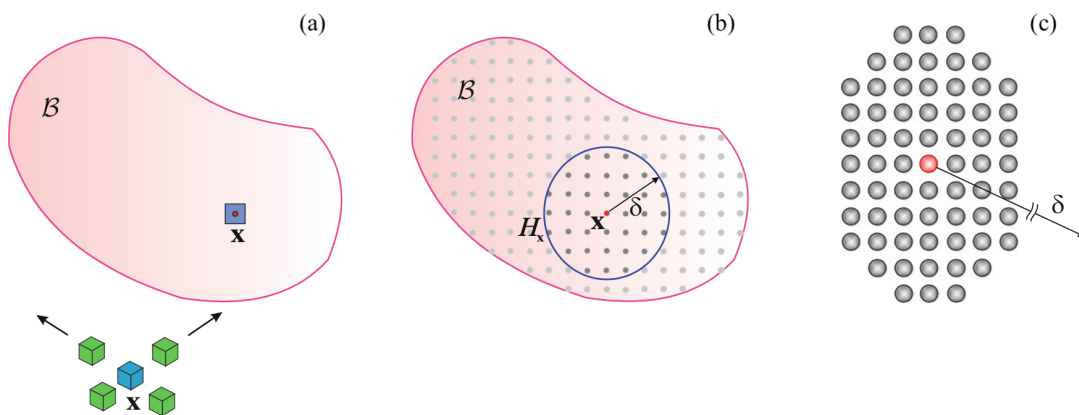


Figure 1.2 : Comparison of (a) Classical (local) continuum mechanics, (b) Peridynamics and (c) Molecular dynamics.

In Figure 1.2 (a), the point x in the body B , has interaction with the other points adjacent to itself. In continuum mechanics, the number of neighbour points is normally 3, 5, and 7 (including itself) for one, two, and three dimensional space, respectively. However, in PD the point x can establish bonds with the points located within a distance δ . Neighbour points in this distance, δ are called as family members of x in

the horizon \mathcal{H}_x . As a nature of non-local theory, the number of family members can be more than in local theory's and it depends on the horizon. Overall, in PD, a continuum body is defined with material points with a volume in space. Each material points can interact with points located with a certain distance that is defined as the horizon. The interaction forces between a material point with other points in the horizon determine that material point's behaviour.

PD as a non-local continuum model is capable of solving dynamic fracture problems, and it does not require a pre-defined guide for dynamic crack propagation [85]. Since PD is based on integro-differential equations instead of spatial derivatives, it complies with problems comprising discontinuities such as cracks [85]. The equation of motion can be directly applied in discontinuous fields. To compute the total force density acting on a specific material volume, integration is used. Moreover, deformation gradients are not used in the formulation [54].

Silling and Lehoucq [88] conducted a convergence study of force densities of PD and the classical elasticity theory to examine the robustness and efficiency of the theory. Besides some researchers applied PD theory in different applications such as, nano-scale structures [89, 90], damage in composite materials under quasistatic, impact or shock loading [91, 92], damage analysis of viscoplastic materials [93, 94], dynamic fracture and crack branching in glass [71, 95], coupling of PD and FEM for failure prediction [96, 97], damage propagation in layered glass under impact loading [98], for anisotropic materials [99], problems of heat conduction [100, 101], cracks generated from corrosion pits [102], and examining composite laminates under explosive loading [103]. Madenci and Oterkus [87] published a book that consists of detailed.

1.3 Motivation of the Thesis

In dynamic fracture mechanics, fracture toughness is a material property that defines a material's characteristics under impact loadings. It describes the resistance of a material to fracture which affected by micro/macro- crack interaction. Rubinstein [41], Rose [29], Brencich and Carpinteri [26] presented analytical methods for investigation of micro/macro- crack interaction with uniformly distributed micro-crack patterns. The solutions that belong to the interaction of intricate micro-crack patterns are not widely

presented in the current literature [28]. One of the most recent studies on the effect of small cracks on a macro-crack propagation is presented in [104]. They provide a relation between various locations, density, and numbers of cracks and macro-crack propagation speed. The models considered in that study are single crack collinear to the main crack, two symmetrical cracks, and horizontal and transverse array of cracks. Another study carried out by Basoglu et al. [28] presents arbitrary micro-crack patterns using the same bond-based PD models. They observed that a crescent-like micro-crack distribution near the macro-crack tip cause the highest shielding effect and so that a considerable increase has shown in material toughness. In both studies, two-dimensional plates involving macro-cracks along their mid-axis are subjected to displacement-controlled tensile-load.

Effects of two-dimensional micro-cracks placed in a three-dimensional body on crack propagation need to be investigated to fill gaps in the literature. Moreover, recent studies have restricted to evaluate of the micro-crack toughening mechanism only with regularly pre-located micro-cracks. This study seeks to obtain data which will help to address these research gaps. One purpose of this thesis was to extend the Peridynamic theory to simulate the stochastically distributed micro-cracks around the macro-crack tip. In that manner, a realistic approach to investigate the relationship between the micro-crack toughening mechanism and crack propagation was aimed. Moreover, the problem described by Kalthoff and Winkler in [105, 106] was adopted to better understand the toughening effect in an impact problem. Part of the aim of this section is to develop a two-dimensional micro-crack script that is compatible with the numerical solution of Peridynamic theory. Thus, the Kalthoff-Winkler problem, widely known in the literature, was used to study the effects of micro-cracks on crack propagation. Moreover, a new two-dimensional crack generation script was developed to be used in numerical solutions of the Peridynamic theory. The investigation of crack propagation and studies on script development also provide a basis for wire rope analysis.

The problem of modelling steel wire ropes with finite elements has been widely addressed. There are two and three-dimensional finite element modelling and stress analysis studies in the literature. The commonly followed method deals with wire rope structures subjected to axial loading and bending forcing. Moreover, much of the current literature on wire ropes pays particular attention to static loading conditions.

Thus far, there is a relatively small body of literature concerned with dynamic loading due to the complexity of the structure. Although PD theory has been adopted in many applications since its development, it needs to be well analysed before being used in complex structures such as wire ropes due to many numerical modelling parameters. Since no commercial software has been produced and it has been implemented with codes written by individual researchers, firstly, convergence analyses should be conducted on studies of wire ropes. A wire rope structure subjected to transverse impact load was modelled within Peridynamic framework to carry out convergence studies. Two pre-defined crack surfaces were located in a section of a wire. A transverse load was applied to the wire section. The crack propagation velocity was considered to examine the effect of numerical parameters on the failure mechanism. These findings contribute in several ways to one understanding of dynamic fracture of wire ropes and provide a basis for modelling of wire ropes using Peridynamic. Numerical parameters thought to be influencing crack propagation have been explored for that purpose.

1.4 Outline of the Thesis

The theoretical structure of bond-based Peridynamic theory was explained in Chapter 2. The fundamental of the Peridynamic equation of motion was briefly reviewed. Damage modelling, crack definition, micro-crack creation, impact modelling, discretization scheme for the equation of motion formula, and convergence studies were described and discussed. The impact modelling in PD was formulated and convergence studies were presented. A flowchart and script to define the cracks or micro-cracks in the PD application were given and explained in detail in this chapter.

After general information related to Peridynamics in the literature, in Chapter 3, the bond-based Peridynamic model was adopted and used to investigate the effect of micro-cracks on the material toughness for a reference impact problem that defined by Kalthoff-Winkler in [105, 106]. Various simulations were carried out. The effective number of micro-cracks that causes the toughening effect was investigated in a constant area. Moreover, the number of micro-cracks that should be pre-built in the body in an expanding area was determined to obtain the toughening effect. Results of numerical studies and discussions are given.

Subsequently, in Chapter 4, a brief summary and literature survey on wire rope structure and modelling were introduced to remind the different aspects of modelling. The chapter starts with a brief failure mechanism analysis of wire ropes. Then, the structure and components of wire ropes and mathematical modelling studies were reviewed. An enhanced literature review was conducted to summarize the numerical models and reported test results in recent years. The detail definitions of the contact phenomena of wire ropes were stated.

In Chapter 5, which is the main body of the thesis study, a theoretical scheme of analysing wire ropes subjected to impact load with Peridynamic theory was proposed. The codes and used programs were given and explained. Then, a series of tests were carried out to examine the effect of transverse impact loading on wire rope cross-sections. The applicability of Peridynamic theory was studied with m -convergence and δ -convergence setups. A set of parameters for preparing wire rope to PD analysis were suggested. The results of models were evaluated and possible consequences of different parameters were discussed. These studies concentrated on crack propagation that caused by impact loading. The crack propagation velocities and fracture mode transitions were showed. The effect of compression waves on the crack propagation was investigated.

In the last part of the thesis, Chapter 6, after summarizing the studies done in general terms, Peridynamic theory applied to the rope structures and the results obtained were discussed. On the other hand, the thesis document was discussed by the author with the studies planned to be done in the future and its application to different problems.

2. METHODOLOGY

The fundamentals of Peridynamic theory and the methodology employed were explained in this chapter. The equation of motion, damage modelling, crack definition, discretization, and convergence schemes in Peridynamic theory were given. Moreover, a comparison study was conducted to compare Peridynamic theory with finite element analysis and analytical solutions.

2.1 Peridynamic Formulation

Silling [85] presented PD theory to overcome the problem of the mathematical framework that is inoperative for discontinuous situations such as crack formation in classical continuum mechanics. The use of partial derivatives to define the relative displacement and force between two particles results in the fact that the equations are naturally undefined in discontinuity regions. PD's equation of motion is based on integral equations, so that it is applicable for both continuity and discontinuity zones. In the bond-based PD theory, first presented in [85], force density vectors between two material points are equal in magnitude and being parallel. This formulation has been extended to state-based PD formulation by Silling et al. [107], which defines force density vectors as unequal in terms of magnitude.

The equation of motion in Peridynamic theory for any material point is given in [84]. It is the formulation of the acceleration of any point at \mathbf{x} at time t :

$$\rho \ddot{\mathbf{u}}(\mathbf{x}, t) = \int_{\mathcal{H}_{\mathbf{x}}} \mathbf{f}(\mathbf{u}(\mathbf{x}', t) - \mathbf{u}(\mathbf{x}, t), \mathbf{x}' - \mathbf{x}) dV_{\mathbf{x}'} + \mathbf{b}(\mathbf{x}, t), \quad (2.1)$$

where $\mathcal{H}_{\mathbf{x}}$ is a spherical region with radius (δ) called horizon, \mathbf{x}' is a family member of the material point \mathbf{x} inside its horizon, \mathbf{u} is the displacement vector, \mathbf{b} is the body load, ρ is the mass density, \mathbf{f} is the force vector that the material point \mathbf{x}' exerts on particle \mathbf{x} , and $dV_{\mathbf{x}'}$ is the infinitesimally small volume of point \mathbf{x}' .

The relative position vector between two material points in the undeformed state is denoted as

$$\boldsymbol{\xi} = \mathbf{x}' - \mathbf{x}. \quad (2.2)$$

The relative displacement vector after deformation in Figure 2.1 is denoted as

$$\boldsymbol{\eta} = \mathbf{u}'(\mathbf{x}', t) - \mathbf{u}(\mathbf{x}, t). \quad (2.3)$$

The current relative position vector in the deformed configuration [84, 87]:

$$\mathbf{y}' - \mathbf{y} = \boldsymbol{\eta} + \boldsymbol{\xi}. \quad (2.4)$$

Position and force vectors of two material points in the reference state and after deformation are shown in Figure 2.1. The \mathbf{x} is a material point and \mathbf{x}' is one of the family members of \mathbf{x} . The blue points represent the Reference positions of two material points. After the body that consists of these material points is deformed, the points relocated and presented with red points.

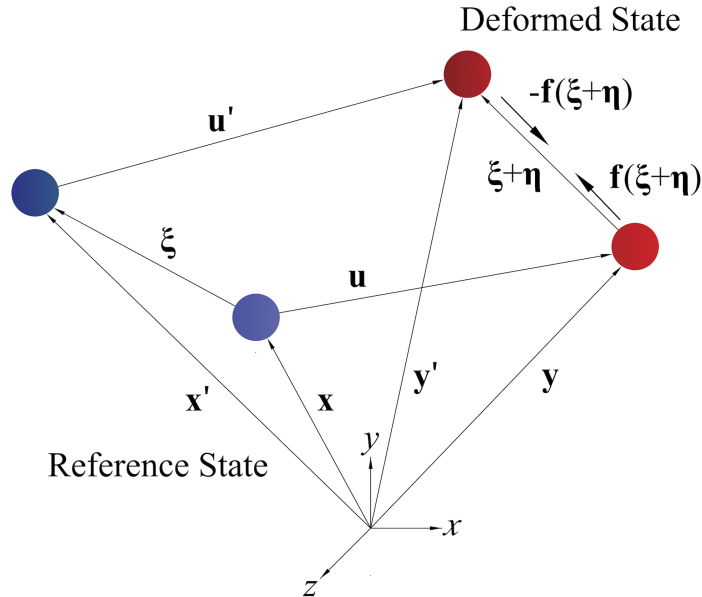


Figure 2.1 : Position and force vectors of two material points.

The interaction between material points \mathbf{x} and \mathbf{x}' is called a bond. A bond connects a material point to any other that only located in the horizon. The idea of extending a bond over a finite distance is the fundamental concept of PD theory. The material

points that build interactions are in direct contact with each other. For a given material point \mathbf{x} , there is a limit distance to create bonds, called the horizon with radius δ , such that

$$|\boldsymbol{\xi}| > \delta \Rightarrow \mathbf{f}(\boldsymbol{\eta}, \boldsymbol{\xi}) = 0 \quad \forall \boldsymbol{\eta}. \quad (2.5)$$

This formulation states that there is no connection between a point \mathbf{x} and material point outside the horizon. To make a connection and act the force between points, the relative position vector length, $|\boldsymbol{\xi}|$ should be smaller than δ . As shown in Figure 2.2 (reproduced from [89]), material points inside the horizon called a family member.

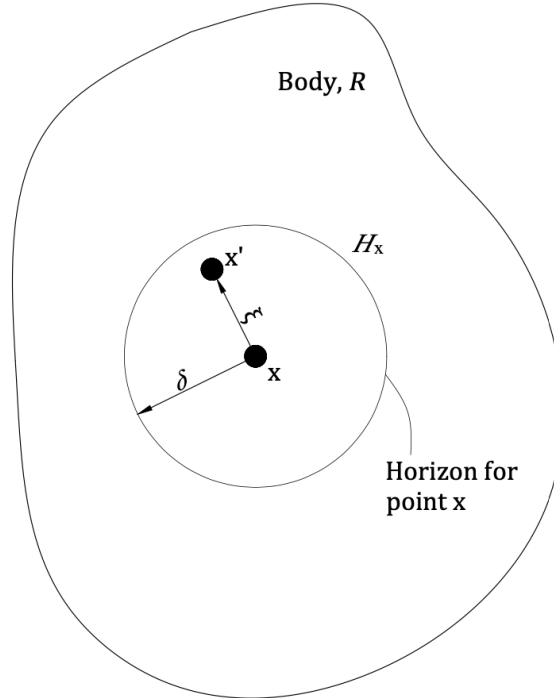


Figure 2.2 : A material point \mathbf{x} can only interact with a family member \mathbf{x}' in the horizon with radius δ .

The conservation of linear momentum is assured with the following properties of pairwise force function \mathbf{f} ,

$$\mathbf{f}(-\boldsymbol{\eta}, -\boldsymbol{\xi}) = -\mathbf{f}(\boldsymbol{\eta}, \boldsymbol{\xi}) \quad \forall \boldsymbol{\eta}, \boldsymbol{\xi}. \quad (2.6)$$

Moreover, the following formulation states conservation of angular momentum in PD,

$$(\boldsymbol{\xi} + \boldsymbol{\eta}) \times \mathbf{f}(\boldsymbol{\eta}, \boldsymbol{\xi}) = 0 \quad \forall \boldsymbol{\eta}, \boldsymbol{\xi}. \quad (2.7)$$

The given equation is the cross product of the pairwise force function vector and the relative current position vector. The result should be zero to make a parallel constraint between the force and position vector.

When a material is considered as micro-elastic, the pairwise force function can derive from a scalar micro-potential w ,

$$\mathbf{f}(\boldsymbol{\eta}, \boldsymbol{\xi}) = \frac{\partial w}{\partial \boldsymbol{\eta}}(\boldsymbol{\eta}, \boldsymbol{\xi}) \quad \forall \boldsymbol{\eta}, \boldsymbol{\xi}. \quad (2.8)$$

The local strain energy density can be calculated by the sum of micro-potentials. Because micro-potential refers to the energy in a bond. The unit is the energy per unit volume squared. The integral of micro-potential over a given volume, such as the horizon, gives the energy per unit volume in the body and the local strain energy density can be obtained follow as

$$W = \frac{1}{2} \int_{\mathcal{H}_x} w(\boldsymbol{\eta}, \boldsymbol{\xi}) dV_{\boldsymbol{\xi}} \quad \forall \boldsymbol{\eta}, \boldsymbol{\xi}. \quad (2.9)$$

The factor of 1/2 should be included in the equation because each material point only has half of the strain energy in a bond. It can be said that the bond between two material points can be evaluated as an elastic spring and a scalar micro-potential function in a single bond can be written as

$$w(\boldsymbol{\eta}, \boldsymbol{\xi}) = \frac{1}{2} c s^2 |\boldsymbol{\xi}|. \quad (2.10)$$

The bond-constant is obtained by comparing the energy densities of Peridynamic and classical continuum theory. They are given in one-, two-, and three-dimensional structures [87]. In three-dimensional space, the bond constant stated as

$$c = \frac{12E}{\pi \delta^4}, \quad (2.11)$$

where E is the elastic modulus or Young's modulus.

As stated in [87], a constraint condition of

$$\kappa = \frac{5\mu}{3} \quad \text{or} \quad \nu = \frac{1}{4}, \quad (2.12)$$

where κ is bulk modulus, μ is the shear modulus, and ν is Poisson's ratio, requires that in bond-based PD, the bond constant can be expressed as

$$c = \frac{30\mu}{\pi\delta^4} \quad \text{or} \quad c = \frac{18\kappa}{\pi\delta^4}. \quad (2.13)$$

The bond-stretch in equation 2.10 can be expressed as [87]

$$s = \frac{|\boldsymbol{\xi} + \boldsymbol{\eta}| - |\boldsymbol{\xi}|}{|\boldsymbol{\xi}|}. \quad (2.14)$$

The derivative of micro-potential gives the pairwise force function \mathbf{f} , as

$$\frac{\partial w}{\partial \boldsymbol{\eta}}(\boldsymbol{\eta}, \boldsymbol{\xi}) = \mathbf{f}(\boldsymbol{\eta}, \boldsymbol{\xi}) = \frac{\boldsymbol{\xi} + \boldsymbol{\eta}}{|\boldsymbol{\xi} + \boldsymbol{\eta}|} f(|\boldsymbol{\xi} + \boldsymbol{\eta}|, \boldsymbol{\xi}) \quad \forall \boldsymbol{\eta}, \boldsymbol{\xi}, \quad (2.15)$$

where f is a scalar-valued function and it is expressed as follows:

$$f(|\boldsymbol{\xi} + \boldsymbol{\eta}|, \boldsymbol{\xi}) = cs. \quad (2.16)$$

2.2 Damage Model in Peridynamics

In PD, the failure criteria can be considered as the bond is broken when the bond stretch s between two material points exceeds a pre-defined critical stretch value s_c . Considering a bond is not recoverable after failure, the history-dependent scalar valued step function $\mu(t, \boldsymbol{\xi})$ can be combined with the bond-force equation as

$$f(|\boldsymbol{\xi} + \boldsymbol{\eta}|, \boldsymbol{\xi}) = cs\mu(t, \boldsymbol{\xi}), \quad (2.17)$$

where

$$\mu(t, \boldsymbol{\xi}) = \begin{cases} 1 & \text{if } s(t', \boldsymbol{\xi}) < s_c \text{ for all } 0 \leq t' \leq t \\ 0 & \text{otherwise.} \end{cases} \quad (2.18)$$

Critical-stretch value s_c determines the maximum relative elongation value in which the bond forces still can be active. In linear-elastic model, the relation between relative elongation or stretch and bond force is linear, as shown in Figure 2.3 (reproduced from [89]). If the stretch of a bond exceeds the critical stretch value, the bond vanishes.

These bonds are not allowed to be repaired after breaking. Thus, the bond breaking or damage can be defined as irreversible and history dependent.

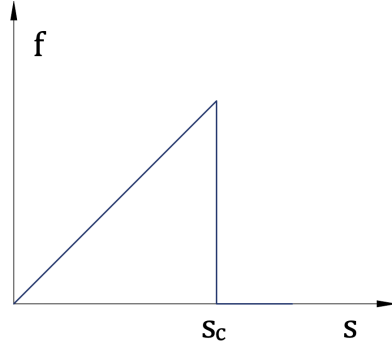


Figure 2.3 : Linear relation between critical stretch and bond force.

In order to determine the critical stretch for a particular material, the critical energy release rate can be used. Silling and Askari [84] derived the critical energy release rate for bond-based peridynamics. This formulation can be used to determine the critical stretch. The following integral is the summation of the work for terminating all interactions between material points located at different sides of fracture surfaces. The integral form of the critical energy release rate is

$$G_c = \int_0^\delta \left\{ \int_0^{2\pi} \int_z^\delta \int_0^{\cos^{-1} z/\xi} \left(\frac{1}{2} c \xi s_c^2 \xi^2 \right) \sin \phi d\phi d\xi d\theta \right\} dz. \quad (2.19)$$

Figure 2.4 [87] shows the points $\mathbf{x}_{(j^-)}$ and $\mathbf{x}_{(k^+)}$ that are placed on opposite sides of the fracture surface. The yellow area with (+) sign is the integral region. The integration in spherical coordinates, ξ, θ, ϕ provide the required work to diminish the connection between $\mathbf{x}_{(j^-)}$ and $\mathbf{x}_{(k^+)}$ in the spherical cap.

The integral formulation of critical energy release rate G_c becomes as follow in three-dimensional analysis,

$$G_c = \frac{1}{2} c s_c^2 \left(\frac{\delta^5 \pi}{5} \right). \quad (2.20)$$

Substituting for bond constants given by equation 2.13 gives the critical stretch as follow,

$$s_c = \sqrt{\frac{G_c}{\left(3\mu + \left(\frac{3}{4} \right)^4 \left(\kappa - \frac{5\mu}{3} \right) \right) \delta}}. \quad (2.21)$$

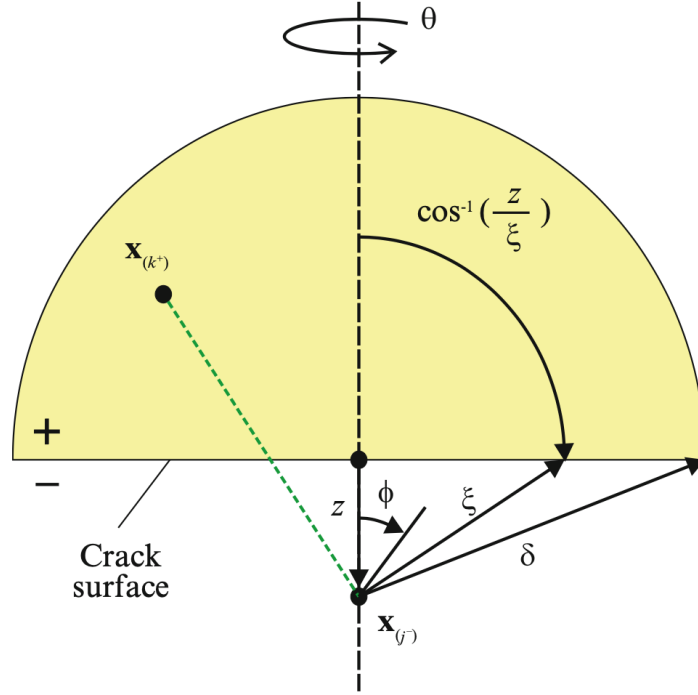


Figure 2.4 : Fracture surface and integration domain for critical energy release rate.

As stated by Madenci and Oterkus [87], this formulation shows that the critical stretch was found to be significantly associated with variable horizon, δ . Therefore, in PD theory, there is a relationship between the value of horizon and a physical material properties, critical energy release rate. The critical stretch value is only usable for linear elastic brittle materials with a known critical energy release rate. In the case of viscoplasticity, the material has a non-linear behaviour and the material properties will become time-dependent. Therefore, the critical stretch value can not be used as a valid failure criterion.

The local damage parameter for a material point concerning broken bonds is defined as [84]

$$\varphi(\mathbf{x}, t) = 1 - \frac{\int_{\mathcal{H}_x} \mu(\mathbf{x}, t, \boldsymbol{\xi}) dV_{\boldsymbol{\xi}}}{\int_{\mathcal{H}_x} dV_{\boldsymbol{\xi}}}. \quad (2.22)$$

The expression defines the local damage in terms of broken bonds. It is the weighted ratio of the number of damaged interactions to the whole initial interaction cluster of a material point.

Figure 2.5 shows a material point and its family members in the horizon at an initial state. After deformation, the bonds connecting family members over the crack surface

with the material point are considered broken [87]. The local damage is expressed between 0 and 1. In the initial state, the local damage is zero, which means the material point can interact with all family members. The local damage formulation can be used as an indicator to identify the fracture. As shown in Figure 2.5, during the fracture surface creation, a material point lost its bonds with family members on the other side of the fracture surface.

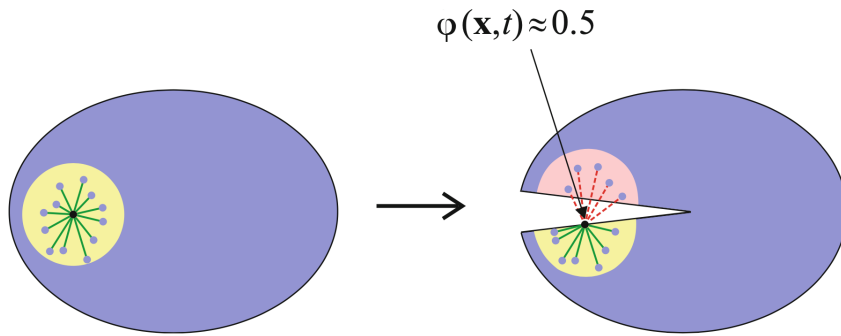


Figure 2.5 : Initial and damaged model.

2.2.1 Fracture modes and crack propagation

Madenci and Oterkus [87] examined the question of using critical stretch as a damage parameter for a linear elastic material. Moreover, the linear elastic material was investigated in some serial of experiments by Ayatollahi and Aliha [108]. The experiments were carried out on a diagonally loaded square plate. Figure 2.6 [87] shows the comparison of experimental results and peridynamic analysis results.

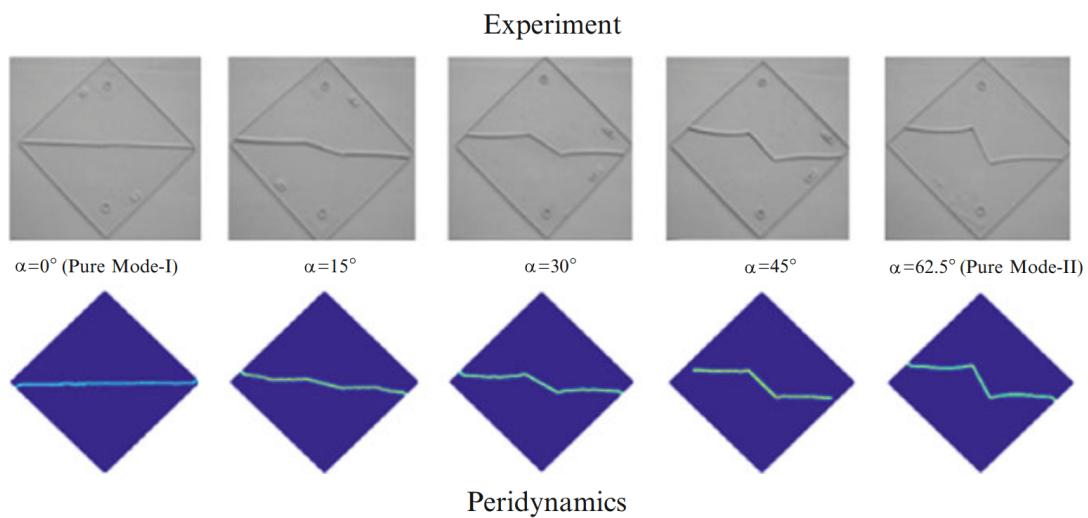


Figure 2.6 : Peridynamic crack propagation and experimental results with various crack orientation angles.

One can find that the fracture modes change from Mode I to Mode II with the initial crack orientation in Figure 2.6. The angle between initial crack and horizontal axis varied with $\alpha = 0^\circ, 15^\circ, 30^\circ, 45^\circ$, and 62.5° . When the crack is located parallel to the horizontal axis ($\alpha = 0^\circ$), the mode I fracture was observed. With the increase of the initial crack angle, e.g. $\alpha = 62.5^\circ$, the fracture mode II governed the crack propagation. The crack paths in simulations have a good agreement with paths in experiments. This example validates the use of critical stretch values to simulate crack propagation paths and fracture modes.

2.2.2 Local damage for crack growth

The horizon in PD is generally chosen as three times the distance between material points, i.e. $\delta = 3\Delta$, for computational efficiency. This formulation directly affects the measure of local damage.

Figure 2.7 [87] shows the local damage of a material point with crack planes located in various positions. In the first case, as shown in Figure 2.7(a), the crack plane is located through the horizon. The all bonds between the material point at the centre and its family members located above the crack plane (dashed line) are eliminated. The local damage is $\phi \approx 0.38$ for the point at the centre. The material point will lose nearly half of its interaction when the horizon extends to infinity. When the crack plane starts from nearly ahead of the material point, as shown in Figure 2.7(b), the number of bonded interactions are increased. Thus, the local damage at the centre point is smaller in that case and it is about $\phi \approx 0.14$. The third state, Figure 2.7(c) shows that the material point at the centre has lost its connection more than the second state and the local damage value is $\phi \approx 0.24$.

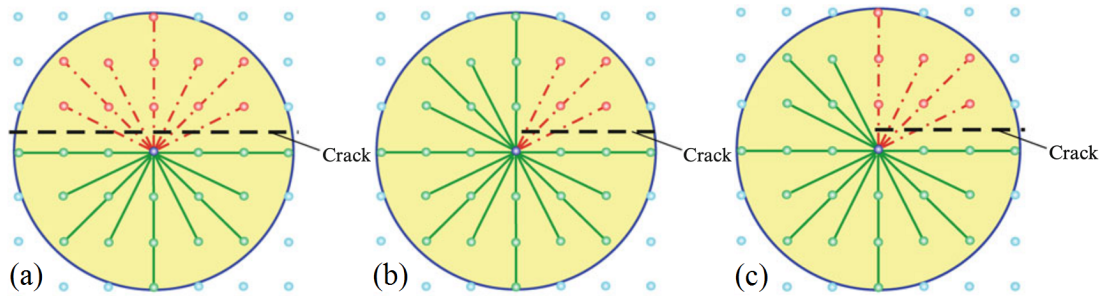


Figure 2.7 : Local damage in PD (a) on the crack plane, (b) in front of the crack tip, and (c) behind the crack tip. The green lines indicate unbroken PD interactions and dashed lines with dots indicate broken PD interactions.

As a result, a crack path can be defined in PD with a horizon $\delta = 3\Delta$. On the other hand, the local damage can not be used to identify the exact crack path without the knowledge of other material points bonds interaction states. To determine a crack path properly, the neighbouring local damage values in a body should be evaluated. Moreover, local damage is directly related to the distance between the crack surface and corresponding material point. If a crack surface does not coincide with the horizon area of a material point, there is no local damage. However, when a crack surface is located at a distance of 0.5Δ , 1.5Δ , and 2.5Δ from a material point, the local damages are found as $\phi \approx 0.38$, $\phi \approx 0.16$, and $\phi \approx 0.02$, respectively. The question of how to identify a crack surface, or determining a section as a fracture arises at this point. Madenci and Oterkus [87] stated that crack surfaces could only be visible at a distance of 2Δ between material point and crack, and also, presented that crack propagation can be determined with an error less than 2Δ . An illustrative example of a crack path indicating the local damage values is shown in Figure 2.8 [87].

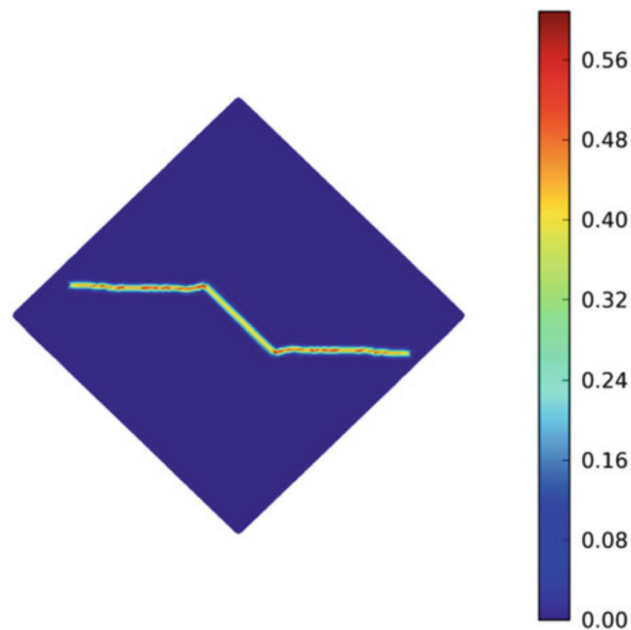


Figure 2.8 : Local damage and crack propagation.

2.2.3 Micro-crack definition

In many engineering applications, cracks may have existed in materials in different positions, angles, and lengths. In PD, removing bonds passing through crack surfaces is a suitable approach to determine a predefined crack. Madenci and Oterkus [87] examined the damage value of the material points by considering their location with

respect to the crack surface. They showed that material points close to the crack tips might have different damage values with respect to the other material points around the crack region. Figure 2.9 shows a pre-defined crack plane and material points exposed to bond-breakage due to the intersection of bonds with this plane. The pre-defined crack plane may be located at any position between the material points in the presented model. The bonds between the material point and its family members are considered as diminished when they intersect with the crack plane that is located between material points. The material points whose horizon intersects with the crack plane are damaged at specific amounts shown on the colour scale.

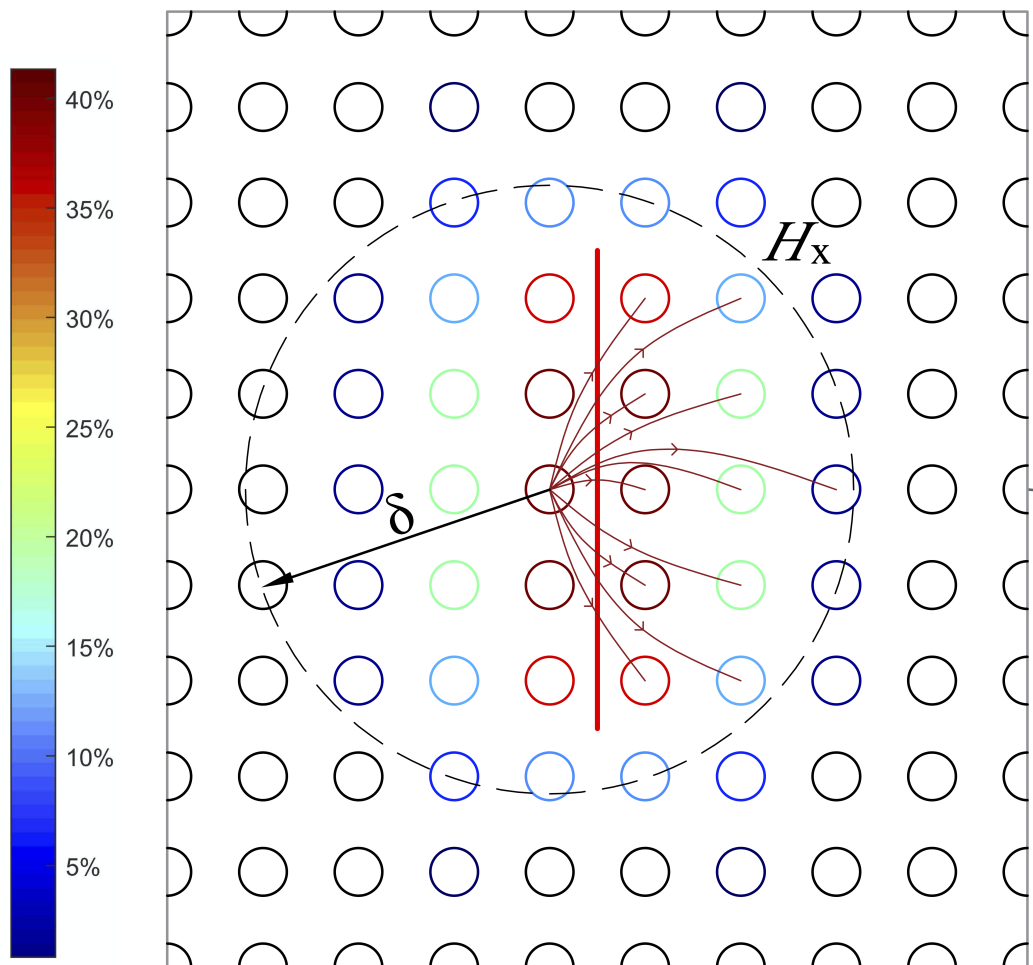


Figure 2.9 : Micro-crack plane (thick continuous line). The broken bonds are shown with lines with arrows.

The amount of damage is directly related to the proximity to fracture plane, and the points closest to the crack plane suffer more damage than distant ones. The crack plane's length can be adjusted to determine whether the fracture is a micro- or macro-crack.

2.3 Impact Modelling

Impact loading can be modelled in PD by defining contact between two bodies. The inter-penetration of bodies is blocked with a certain algorithm. The target body is defined as deformable, but it is possible to define the impactor as either deformable or rigid. The contact modelling of a rigid impactor and deformable impactor need different techniques.

2.3.1 Rigid impactor

As shown in Figure 2.10 [87], a rigid impactor has a velocity towards to a target material at time t . While the impactor is not deformable during analysis, the target body is governed by PD equation of motion. In the simulation, the inter-penetration between bodies should not be allowed while contact modelling. The rigid impactor interpenetrates the target time $t + \Delta t$. This is the first step of the contact between two bodies. The red coloured material point should not be inside the impactor in Figure 2.10. To satisfy the real physical conditions, the points inside the impactor have moved to its new position at time $t + \Delta t$. The algorithm moves the material points to near of impactor surface. This is how the contact surface between two bodies defined in PD.

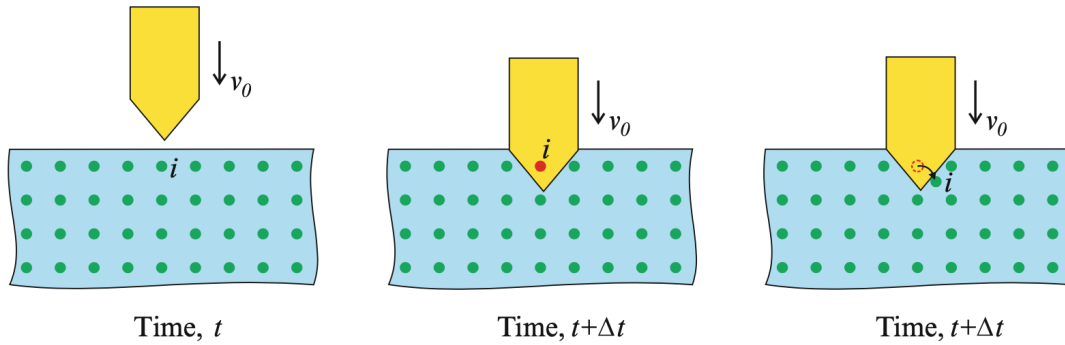


Figure 2.10 : Representation of contact between a rigid impactor and deformable target subjected to impact load.

The velocity of a material point, $\mathbf{x}_{(k)}$ that has moved in a new position at time step $t + \Delta t$ can be formulated as [87],

$$\bar{\mathbf{v}}_{(k)}^{t+\Delta t} = \frac{\bar{\mathbf{u}}_{(k)}^{t+\Delta t} - \mathbf{u}_{(k)}^t}{\Delta t}, \quad (2.23)$$

where $\bar{\mathbf{u}}_{(k)}^{t+\Delta t}$ represents modified displacement vector at time $t + \Delta t$ and $\mathbf{u}_{(k)}^t$ is the displacement vector at time t . Δt refers to the time increment.

The moving material point $\mathbf{x}_{(k)}$ contributes to the reaction force from target to the impactor at time $t + \Delta t$. $\mathbf{F}_{(k)}^{t+\Delta t}$ can be found by

$$\mathbf{F}_{(k)}^{t+\Delta t} = -1 \times \rho_{(k)} \frac{\left(\bar{\mathbf{v}}_{(k)}^{t+\Delta t} - \mathbf{v}_{(k)}^{t+\Delta t} \right)}{\Delta t} V_{(k)}, \quad (2.24)$$

where $\mathbf{v}_{(k)}^{t+\Delta t}$ is the velocity at time $t + \Delta t$ before moving the material point $\mathbf{x}_{(k)}$. The ρ_k and V_k are the density and volume, respectively.

The total reaction force $\mathbf{F}^{t+\Delta t}$ at time $t + \Delta t$ is the summation of the forces generated from all material points that were initially inside the impactor. The total force can be expressed follow as,

$$\mathbf{F}^{t+\Delta t} = \sum_{k=1} \mathbf{F}_{(k)}^{t+\Delta t} \lambda_{(k)}^{t+\Delta t}, \quad (2.25)$$

where

$$\lambda_{(k)}^{t+\Delta t} = \begin{cases} 1 & \text{inside impactor} \\ 0 & \text{outside impactor} . \end{cases} \quad (2.26)$$

2.3.2 Flexible impactor

In the flexible impactor model, both impactor and the target body are considered deformable. They are both governed by the PD equation of motion. However, the continuum mechanics requires to prevent sharing the same position by multiple points. Therefore, a critical distance r_{sh} is defined to avoid intersections. Thus, two material points are forced to repel each other to create contact. The short-range repelling force between points is formulated as [109]

$$\mathbf{f}_{sh}(\mathbf{y}_{(j)}, \mathbf{y}_{(k)}) = \frac{\mathbf{y}_{(j)} - \mathbf{y}_{(k)}}{|\mathbf{y}_{(j)} - \mathbf{y}_{(k)}|} \min \left\{ 0, c_{sh} \left(\frac{|\mathbf{y}_{(j)} - \mathbf{y}_{(k)}|}{2r_{sh}} - 1 \right) \right\}, \quad (2.27)$$

where parameters can be chosen as short-range constant $c_{sh} = 5c$ and critical distance $r_{sh} = \Delta 2$.

2.4 Numerical Solution Method

The solution of Peridynamic equation of motion needs numerical techniques for spatial and time integrations due to the integro-differential equation structure that is not easily solved with analytical solutions [87]. The spatial integration approach was employed using a meshless scheme for simplicity purposes. For this reason, a body or a domain is divided into volumes with certain numbers. These volumes can be called collocation or material points (see Section 2.4.1). Numerical techniques need the convergence of the results. To efficient use of computational sources, the optimum values of parameters should be determined. An examining of PD parameters in terms of numerical convergence is given in Section 2.4.2.

The volume of each material point that affects spatial integration consists of the whole volumes of material points in a horizon can intersect with horizon boundaries. The problem of truncated volumes of material points arises on the surface of a horizon. To avoid this misleading volume effect, a volume correction factor is defined and formulated. Please see the reference [87], Section 7.2. The backward and forward difference explicit integration schemes are used to apply time integration. The using of an explicit scheme is needed to evaluate a convergence study to provide stability of analysis. The time integration and the convergence studies are given in the reference [87], Section 7.3 and Section 7.4, respectively. To apply PD to static and quasi-static problems, Kilic and Madenci [110] presented Adaptive Dynamic Relaxation (ADR) technique. The inertial terms in PD equation of motion avoided the system converging to a static state (see [87], Section 7.5). The other subjects and applications in numerical modelling of PD, such as surface effects, application of initial and boundary conditions, no-fail zone, spatial partitioning, and parallel computing are given in detail in [87].

2.4.1 Discretization in peridynamics

To solve the PD equation of motion given in equation 2.1 is usually not possible by analytical tools. Hence, the initial continuum body is discretized into points with specific volumes to solve the PD equation of motion. The discretized form of the governing equation for the material point k by considering all material points inside the horizon can be written as

$$\rho_k \mathbf{u}_k^n = \sum_j \mathbf{f}(\mathbf{u}_j^n - \mathbf{u}_k^n, \mathbf{x}_j - \mathbf{x}_k) V_j + \mathbf{b}_k^n, \quad (2.28)$$

where \mathbf{u}_k^n represents the displacement of a material point k at the n th time-step. The volume of material point j is defined as $V_j = (\Delta x)^3$ in a three-dimensional problem where Δx denotes the constant grid spacing [84].

2.4.2 Numerical convergence scheme

Some important parameters affect the computational process and analysis, such as the distance between material points Δ , the horizon radius δ . The purposes of high accuracy and minimum computational time require examining and adjusting these parameters. Silling and Askari [84] presented that the horizon value can be determined with regard to length dimensions. Madenci and Oterkus [87] stated that the horizon does not have as a physical meaning in macro-scale and can be determined with benchmarks to obtain the most efficient analysis. They performed some serial tests on a one-dimensional bar subjected to strain loading. The horizon size varies in different numbers: $\delta = \{1, 3, 5, 10, 25, 50\}\Delta$. The convergence tests results showed that $\delta = \Delta$ and $3\delta = \Delta$ models should be chosen to sustain the accuracy. Figure 2.11 shows the effect of two horizon size; (a) $\delta = \Delta$ and (b) $\delta = 3\Delta$, on the crack propagation and branching in the example of a square plate with a central crack subjected to a velocity of $V_0 = 50$ m/s [87].

Higher values of horizon cause excessive wave dispersion and thus, a discrepancy is observed between numerical and analytical results. Moreover, increasing of material points results in an excessive number of family member for a material point. That will result in higher computational time. On the other hand, $\delta = 3\Delta$ should be chosen instead of $\delta = \Delta$. Otherwise, proper crack propagation can not be obtained. The crack propagates with grid dependency and branching can not occur.

The numerical convergence studies on the analysis of wire rope subjected to impact loading were discussed in Chapter 5. In question convergence studies were conducted to investigate proper horizon size and number of material points in a family of a material point, so on the distance between material points. As stated in [111], three types of convergence studies were carried out. The m-convergence is the first type of convergence. m is a multiplier in the definition of horizon formula: $\delta = m \times \Delta$. Thus,

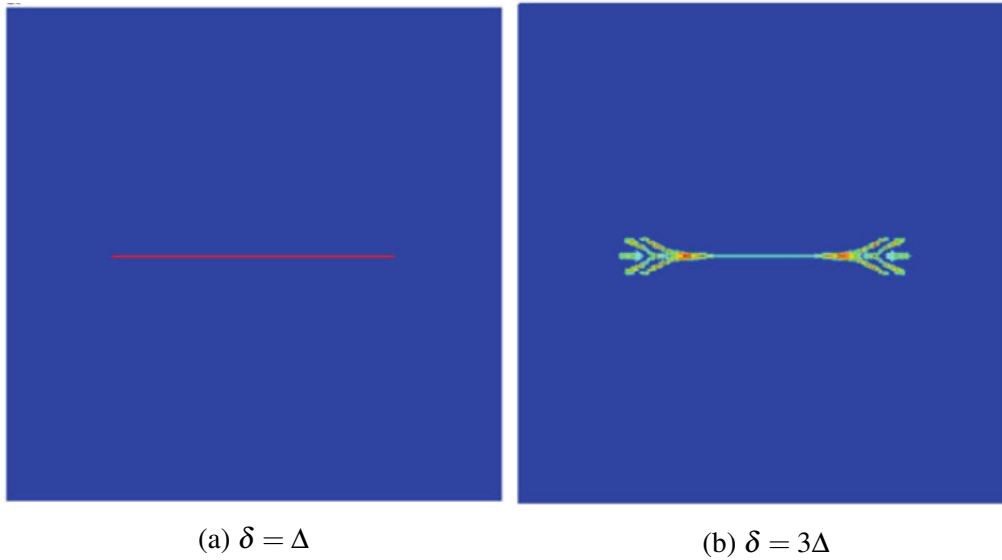


Figure 2.11 : A case study to examine the horizon size effect on the crack propagation and branching. The plate is subjected to $V_0 = 50$ m/s along vertical axis.

the number of family members can be adjusted and the horizon can be dependent on the distance between material points (Δ). In this type of convergence, m numbers are changing while δ is fixed. The second type of convergence is called δ -convergence that investigates the effect of horizon sizes while m number is constant. The detail explanation and examples were given in Section 5.3.1 and 5.3.2.

2.5 Test Suit and Model Validation

Peridynamic theory explained within the scope of this thesis study has been tested with a problem found in the literature. Thus, the validity of the developed script and its comparison with the results published in the literature were made.

A benchmark problem was conducted to compare Peridynamic theory with classical continuum mechanics, i.e., analytical and finite element analysis. Failure mode in PD was turned off to avoid crack initiation and propagation. Because the loading is uni-axial static and only displacements in the main axes have examined this comparison study's scope.

The benchmark problem concerned an isotropic rectangular thin plate subjected to uni-axial static tension. Figure 2.12 shows a rectangular plate subjected to uniform tension, σ_0 .

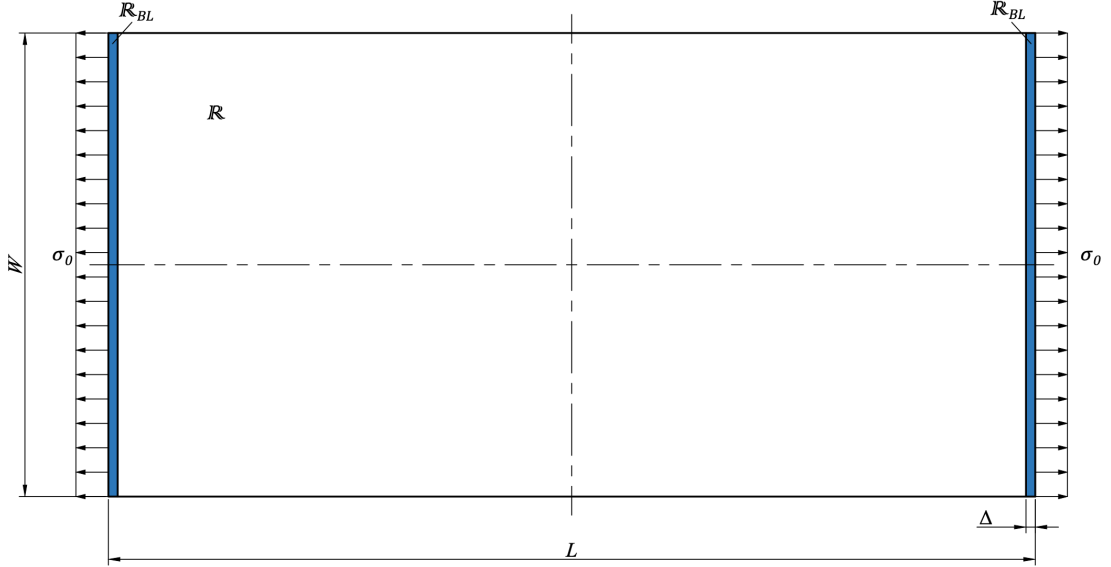


Figure 2.12 : Geometry of a plate subjected uni-axial tension.

The dimensions of the plate are $L = 1000$ mm, $W = 500$ mm, and $h = 10$ mm. The material properties of the plate are Young's modulus, $E = 200$ GPa; Poisson's ratio, $\nu = 1/3$; mass density, $\rho = 7,850$ kg/m³. The applied load is uni-axial tension loading, $\sigma_0 = 200$ MPa. Initial and boundary conditions, PD discretization and time integration parameters were given in Table 2.1.

Table 2.1 : PD model parameters of the isotropic plate under uni-axial tension.

Parameter	Value
Number of material points in the x-direction, $ndivx$	100
Number of material points in the y-direction, $ndivy$	50
Number of material points in the z-direction, $ndivz$	1
Total number of particles, $ndivx \times ndivy \times ndivz$	5,000
Spacing between material points, Δ	10 mm
Incremental volume of material points, ΔV	1×10^{-6} m ³
Boundary layer volume, ΔV_{Δ}	50×10^{-6} m ³
Applied body force density, $b_x = (\sigma_0 Wh)\Delta V_{\Delta}$	2×10^{10} N/m ³
Horizon, δ	3.015Δ
Incremental time step size, Δt	1.0 s
Total number of time steps	1,000

The body was free of any displacement constraints in PD. However, a displacement constraint on y-axis and rotation constraint around z-axis were applied to left and right edges in FEM analysis to avoid rotation of the body. The tension on each side of the structure was applied as a body force density in the boundary layer. Figure 2.13(a) and (b) show uniform discretization and meshing of the plate in PD and FEM, respectively.

Two-dimensional finite element analysis model of the plate was generated in the Abaqus/CAE software. The material properties were defined as isotropic elastic. The plane stress approach was considered owing to the simplicity of the problem. The part was defined as 2-D planar deformable shell type. In the meshing process, quad element shape and medial axis algorithm were chosen to obtain a regular mesh. The mesh size was controlled with a constant number, 5 mm. Therefore, the four-node bilinear plane stress quadrilateral element (CPS4R) with reduced integration and hourglass control was used. The model consists of 20,000 mesh elements and 20,301 nodes.

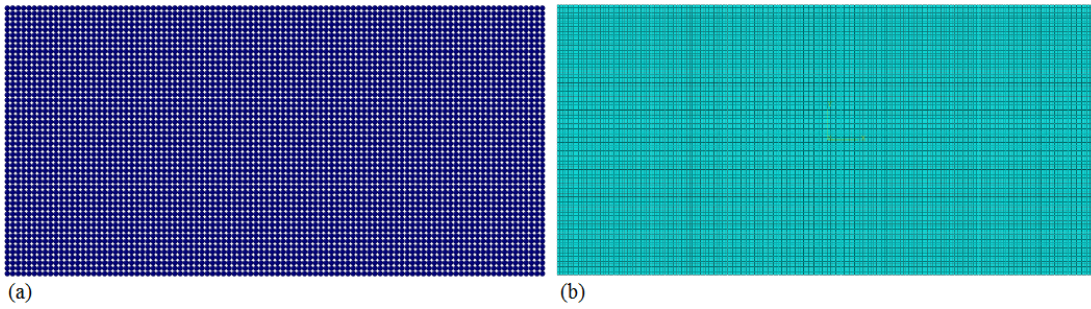


Figure 2.13 : (a) Discretization in PD and (b) meshing in FEM.

Displacements of material points were monitored to achieve a steady-state solution. The sufficient number of time steps is 1,000 used in the analysis. Figure 2.14 shows the comparison of the PD and FEM in terms of displacements $u_x(x, y = 0)$ and $u_y(x = 0, y)$.

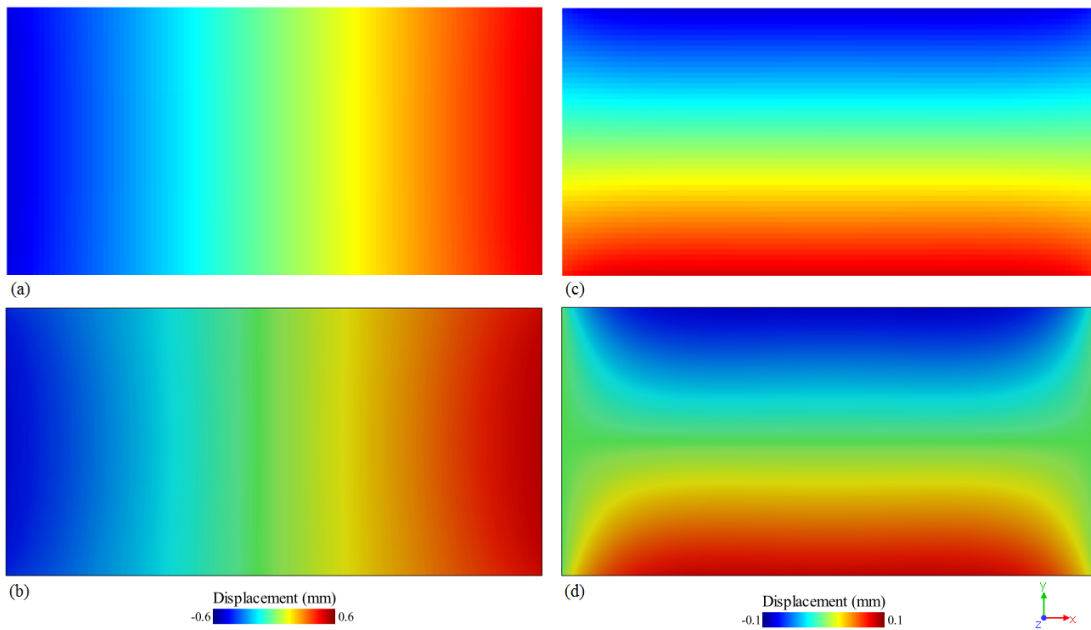


Figure 2.14 : Displacements (a) $u_x(x, y = 0)$ for PD, (b) $u_y(x = 0, y)$ for PD, (c) $u_x(x, y = 0)$ for FEM, and (d) $u_y(x = 0, y)$ for FEM.

The displacements in PD for $u_x(x, y = 0)$ and $u_y(x = 0, y)$ were given in Figure 2.14(a) and (c), respectively. Figure 2.14(b) and (d) represent finite element analysis displacements for $u_x(x, y = 0)$ and $u_y(x = 0, y)$, respectively.

Although displacements in x -axis show a similar pattern in both PD and FEM, they differentiate near edges for u_y analyses, as shown in Figure 2.14(c) and (d). The applied boundary conditions in FEM lead to distortion in the analysis. Boundary conditions that sustain horizontal stability in FEM lead to a distortion in the analysis. This effect causes an imperceptible misrepresentation near edges. However, it does not affect the displacements in $y = 0$ and $x = 0$ significantly. Therefore, it is not very important in the comparison analysis.

The analytical solutions for $u_x(x, y = 0)$ and $u_y(x = 0, y)$ were given as,

$$u_x(x, y = 0) = \frac{\sigma_0}{E}x \quad \text{and} \quad u_y(x = 0, y) = -\nu \frac{\sigma_0}{E}y. \quad (2.29)$$

Figure 2.15 and Figure 2.16 show the comparison of displacements in PD, FEM, and analytical solutions.

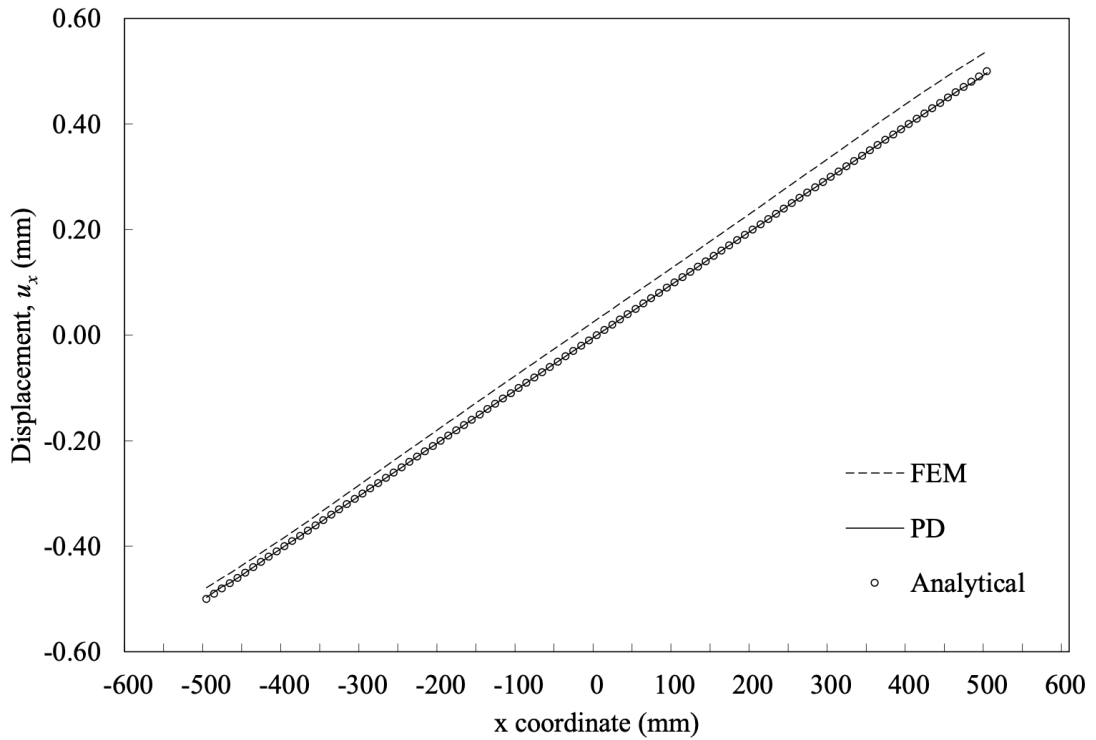


Figure 2.15 : Displacement along the centre x -axis.

The graphs represent similar characteristics in PD, FEM, and analytical results. The close agreement between PD and analytical results was observed. This comparison study confirms the validity of Peridynamics in a static loading problem.

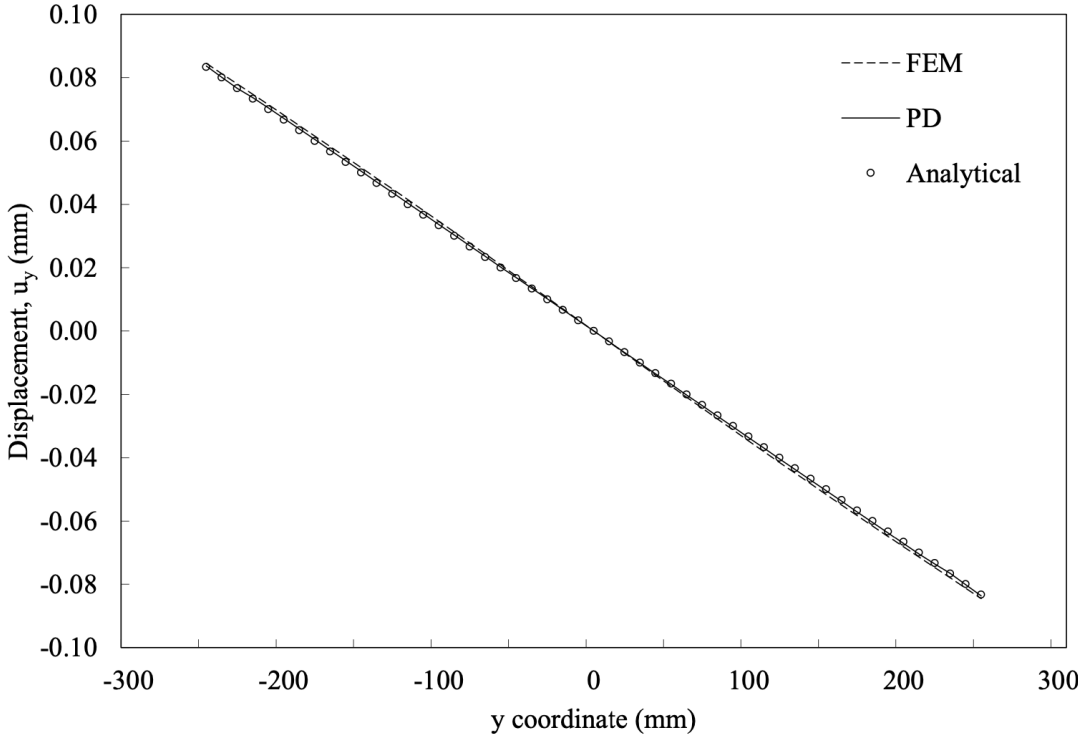


Figure 2.16 : Displacement along the centre y-axis.

3. KALTHOFF WINKLER EXPERIMENT

The Kalthoff–Winkler experiments [105] is a classical impact study examining the crack propagation under various impact conditions. It was performed with the high-strength maraging steel plate (X2NiCoMo 18 9 5) having two parallel notches. The plate is impacted by a steel impactor, as shown in Figure 3.1 [105]. Kalthoff [106] stated that the high-strength maraging steel shows an almost linear-elastic behaviour and the linear-elastic equations can describe the stress distribution around the crack tip. When shear bands control the fracture at loading rates, crack propagation is nearly parallel to the notch (Mode II). On the other hand, at low rates of loading, a mode transition occurs. The crack propagates as Mode I and micro-elastic PD theory is valid to simulate this brittle fracture as stated by Silling [112]. As indicated in [105], the projectile impact with a specific velocity results in a brittle fracture in the target body and this study only focused on this failure mode.

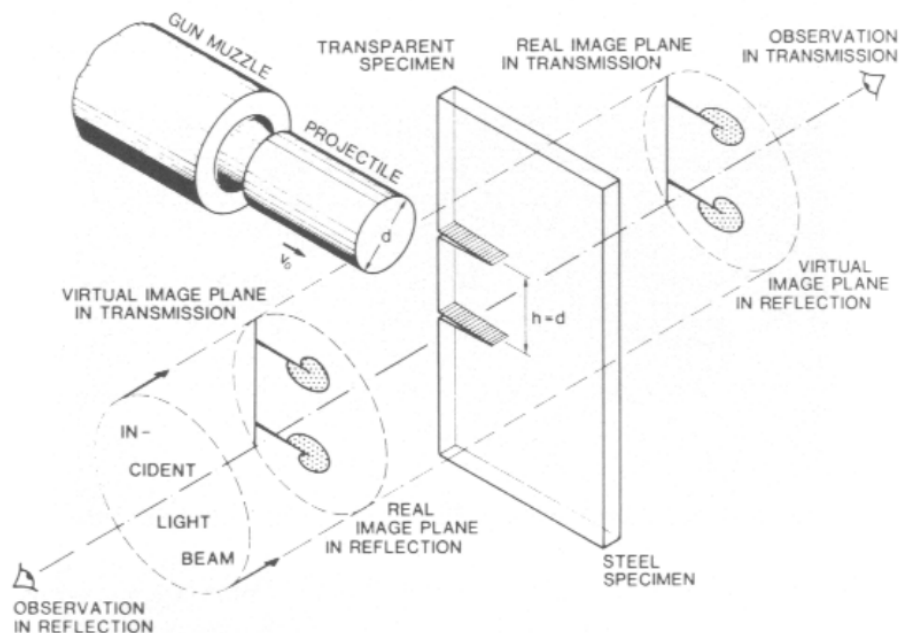


Figure 3.1 : The Kalthoff–Winkler experimental setup.

In recent years, several authors have suggested various approaches to modelling the Kalthoff–Winkler problem. Silling [107, 112] presented the PD solution of the problem

as a part of the validation process of PD theory. The crack propagation angle from the vertical axis was determined by bond-based PD in [87]. Ren et al. [113, 114] proposed the dual horizon PD formulation to reduce the calculation cost and examined the problem in this aspect. Amani et al. [115] proposed implementing state-based PD for thermo-plasticity to simulate the Kalthoff–Winkler problem effectively. Gu et al. [116] extend this study by implementing non-uniform discretization and Voronoi diagrams in PD. Also, the effect of plate dimensions and model parameters such as impact velocity, plate thickness on the crack propagation speed, and the crack angle were investigated with the state-based PD model [14]. Moreover, Trask et al. [117] applied a mesh-free quadrature rule for the discretization of PD material points and verified the model with results from the Kalthoff–Winkler experiment. On the other hand, a reformulated thermo-visco-plastic model study was made to demonstrate the effect of impact velocity on the crack propagation speed [118].

To the author’s best knowledge, the effect of micro-cracks on crack propagation in a material subjected to an impact load stands out as a gap in the literature that needs further investigation. Therefore, in this chapter, bond-based PD is applied to monitor the effect of micro-cracks on dynamic crack propagation. This chapter examines the relationship between stochastically predefined defects and the toughening mechanism in the Kalthoff–Winkler problem using bond based PD. A two-dimensional micro-crack definition and examining the effect of stochastically pre-located micro-cracks on the three-dimensional body using PD theory are considered as a novel approach.

The dimensions of the plate in Figure 3.2(a) are $L = 0.200$ m, $W = 0.100$ m, and $h = 0.009$ m. The distance between the notches (slits) is $d = 0.050$ m, and they are located symmetrically with a length of $a = 0.050$ m. The notch thickness is $n = 0.0015$ m. In the initial state, plate boundaries are traction-free and at rest. The cylindrical impactor is assumed to be a rigid body with sizes of $D = \phi 0.050$ m and $H = 0.050$ m. The mass of the impactor is 1.57 kg. The velocity of the impactor is $v = -32$ m/s through the y axis. The discretized model of the steel body is generated with $201 \times 101 \times 9$ material points along x , y , and z axes, respectively (Figure 3.2(b)). The spacing between material points (grid size) is determined as $\Delta = 0.001$ m in all directions, and the radius of the horizon is $\delta = 3.015 \times \Delta$ as in [87].

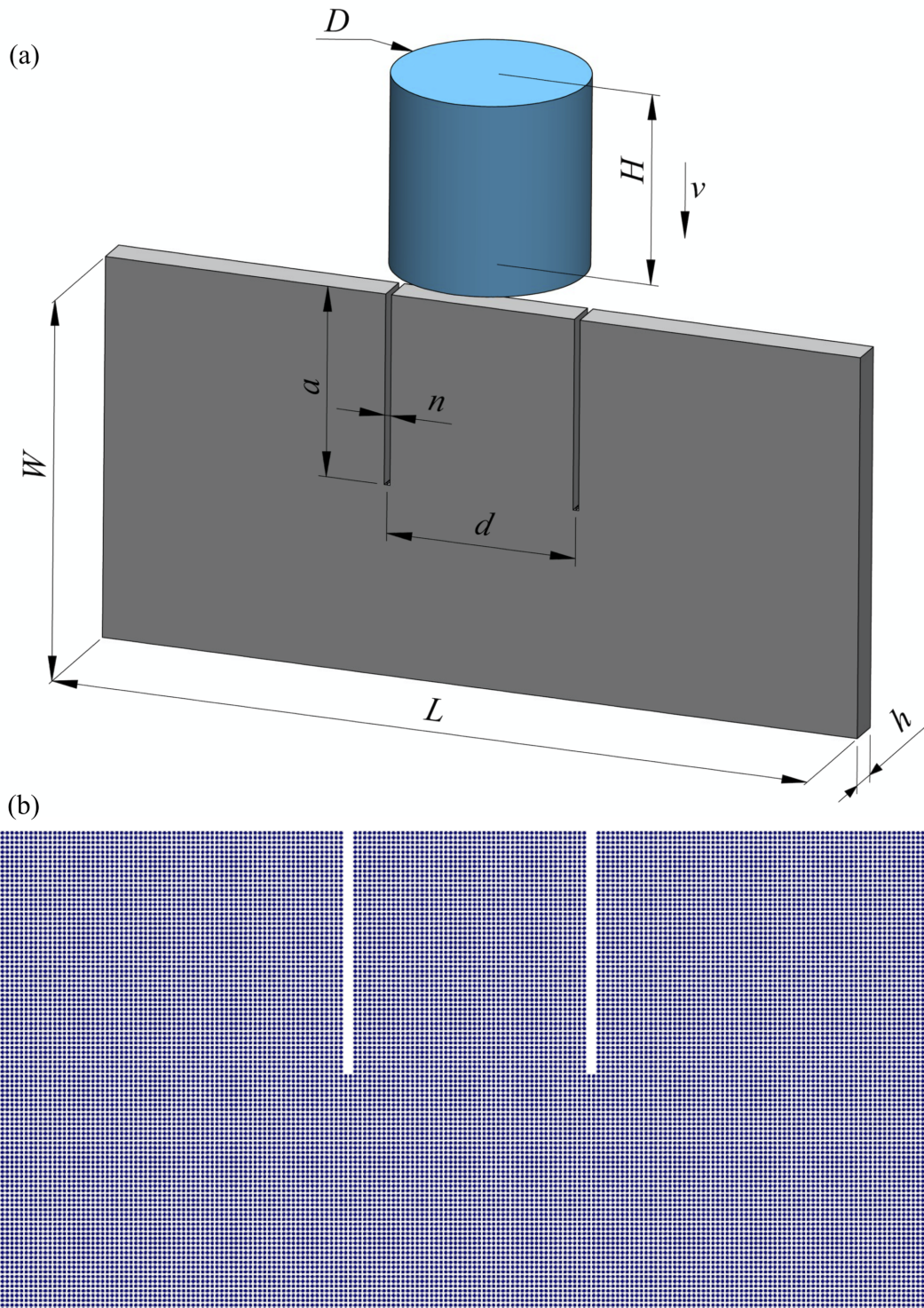


Figure 3.2 : The Kalthoff–Winkler (a) experimental setup and (b) peridynamic discretization model.

The total number of particles is 180,873. The time-step in simulation is specified as $\Delta t = 8.7 \times 10^{-8}$ s, and the critical-stretch is defined as $s_c = 0.01$, as suggested in [87]. The dimensions and properties of the model and Peridynamic simulation parameters used in the study were given in Table 3.1.

Table 3.1 : Dimensions and parameters in Kalthoff-Winkler simulations.

Parameter	Value
L	0.200 m
W	0.100 m
h	0.009 m
d	0.050 m
a	0.050 m
n	0.0015 m
D	$\phi 0.050$ m
H	0.050 m
Rigid impactor mass	1.57 kg
v in y axis	-32 m/s
Δ	0.001 m
δ	$3.015 \times \Delta$
$ndivx$	201
$ndivy$	101
$ndivz$	9
Total number of particles	180,873
Δt	$\Delta t = 8.7 \times 10^{-8}$ s
s_c	0.01

The material properties of the steel plate are the same as in [87] and given in Table 3.2.

Table 3.2 : Material properties of maraging steel.

Young's modulus, E	Poisson's ratio, ν	Mass density, ρ
191 GPa	0.25	8000 kg/m^3

3.1 Benchmark Problem

“The crescent-shaped micro-crack pattern” case defined in [28] is demonstrated to show that the micro-crack definition and the bond-based PD implementation are applicable for the Kalthoff–Winkler problem. Then, the effects of the location of micro-cracks and their density on the crack propagation velocity are presented in next sections.

To examine the effect of micro-cracks on the toughening mechanism and the macro-crack propagation speed, various micro-crack pattern models were studied in [28]. They proposed that the crescent-like distribution of micro-cracks is the most effective among all models to resist crack propagation and increase the material's toughness. In the benchmark problem, the crescent-shaped micro-crack pattern

was adapted to the Kalthoff–Winkler experiment. Figure 3.3 shows that predefined micro-cracks are placed around the notch tip and along the main crack path that was observed in the reference model of the Kalthoff-Winkler experiment without micro-cracks (Figure 3.4(a)).

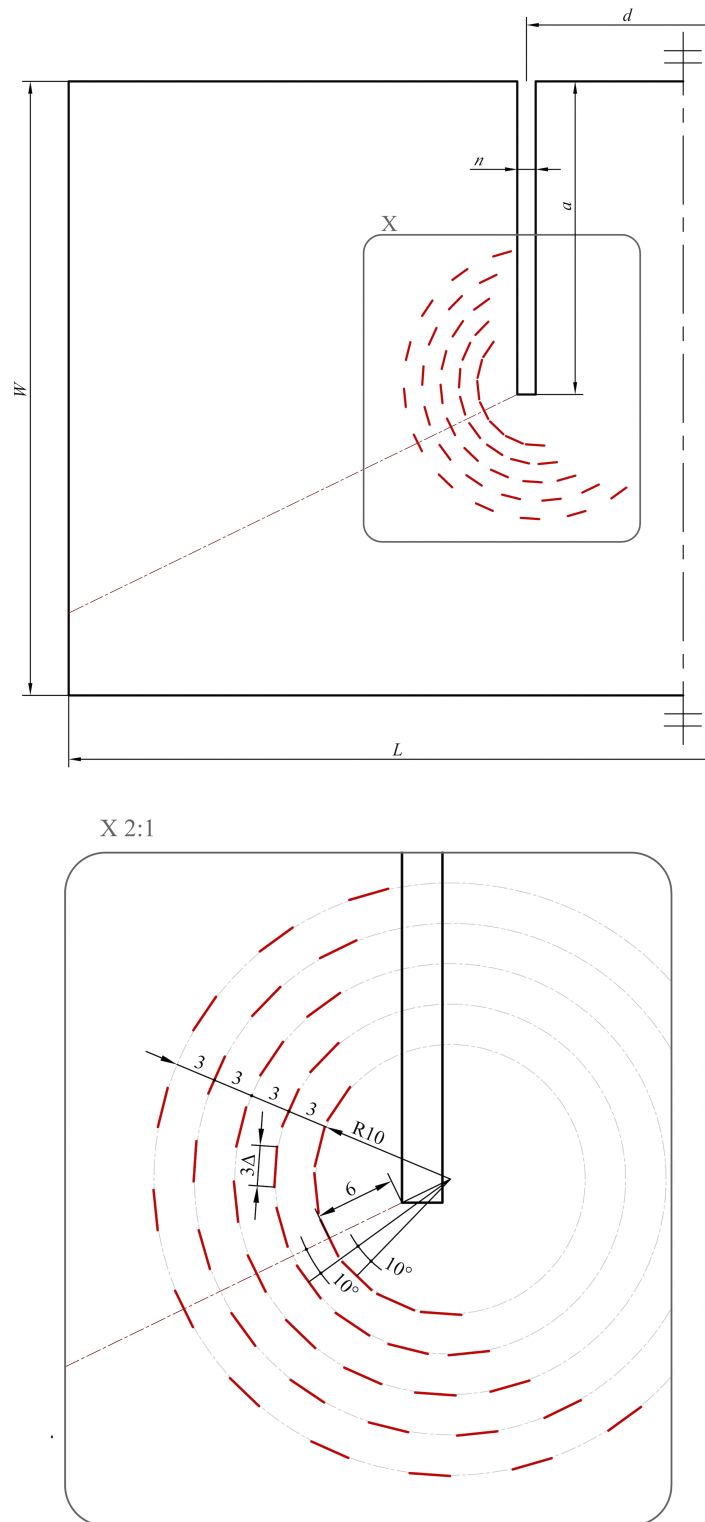


Figure 3.3 : Geometric details of the benchmark study: crescent-like micro-crack pattern.

In the reference model, no micro-cracks are defined in the material as in the experiment and there are only two notches that dominate the initiation points of macro-cracks. The main crack initiates the propagation at $30.5 \mu\text{s}$ (350th time-step). The crack propagation reaches the right and left edges at $91.4 \mu\text{s}$ (1050th time-step) (Figure 3.4(a)), and the average velocity is 1345 m/s . Considering the cracks' required time to reach edges, all models in this study were run to $117.5 \mu\text{s}$ (1350th time-step). Although the fracture process is completed at 1050th time-step, model time was determined as 1350 time-step to observe the damage path properly.

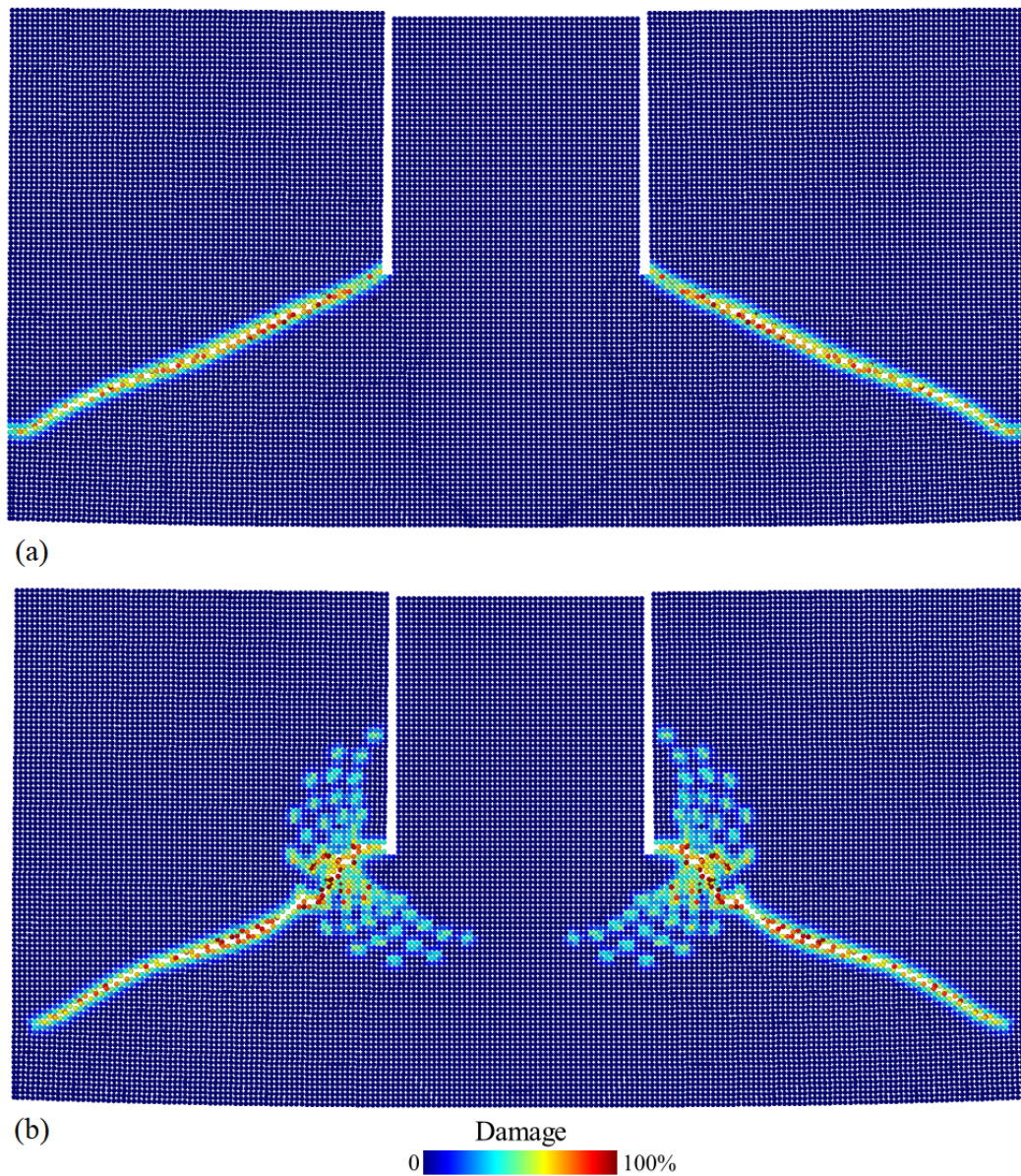


Figure 3.4 : (a) Crack propagations in Kalthoff–Winkler experiment (without micro-crack case) and (b) in the benchmark problem at $91.4 \mu\text{s}$.

The damage pattern of the benchmark model at $91.4 \mu\text{s}$ is presented in Figure 3.4(b). The main crack starts occurring at $30.5 \mu\text{s}$ as same with without micro-crack model in the benchmark problem. However, the crack cannot reach the edge at $91.4 \mu\text{s}$ due to the decrease in propagation velocity.

To compare the cases at the final stage, the crack path of the reference model at $95.7 \mu\text{s}$ is given in Figure 3.5(a). The crack propagation of crescent-shaped micro-crack case reaches the edge at $95.7 \mu\text{s}$ (1100th time-step) (Figure 3.5(b)), and the average velocity is 1188 m/s .

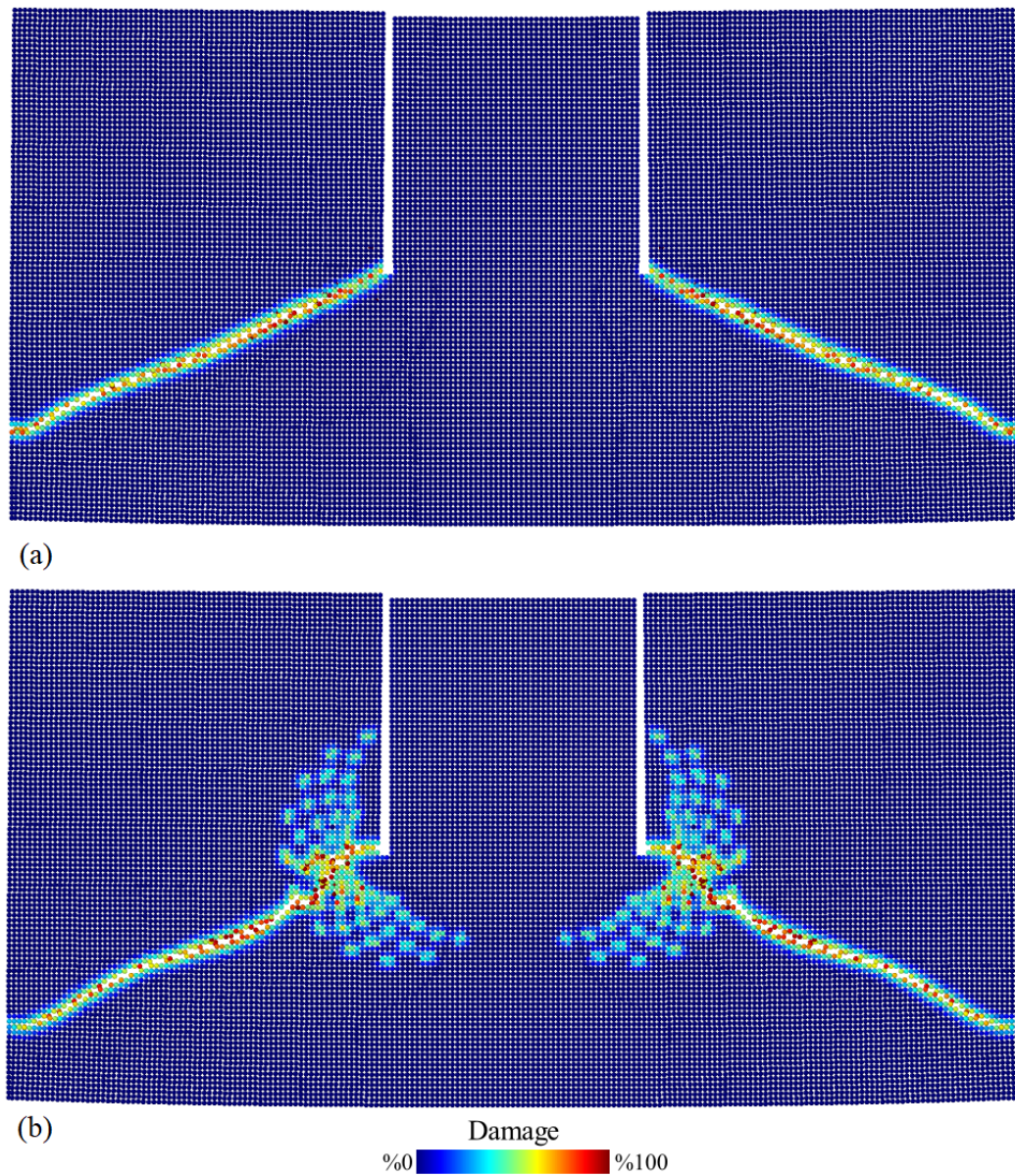


Figure 3.5 : (a) Crack propagations in Kalthoff–Winkler experiment (without micro-crack case) and (b) in the benchmark problem at $95.7 \mu\text{s}$.

Herein, the crack propagation velocity of the benchmark model with micro-cracks reduces about 12% compared to the original experiment model.

Brenich and Carpinteri [26] stated that opening and coalescence of micro-cracks cause stress redistribution and energy dissipation mechanisms. Using part of input mechanical energy by the pre-existing micro-cracks weakens the propagation of the main crack and creates a shielding effect called toughening by micro-cracks. The deceleration in main macro-crack velocity is a result of this toughening mechanism. Therefore, this validation study confirms that the presence of micro-cracks can cause a fracture toughening effect that reduces the crack propagation velocity in this impact loading simulation.

3.2 Stochastically Distributed Micro-Cracks

To analyse randomly distributed micro-cracks with analytical methods is more challenging. Thus, with the bond-based PD method, effects of micro-cracks on macro-crack propagation by varying micro-crack amounts and densities were examined in this section.

3.2.1 Micro-cracks with varying densities

Three different densities of micro-crack cases are investigated in the reference region defined as in Figure 3.6. The micro-crack patterns are stochastically determined, and they are of the same length. In the first model, the default density of micro-cracks in the reference zone is defined as $n_0 = N_0/A_0$ where N_0 is the number of micro-cracks and A_0 is the area of the reference region. Three simulations were performed with varying density of micro-cracks, $n_0 = \{0.75, 1, 1.25\}$ in the reference area A_0 . The results of the parametrized density of micro-cracks are used to compare the crack propagation speed of without micro-cracks case.

The simulation of the original experiment without micro-cracks can be seen for comparison purposes in Figure 3.4(a). In the current model, macro-cracks start to propagate at 30.5 μs . Macro-cracks reach edges approximately at 91.4 μs . In Figure 3.7(a), the density of micro-cracks in the reference area (A_0) is assigned as $n_0 \times 0.75$ and the macro-cracks propagation is given at 91.4 μs . It can be seen that the macro-cracks reach the edge within the same time according to the case

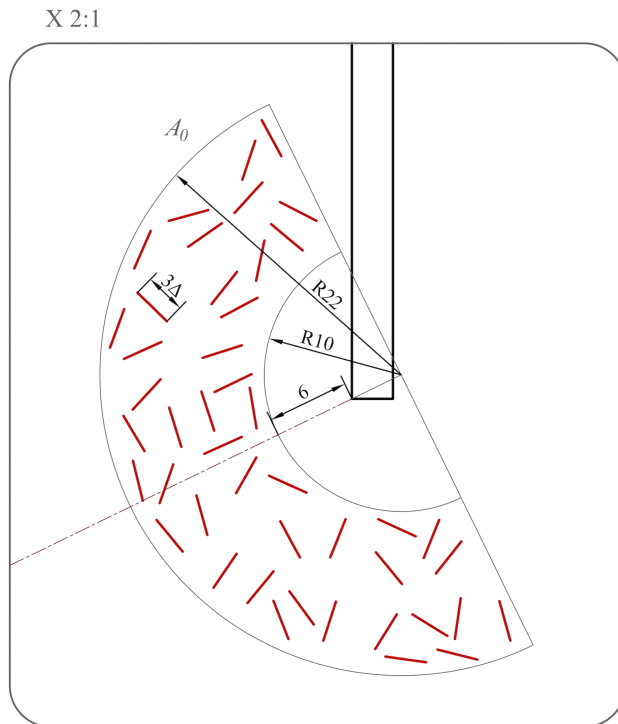
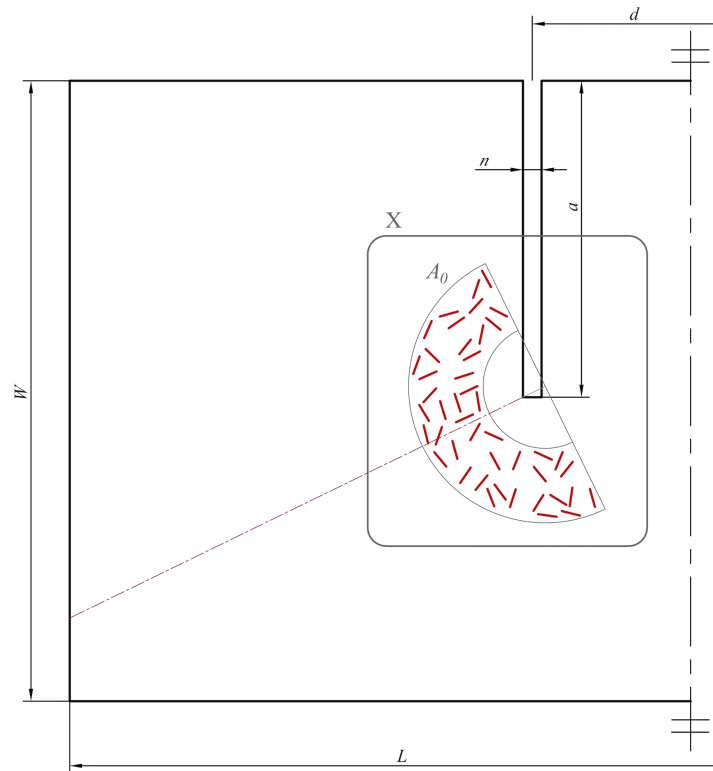


Figure 3.6 : Geometric details of the micro-crack pattern in the reference zone A_0 with the reference density n_0 .

without micro-cracks. The case of $n_0 \times 1$ is shown in Figure 3.7(b). When the tip of macro-cracks at $91.4 \mu\text{s}$ is examined, the propagation speed of macro-cracks decreases with the increase in the density of micro-cracks and macro-cracks, which can precisely

reach the edge after $91.4 \mu\text{s}$. In Figure 3.7(c), the density of micro-cracks is increased compared to the reference model with the multiplier 1.25. Propagation of macro-cracks slows down more according to without micro-cracks, $n_0 \times 0.75$, and $n_0 \times 1$ cases.

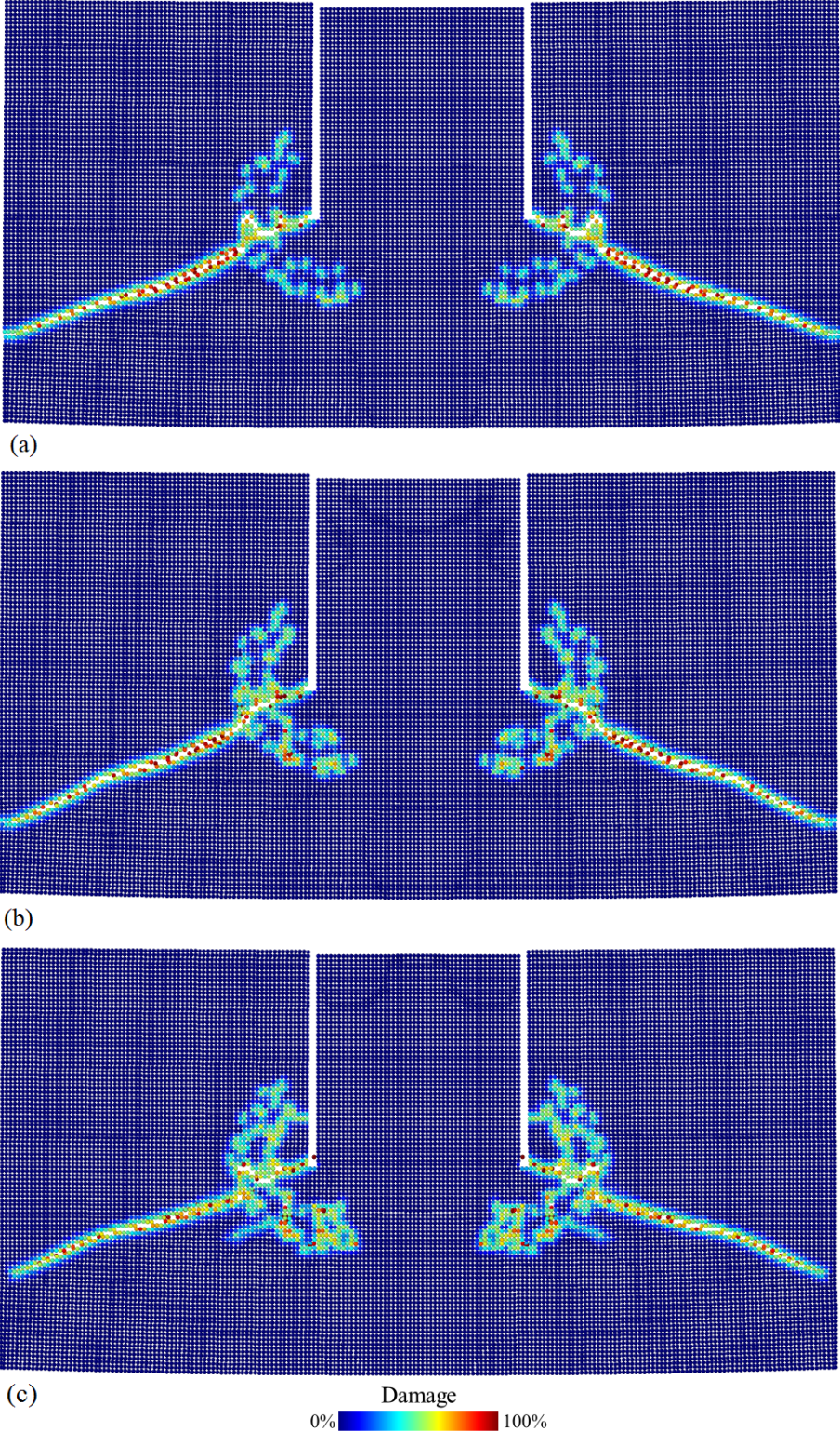


Figure 3.7 : The crack path of the case (a) $n_0 \times 0.75$, (b) $n_0 \times 1$, and (c) $n_0 \times 1.25$ cases at $91.4 \mu\text{s}$ (1050th time-step).

Due to the change in macro-cracks propagation path angle, cracks reach the edge approximately simultaneously as the $n_0 \times 1$ case. The crack patterns in all simulations are nearly straight and very similar to patterns in [14, 87, 113, 114, 116]. Once macro-cracks pass over the reference zone of micro-cracks, velocities of macro-crack tips can be determined for each model. In Figure 3.8, the velocity data is presented after 52.2 μs when the macro-crack tips can be observable after passing the reference region of micro-cracks. Considering that macro-cracks reaching the edge of the body at 91.4 μs in the case of without micro-cracks, the velocity comparisons should be considered up to this time. Crack propagation without micro-cracks and with pre-determined micro-cracks with different densities are quantitatively compared by calculating the velocities of macro-crack tips from 52.2 to 91.4 μs .

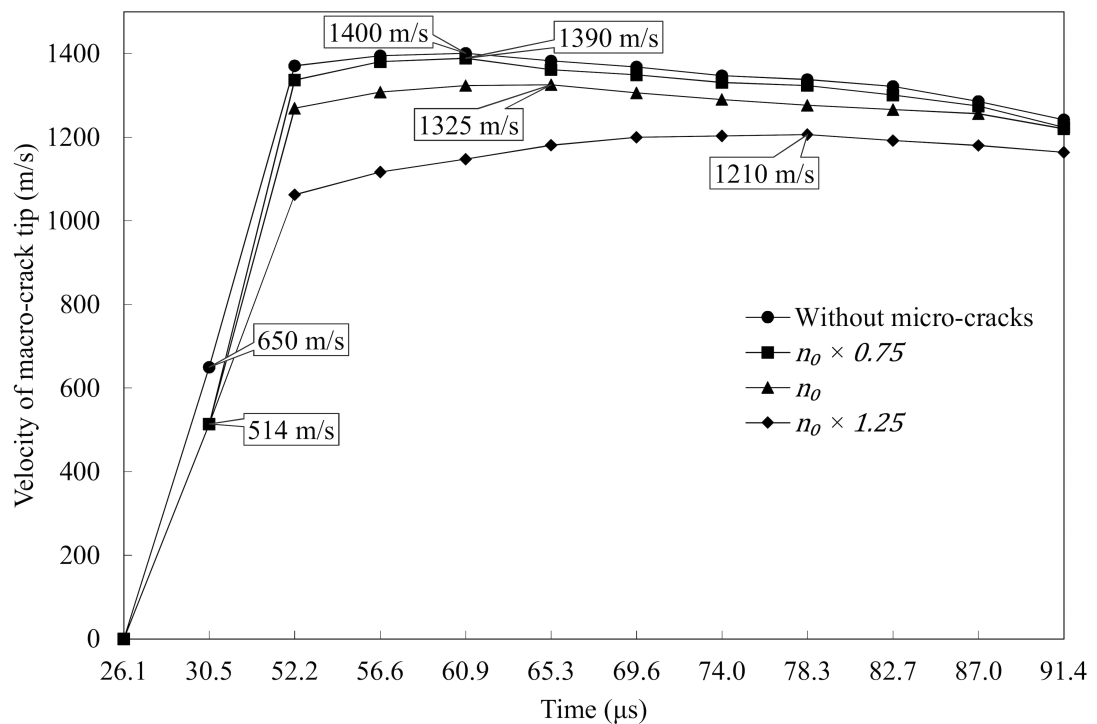


Figure 3.8 : The macro-crack propagation velocities of without micro-crack and with micro-crack cases with densities $n_0 \times \{0.75, 1, 1.25\}$ between 52.2 and 91.4 μs . The initial and maximum velocities are shown with black boxes.

The average velocities of without micro-crack case and with micro-crack cases with densities, $n_0 = \{0.75, 1, 1.25\}$ are 1345 m/s, 1327 m/s, 1284 m/s, and 1165 m/s, respectively. In without micro-crack case, average velocities and the trend agree with models in [58, 76, 77] that validate the current approach for the problem. Moreover, Gu et al. [116] and Guo and Gao [14] emphasized that the macro-crack initiation time

is about $30 \mu\text{s}$ that is very close to the values in the experiment ($29 \mu\text{s}$) and the current model ($30.5 \mu\text{s}$). Without micro-cracks and the low-density of micro-cracks ($n_0 \times 0.75$) conditions show similar trends since their velocities are very close to each other. In addition to this, in the case of $n_0 \times 1$, the trend seems similar despite the average velocity decreases. In without micro-cracks and $n_0 \times 0.75$ models, the macro-crack propagation velocities reach a maximum in approximately $60.9 \mu\text{s}$. However, in the cases of $n_0 \times 1$ and $n_0 \times 1.25$ macro-cracks, the time to reach the maximum speed has a delay with $65.3 \mu\text{s}$ and $78.3 \mu\text{s}$, respectively. In addition to this, while the velocity profiles of the without micro-crack and $n_0 \times 0.75$ cases are very similar, more dense models ($n_0 \times 1$ and $n_0 \times 1.25$) lead to deceleration in macro-crack propagation according to their number of micro-cracks. In conclusion, models show that the number of micro-cracks in the same area is an important parameter in toughening mechanism. Besides, in $n_0 \times 1.25$ case, the initial velocity is relatively low compared to the other three models.

3.2.2 Micro-cracks with various number

The effect of the number of micro-cracks on the toughening mechanism is investigated in this section. In Figure 3.9, geometrical details of A_0 : the reference area in Section 3.2.1, A_1 : the inner area, and A_2 : the outer area, including A_0 and A_1 are given.

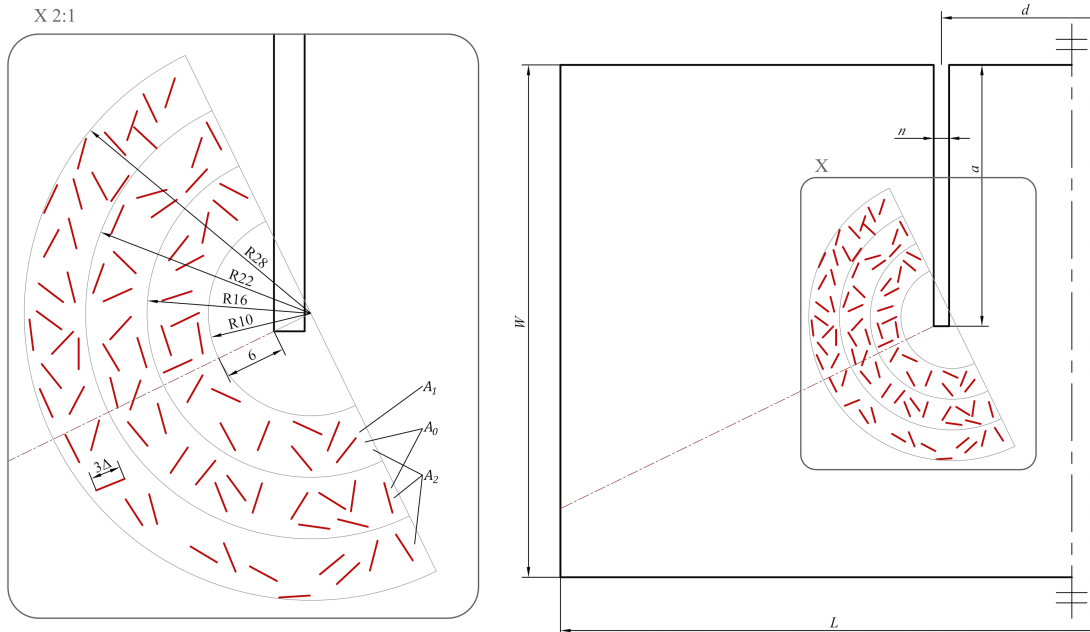


Figure 3.9 : Geometric details of the micro-crack pattern in A_0 , A_1 , A_2 regions with a micro-crack density of n_0 .

Two more micro-crack zones around the notch tips were defined. The densities of micro-cracks are preserved as n_0 in all zones by changing the number of micro-cracks depending on the area. Figure 3.10 shows the crack propagations.

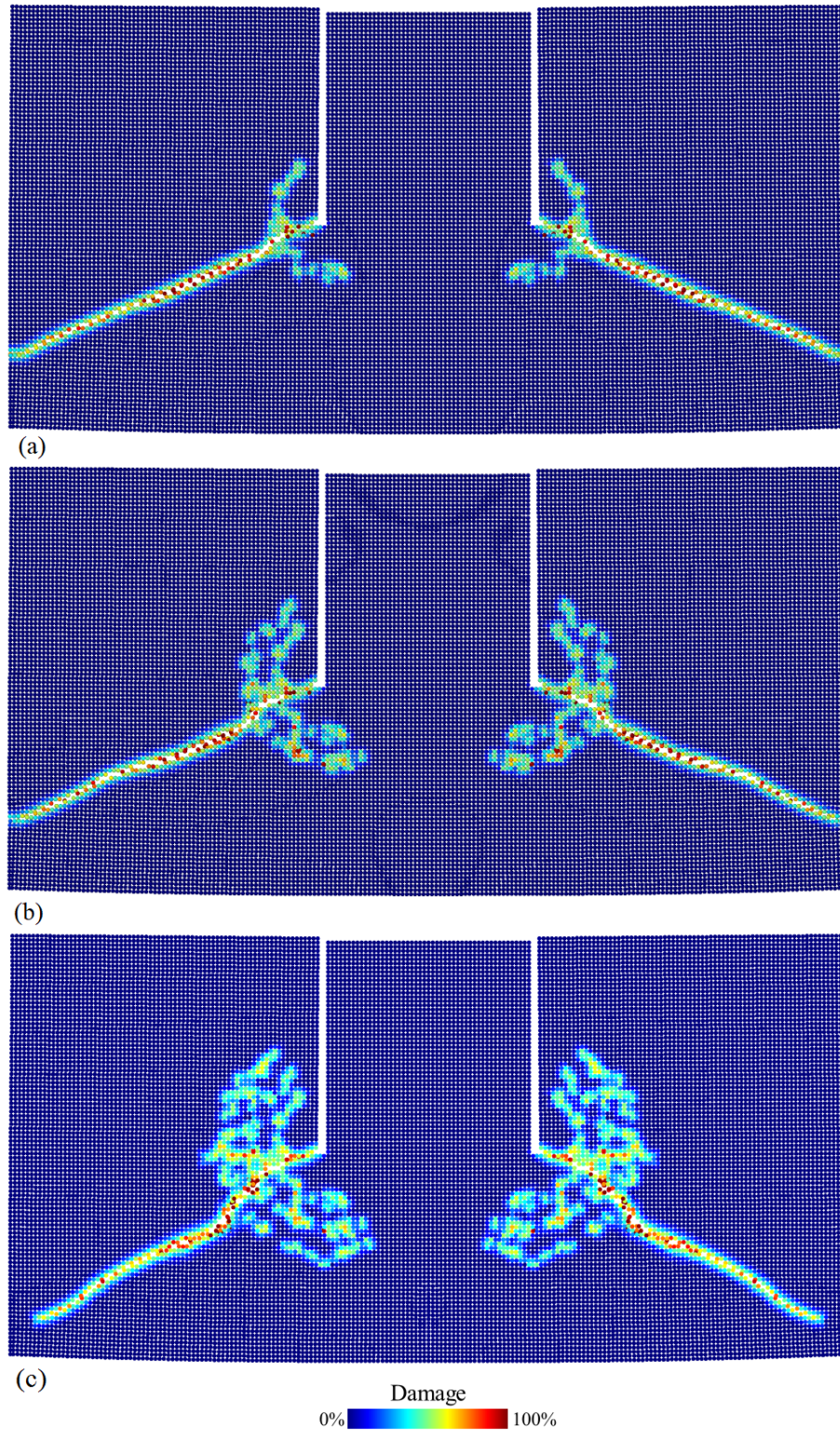


Figure 3.10 : The crack path of cases (a) A_1 (b) A_0 , and (c) A_2 cases at $91.4 \mu\text{s}$ (1050th time-step).

All regions that contain several micro-cracks proportional to their area are compared to the original experiment simulation in Section 3.2.1. Macro-crack propagation without micro-cracks was presented in Figure 3.4(a). In the inner region A_1 , the pattern that contains the least number of micro-cracks does not produce a significant change in the propagation of macro-cracks (Figure 3.10(a)). The required time for macro-cracks to reach the vertical edge is the same as in without micro-cracks case ($91.4 \mu\text{s}$). Micro-crack pattern in the region A_0 decreases the macro-crack propagation velocity. As seen in Figure 3.10(b), the macro-cracks can reach the edge exactly after $91.4 \mu\text{s}$. The region A_2 contains the greatest number of micro-cracks defined by increasing the number of micro-cracks with keeping constant the density. The crack propagation path obtained from the simulation result can be seen in Figure 3.10(c). While complete fracture occurs at $91.4 \mu\text{s}$ in without micro-cracks case, macro-crack propagation in A_2 case cannot reach vertical edges of the body before $104.4 \mu\text{s}$ due to the high number of micro-cracks.

In Figure 3.11, macro-crack propagation velocities between the $52.2 \mu\text{s}$ and $91.4 \mu\text{s}$ are given for the without micro-cracks and with micro-cracks cases (A_0 , A_1 , and A_2).

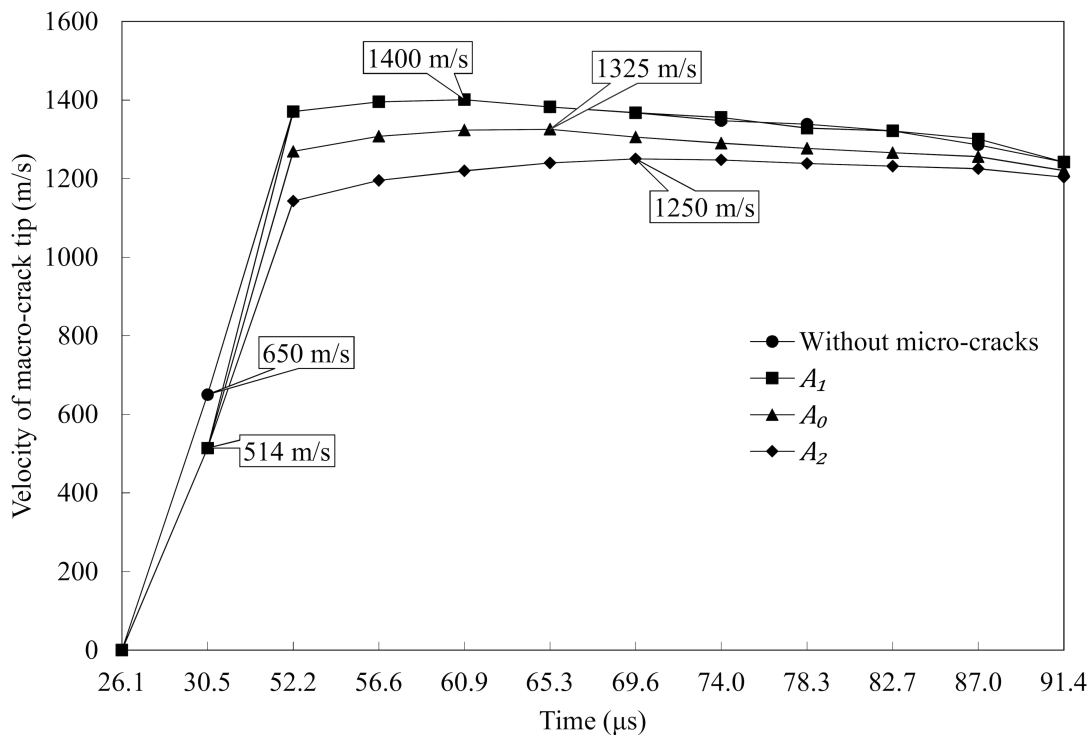


Figure 3.11 : The macro-crack propagation velocities of without micro-cracks, A_1 , A_0 , and A_2 cases between 52.2 and $91.4 \mu\text{s}$. The initial and maximum velocities are shown with black boxes.

Average velocities during that time interval are 1345 m/s, 1284 m/s, 1347 m/s, and 1219 m/s, respectively. Although some deviations are observed at 74.0 μs , 78.3 μs , and 87.0 μs , the propagation of cracks in the cases without micro-cracks and A_1 are very similar. Therefore, it can be deduced that the toughening mechanism can only be triggered with a sufficient number of micro-crack clusters. However, there is a significant reduction in the average velocity of the reference area case A_0 and the largest area case A_2 . The acceleration of the cracks tip in the A_0 and A_2 cases show similar trends with the other cases. On the other hand, the profiles reach their maximum velocities with a delay compared to other models. In the cases of without micro-cracks and A_1 maximum values are reached at about 60.9 μs , while in A_0 and A_2 cases, the maximum velocities are reached at 65.3 μs and 69.6 μs , respectively. Also, velocity differences between the four models decrease as the time advances. Guo and Gao [14] explained the crack propagation and dynamic failure according to the wave propagation, especially “compressive wave” in [106]. They stated that Mode II crack propagation is driven by this wave until 60 μs . After that time, the shape of compressional wave is distorted and the effective Mode II crack propagation ends. After that, waves reflected by the boundary drive the crack propagation and weaken the propagation process [14]. The micro-cracks located on the path of compression waves can cause a distortion effect on these waves. Thus, the shape of the waves becomes vague early and its effect on the crack propagation weaken. In this study, the maximum velocity of without micro-cracks case is observed at 60.9 μs (Figures 3.8 and 3.11).

Conversely, maximum values are delayed to 65.3 and 69.6 μs (Figure 3.11) and even to 78.3 μs (Figures 3.8), and average velocities decrease in cases with sufficient micro-crack patterns in terms of toughening mechanism. Hence, the delay in reaching the maximum velocities and the decrease of average velocities can be caused by compression waves being distorted early and reaching the edge lately because of micro-cracks on the wave path.

Consequently, while the less density of stochastically located micro-cracks around the crack tip does not affect toughening mechanism, adding more micro-cracks in the same area can reduce the crack tip velocity and increase the toughness with an appreciable difference. The results show that the insufficient number of micro-cracks are inadequate to slow down crack tip’s propagation velocities. The density of

micro-cracks in a constant area and the number of micro-cracks in expanding areas are significant parameters on the toughening mechanism of a material. Using fracture modelling competence of PD can help improve understanding of the design of more endurance geometries. Modelling results provide the solution of certain cases, either the length or distances of micro-cracks can be investigated in future studies. Overall, considering the trends of models together, it is observed that velocity differences between models decrease as the macro-cracks approach edges of the body. This part of the dissertation was published as an article in the journal (see [119]).

4. WIRE ROPES

Wire ropes and generally cable systems can experience unexpected breakage during material handling processes. Since the usage area of cable systems spans a wide range, the failure and damage of ropes are of interest to various research fields including mining, civil, and mechanical engineering. Wire rope damage directly affects the material handling process in any plant such as ports, decks, or ships. The failure of wire ropes brings risks in terms of load damage or loosing and can cause accidents resulting in serious injuries.

Consequently, a deep understanding of wire ropes' failure mechanism is an important research topic to avoid unexpected damage. Unfortunately, many researchers have studied only certain loading conditions, such as bending or tensional loading, using finite element analysis. The impact loading in the both axial or transverse direction to wire rope still requires more investigation. An impact load can result in an undetermined mechanical response of the rope.

Corrosion, insufficient lubrication, porosities in the working area, and wear can decrease the strength of wire ropes. It should be noted that ropes should be checked for broken wires and, inspected and maintained within a certain period during working. In general, ropes should be examined at least once per month or more often, in accordance with the instruction of the competent person in a typical material handling area. Depending on the rope's condition, the competent person may deem it necessary to reduce the time interval between examinations.

In a special examination, the wire rope should be carefully examined if an incident has occurred which could have caused damage to the wire rope and/or its termination, or if a rope has been brought back into operation after dismantling followed by reassembly.

There are some points that need to be covered by the examination. Although a wire rope should be examined throughout its length, a particular care should be taken at the following locations:

- The termination points of both moving and stationary ropes,
- That part of the rope which passes through the block or over sheaves,
- In the case of systems performing repetitive operations, any part of the rope which lies over sheaves while the system is in a loaded condition
- That part of the rope which lies over a compensating sheaves
- Any part of the rope which may be subject to abrasion by external features,
- Internals of the rope, for corrosion and fatigue
- Any part of the rope exposed to wear.

The result of the examination should be recorded in the examination record for the system. The rope should be examined in the area where it passes out from the termination, as this position is critical for the onset of fatigue (wire breaks) and corrosion. The terminal fittings themselves should also be examined for signs of distortion or wear. When broken wires are evident close to, or within, the termination, it may be possible to shorten the rope and re-fit the terminal fittings. However, the wire rope's resulting length should be sufficient to allow for the minimum required number of rope wraps on the drum.

Non-destructive testing (NDT) by electromagnetic techniques may be used as an aid to visual inspection to determine areas and levels of rope deterioration. When it is the intention to use electromagnetic means of NDT as an aid to visual examination, the rope should be subject to an initial electromagnetic NDT examination as soon as possible after the rope has been installed.

Discard decisions about wire rope focus most predominantly on the number of broken wires, but other damage mechanisms such as wear, corrosion, distortion, and mechanical damage must also be considered. The decision to discard a wire rope must be based not on whether the rope has become unsafe, but whether it will become unsafe before the next inspection.

To ensure the health and safety of wire ropes, one should follow the recent standards and instructions provided by manufacturers.

Figure 4.1 shows a damaged wire rope. The broken wires can be seen in the outer strand. On visual inspection of the wire rope, several fractures of the individual wires were observed. Internal corrosion and wear were observed on the inner surface of the outer strands of the wire rope. This effect caused that material becomes more brittle under more humid climate conditions.



Figure 4.1 : A damaged wire rope.

According to Mahmoud [120], environmental effects can cause an adverse effect on not only wire cross sectional area reduction, but also on ductility loss. The influence of hydrogen embrittlement can result in a fracture of a wire with a minimal necking, as shown in Figure 4.2 [120]. The reduced ductility means that the wire structure can show a brittle regime of fracture under loading.

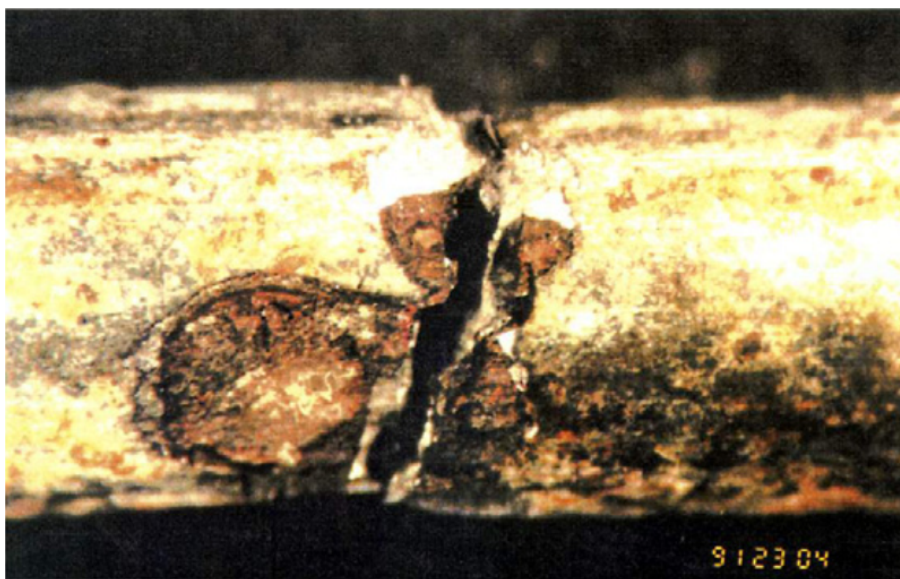


Figure 4.2 : Brittle wire fracture with minimal necking.

Therefore, reasons for the catastrophic fracture of the wire rope need more investigation with the aspect of crack initiation and propagation.

The classical equilibrium equations of wire ropes were derived by Love. Most of researchers presented analytical solutions and physical models based on this equilibrium equations in the literature. The modelling of wire ropes is a very challenging work due to the complex geometry of multi-lay strands. In theoretical studies, most of the varying aspects depended on non-frictional and contact-less cases. Numerical studies provide solutions that take into account the effect of friction, contact, and boundary conditions [121].

In this chapter, the structure and components of wire ropes were introduced. The different type of wire ropes and lay types were presented. After revisiting the historical usage, the modern day strand types such as Seale, Filler, and Warrington were defined with examples.

A literature review was presented to investigate the different aspects of wire rope modelling and analysis. The fundamental theory of cable systems and wire ropes were explained and then, four theoretical models; Purely tensile or fibre model, Semi-continuous strand model, Theory of thin rods model, Helical rod model were explained. An enhanced literature review was conducted to summarize the numerical models and reported test results in recent years in the third section.

4.1 Structure of Wire Ropes

The oldest records of ropes were found on Egypt drawings and dated approximately 12000 to 9000 BC. These were made of hides, hair, and plants. Human civilization used ropes for lifting, dragging heavy loads. With the industrial revolution, the modern type of wire ropes was developed and used in silver mines in Harz Mountains in 1834 [121].

Basic geometry and components of a wire rope are shown in Figure 4.3 [122]. The strand is composed of helically shaped wires. Outer strands are wrapping around the core strand. Each strand has a centre wire that determines the geometrical coordinates of the helical path. The acting load on the rope mostly carried by the strands. The core member is guiding for helical wrapping strands.

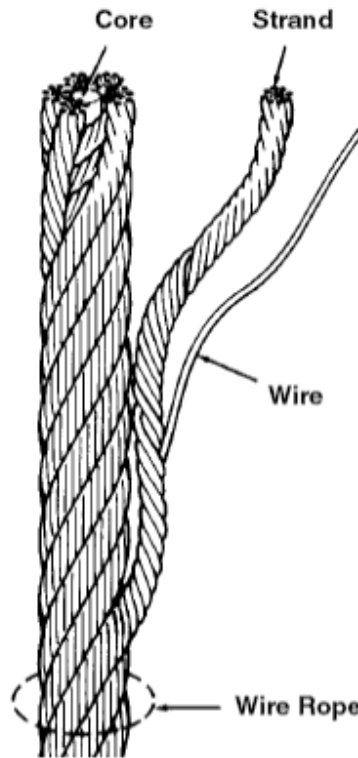


Figure 4.3 : Components of a wire rope.

The wire ropes are named by the laid direction of the strands around the core. Various lay types of wire ropes are given in Figure 4.4. Right regular lay (sZ), left regular lay (zS), right lang lay (zZ) and left lang lay wire (sS) cores are defined.

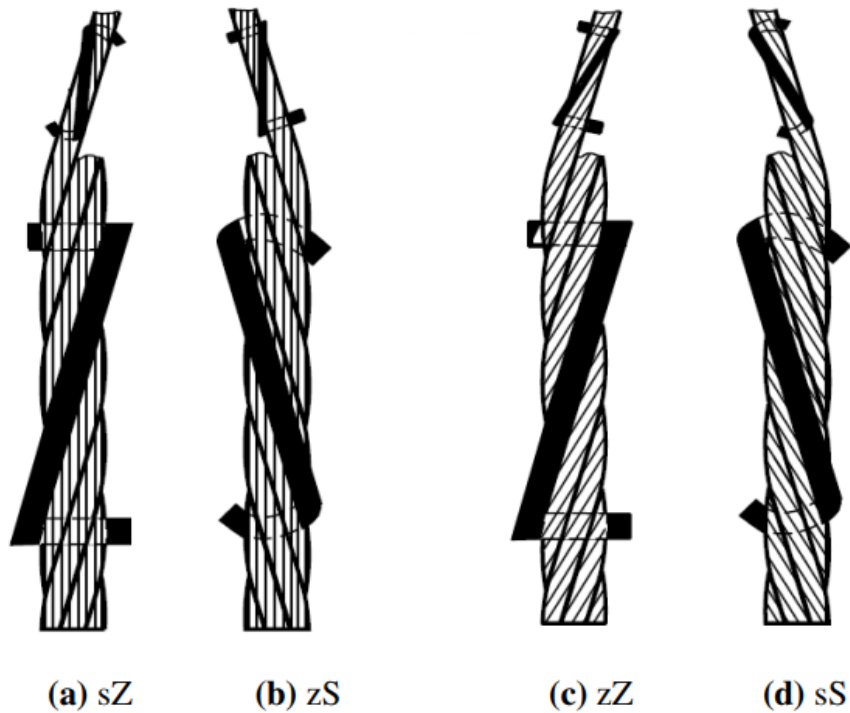


Figure 4.4 : Wire rope lay types: (a) right regular lay (sZ), (b) left regular lay (zS), (c) right lang lay (zZ), (d) left lang lay wire (sS).

In Figure 4.4(a), wires are wrapping around outer strands in left way and these strands composed the wire rope in the opposite right direction. In the "sZ" symbol, the small "s" represents the left lay direction of a wire and the capital "Z" represents the right lay direction of a strand around the core [122]. The centre core is a simple straight strand for all types [121]. Outer strands form a helical path around the centre core. Various types of wire ropes can be designed with different numbers of wires and strands, and lay directions for different applications. In Figure 4.5, a fundamental wire rope axial section is given. Six helical wires are wrapping around a straight centre core and it is called as 1x6 wire strand.

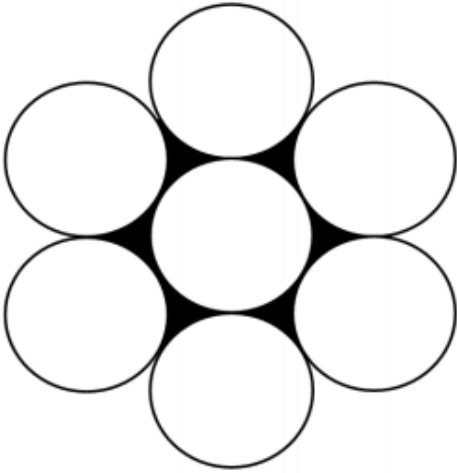


Figure 4.5 : Cross sectional view of 1x6 wire strand.

Seale, Filler, and Warrington are the most commonly used types of wire ropes [121]. The cross sectional areas of these primary strands are given in Figure 4.6.

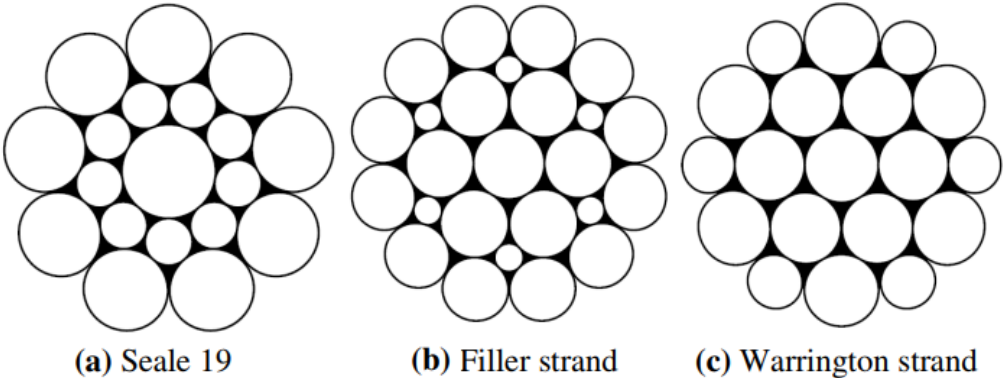


Figure 4.6 : Basic strand types.

The independent wire rope core (IWRC) is given in Figure 4.7. It is termed as 6x36 Warrington-Seale wire rope with a steel core.

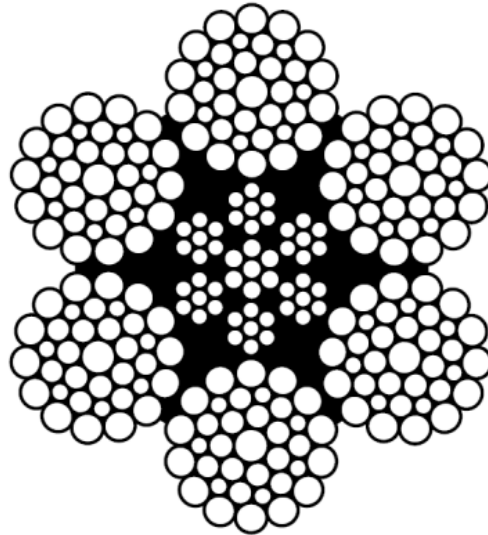


Figure 4.7 : 6x36 Warrington-Seale (IWRC) type wire rope with a steel core.

A rotating and a rotation resistant wires rope are given in Figure 4.8(a) and (b), respectively [123]. The opposite placement of inner and outer core provides a rotation resistance under axial loading.

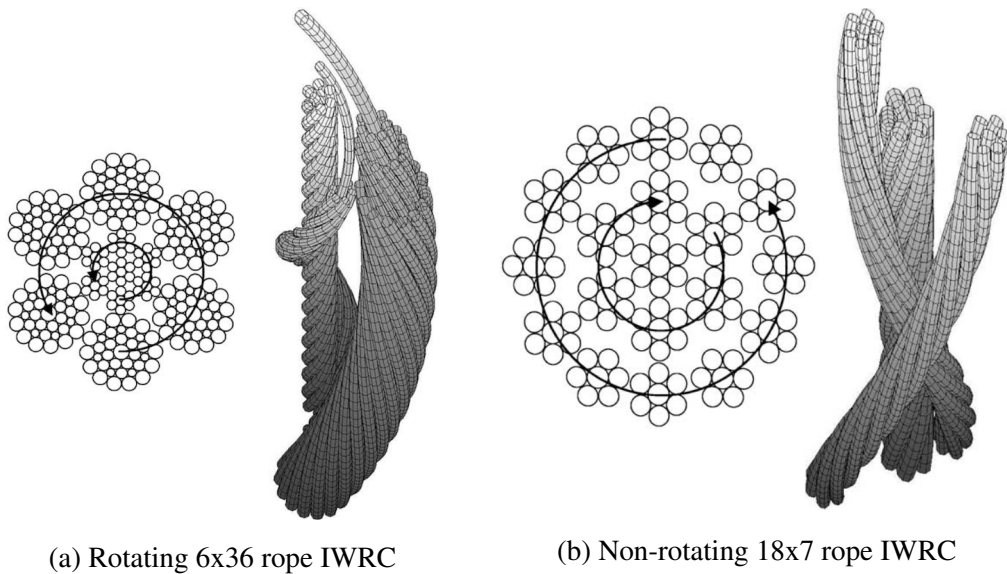


Figure 4.8 : The schematic cross section description of the strands of rotating and non-rotating IWRC.

4.2 Theory of Wire Ropes

Steel wire ropes are widely used for various applications, especially in elevators, cranes, ships, and other handling operations. Therefore, they consist of an important research subject in both mechanical and civil engineering. From 1970's to the present,

wire rope theory and its complex structure were extensively studied by a number of researchers.

Love (1944) presented the well-known general theory of rods and governed the equilibrium equations of a thin rod on an arc section [124]. The studies on wire ropes mostly have based on these formulations. The equilibrium equations are a starting point for most of analytical and numerical solutions of wire ropes. Timoshenko [125] investigated and defined the mechanical behaviour of wire ropes in his book. A restricted and linearised form of equations governed by Green and Laws [126] to obtain stresses in helical wires in cables. Hruska [127] proposed simple constraints to investigate the mechanical behaviour of wire ropes.

4.2.1 Theoretical models

A brief introduction to theoretical models of cable and wire ropes is presented. There are four main types of models of wire ropes.

4.2.1.1 Purely tensile or fibre model

Hruska [127] presented the purely tensile model in 1951. In this simple model, there is no boundary condition. The contact was defined as purely radial and contradiction was not taken into account. Ropes were only subjected to tensile loading and moments were not applied. The friction was neglected and the whole strand deflection can be thought of as infinitely small. Knapp [128] extended the theory by including compression of the core. Velinsky [129] developed a theory for the analysis of fibre-core wire rope subjected to an axial force and twisting moment. After solving the linear theory equations, the theory is applied to Seale fibre-core wire ropes. The theoretically obtaining Young's modulus and Poisson's ratio of the structure showed similar results with the experiment.

4.2.1.2 Orthotropic sheet model

Hobbs and Raoof [130] introduced the semi-continuous strand model, also known as the orthotropic sheet model. In this model, homogenized wire layers were thought of as an equivalent orthotropic cylindrical sheet. Modelling multi-layered strands and theoretical analysis of large-diameter wire ropes can be studied using this model [131]. In some studies [132–136], each layer was replaced with a cylinder of orthotropic,

transversely isotropic body. A linear static elastic model was developed to model more complex geometries subjected to axial loads using discrete thin rod theory [137, 138]. This model focused on the problem of asymmetry in earlier models and the generation of a general model to examine the pre-slip response of helical strands. Moreover, wire/core friction contacts were taken into account by a constant curvature bending.

4.2.1.3 Theory of thin rod

Ramsey [139] introduced the theory of thin rod in 1988. The theory was a derivation and application of the direct approach presented by Green and Laws [126]. Stresses in helical wires in cables were determined with various loading conditions.

4.2.1.4 Helical rod model

The model presented by Phillips and Costello [140] was based on the formulations derived by Love [124]. Costello and other authors' works had continued in the subject, such as contact stresses in thin twisted rods [141], large deflections of helical spring due to bending [142], analytical Investigation of wire rope [143], a simplified bending theory for wire rope [144], stresses in multi layered cables [145], wire rope with complex cross sections [146], static response of reduced rotation rope [147], effective modulus of twisted wire cables [148], a more exact theory for twisted wire cables [149], axial impact of twisted wire cables [150], bird-caging in wire rope [151], torsional stiffness of twisted wire cables [152], viscoelastic response of a strand [153], effective length of a fractured wire in wire rope [154], analysis of wire ropes with internal wire rope cores [155]. Moreover, Costello published a book that presented a general view of studies [156].

4.3 Literature Review

As a result of their complex structure, analysing each strand in a rope to determine deformations and stress distributions along a rope is challenging. Some researchers have presented analytical solutions of wire rope theory with certain assumptions.

The basic theory for wire ropes under tensile loading with regarding to tension and torsion was studied in [127, 157]. It neglected the boundary conditions. The theory did not cover the contact stresses. Costello [156] and Utting and Jones [158, 159]

created a more general form. In their solution, a wire in a wire rope can be considered as a helically curved rod. Moreover, the rope geometry and inter-wire contacts were defined with various assumptions.

A simplified finite element analysis model for armoured ropes was proposed by Carlson et al. in [160]. Cutchins et al. [161] studied damping isolators. The vibration isolation and shock absorption ability of wire ropes were modelled and analysed in there. Chiang [162] studied on characterizing a simple stranded wire cable under axial loading.

Moreover some researchers used various methodologies and modelling technique to analyses and design wire ropes and related mechanisms [163, 164]. Cardou and Jolicoeur [165] examined design criteria of wire ropes and compared analytical models. The theory of slender curved rods was used to determine the extension of a strand subjected to axial and torsional loading [166]. Shield and Costello [167, 168] examined the effect of wire rope mechanics on the material properties of cord composites with both an elasticity approach and an energy approach. Moreover they investigated the bending of cord composite plates [169]. The bending of cord composite cylindrical shells was also examined in [170,171]. Velinsky [172] developed an analysis of stiffened, wire-strand based structures with compressive forcing.

The analytical solutions to obtain contact stresses in multi-layered strands with a metallic core were governed in [173]. Jiang et al. [174] used three-dimensional solid brick elements to develop a concise FEM model for a wire rope. The model that contains structural and load symmetries combined the effect of different loading types. Nawrocki et al. [175] developed a finite element model for simple straight wire rope strands.

Some of the important articles about wire rope modelling, analysis, and experiments are summarized from this point.

Phillips and Costello [140] proposed a procedure for determining the stresses in twisted wire cables. They took into account large changes in helix angle caused by loading. With some representative examples, the contact line loads between each wires were determined. The contact line load increased with increasing axial loading on the cable up to a top point and then decreased. This was caused by the straightening of the cable

wires, such as the increasing of helix angle. Their findings indicated that the change in helix geometry due to loading should be considered an important parameter to solve governing equations.

Machida and Durelli [176] determined the axial force, bending, and torsion moments in a helical wire. Besides, the axial force and twisting moment were investigated in a 7-wire strand subjected to axial and torsional displacements. Experimental strain analysis and theoretical results were compared to explain that the minimal contact force and resultant frictional forces were too small due to small lay angle and large helix angle.

Costello and Phillips [148] investigated the effective modulus of twisted wire cables by a load-deflection relation for two types of end conditions. They also showed that cables that had fixed ends against rotation were stiffer than that had free ends. The end conditions were important factors that determine the cable stiffness. In the paper, friction was neglected and wires were assumed as extensible.

Costello and Miler [122] developed a theory that determined the static response of a wire rope. The wires of a strand were wound in different directions. The axial strain was given as a function of the axial forces for two examples, i.e.: ropes with zero end-moment and ropes restrained against rotation. The results indicated that a lang lay rope should never be used if the ends are free to rotate. A lang lay rope under tension shows no significant stiffness due to running out of the lay.

In 1980, Costello and Miler [147] presented a reduced rotation wire rope model in which friction is neglected. They also provided experimental results for a 1x19 wire rope.

Velinsky et al. [146] predicted the behaviour of a wire rope with complex cross sections with regard to axial static response. They indicated that when a wire rope was restricted to rotate, maximum normal stress was obtained in the centre.

Lanteigne [177] studied the mechanical behaviour of aluminium conductor steel reinforced conductors subjected to static loads that combine tension, torsion and bending. The developing stiffness matrix was presented and results in bending forcing showed similar characteristics with Costello [145].

Chien and Costello [154] investigated the effective length of a fractured wire. The contact loads between the wires and Coulomb type friction were taken into account. They proposed that the effective length to the pitch of the outer strand can be constant value for certain cross sections.

Phillips and Costello [155] determined the stresses of an each wire in a complex wire rope with a wire rope core. The forcing scenarios were tension, torsion, and bending over a sheave. The friction was neglected. They found that the effective modulus of elasticity was higher than previous studies for an IWRC.

Velinsky [129] developed the non-linear theory on analysing complex wire ropes. The bending and twisting of thin rods were taken into account in the non-linear equations. A 6x19 Seale wire rope was tested. In comparison to the non-linear theory and linear theory, they showed similar results in most cases.

Kumar et al. [178] developed a closed form solution for elastic deformations in multi-layered strand subjected to tensile and torsional forcing. The layout of layers, number of wires, and direction and magnitude of lay angles were found as significant parameters of deformation characteristics. Besides, they proposed examples that demonstrate their solutions.

Velinsky [179] developed a methodology for modelling a wire strand in which non-linear equations were numerically solved. Then, with the curve fitting, polynomial expressions for designing a wire rope was proposed.

Jiang [180] examined non-linear and linear analysis of wire ropes with a general formulation that consisted of seven stiffness and deformation constants. Both wire ropes with the complex cross sections and basic wire strands can be analysed with this given general formulation. Jiang et al. [181] studied on finite element model of a wire strand to examine the effect of ending conditions. To reduce the computational sources, the strand was considered cyclic symmetric. The contact forces and relative deformations trough the contact lines were taken into account were analysed regarding the fixed-end conditions. Jiang et al. [174] developed a helically symmetric finite element model for a three-layered straight wire rope. They compared the results with Costello's elasticity theory [156] and experimental data of Utting and Jones [158, 159].

Yardibi [182] examine the stresses of a wire subjected to axial loading and bending of wire ropes in his thesis. Then, Şentürk [183] studied modelling and analysis of wire rope strand under axial loading using FEM.

Nawrocki and Labrosse [175] developed a finite element model using Cartesian iso-parametric formulation to consider inter-wire motions.

Elata et al. [184] examined the mechanical behaviour of a wire rope with an independent wire core (IWRC). The model considered the double-helix structure of each wire and relation between wire level stress and overall applied load.

Ghoreishi et al. [185] presented a model for axial behaviour of synthetic ropes. The presented model contained six helical wires wrapped around a straight core. A normal force and torque were applied. However, the model was only validated within limited small helix angles. Ghoreishi et al. [186] developed a continuum model for multi-layered fibrous structures subjected to axial loads. The structure was considered a set of coaxial helices characterized by their external lay angle and radius. The axial loads were static and constitutive material was assumed as linear. The friction between fibres was neglected. This analytical model was proposed as a useful closed form formulation, which allowed to optimize the rope constructions.

4.3.1 Experimental studies

Durelli et al. [187] conducted a series of tests to examine the strain and stresses characteristics of steel strands subjected to axial loadings. They found that strains in some wires were not linearly related to the load. Moreover, the points in different wires at a transverse cross section of a strand did not carry the same stress. They proposed some possible source of this behaviour; local variation in wire geometry, external particles and related friction variations between wire and core. They also determined the effective Young's Modulus of the strand restricted as $\tilde{165}$ GPa.

Utting and Jones [188] reported experimental test results of wire rope strands subjected to static axial loads. The strands were restrained at both ends and strain gage load cells gave tensile load data and the associated twisting moment. The presented experimental results of extension and rotation movements were in good agreement with the corresponding theoretical predictions. They also carried out tests on straight

single steel strands consisting of seven wires subjected to axial loads with various end conditions [158, 159]. As a result, a mathematical model of a strand was developed to obtain the change of helix angle, Poisson's ratio effects, wire flattening, and friction between core and wires.

Raooof and Hobbs [189] conducted experimental studies to examine the torsional characteristics of structural strands. The torsional stiffness for static and dynamic cases and hysteresis graphs were given for axially preloaded strands.

Bateman et al. [190] developed a computer simulation that models the roadway wire rope safety fence impacted by a vehicle to reduce the number of real scale crash tests. The model was based on the vehicle's dynamic motion and quasi-static mechanical response of the wire rope.

Onur and İmrak [191] investigated the fatigue lifetime of 6x36 Warrington-Seale wire rope bending over a sheave with various diameters. The study extended to the experimental and theoretical investigation of a wire rope subjected to normal load [192].

4.3.2 Recent studies on impact load and contacts in wire rope modelling

A review of recent studies that examine wire ropes subjected to impact load was given in this section. Moreover, articles considering contact states were also examined.

Cardou and Jolicoeur [165] summarized the contact modes under ideal conditions such as wire diameters and lay angles having exactly their nominal value. The first contact mode is radial contact: the wires in the same layer do not touch each other, but only do to those in adjacent layers. The second contact mode is lateral contact: the wires in the same layer are in contact, but they do not touch with the adjacent layers. The last mode is the mixed type: the wires are in contact with both those in the same layer and adjacent layers. Both radial and lateral contact occur. Cardou and Jolicoeur stated that one of these contact types should be selected in analysis because of static indeterminacy [165].

The detail definitions of the contact phenomena of wire ropes were stated by Hobbs and Raooof [193]. They stated that two types of inter-wire contact were observed in a typical multi-layered helical wire strand, as seen in Figure 4.9. The first contact type

is between wires in a given single layer, which governs the hysteresis characteristics under cyclic loading and affects the stiffness in overall axial, torsional, and free bending cases. Mode A in Figure 4.9 simply simulates this contact type between adjacent "parallel" wires. Hobbs and Raof evaluated this class of contact was similar to the line contact between parallel cylinders in terms of contact stress theory. In a 1x6 strand, these line contacts can be observed between outer wires and the core wire.

The mode B in Figure 4.9 is the other type of inter-wire contacts occurring between the layers of a helical strand which is termed as trellis contact. There is an oblique angle between the crossing layers. The contact stresses are higher than the line contacts because of the small cross sectional area as expected. The high stress concentrations can occur in the contact area because of trellis contact, especially in transverse loading conditions. The elastic, hysteric and fatigue properties of a wire rope can only be understood by examining how these two significant contact mechanism modelled.

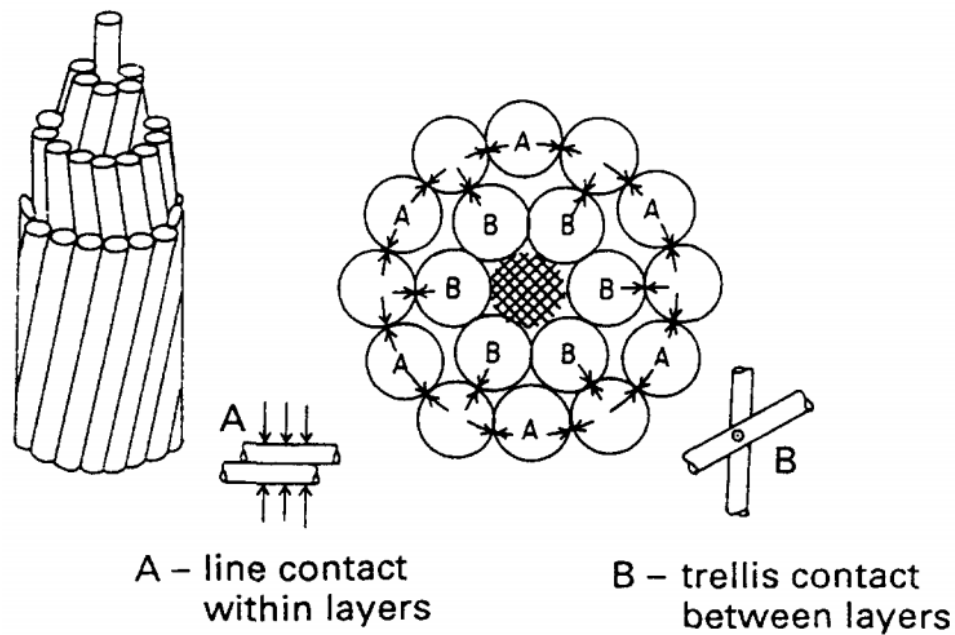


Figure 4.9 : The contact types between wires in a helical strand.

Foti and Roseto [194] modelled the elastic-plastic behaviour of metallic strands with a new formulation. They defined two basic internal contact modes. In Figure 4.10(a), the radial contact and in Figure 4.10(b) the lateral contact states are given. In the radial contact case, surfaces of outer wires are in contact with the surface of the core, but not among them. Conversely, in the second case, contacts only existed between outer

wires, not between core and outer wires. These modes were defined by Hobbs and Raoof [193] and Cardou and Jolicoeur [165] in 1996 and 1997, respectively.

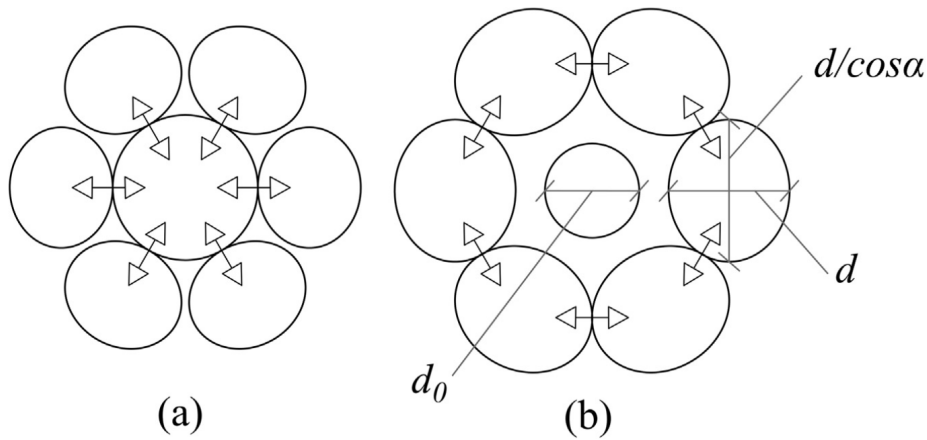


Figure 4.10 : Definition of contact modes in a cross section of view of a strand, (a) radial contact and (b) lateral contact. d and d_0 are diameters of the outer wire and core, respectively. α is the lay angle.

In the same study, Foti and Roseto [194] stated that the definition of the internal contact among wires was based on surface-to-surface contact pairs approach. It took into account both possible relative sliding between wires and deformability of contact surfaces. The classic Coulomb's law was used as a friction model. They used CONTA 174 and TARGE 170 elements to model each contact pair and an Augmented Lagrangian algorithm was defined to enforce contact compatibility conditions. Then, Pure Penalty algorithm was preferred to minimize the sensitivity of the solution to the normal contact stiffness. One of the important subjects in the study is that neglecting of wire flattening phenomena formed by the deformation of the contact surface between wires and core. Although this surface deformation can result with a cross section profile of a wire, it was neglected for practical purposes as in many studies.

Jiang et al. [174, 195] proposed a finite element model considering plastic deformation and internal contact conditions. They used three-dimensional solid brick elements for the discretization of bodies. They stated that contacts between the centre and outer wires were modelled using contact elements that provide positive pressure transfer between surfaces. Figure 4.11 shows the condensed mesh at the near edge of the contact region. To sustain the computational efficiency, the outer regions can be modelled with coarse meshes. Therefore, the Coulomb friction sliding can be simulated by surface-to-surface contact approach.

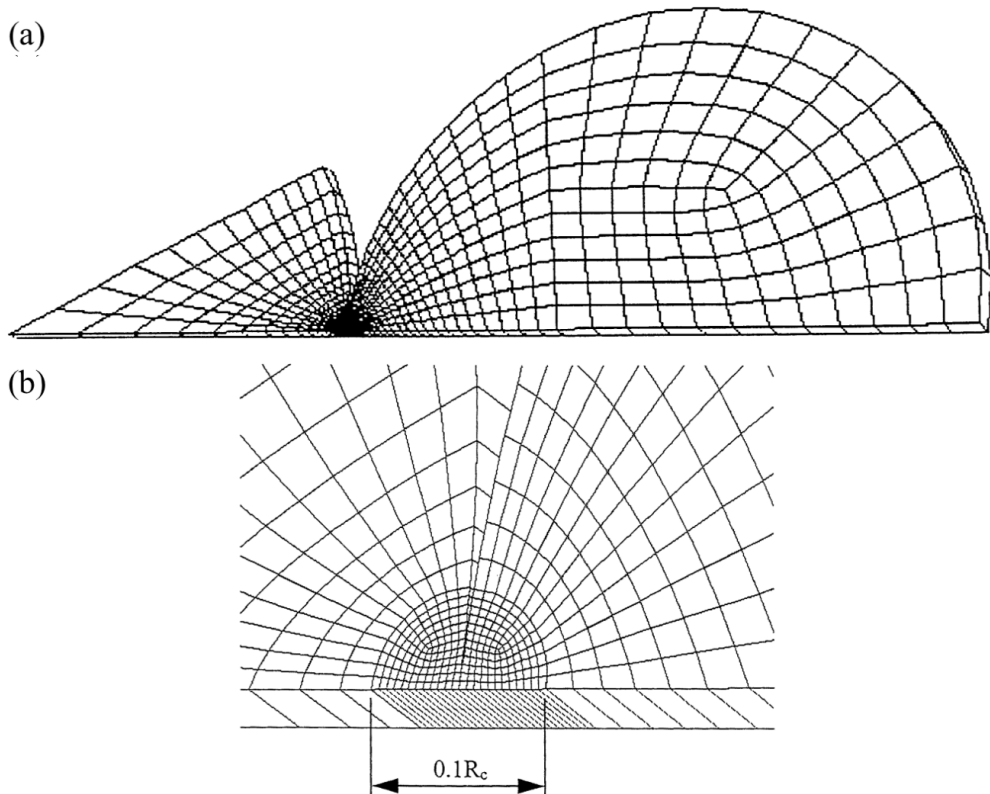


Figure 4.11 : Finite element mesh of a slice of 1/12 of a 7-wire strand (a) global view, (b) detailed view in contact region. R_c is the radius of the centre core.

Jiang et al. [196] presented work on statically indeterminate contacts in axially loaded wire strand. They proposed that 10^{-5} of the wire radius is a suitable error for maximum penetration between contact surfaces. The finite element mesh model of the unstable contact condition is given in Figure 4.12.

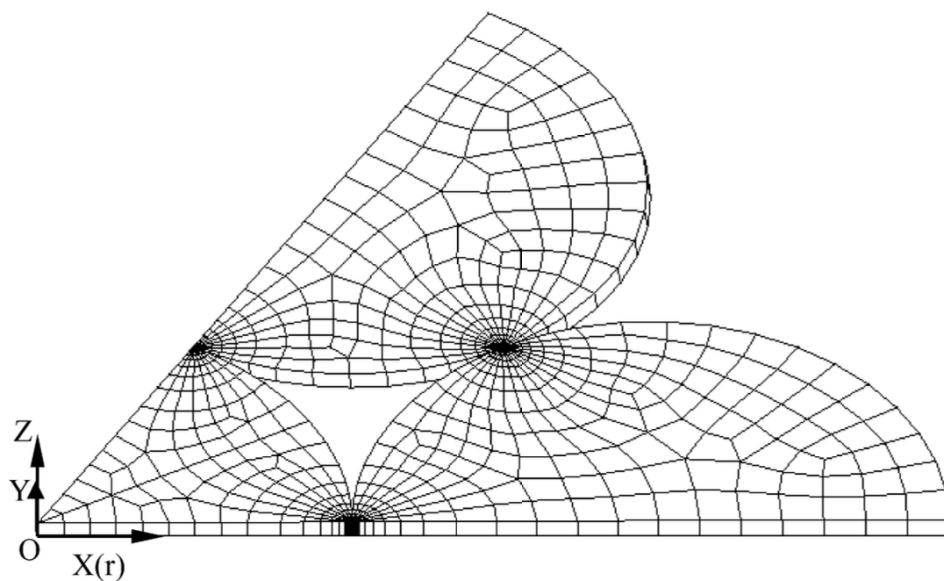


Figure 4.12 : Finite element mesh of a mixing type contact. More dense mesh structures are applied to the contact regions.

Jiang [197] examined the mechanical behaviour of a simple wire strand under pure bending. In this study, the contact elements between the surfaces were used to simulate the surface-to-surface contact with the Coulomb friction sliding. In this model, the diameter of the centre core diameter is greater than the outer wires'. Therefore, wires on the outer layers do not have contacts with each other.

The mesh in the FEM analysis made by Jiang [197] is given in Figure 4.13. The concentrated mesh can be seen in the vicinity of the contact region.

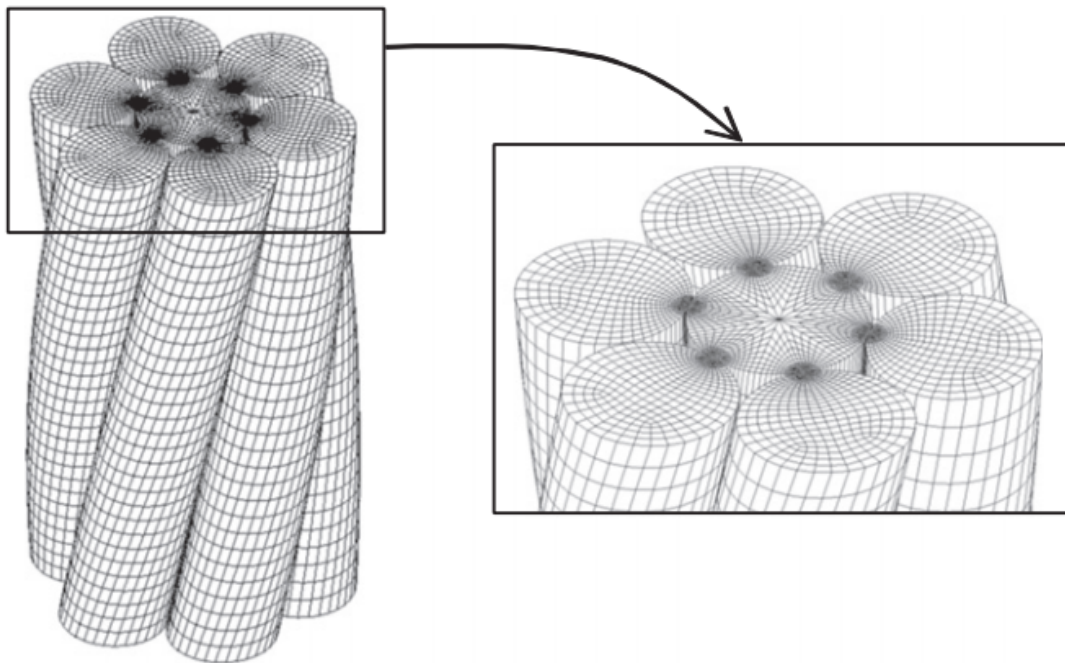


Figure 4.13 : Increased mesh number in the contact region.

Argatov et al. [198] examined the wear characteristics of wire ropes subjected to cyclic bending over a sheave. They modelled the contact deformation and the transverse contraction of a simple helical wire.

Fontanari et al. [199] investigated the elasto-plastic mechanical behaviour of a Warrington-Seale type of wire rope using finite element method. The mesh volumes consisted of eight node brick elements, as seen in Figure 4.14. The radial dimension of a mesh was lower than $1/12$ of the wire radius and the longitudinal length was at least $1/10$ of the axial span to make the analysis mesh independent. The contact of the wires was modelled by surface-surface contact definition with four nodes contact elements. Figure 4.14 shows contacts that defined between wires in different layers. The contacts between wires in the same layers were not defined.

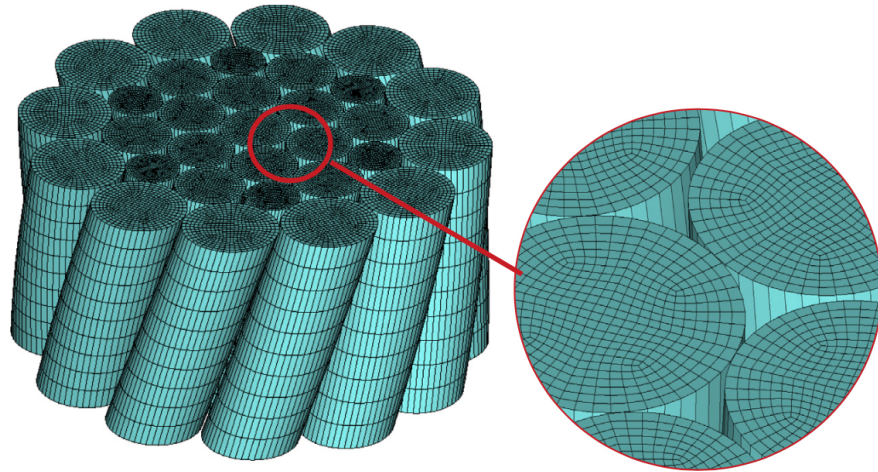


Figure 4.14 : Finite Element mesh of a Warrington-Seale (WS12+6/6+6+1) strand and the detail view of contact.

Fontanari et al. [200] presented more detail on contact definition of a meshed body in the article about fire behaviour of steel wire ropes. In this paper, the body of wires was discretized using 8-nodes brick structural elements. Then contacts were defined as surface-to-surface four nodes contact elements. They stated that an iterative convergence analysis was made to obtain to minimize the number of contact pairs. The 3D model of the mesh and contact surfaces of the wire can be seen in Figure 4.15.

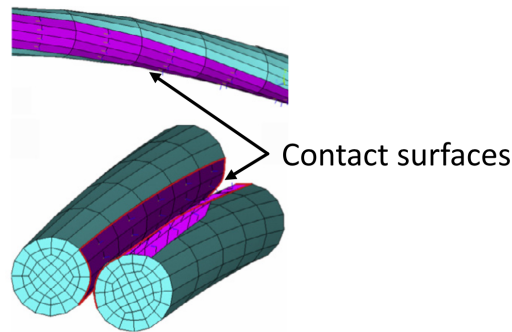


Figure 4.15 : Identification of the contact surfaces with four surface approach.

Bruski [201] presented a study on bending properties of a commonly used wire rope in cable barriers: 3x7 19 mm. In this paper, numerical studies by using FEM were compared to experimental tests. The relationship between moment and curvature was investigated. The inter-contact definition of wires in the study was based on a penalty-based mortar contact algorithm as in [202].

Huang et al. [203] proposed a co-simulation method based on multi-body dynamics and FEM to determine the dynamic responses of a wire rope in a hoisting system of a crane. They presented a detail contact modelling definition in the study. The two types

of contacts in the multi-layered strand wire rope were stated as explained in previous studies. The first the contact between two wires in a neighbour layer and the second is the contact between adjacent parallel wires in the same layer, which can be seen in Figure 4.10. The contact modelling used in this study is surface-to-surface contact type with a finite sliding between wires. In addition, the tangential behaviour was modelled with penalty friction formulation with the coefficient of 0.15. The two end surface of wire ropes were coupled kinematically to apply the concentrated forces on the end surfaces.

Judge et al. [204] modelled spiral strand cables in 3D and examined stresses in various cross sections. The contacts between wires in the same layer and between a wire and the core were modelled as surface-to-surface to simplify the construction. To define the contact surface, `AUTOMATIC_SINGLE_SURFACE` in LS-DYNA was used in the simulations. The friction coefficient was given as 0.115 in all simulations.

Karathanasopoulos et al. [205] modelled a strand in 2D for examining the elasto-plastic axial-torsional response of a helical wire rope. In order to define the radial contact of the helical wires with the central core, node-to-node contact pairs were used considering fully kinematically coupling. The mesh and contacts between inter-wires are shown in Figure 4.16 [205].

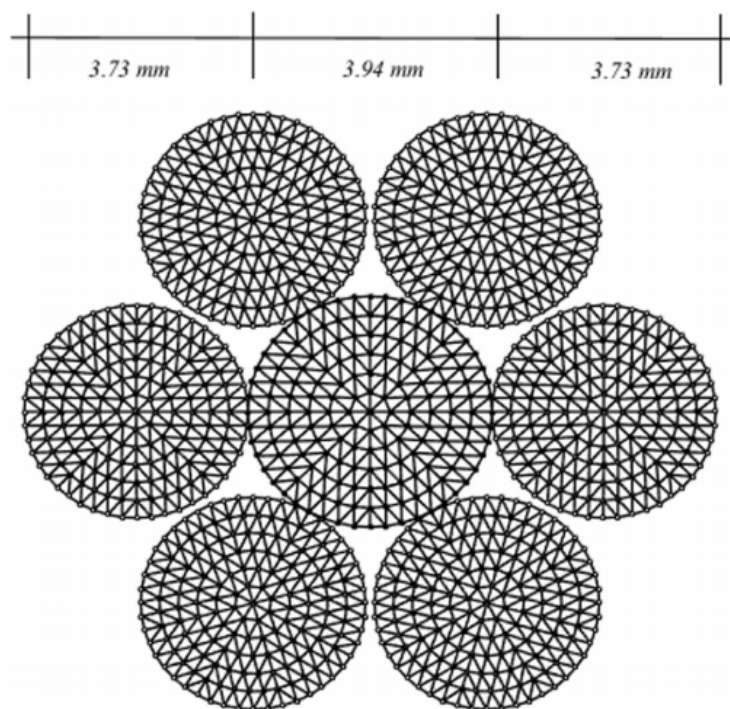


Figure 4.16 : Dimensions and 2D mesh of a helical strand.

İmrak and Erdönmez [206] introduced a technique of modelling wire rope with IWRC. The new technique was then applied for both right regular lay and lang lay IWRCs and conducted FEM analysis with various loading conditions for validation [207].

Erdönmez and İmrak [208] proposed to use of the Frenet-Serret frame for generation helical structures. A circle or a quadrilateral were swept to generate both single helical and nested helical solid structures by using the moving trihedron along the centreline of the helical geometry. Moreover, an algorithm was presented to model helical structures without length limitation with an accurate and valid mesh. Then, a FEM analysis was conducted under an axial strain loading condition. A helical line of contact was obtained between the centre wire and the outer helical wires, shown in Figure 4.17(a). When using finer mesh in models, smoother helical line of contact between wires occurred Figure 4.17(b) [208].

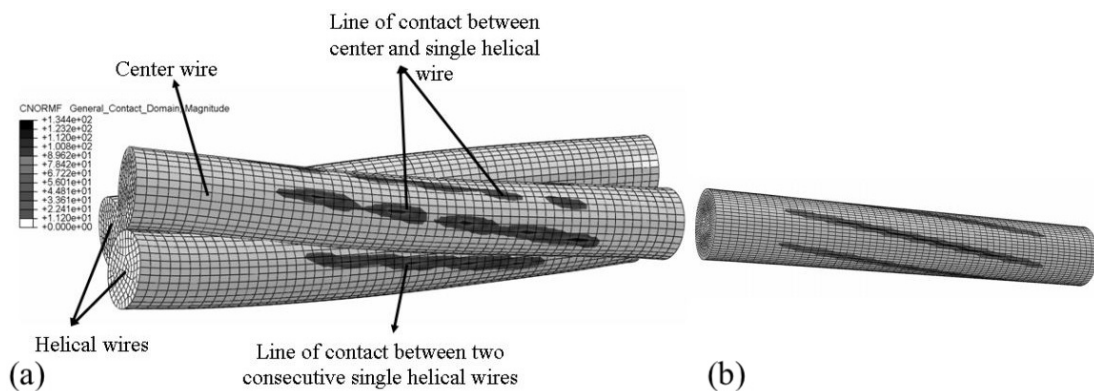


Figure 4.17 : Contact force distribution on (a) simple straight strand and (b) centre wire with finer mesh.

Erdönmez [209] generated a three-dimensional solid model of a triple helix geometry. Then, a generalized form procedure was presented to define parametric equations to model n-tuple helical geometries.

Erdönmez [210] addressed one of the problematic issues on the meshing process of wire ropes. The proposed method to model the mesh of classical and compacted wire strand is shown in Figure 4.18(a) and (b), respectively. Comparison of contact force distribution for related wire strand configurations was also given in Figure 4.18(c) and (d). The loading was the static strain in the axial direction of the wire strand. Linear hexahedral elements of type C3D8R were used in mesh process.

Erdönmez [211] proposed a multi-layered compacted wire rope model that allows users to create any length of compacted independent wire rope core geometry by changing wire radius and pitch length.

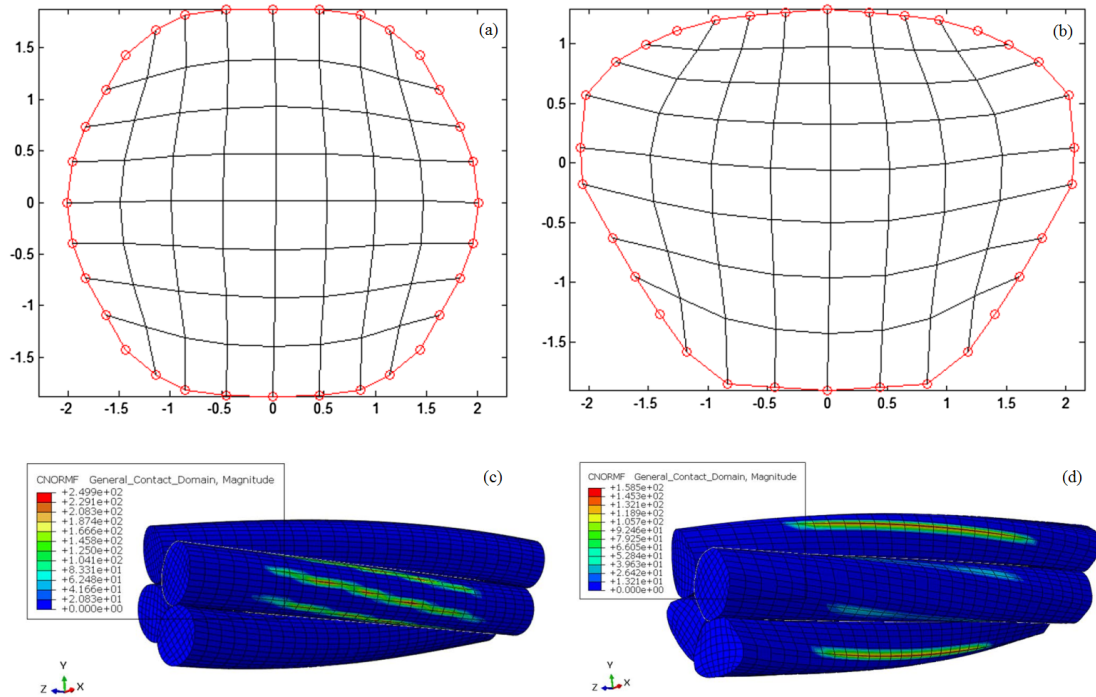


Figure 4.18 : Meshing of (a) straight centre wire and (b) outer compacted wire. Comparison of contact force distribution along (c) classical and (d) compacted wire strand.

Kastratović et al. [212] studied the crack propagation in a single wire in a strand under the axial loading, shown in Figure 4.19. The relation between crack depth and stress intensity factors were given in this article.

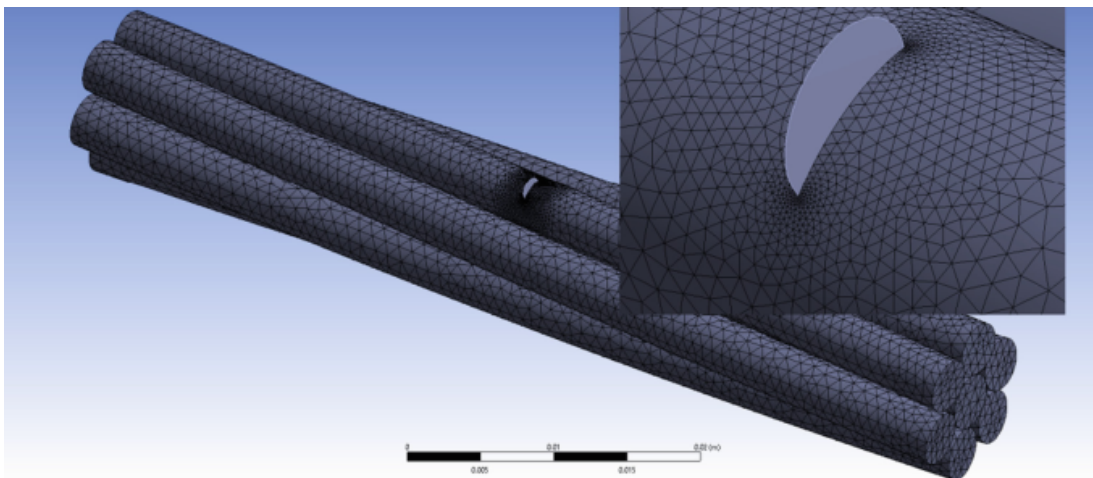


Figure 4.19 : Meshing of wire strand with a pre-crack.

5. MODELLING OF WIRE ROPES USING PERIDYNAMIC THEORY

This chapter provides a brief overview of the coding process and managing outputs. It then goes on to modelling wire ropes using Peridynamic theory. Firstly, it is aimed to provide information on coding and analysing of Peridynamic models. A script for micro-crack creation was given to ensure the reproducibility of simulations in this study. The algorithm of material point generation for wire section was also given. Sharing the knowledge of handling with outputs was considered a guide for everyone who studies Peridynamics and similar output files. In the following section, an introduction to modelling of wire ropes in Peridynamic theory was given. The contact states and loading conditions were discussed. Case studies were prepared. Convergence studies were carried out to explore the applicability of Peridynamic theory on wire sections. These studies have concentrated on assessing crack propagation in wire ropes subjected to impact loading. The proposed discretization parameters of wire rope stands were discussed in the aspect of Peridynamic modelling.

5.1 Codes and Software

Fortran language has been still a powerful and fast way in solution of numerical methods, however, the lack of visualization abilities requires to use of some other programs in post-processing of the results. To overcome this issue, results obtained from a Fortran code need to be exported to another program, e.g. Matlab or Ovitto. The Kalthoff-Winkler Fortran codes provided by Madenci and Oterkus [87] writes results to MATLAB files. These files are `cxcg.m`, `cycg.m`, `czcg.m`, `uxcg.m`, `uycg.m`, `uzcg.m`, `vxcg.m`, `vycg.m`, `vzcg.m`, and `dmgcg.m`. The naming of the file names is based on the physical properties and axes names. For example, in the first group, `cxcg.m` means the x coordinates of the material points, `cycg.m` contains the y coordinates of the material points, and `czcg.m` consists of z coordinates of the material points. In the second group, `uxcg.m`, `uycg.m`, and `uzcg.m` contain the displacements of each material points in x , y , and z axes, respectively.

The third group `vxcg.m`, `vycg.m`, and `vzcg.m` stores the data of velocity components of each material points in x , y , and z axes, respectively. The file `dmgcg.m` is damage values of each material points. In question Fortran code can be downloaded from the book's publisher database [213]. For users who are not familiar with Fortran language (old but fast), Matlab is recommended. It is hoped that explanations in this and the next sections will contribute to a deeper understanding of numerical modelling of Peridynamic theory. The reader should bear in mind that the Matlab code is not as fast as Fortran code provided in [87]. It should be noted that using of parallel computing in Matlab can decrease the simulation time. On the other hand, Matlab presents a very user friendly environment. It is an interpreter and does not need compiling. Thus, the debugging process can be more comfortable for new programmers. Moreover, embedded visualization tools in Matlab allow users to create and check out geometries and other physical properties in an easy and fast way. Different methods can have been proposed to work on the solution of Peridynamics and other numerical methods. However, in the first step, it may be helpful to start in Matlab. A user can use the workspace, observe bugs, and plot the geometries easily. However, after pre-processing, compiling the script in Fortran language is strongly recommended for the efficiency purposes. In the third step, the user needs a visualization tool and transfer data to another program, such as Matlab and Ovitio. In the next sections, plotting the results in Ovitio and Matlab is explained.

5.1.1 Handling with Outputs

A Fortran program for the Kalthoff-Winkler PD simulation was given by Madenci and Oterkus [87]. This program print results in `*.m` files, as stated in the previous section. In the next two sections, two programs for handling these `*.m` files were proposed and compared. Moreover, basic scripts used in the plotting process were given.

5.1.1.1 Outputs in Matlab

The list of `*.m` files produced from the Fortran code is given in Table 5.1. It should be noted that files only contain data of the simulation results in the last time step, 1350 as stated in [87]. In the original configuration, time series are not stored in these files. To overcome this issue, a new script is presented in the next section. A basic program is given to plot results in Matlab without any modification (Appendix A).

Table 5.1 : Output *.m files of Fortran program of Kalthoff-Winkler problem.

File name	Description
cxcg.m	Coordinates of material points in x axis
cycg.m	Coordinates of material points in y axis
czcg.m	Coordinates of material points in z axis
dmgcg.m	Damage of material points
uxcg.m	Displacements of material points in x axis
uycg.m	Displacements of material points in y axis
uzcg.m	Displacements of material points in z axis
vxcg.m	Velocities of material points in x axis
vycg.m	Velocities of material points in y axis
vzcg.m	Velocities of material points in z axis

The script should be in the same folder as the output files obtained from the Fortran program. The user can change the variable names in the scatter plot function to plot other outputs. Figure 5.1 shows a figure output of this script.

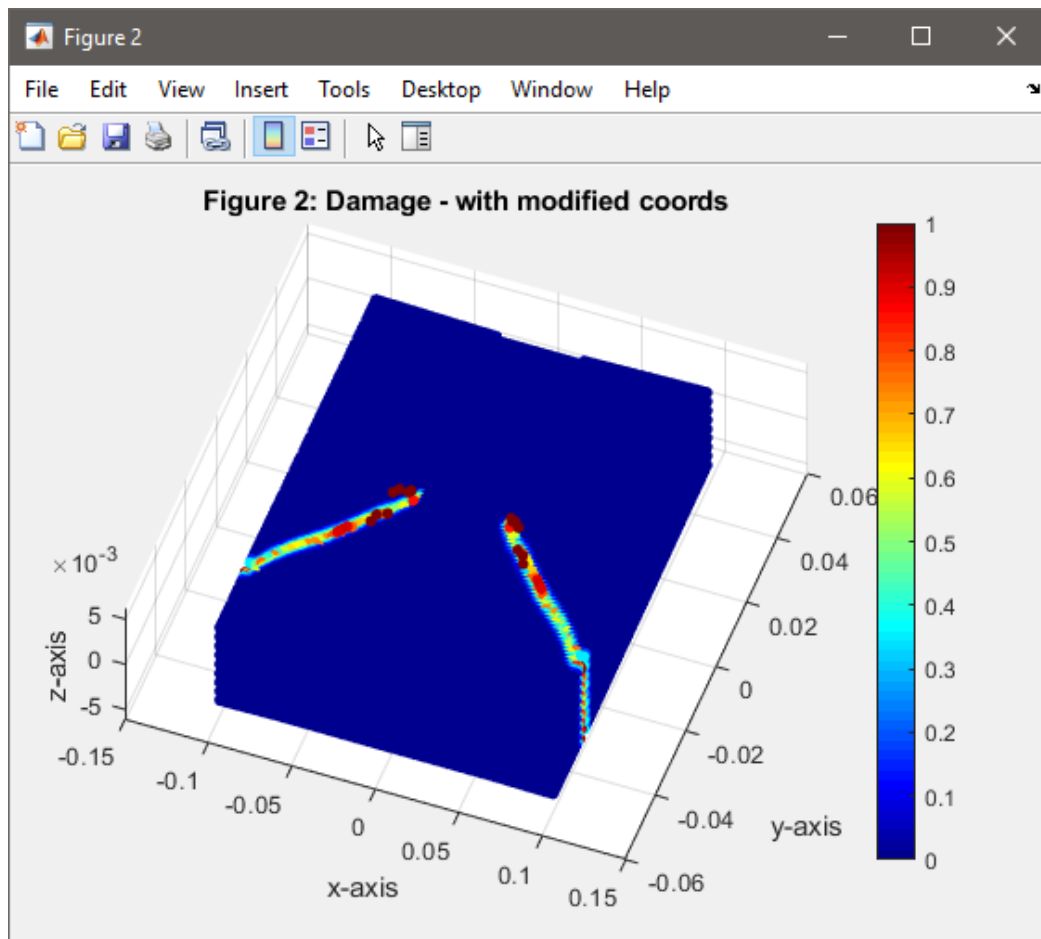


Figure 5.1 : A plot window in Matlab generated with the script in Appendix A.

In the script, only three figures were plotted: displacement in y axis, velocity in y axis, and damage. It should be noted that these results are outputs of the last time-step in the

simulation. Therefore, they only represent the last state of the points. The script also produces an alternative three-dimensional representation for damage with modified coordinates, as shown in Figure 5.1.

5.1.1.2 Outputs in Ovito

The Open Visualization Tool (OVITO) is a 3D visualization software developed by Stukowski [214]. The free-basic version can be used to plot Peridynamic simulation results. It is designed to plot the atomistic and particle simulation data. A Matlab script is provided in Appendix B to save the vectors in Matlab as a *.xyz file. The detailed information about *.xyz file type can be found in [215]. It has several variations; in general, it consists of coordinates and other properties of particles. It allows the user to save the properties of a particle as time-series. The script given in Appendix B, only converts the output files from the end of the simulation. A preview window from Ovito that plotted from files from the script in Appendix B is given in Figure 5.2. In addition to this, there is a faster and useful way to plot the damage and other physical quantities in Ovito.

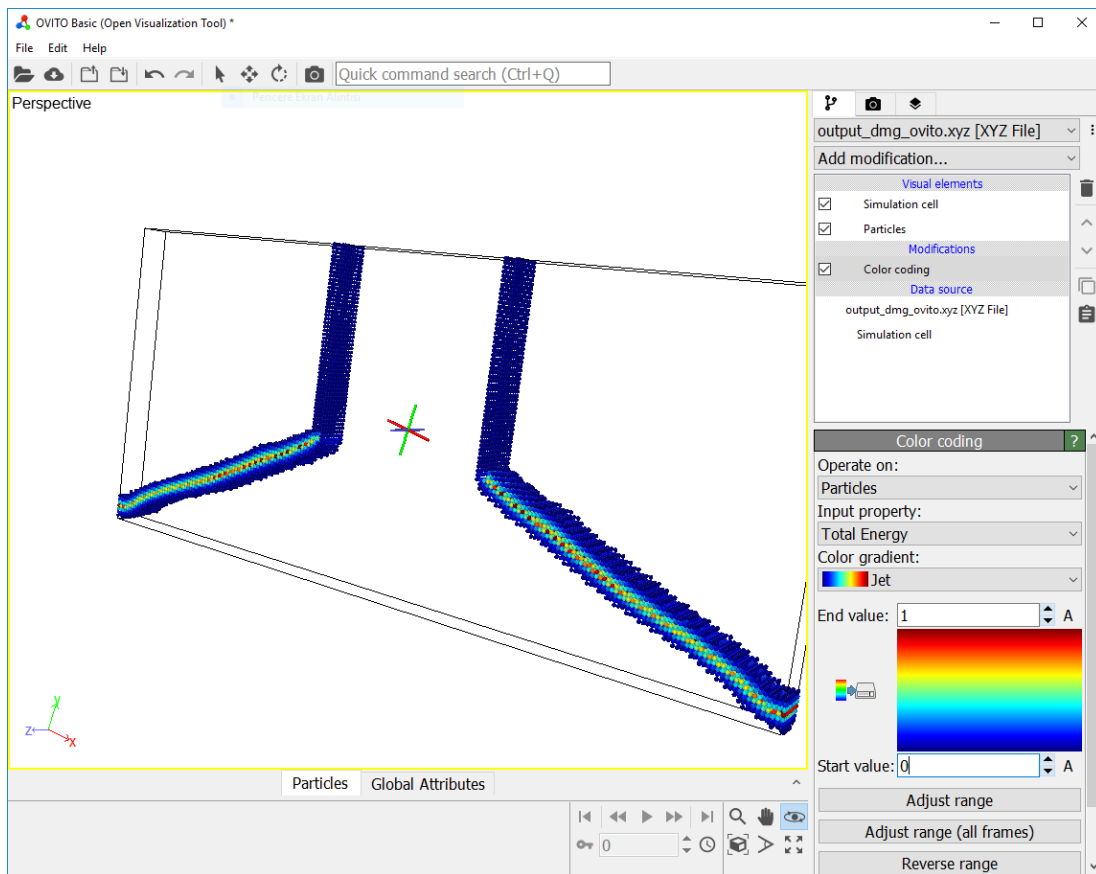


Figure 5.2 : A preview window from Ovito. The input file is from Appendix B.

The script given in Appendix C can be inserted at the end of each time iteration in question Kalthoff-Winkler Fortran code. The script creates a *.xyz file, named as Results.xyz. This file consists of 13 columns as shown in Figure 5.3.

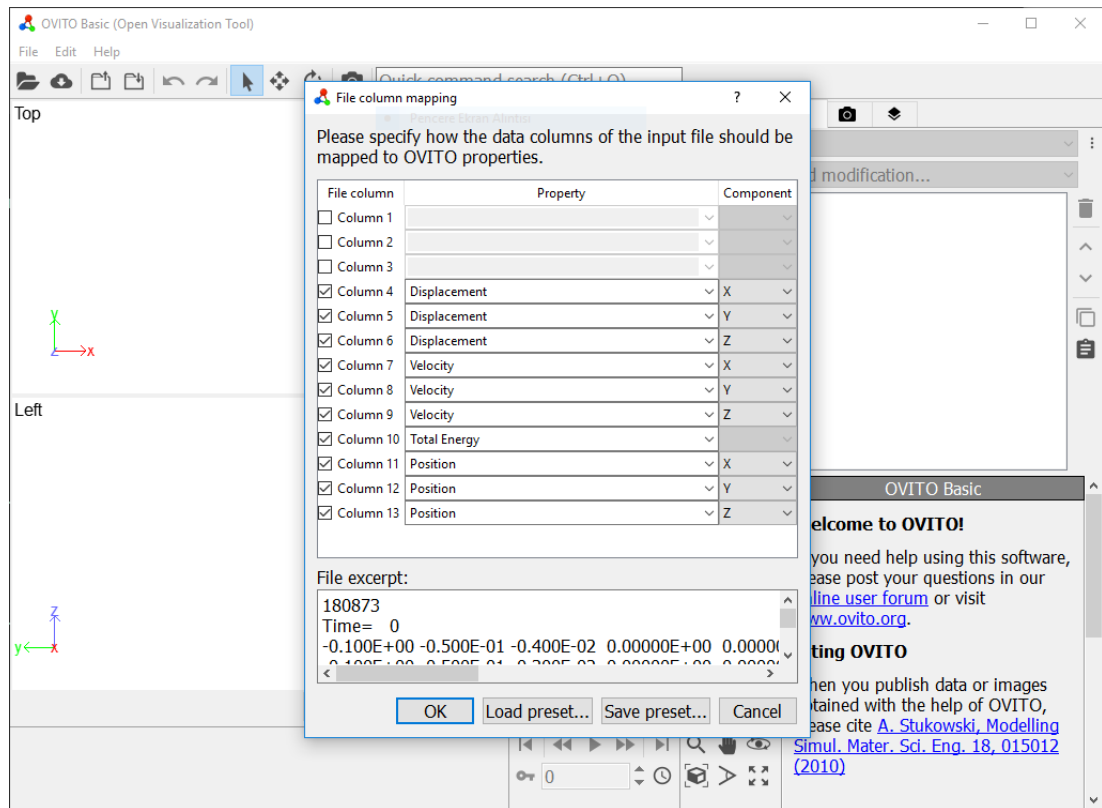


Figure 5.3 : The definitions of the physical properties of particles in Ovito.

The first three columns store the x, y, z coordinates, respectively. They can be used to examine model with constant coordinates. However, to see the displacement of points, the last three columns should be chosen. The columns between 4-6 are displacement data in the same order. Columns 7, 8, and 9 are velocities. Column 10 is the damage and it can be labelled in Ovito as *Total Energy*. After, in Add Modification menu, colour coding can be added and connected to Total Energy. The last three columns, 11-13, consist of the last position coordinates of particles. A user can choose both these last three columns or first three columns for indicating positions of particles.

Figure 5.4 shows an example view of the Kalthoff-Winkler problem at a time-step. Colour coding modification was used to plot the damage in the body. Start and end values are set to 0 and 1. Since the local damage is defined as a proportion, the scale can be adjusted between 0 and 1. Then, it can be converted to percentages. The colour coding is jet.

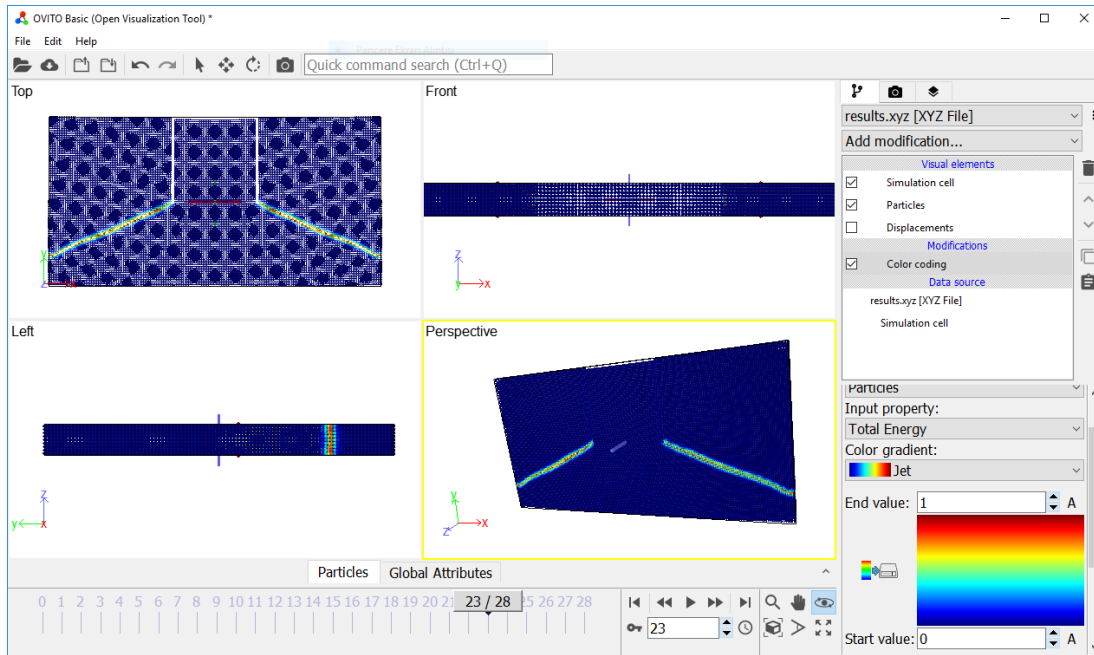


Figure 5.4 : A preview window of particles as time-series in Ovito.

5.1.2 Micro-Crack Code

The micro-crack definition in Peridynamic was given in Section 2.2.3. Figure 2.9 shows a micro-crack line located between material points. The algorithm used to define in question micro-cracks is depicted as a flowchart in Figure 5.5. It is a precise step-by-step series of instructions to create a crack plane in a Peridynamic theory. A developed script is given in Appendix D by using this flowchart. It is coded in Fortran language. This script can be inserted in the Kalthoff-Winkler Fortran code or any type of Peridynamic analysis code. This recipe considers that the user has already defined the location of cracks. It starts with identifying pre-defined the micro-crack plane locations. Coordinates and lengths of micro-crack planes are ridden from an external text file. An example text file that contains crack information is given in Appendix D.1. Here, the first three columns are x , y , and z coordinates of the top of the crack, respectively. The coordinates in z direction are all zero to obtain a complete crack plane through the z axis. The script initiates forming of a crack plane from these top point coordinates within a given length. The generated crack plane is perpendicular to xy plane. The inclination of the plane is determined with the CCW angle between the crack plane and y axis. It is given for each crack in the fourth column.

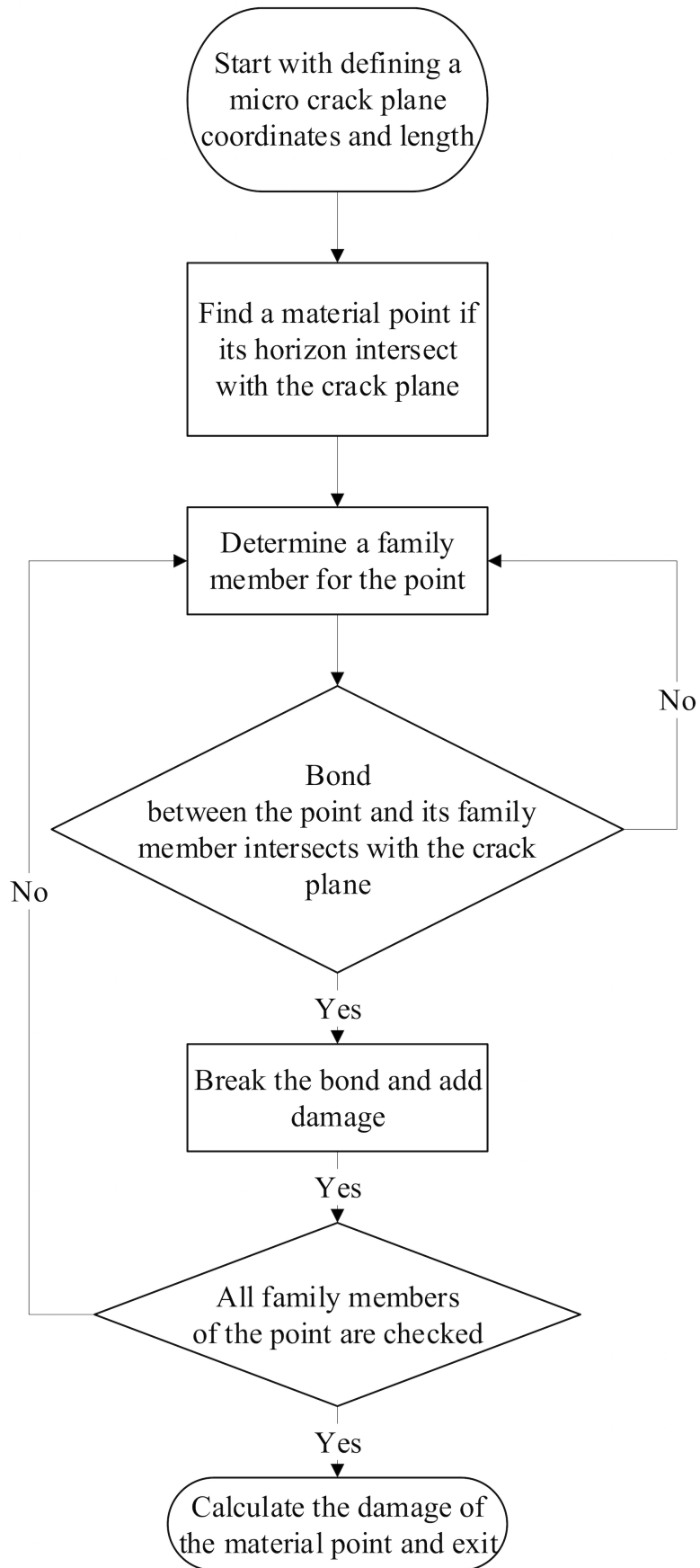


Figure 5.5 : The flowchart used for the determination of broken bonds to define micro-cracks.

In the end column, lengths of crack planes in xy plane are stored. This **.txt* file is imported at the first step of the algorithm. Then, material points are checked out to identify of which have a horizon that intersects with the crack planes. In the next step, every family members of a material point are evaluated if the bonds intersect the crack planes. The determined bonds are flagged as broken. The damaged material points is depicted in Figure 5.6 that visualized in OVITO. The crack plane is indicated with a red continuous line.

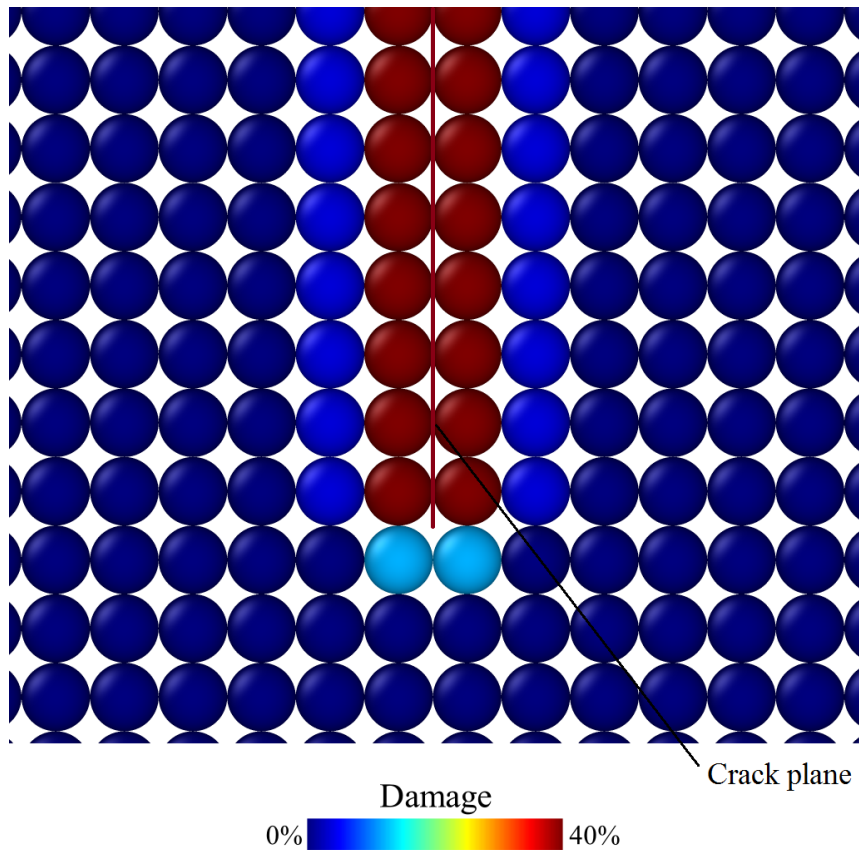


Figure 5.6 : The damaged material points and the crack line in OVITO.

5.2 Wire Rope Modelling Code

The Matlab codes for modelling a single wire section was given in Appendix E. Matlab is a very user friendly tool for designing 3D models with particles. The given script uses the *length_x*, *height_y*, and *width_z* data to define a box that contains the wire cross section. The parameter, *diameter* is used to determine the radius of the wire. To avoid numerical errors, *tol* value is used in comparing processes. *ndivx*, *ndivy*, and *ndivz* are numbers of material points in *x*, *y*, and *z* axes, respectively. *dx* is the distance between material points. Then, the script determines coordinates of material points in

nested for loops. The if condition in the inner for loop evaluates the circle expression, and assigns coordinate values when they are within the radius of the cross section. Figure 5.7 shows the output of the Matlab script for different discretization values.

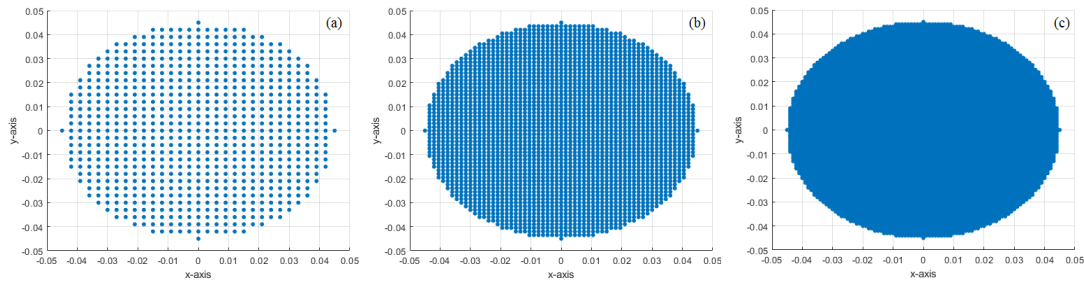


Figure 5.7 : Wire sections generated with the script given in Appendix E. *ndivx* and *ndivy* are (a) 31, (b) 61, and (c) 91.

Different algorithms, such as polygon based outer surface can be used for wire cross section modelling. The existing literature on Peridynamic modelling lacks clarity regarding the discretization of circular shaped structures. This basic modelling approach has been proposed in this study, considering to form a basis for future studies.

In general, Matlab and Fortran have advantages in different aspects for numerical modelling. Although choosing a compiler or interpreter is affecting the simulation time, debugging and visualization requires different programs. Overall, Fortran is the fastest language in numeric simulations. Ovito can be used to visualize the time-series results owing to easy handling ability on particle simulations. On the other hand, Matlab is a very useful program both in the run and plot damages, velocities, and deformations.

5.3 Modelling of Wire Ropes using Peridynamic Theory

A fundamental 1x6 helical wire rope strand structure was taken into account for investigating wire failure mechanism with Peridynamics. It is apparent that the central core and outer wires are in contact, whereas wires in the outer layer have no contact along the circumferential direction in Figure 5.8. This contact condition modelling refers to the model that termed as radial contact by Cardou and Jolicoeur [165] and termed as trellis contact by Hobbs and Raouf [193]. A recent study based on this model examined the elasto-plastic mechanical response of the wire rope [205], shown in Figure 4.16.

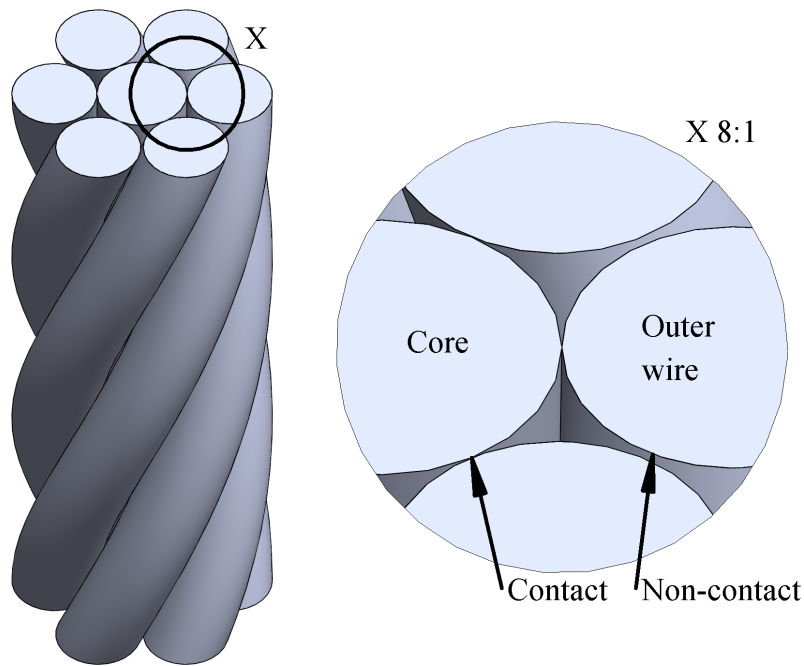


Figure 5.8 : 3D view of a 1x6 wire rope with 1/2 lay length and contacts.

The case study in this work is given in Figure 5.9. The impact of the steel 1x6 wire-rope with a cylindrical impactor is the main objective of this section.

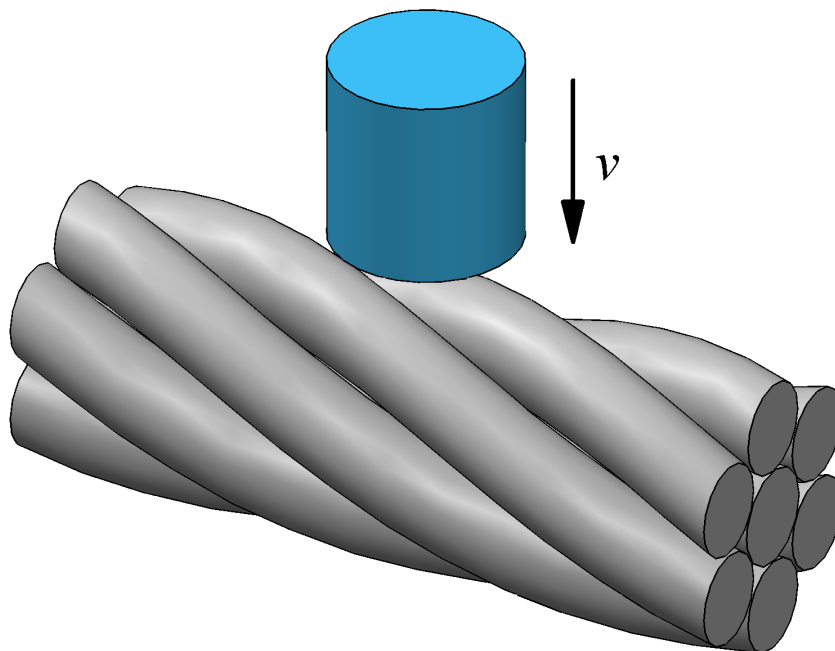


Figure 5.9 : 3D view of a wire rope subjected to impact load.

Much of the literature on modelling the mechanical behaviour of wire ropes seems to have been based on loads consisted of axial tension or bending moments. Most of studies summarized in previous sections have suffered from lack of transverse impact loading. Chaplin [216] stated that the nature of the helical structure of a wire rope

leads to radial load components due to applied stresses. However, the radial forces can also affect the outer wires from an external source. The model presented in Figure 5.9 simulates a transverse impact load on a wire rope. It is assumed that the impactor is a rigid body.

Finite Element Method has been commonly used to model and analyse wire ropes. That is why previous studies of modelling wire ropes have not dealt with discretization problem but creating a mesh of the body. Three dimensional mesh elements allow creating finite volumes of wires. However, in Peridynamics, a body consists of meshless discretization scheme as opposed to FEM. Further research is needed to better understand how a wire rope system can be discretized in Peridynamics.

A single wire section was taken into account to investigate the crack propagation in a wire rope subjected to transverse impact load. Two symmetrical pre-cracks were placed in the wire section as can be seen in Figure 5.10.

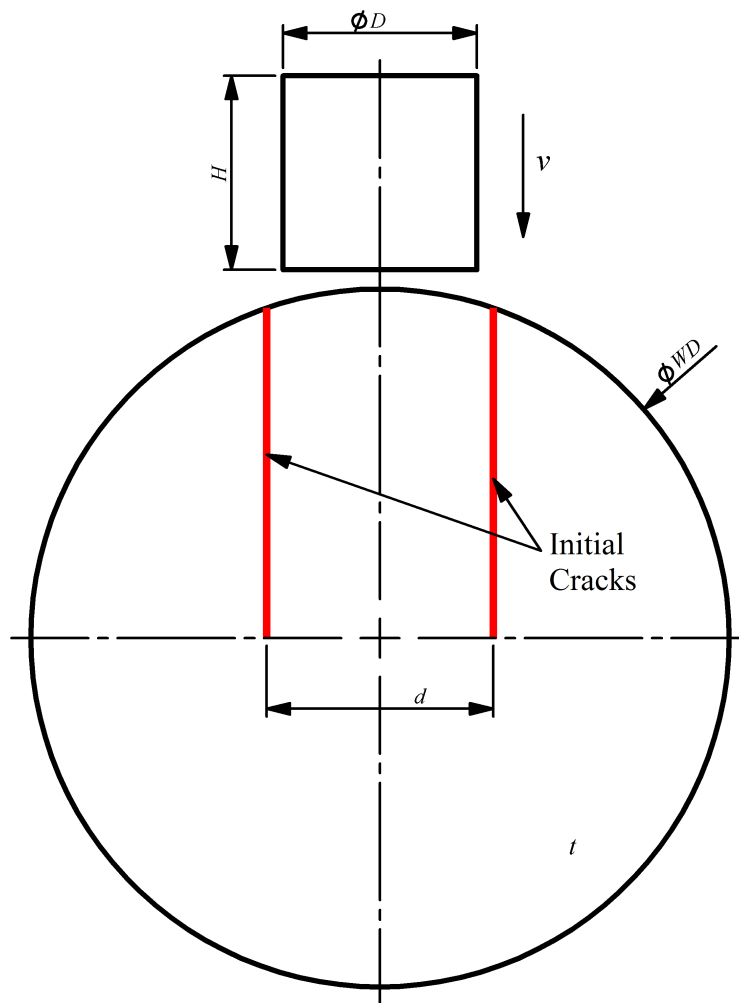


Figure 5.10 : Dimensions of a single wire subjected to impact load.

The same algorithm used in Section 2.2.3 was adopted with some modifications (see Figure 2.9 and Figure 5.5). However, to examine the crack propagation properly, two main cracks were defined in this simulation. The length of cracks were determined to obtain the crack propagation to the edges. The cracks started from the top surface of the wire and ended at the centre of the wire. No boundary conditions were applied to the wire section. Initially, the wire section was free of displacement and at rest.

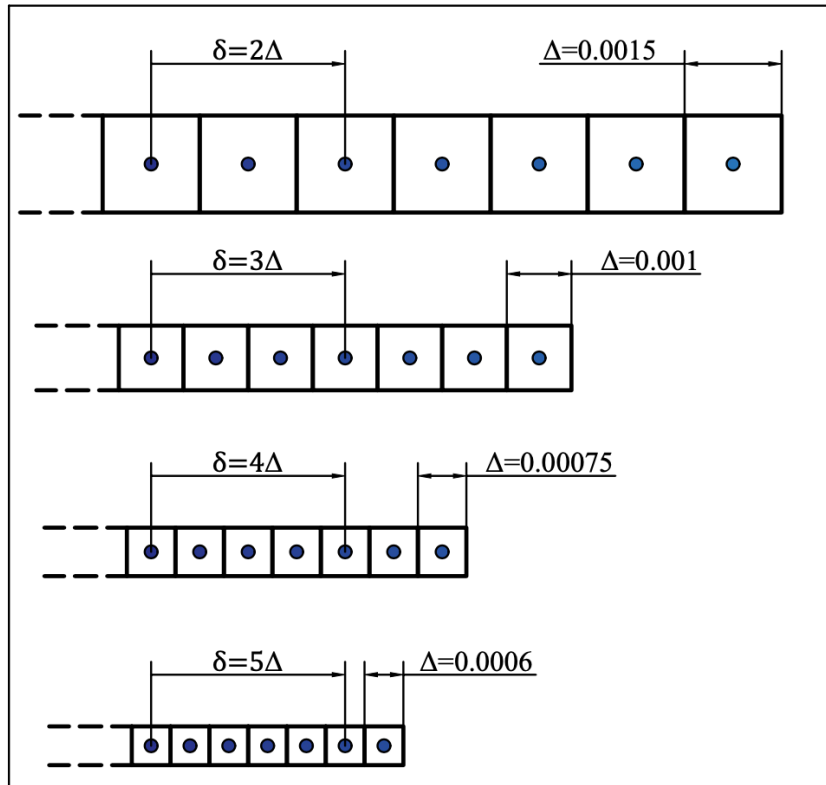
The dimensions of both impactor and a single wire model containing two symmetrical pre-cracks are given in Table 5.2. This model was designed to examine only a single wire section subjected to transverse load, as shown in Figure 5.10. The pre-defined cracks propagate with different velocities with regard to setup parameters. Therefore, a single circular wire should be investigated under impact loading due to complex contact states between wires in a strand.

The diameter of the cylindrical rigid impactor is $D = \phi 0.025$ m, the height of the impactor is $H = 0.025$ m. The mass of the impactor is 0.785 kg. The velocity of the impactor is $v = -32$ m/s through the y axis. The diameter of the wire section is $WD = \phi 0.090$ m. The distance between the pre-cracks is $d = 0.029$ m, and they are located symmetrically with regard to the vertical axis. The thickness of the wire section is $t = 0.003$ m.

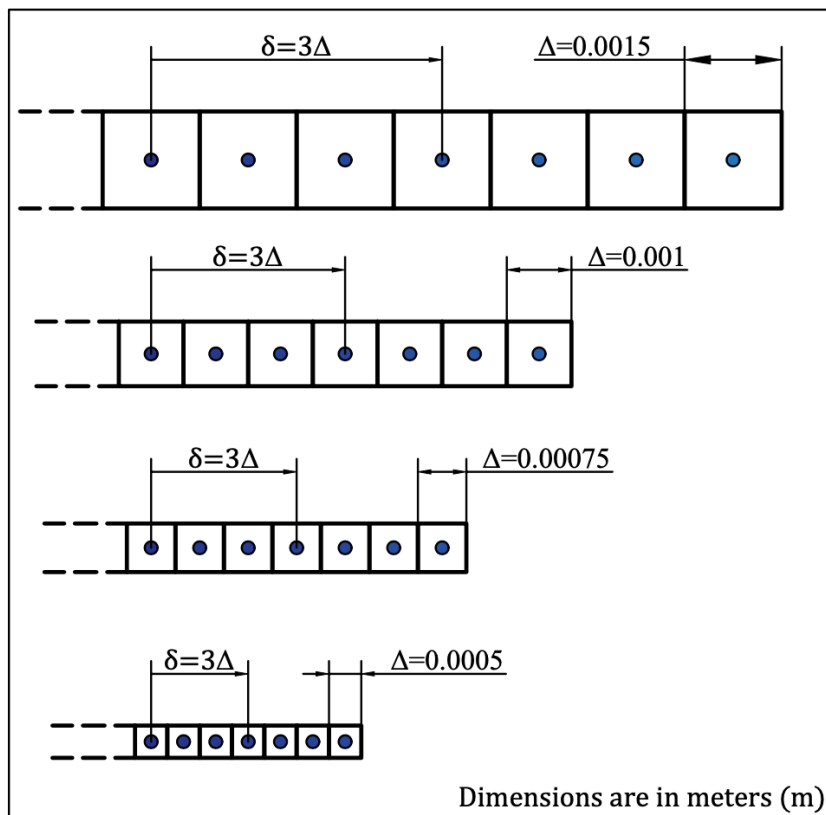
Table 5.2 : Dimensions and mechanical properties of impactor and single wire model.

Parameter	Value
D	$\phi 0.025$ m
H	0.025 m
v	32 m/s
WD	$\phi 0.090$ m
d	0.029 m
t	0.003 m
Rigid impactor mass	0.785 kg
Poisson's ratio, ν	0.25
Young's modulus, E	191 GPa
Mass density, ρ	8000 kg/m ³

A series of numerical convergence studies were designed to determine correct parameters for a wire rope structure in Peridynamics. In order to understand how discretization and horizon size affect the dynamic crack propagation, a series of convergence tests setup was proposed in Figure 5.11.



(a) m-convergence (constant horizon radius, δ)



Dimensions are in meters (m)

(b) δ -convergence: constant material points number in a horizon

Figure 5.11 : Convergence tests setup in 1-D for simplicity: (a) m-convergence (constant $\delta = 0.003$ m), (b) δ -convergence (constant $m = 3$).

The convergence schemes in Peridynamics consisted of spatial variables such as horizon size and the number of neighbour material points in a horizon [111]. In the m-convergence step, m determines number of material points in the horizon. In this type of convergence, the horizon size is constant, but the number of material points in the horizon increased because of smaller Δ (distance between two material points) as shown in Figure 5.11(a). The second type of convergence is δ -convergence. As opposed to m-convergence, in this type of convergence, the material points in a horizon are constant, whereas the horizon becomes smaller as depicted in Figure 5.11(b).

5.3.1 Convergence tests: m-convergence

The parameters of m-convergence test suit are given in Table 5.3. The number of material points was generated with $n_{divx} \times n_{divy} \times n_{divz}$ material points along x , y , and z -axes, respectively. n_{divx} , n_{divy} , and n_{divz} determines the distance between material points Δx , Δy , and Δz , because dimensions of the wire section is constant. The four m parameters are used with the constant horizon. The constant horizon δ is 0.003 m with $m = 2, 3, 4$, and 5 . The number of total material points are 8,460 for $m = 2$; 25,440 for $m = 3$; 56,440 for $m = 4$; and 105,984 for $m = 5$. The time-step is specified as $\Delta t = 8.7 \times 10^{-8}$ s, and the critical-stretch is defined as $s_c = 0.01$ as suggested in [87].

Table 5.3 : m-Convergence test setup and parameters.

m	2	3	4	5
Horizon, δ (m) - constant	0.003	0.003	0.003	0.003
n_{divx}	61	91	121	151
n_{divy}	61	91	121	151
n_{divz}	3	4	5	6
Diameter of the wire (m)	0.09	0.09	0.09	0.09
Thick in z direction (m)	0.003	0.003	0.003	0.003
Particle radius (m)	0.000750	0.000500	0.000375	0.000300
$\Delta x, \Delta y, \Delta z$ (m)	0.001500	0.001000	0.000750	0.000600
m	2	3	4	5
Volume of a material point (m^3)	3.38E-09	1.00E-09	4.22E-10	2.16E-10
Total node number	8,460	25,440	56,440	105,984
Points in contact layer	15	19	21	25
Contact length (m)	0.0210	0.0180	0.0150	0.0144

The four test setups are given in Figure 5.12. The damage scale is defined between 0-100% and will be used in the next figures.

In equation 2.22, $\varphi(\mathbf{x}, t)$ was defined as a weighted ratio of the number of damaged bonds to the number of initial bonds. It varies between 0 and 1. However, the damage value was represented between 0 - 100% to demonstrate the proportion of the number of bonds being broken. 0% means that all bonds of a material point are in bond, and with increasing the damage percentage, bonds of a material point are breaking. In this initial state, wire sections have pre-defined cracks. The single points in the top layers are deleted to create a planer contact surface between projector and wire section. The horizon size $\delta = 0.003$ m is constant in this setup.

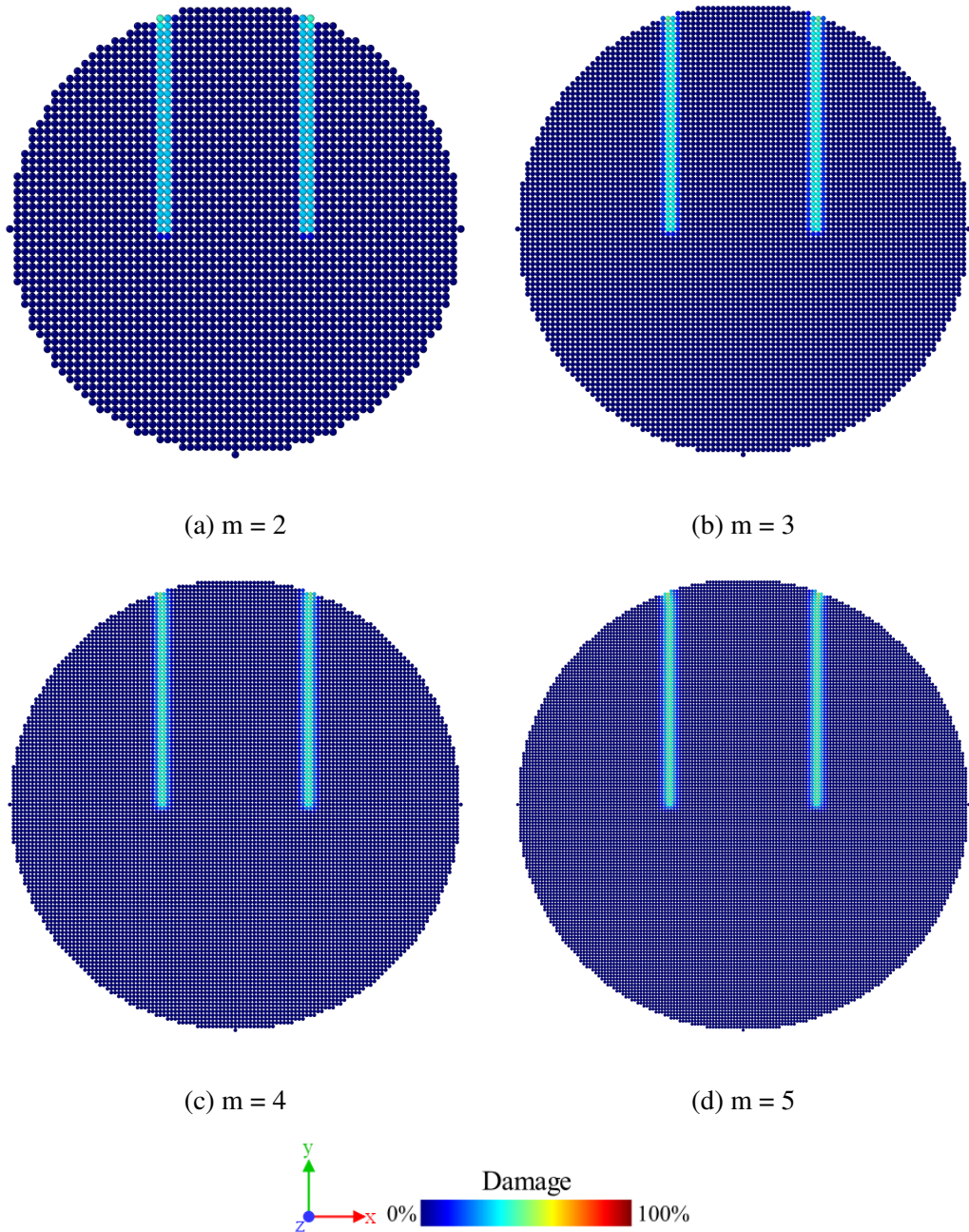


Figure 5.12 : The discretized wire section with two pre-cracks for horizon size $\delta = 0.003$ m at the initial state.

In all simulations, the crack propagation initiates at $21.8 \mu\text{s}$ (250th time-step). In Figure 5.13, the crack propagations in the wire sections can be seen at $47.9 \mu\text{s}$ (550th time step). In this model, cracks can reach the edge at only at $m = 2$ case. There is no complete failure in $m = \{3, 4, 5\}$ models.

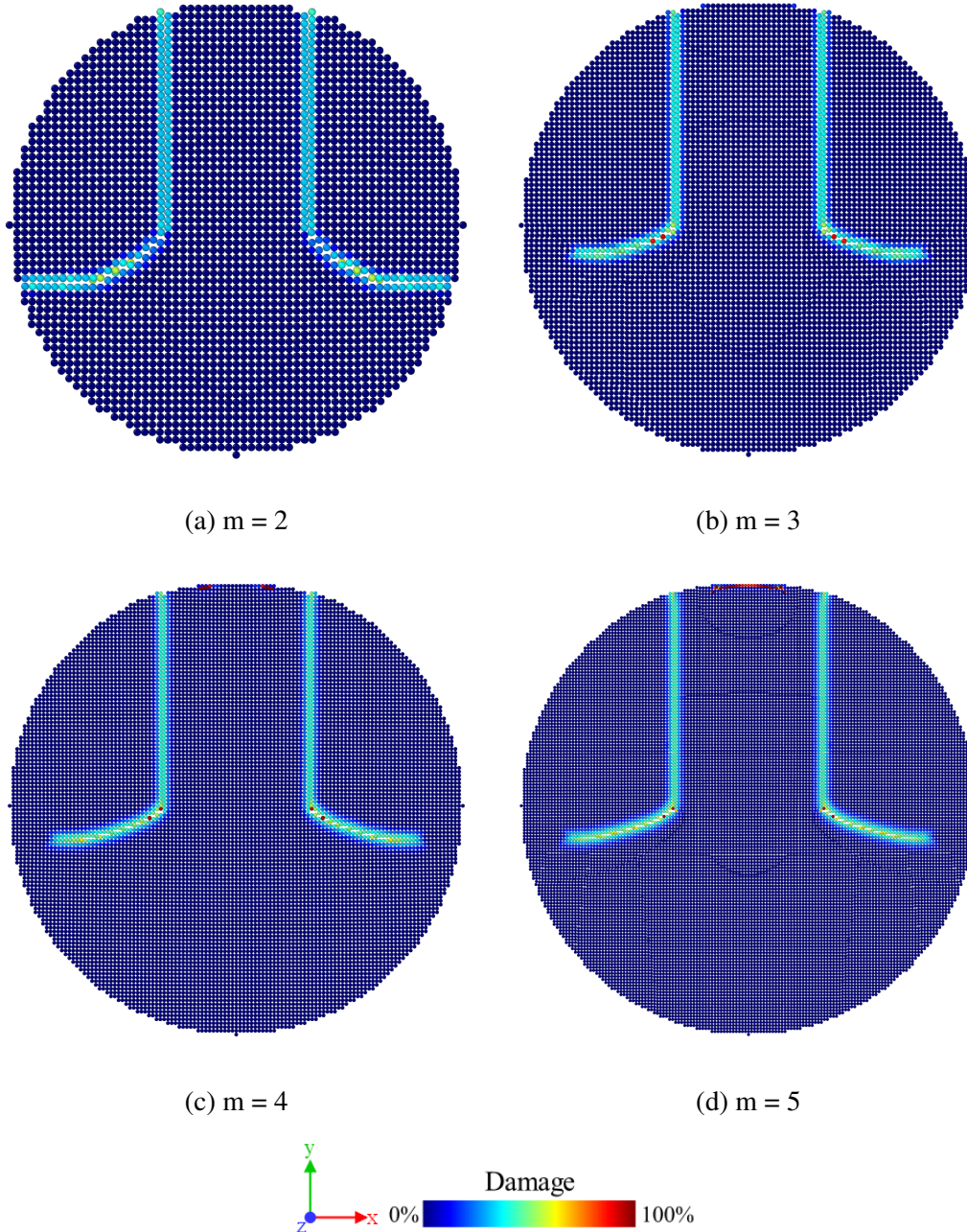


Figure 5.13 : The crack propagation for horizon size $\delta = 0.003 \text{ m}$ at $47.9 \mu\text{s}$ (550th time step).

The crack propagations at $60.9 \mu\text{s}$ (700th time-step) are shown in Figure 5.14. In this time step, cracks in all scenarios reach the edge and complete failure of the wire section was observed. Overall, the complete failure for each case can be observed at

52.2 μs for $m = 2$ case and at 60.9 μs for $m = \{3, 4, 5\}$ cases. From these figures, a significant difference in terms of damage can be observed in the top layers of models. As a reminder, in Table 5.3, the contact length of each model were given as for $m = 2$: 0.0210, $m = 3$: 0.0180, $m = 4$: 0.0150, and $m = 5$: 0.0144. The contact between the impactor and the top layer of the section decreases while the m number increases. The model $m = 2$ has the largest contact line; this effect may have provided protection to particles at the top layer. With decreasing the contact line, damages in the top layer become more visible.

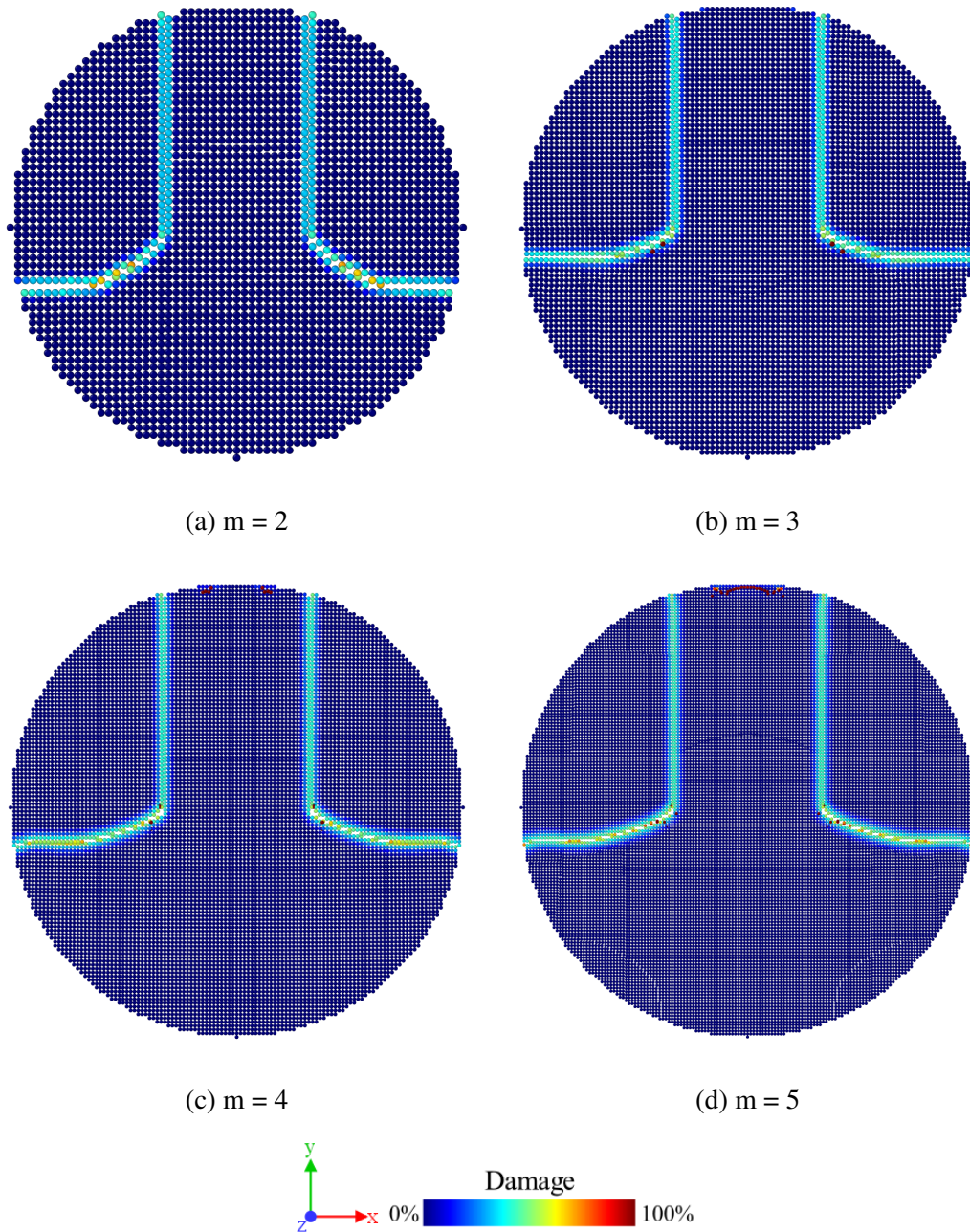


Figure 5.14 : The crack propagation for horizon size $\delta = 0.003$ m at 60.9 μs (700th time step).

Figure 5.15 shows the crack propagation velocities for m-convergence tests. Although the complete simulation duration is 117.5 μs , the duration between 17.4-56.6 μs was given because of comparison purposes. The crack does not propagate after reaching edges. From Figure 5.15 the cracks in all cases ($m = \{2, 3, 4, 5\}$), starts to propagate at 21.8 μs . After a transient zone where between 21.8 and 34.8 μs , velocities show a stable characteristics. Cracks propagate with a constant velocity until reaching to edges. $m = 2$ model differs from $m = \{3, 4, 5\}$ models in average velocity and time of end of crack propagation. The model $m = 2$ reaches edges 8.7 μs earlier than others.

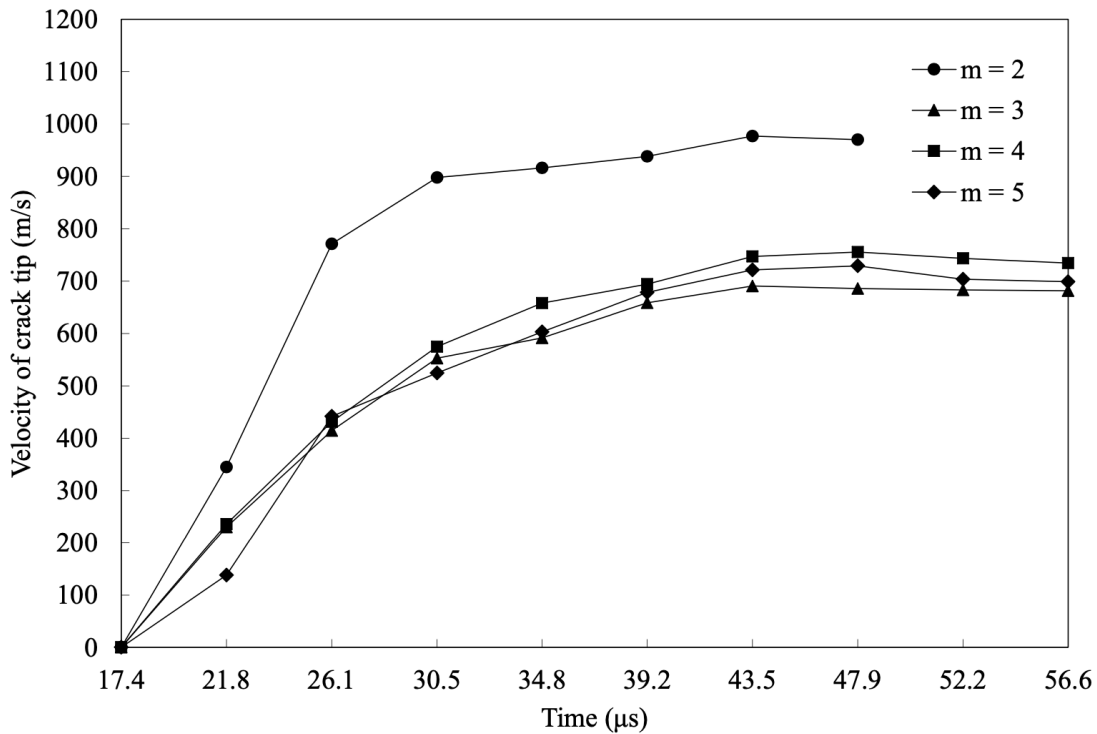


Figure 5.15 : The crack propagation velocities of m-convergence test cases between 17.4 and 56.6 μs .

The displacement in the y-direction along the central x axis of the wire section is given in Figure 5.16. The $y = 0$ line is given in black line for referring to the initial condition. This demonstration shows that displacements along the central x axis in cases $m = \{3, 4, 5\}$ present similar results. However, $m = 2$ case differs from other scenarios. As a consequence, $m = 2$ model seems inadequate to model the wire section. These results also indicate another important point in terms of increasing the number of family members. The crack propagation velocities and deflection characteristics in $m = \{3, 4, 5\}$ models are very similar. Therefore, there is no need for increasing the m number, and computational time and cost.

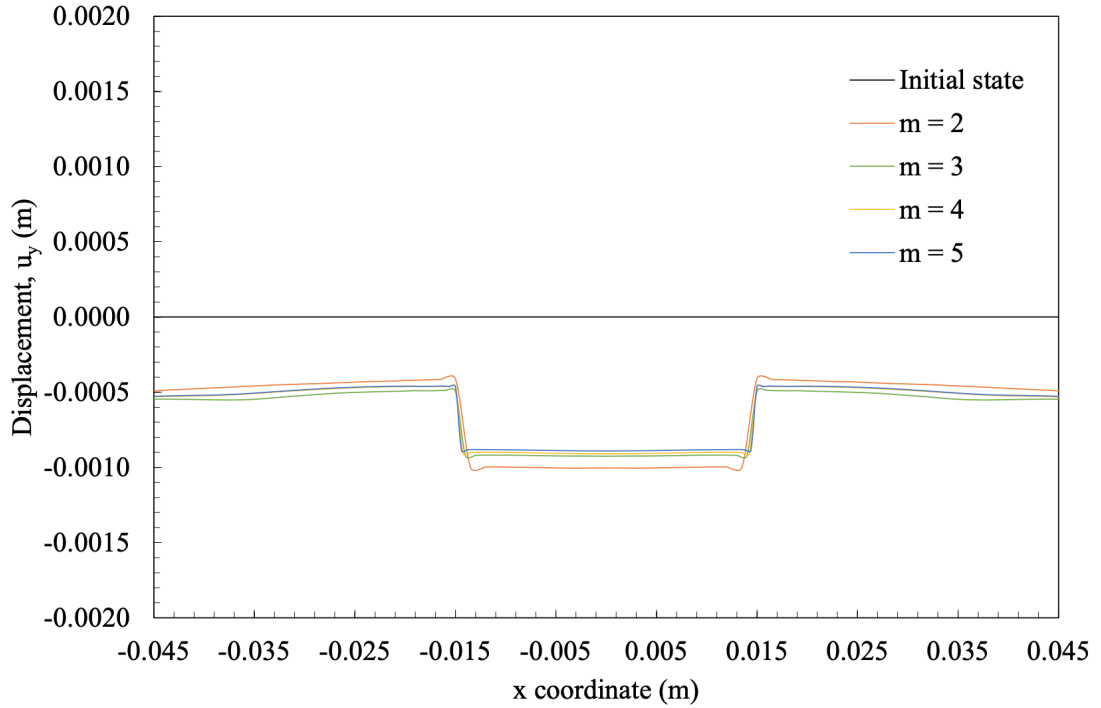


Figure 5.16 : Displacement in the y-direction of m-convergence tests along the central x axis at $56.6 \mu\text{s}$.

5.3.2 Convergence tests: δ -convergence

The parameters of δ -convergence test suit are given in Table 5.4. The number of material points was generated with $\text{ndiv}_x \times \text{ndiv}_y \times \text{ndiv}_z$ material points along x , y , and z -axes, respectively.

Table 5.4 : δ -Convergence test setup and parameters.

Horizon, δ (m)	0.0045	0.003	0.00225	0.0015
m - constant	3	3	3	3
ndiv _x	61	91	121	181
ndiv _y	61	91	121	181
ndiv _z	3	4	5	7
Diameter of the wire (m)	0.09	0.09	0.09	0.09
Thick in z direction (m)	0.003	0.003	0.003	0.003
Particle radius (m)	0.000750	0.000500	0.000375	0.000250
$\Delta x, \Delta y, \Delta z$ (m)	0.001500	0.001000	0.000750	0.000500
Volume of a material point (m ³)	3.38E-09	1.00E-09	4.22E-10	1.25E-10
Total node number	8,460	25,440	56,440	178,108
Points in contact layer	15	19	21	27
Contact length (m)	0.0210	0.0180	0.0150	0.0130

As stated in m-convergence tests, $ndivx$, $ndivy$, and $ndivz$ determines the distance between material points Δx , Δy , and Δz , because dimensions of the wire section are constant. In tests, four horizon parameters were used with constant m . Horizon values were chosen as $\delta = \{0.0045, 0.003, 0.00225, 0.0015\}$ m. The number of material points in each horizon volume was kept constant as $m = 3$.

In order to obtain constant m , the number of material points ($ndivx$, $ndivy$, and $ndivz$) in each direction was adjusted as shown in the Table 5.4. The distance between material points (Δx , Δy , and Δz) in each direction were adjusted to preserve the same m in every direction. The constant m value is 3 with various horizon sizes.

The number of total material points are 8,460 for $\delta = 0.0045$ m; 25,440 for $\delta = 0.003$ m; 56,440 for $\delta = 0.00225$ m; and 178,108 for $\delta = 0.0015$ m. The time-step is specified as $\Delta t = 8.7 \times 10^{-8}$ s, and the critical-stretch is defined as $s_c = 0.01$ as suggested in [87].

The convergence test suits are given in Figure 5.17. The damage scale of material points is defined between 0-100%. In equation 2.22, $\varphi(\mathbf{x}, t)$ was defined as a weighted ratio of the number of damaged bonds to the number of initial bonds. It varies between 0 and 1. However, the damage value was represented between 0 - 100% to demonstrate how many percent of bonds are broken. 0% means that all bonds of a material point are in bond, and with increasing the damage percentage, bonds of a material point are breaking. The initial state is identical to the δ -convergence test. There are two symmetrical pre-defined cracks in the wire. The horizon sizes are $\delta = \{0.0045, 0.003, 0.00225, 0.0015\}$ m and the $m = 3$ is constant for each case. It should be noted that the model with $\delta = 0.0045$ has very a course discretization because of the small number of material points in each direction.

Figure 5.18 shows the crack propagation at 47.9 μs (550th time-step). As similar to m-convergence tests, cracks in δ -convergence tests were started to propagate at 21.8 μs (250th time-step). At this time, what stands out in this figure is the rapid propagation of cracks in the model $\delta = 0.0015$. Cracks reach to edges of wire sections only in $\delta = 0.0015$ case. Moreover, the thickness of crack path is thinner in the model $\delta = 0.0015$ than others. It can be observed that decreasing the horizon size with the constant number of family members increases the crack propagation velocity.

Figure 5.19 consists of the last states of simulations at 700th time-step. The crack propagations at $60.9 \mu\text{s}$ can be seen in figure. Cracks in the three cases ($\delta = \{0.003, 0.00225, 0.0015\}$) reach edges and complete failure occurs. As opposed to the other three models, crack propagation in the $\delta = 0.0045$ with $m = 3$ case stopped after an initial fracture. The crack tip propagation ends in $39.2 \mu\text{s}$. On the other hand, the other three models show different velocity characteristics. The crack propagation ends in $\delta = 0.003$ m case at $60.9 \mu\text{s}$ (Figure 5.19(b)).

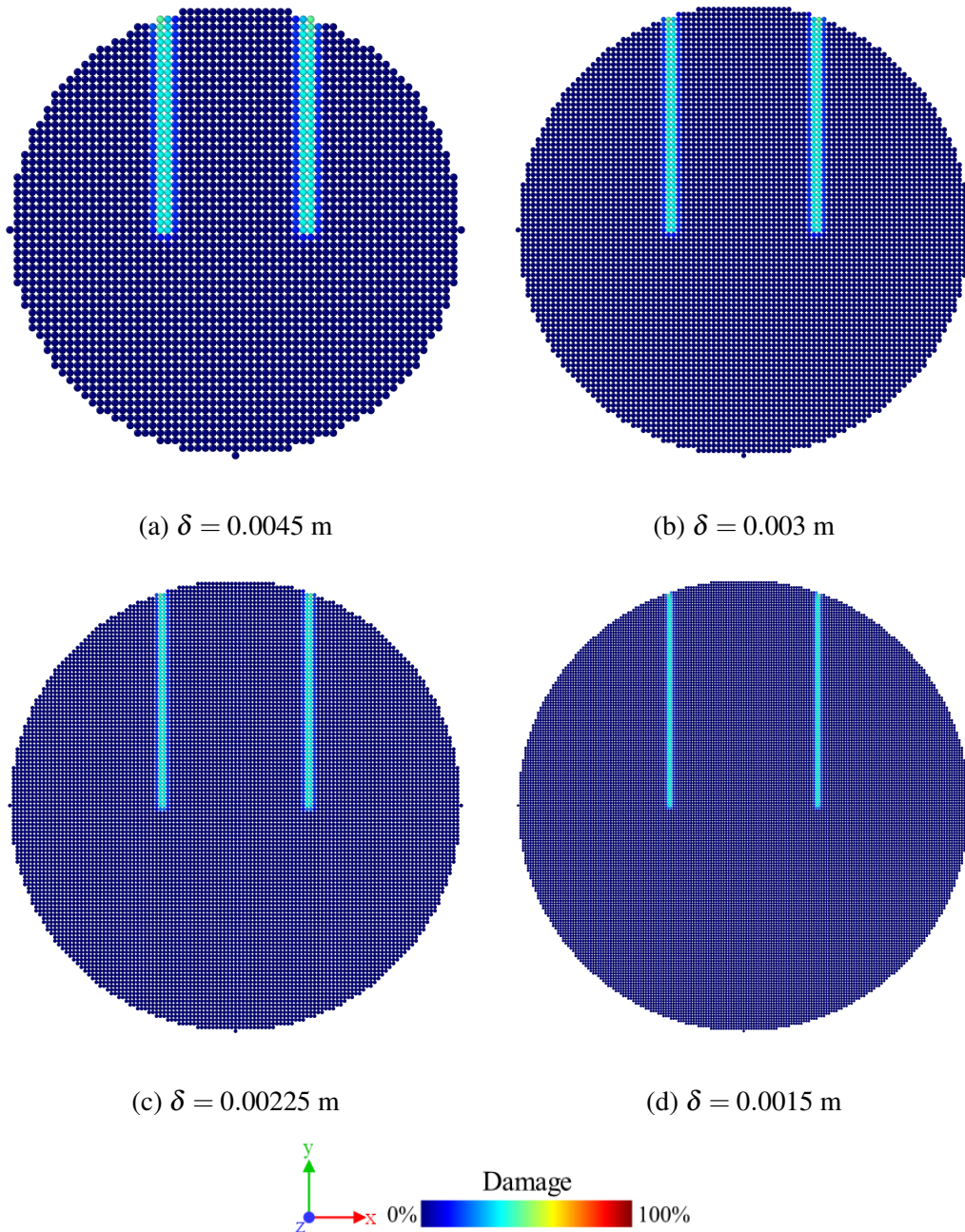


Figure 5.17 : The discretized wire section with two pre-cracks for $m = 3$ at the initial state.

However, crack propagations in cases $\delta = 0.00225$ m and $\delta = 0.0015$ m complete their advancing and reach the edges at $52.2 \mu\text{s}$ and $47.9 \mu\text{s}$, respectively. These differences can be observed in the time-velocity graph in Figure 5.20.

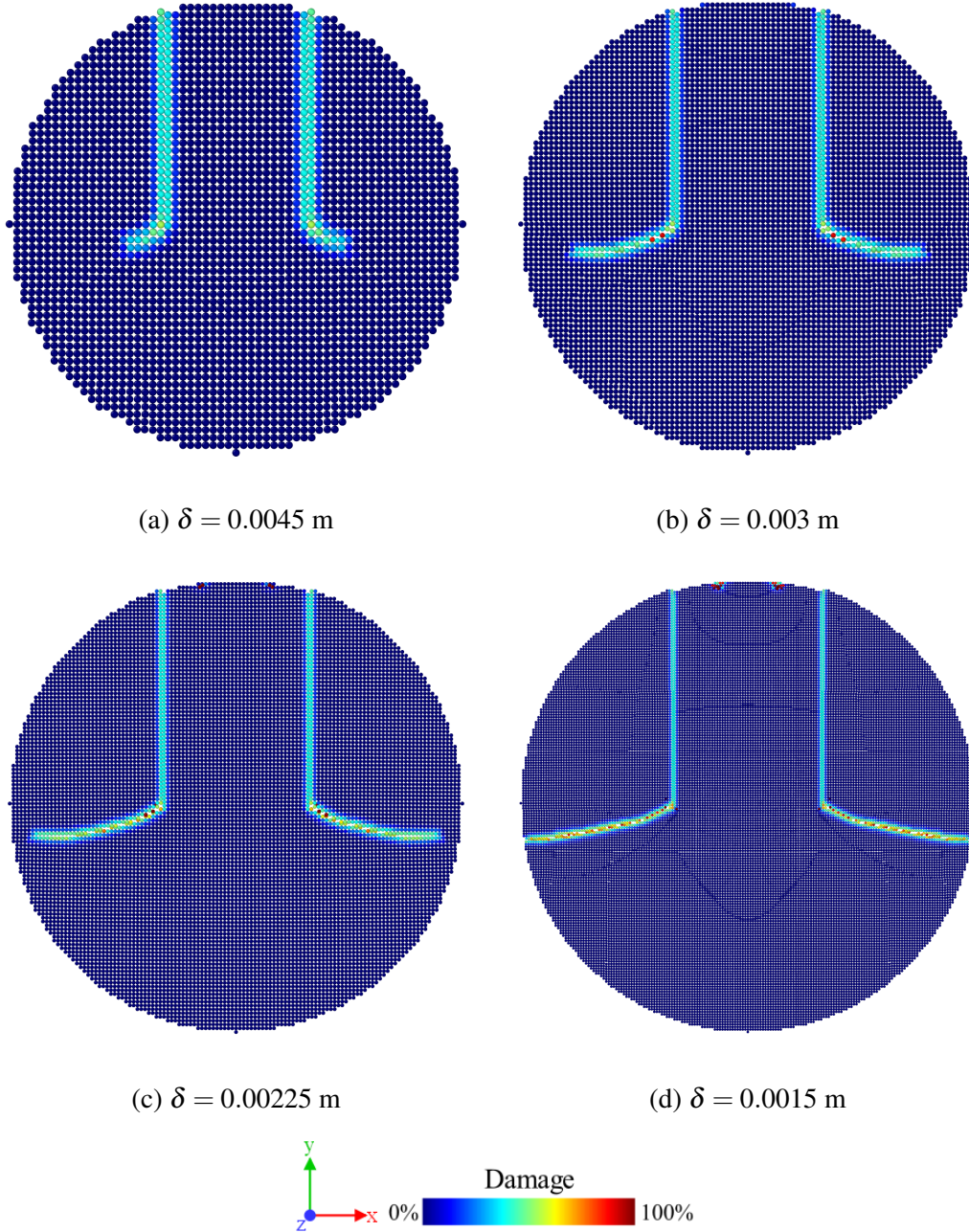


Figure 5.18 : The crack propagation for $m = 3$ at $47.9 \mu\text{s}$ (550th time step).

In Figure 5.19, as similar to m -convergence models, material points in the top contact layer were damaged with different amounts. In Table 5.4, the contact length of each model were given as for $\delta = 0.0045$: 0.0210, $\delta = 0.003$: 0.0180, $\delta = 0.00225$: 0.0150, $\delta = 0.0015$: 0.0130. The contact between the impactor and the top layer of the section decreases while the δ decreases. The model $\delta = 0.0045$ has the largest contact

line; this effect may have provided protection to particles at the top layer. On the other hand, it may avoid the progression of compressional wave properly. With decreasing the contact line, the damaged in the top layer becomes more visible.

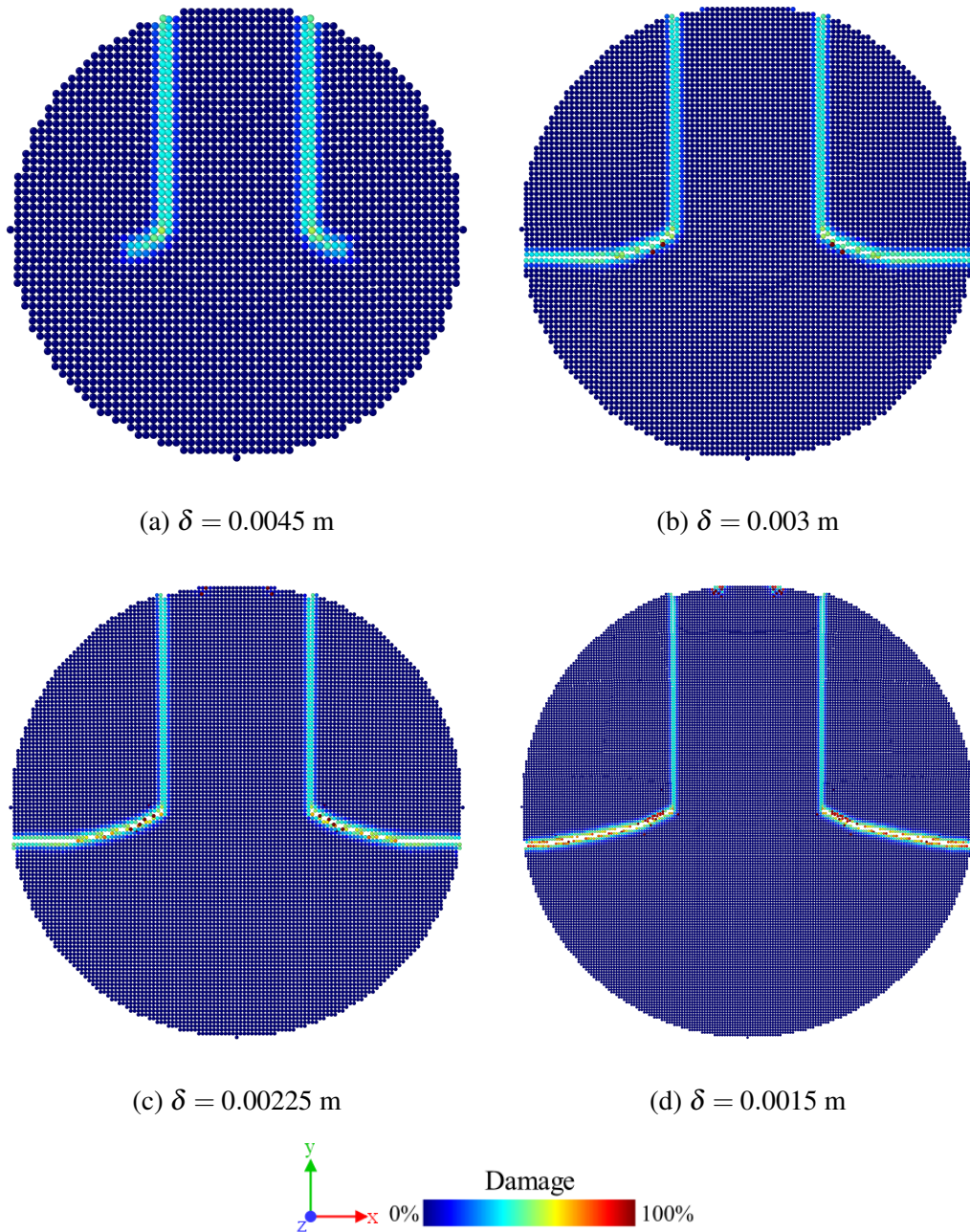


Figure 5.19 : The crack propagation for $m = 3$ at $60.9 \mu\text{s}$ (700th time step).

The crack propagation velocities for δ -convergence tests are given in Figure 5.20. The total simulation duration is $117.5 \mu\text{s}$ to see a complete failure. However, in Figure 5.20, the time between 17.4 and $47.9 \mu\text{s}$ due to comparison purposes. As can be seen in the Figure cracks in all cases $\delta = \{0.0045, 0.003, 0.00225, 0.0015\}$ starts to propagate at $21.8 \mu\text{s}$. Nevertheless, the model $\delta = 0.0045$ cracks initiate to advance with a low

velocity with regard to other models. Then, it barely propagates and stopped at 39.2 μs . This result provides valuable information about the discretization of the circular wire section model. The model $\delta = 0.0045$ does not seem suitable for PD modelling of a wire section with given parameters in Table 5.4. After a transient zone, between 21.8 and 30.5 μs , it can be said that the velocities tend to be constant over time. Overall, the average crack propagation velocities increase with smaller horizon values.

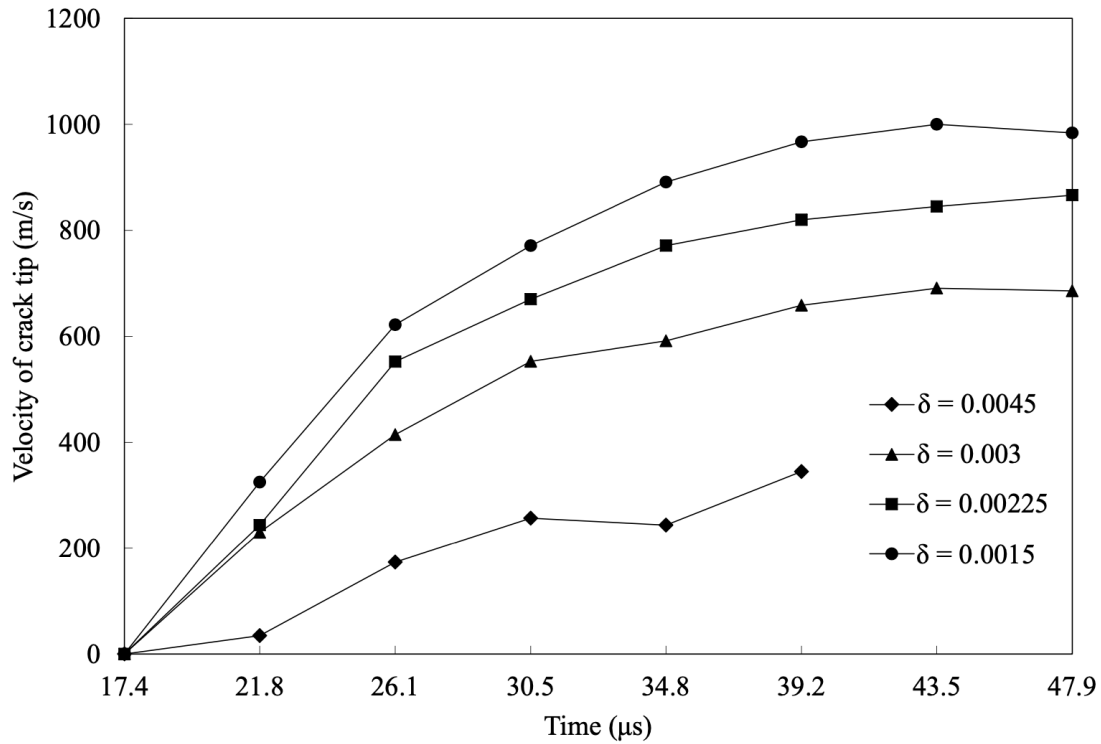


Figure 5.20 : The crack propagation velocities of δ -convergence test cases between 17.4 and 47.9 μs .

As given in m-convergence study, the displacement in the y direction along the central x axis was presented in Figure 5.21. The initial state of x axis was given in black line for referring to the initial condition. Interestingly, the deflection on the non-damaged centre area was observed to similar in each model. However, in the crack path region, the deflections differ from each other. The largest displacement along the x axis can be observed in model $\delta = 0.0045$ and it is decreasing with smaller horizons. There is a need to compare the crack propagation paths at the end of simulations. The final states of models at 60.9 μs is clearly seen in Figure 5.19. Figure 5.19 (a) can not be taken into consideration because of the failure of propagation. An evaluation is carried out between models $\delta = \{0.003, 0.0025, 0.0045\}$.

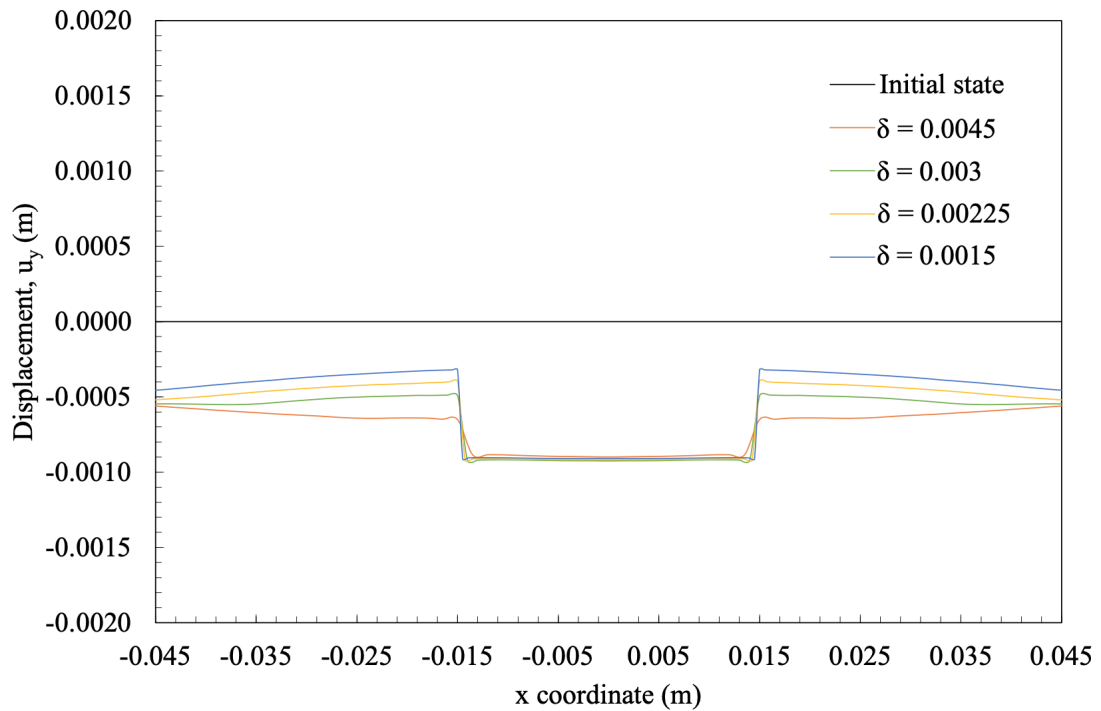


Figure 5.21 : Displacement in the y -direction of δ -convergence tests along the central x axis at $47.9 \mu\text{s}$.

In Figure 5.19(b), the crack starts to propagate with a certain angle with x axis. Then, it immediately continues advancing along the x axis. This direction changing refers to a mode transition. Firstly, it starts with Mode II (in-plane shear), after that, the path becomes parallel to the horizontal axis and Mode I (opening) mode becomes dominant in propagation. This transition can also be detected in Figure 5.19(c), but with small amount. In the last model, $\delta = 0.0015$ (Figure 5.19(d)), the mode transition disappeared. As a consequence, the differences in deflections and propagation velocities can be explained with the mode transitions.

5.3.3 Convergence tests comparison

Table 5.5 shows the average crack propagation velocity of each model. In the end column of the Table, normalized values with regard to the chosen reference model $m = 3$ with $\delta = 0.00300$ were given in percentages. Compared with average velocities in m -convergence tests, velocities in δ -convergence tests differentiate much more. The average velocities for m -tests are also in agreement with Figure 5.15. According to these data, it can be inferred that the minimum value of m (as an indicator of material points within a horizon) should be 3 for the given model with these parameters and

dimensions. The average velocities of $m = 3, 4,$ and 5 models are very close to each other. The average velocities for δ -tests indicate that the horizon values can affect the crack propagation, which is also shown in Figure 5.20.

The data for $\delta = 0.00450$ test should be considered as an outlier. Because the crack did not propagate in contrast to other models.

Table 5.5 : Average velocity data.

Model	Velocity (m/s)	Normalized to ref. (%)
m-tests		
$m = 2$	831	142
$m = 3$ (ref.)	587	100
$m = 4$	627	107
$m = 5$	592	101
δ -tests		
$\delta = 0.00450$	211*	36*
$\delta = 0.00300$ (ref.)	587	100
$\delta = 0.00225$	704	120
$\delta = 0.00150$	794	135

*Outlier because of non-propagating crack

5.3.4 Wave propagation

The velocity form wave progression in the vertical direction was given in Figure 5.22 for the case with $m = 3$ and $\delta = 0.003$ m. The time duration is between 0-47.9 μ s because after that time, waves becomes vague.

Figure 5.22(a) shows the initial state. The projectile has not been impacted yet and there is no contact between the impactor and the body. The contact starts at 4.4 μ s, which initiates a wave (Figure 5.22(b)). Waves can reach the pre-defined crack tip at 13.1 μ s. This is the time of forming the Mode II shear loading due to wave progression (Figure 5.22(d)). This wave is termed as the compressive wave. However, the crack propagation starts when the compression wave reaches the bottom at 21.8 μ s. Here, the reflected waves from the bottom cause a velocity difference around the crack tip that initiates and amplifies the crack propagation.

After sequential loading, waves come from the impactor and reflected from the bottom encounter and this resulted in a distortion in the shape of waves at 47.9 μ s (Figure 5.22(l)).

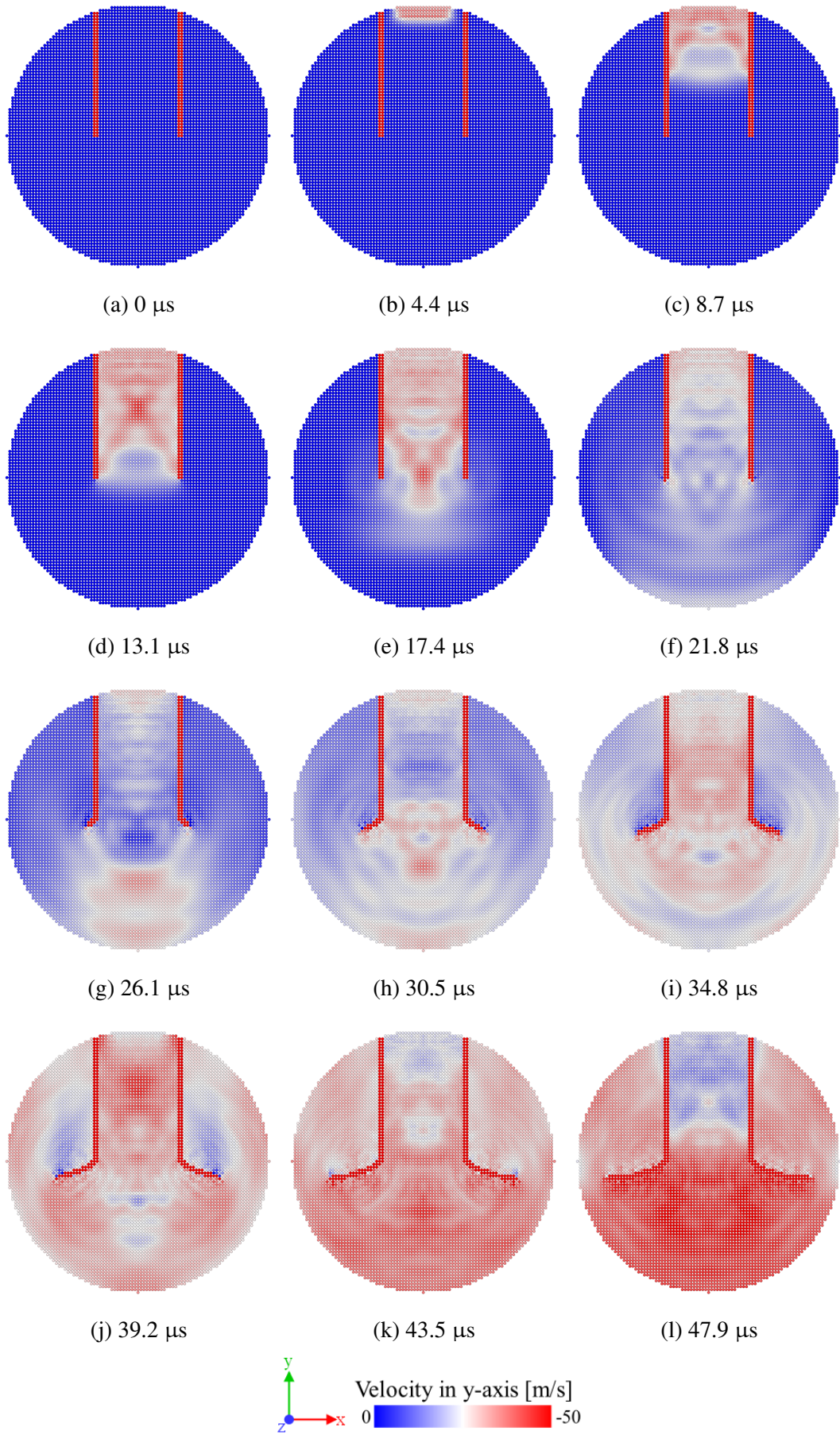


Figure 5.22 : The wave propagation on the case with $m = 3$ and $\delta = 0.003$ m.

For a detailed inspection, all models' wave propagation was given in Appendices F and G from 0 to 60.9 μs .

The wave propagation of m-convergence test suit for $m = \{2, 3, 4, 5\}$ with constant $\delta = 0.003$ m were given in Appendix F. The time durations are given as follow, in Figure F.1: 0-13.1 μs ; in Figure F.2: 17.4-30.5 μs ; in Figure F.3: 34.8-47.9 μs ; and in Figure F.4: 52.2-60.9 μs .

The wave propagation of δ -convergence test suit for $\delta = \{0.0045, 0.003, 0.00225, 0.0015\}$ m with constant $m = 3$ were given in Appendix G. The time durations are given as follow, in Figure G.1: 0-13.1 μs ; in Figure G.2: 17.4-30.5 μs ; in Figure G.3: 34.8-47.9 μs ; and in Figure G.4: 52.2-60.9 μs .

6. CONCLUSIONS

The purpose of the current study was to examine the dynamic fracture in materials subjected to impact load. These findings contribute in several ways to our understanding of dynamic fracture mechanism and provide a basis for numerical analysis of wire ropes subjected to impact load.

The bond-based Peridynamic model was used to understand the dynamic crack propagation, the compressional wave, and effect of micro-cracks on the material toughness for a classical impact loading problem, Kalthoff-Winkler. The one most obvious finding to emerge from this part of the study is that the less than a certain number of randomly located micro-cracks around the crack tip has no positive effect on fracture toughening mechanism. Nevertheless, adding more pre-defined micro-cracks in the same region can decrease crack propagation velocity and significantly increase toughness. The second major finding was that there needs a certain number of micro-cracks for occurring of toughening effect. Moreover, an insufficient number of micro-cracks can not decelerate the propagation of cracks. A certain number of micro-cracks should be placed in the body in order to obtain the toughening effect. In general, therefore, it seems that the density of micro-cracks in a constant area and the number of micro-cracks in expending areas are significant parameters on toughening mechanism in a brittle material subjected to impact load. The results of this investigation complement those of earlier studies. These findings support PD's competence as an alternative to classical continuum mechanics for modelling of fracture and thus, designing of strengthen geometries. Although the study has successfully demonstrated that crack propagation and fracture characteristics, it has certain limitations in terms of properties of micro-cracks. The length and distances of micro-cracks can be investigated in future studies. This would be a fruitful area for further work. More test cases on the distribution of micro-cracks would help researchers establish a greater degree of knowledge.

A serial of studies was then carried out to constitute a basis for analysing wire ropes subjected to impact load with PD theory. The analysis and example tests focused on examining crack propagation in a wire section under transverse loading. The axial loading can cause a radial load component because of the helical structure of a wire rope. On the other hand, radial loads do not have to be formed because of the axial load; they can be applied from an external source. Surface shears can be created due to radial loads that react with the normal or transverse tension. A certain number of wire in a rope can break, and this does not cause losses in overall rope strength if the breakage of the strands were well distributed. However, damaging a certain number of wire could have resulted in a catastrophic failure. Understanding the failure mechanism of a single wire, a strand, and whole wire rope structure is vitally important in that aspect. This part of the study has examined the parameters which were thought to contribute to the analysis of wire rope failures with PD theory. Findings of the m-convergence test suit inferred that the minimum value of m (as an indicator of material points within a horizon) should be 3 for the given model with these parameters and dimensions. Besides, the average velocities in $m = \{3, 4, 5\}$ models do not differ significantly. On the other hand, δ value has more effect on crack velocities than m value. Results indicated that the horizon value, $\delta = 0.00450$ is not applicable for the model with given parameters. The δ -test suit provide valuable knowledge on crack propagation in a wire's cross section. Taken together, these results suggest that there is an association between crack propagation and horizon size. With the understanding of wave progression and mode transition relation, the model $\delta = 0.0015$ can be considered as a better parameter choice for the given model. The Mode I crack opening transition in the reference model indicates a routing of the crack in the horizontal direction.

This study aims to contribute to this growing area of research by exploring the effect of the micro and macro crack relation on the dynamic brittle failure mechanisms. For the past decades, studies of numerical analysis of wire rope modelling have been restricted to axial static loading using Finite Element Method. The test suits presented here provides one of the first investigations into how model the crack propagation and related failure mechanism of wire ropes using Peridynamics. The importance and originality of this study is that it explores, for the first time, the effect of PD

model parameters for a given wire rope cross section subjected to impact load. This study provides new insights into the analysis of wire ropes with a non-local continuum model, Peridynamics. The generalisability of these results is subject to certain limitations. For instance, the complete analysis of a strand provides a more accurate analysis of fracture and failure in wire ropes. Also, more test suit can be designed to obtain more accurate wire rope geometry. Notwithstanding these limitations, the study provides a basis for understanding of crack propagation in wire ropes.

Further studies, which take the complete structure of wire rope into account, will need to be undertaken. This study lays the groundwork for future research into the failure mechanism of wire ropes subjected to impact loads. The contact of the wires forming the rope on each other will be the basis of further studies to be done, modelling the wires as circular cross-section and elliptical in angular cross-section. As experimental studies, the development of a micro-crack to be created on the wire should be examined experimentally and the results obtained with Peridynamics model should be compared.

REFERENCES

- [1] **İnan, M.** (1964). *Düzlemde Elastisite Teorisi*, İstanbul Teknik Üniversitesi, İnşaat Fakültesi Talebe Cemiyeti Yayınları, Sayı: 3, İstanbul.
- [2] **Anderson, T.L.** (2017). *Fracture Mechanics: Fundamentals and Applications, Fourth Edition*.
- [3] **Cox, B.N., Gao, H., Gross, D. and Rittel, D.** (2005). Modern topics and challenges in dynamic fracture, *Journal of the Mechanics and Physics of Solids*, 53(3), 565–596.
- [4] **Hu, W.** (2012). Peridynamic models for dynamic brittle fracture, *Ph.D. thesis*, University of Nebraska-Lincoln, <http://search.proquest.com/docview/1009243071?accountid=45156>.
- [5] **Ravi-Chandar, K. and Knauss, W.G.** (1984). An experimental investigation into dynamic fracture: I. Crack initiation and arrest, *International Journal of Fracture*, 25(4), 247–262.
- [6] **WOODWARD, R.L., BAXTER, B.J., PATTIE, S.D. and McCARTHY, P.** (1991). Impact Fragmentation of Brittle Materials, *Le Journal de Physique IV*, 01(C3), C3–259–C3–264.
- [7] **Willis, J.R. and Movchan, A.B.** (1995). Dynamic weight functions for a moving crack. I. Mode I loading, *Journal of the Mechanics and Physics of Solids*, 43(3), 319–341.
- [8] **Willis, J.R. and Movchan, A.B.** (1997). Three-dimensional dynamic perturbation of a propagating crack, *Journal of the Mechanics and Physics of Solids*, 45(4), 591–610.
- [9] **Morrissey, J.W. and Rice, J.R.** (1998). Crack front waves, *Journal of the Mechanics and Physics of Solids*, 46(3), 467–487.
- [10] **Ramanathan, S. and Fisher, D.S.** (1997). Dynamics and instabilities of planar tensile cracks in heterogeneous media, *Physical Review Letters*, 79(5), 877–880.
- [11] **Bouchaud, E., Bouchaud, J.P., Fisher, D.S., Ramanathan, S. and Rice, J.R.** (2002). Can crack front waves explain the roughness of cracks?, *Journal of the Mechanics and Physics of Solids*, 50(8), 1703–1725, 0108261.
- [12] **Sharon, E., Cohen, G. and Fineberg, J.** (2001). Propagating solitary waves along a rapidly moving crack front, *Nature*, 410(6824), 68–71.

- [13] **Bonamy, D. and Ravi-Chandar, K.** (2003). Interaction of shear waves and propagating cracks, *Physical Review Letters*, 91(23).
- [14] **Guo, J.S. and Gao, W.C.** (2019). Study of the Kalthoff–Winkler experiment using an ordinary state-based peridynamic model under low velocity impact, *Advances in Mechanical Engineering*, 11(5), 168781401985256, <http://journals.sagepub.com/doi/10.1177/1687814019852561>.
- [15] **Kalthoff, J.F.** (1988). Shadow Optical Analysis Of Dynamic Shear Fracture, *Optical Engineering*, 27(10).
- [16] **Zhou, M., Ravichandran, G. and Rosakis, A.J.** (1996). Dynamically propagating shear bands in impact-loaded prenotched plates - II. Numerical simulations, *Journal of the Mechanics and Physics of Solids*, 44(6), 1007–1021.
- [17] **Ravi-Chandar, K.** (1995). On the failure mode transitions in polycarbonate under dynamic mixed-mode loading, *International Journal of Solids and Structures*, 32(6-7), 925–938.
- [18] **Rittel, D. and Maigre, H.** (1996). An investigation of dynamic crack initiation in PMMA, *Mechanics of Materials*, 23(3), 229–239.
- [19] **Kalthoff, J.F.** (2003). Failure methodology of mode-II loaded cracks, *Strength, Fracture and Complexity*, 1(3), 121–138.
- [20] **Rittel, D., Maigre, H. and Bui, H.D.** (1992). A new method for dynamic fracture toughness testing, *Scripta Metallurgica et Materiala*, 26(10), 1593–1598.
- [21] **Li, X., Yang, H., Zan, X., Li, X. and Jiang, X.** (2018). Effect of a micro-crack on the kinked macro-crack, *Theoretical and Applied Fracture Mechanics*, 96, 468–475, <https://www.sciencedirect.com/science/article/pii/S0167844217305694><https://linkinghub.elsevier.com/retrieve/pii/S0167844217305694>.
- [22] **Ravi-Chandar, K. and Yang, B.** (1997). On the role of microcracks in the dynamic fracture of brittle materials, *Journal of the Mechanics and Physics of Solids*, 45(4), 535–563.
- [23] **Sharon, E., Gross, S.P. and Fineberg, J.** (1996). Energy dissipation in dynamic fracture, *Physical Review Letters*, 76(12), 2117–2120.
- [24] **Washabaugh, P.D. and Knauss, W.G.** (1994). A reconciliation of dynamic crack velocity and Rayleigh wave speed in isotropic brittle solids, *International Journal of Fracture*, 65(2), 97–114.
- [25] **Loehnert, S. and Belytschko, T.** (2007). Crack shielding and amplification due to multiple microcracks interacting with a macrocrack, *International Journal of Fracture*, 145(1), 1–8.

- [26] **Brenchich, A. and Carpinteri, A.** (1998). Stress field interaction and strain energy distribution between a stationary main crack and its process zone, *Engineering Fracture Mechanics*, 59(6), 797–814, <https://www.sciencedirect.com/science/article/pii/S0013794497001586>.
- [27] **Bleyer, J., Roux-Langlois, C. and Molinari, J.F.** (2017). Dynamic crack propagation with a variational phase-field model: limiting speed, crack branching and velocity-toughening mechanisms, *International Journal of Fracture*, 204(1), 79–100.
- [28] **Basoglu, M.F., Zerín, Z., Kefal, A. and Oterkus, E.** (2019). A computational model of peridynamic theory for deflecting behavior of crack propagation with micro-cracks, *Computational Materials Science*, 162(November 2018), 33–46, <https://doi.org/10.1016/j.commatsci.2019.02.032>.
- [29] **ROSE, L.R.** (1986). Effective Fracture Toughness of Microcracked Materials, *Journal of the American Ceramic Society*, 69(3), 212–214, <https://doi.org/10.1111/j.1151-2916.1986.tb07409.x>.
- [30] **Li, X., Li, X. and Jiang, X.** (2017). Influence of a micro-crack on the finite macro-crack, *Engineering Fracture Mechanics*, 177, 95–103, <https://www.sciencedirect.com/science/article/pii/S0013794416305100>.
- [31] **Xiaotao, L., Xu, L., Hongda, Y. and Xiaoyu, J.** (2017). Effect of micro-cracks on plastic zone ahead of the macro-crack tip, *Journal of Materials Science*, 52(23), 13490–13503.
- [32] **Johnson, E.** (1992). Process region changes for rapidly propagating cracks, *International Journal of Fracture*, 55(1), 47–63.
- [33] **Yang, B. and Ravi-Chandar, K.** (1996). On the role of the process zone in dynamic fracture, *Journal of the Mechanics and Physics of Solids*, 44(12), 1955–1976.
- [34] **Rafiee, S., Seelig, T. and Gross, D.** (2003). Simulation of dynamic crack curving and branching under biaxial loading by a time domain boundary integral equation method, *International Journal of Fracture*, 120(3), 545–561.
- [35] **Rafoee, S., Gross, D. and Seelig, T.** (2004). The influence of microcrack nucleation on dynamic crack growth - a numerical study, *Engineering Fracture Mechanics*, 71(4-6), 849–857.
- [36] **Seelig, T. and Gross, D.** (1997). Analysis of dynamic crack propagation using a time-domain boundary integral equation method, *International Journal of Solids and Structures*, 34(17), 2087–2103, [http://dx.doi.org/10.1016/S0020-7683\(96\)00133-3](http://dx.doi.org/10.1016/S0020-7683(96)00133-3).
- [37] **Seelig, T. and Gross, D.** (1999). On the interaction and branching of fast running cracks - A numerical investigation, *Journal of the Mechanics and Physics of Solids*, 47(4), 935–952.

- [38] **Hawong, J.S., Kobayashi, A.S., Dadkhah, M.S., Kang, B.S. and Ramulu, M.** (1987). Dynamic crack curving and branching under biaxial loading, *Experimental Mechanics*, 27(2), 146–153.
- [39] **Ramulu, M. and Kobayashi, A.S.** (1985). Mechanics of crack curving and branching - a dynamic fracture analysis, *International Journal of Fracture*, 27(3-4), 187–201.
- [40] **Shukla, A., Nigam, H. and Zervas, H.** (1990). Effect of stress field parameters on dynamic crack branching, *Engineering Fracture Mechanics*, 36(3), 429–438.
- [41] **Rubinstein, A.A.** (1985). Macrocrack interaction with semi-infinite microcrack array, *International Journal of Fracture*, 27(2), 113–119.
- [42] **Ducourthial, E., Bouchaud, E. and Chaboche, J.L.** (2000). Influence of microcracks on a propagation of macrocracks, *Computational Materials Science*, 19(1-4), 229–234, <https://www.sciencedirect.com/science/article/pii/S0927025600001592>.
- [43] **Petrova, V., Tamuzs, V. and Petrova, V.** (2000). A survey of macro-microcrack interaction problems, *Applied Mechanics Reviews*, 53(5), 117–146, <https://doi.org/10.1115/1.3097344>.
- [44] **Soh, A.K. and Yang, C.H.** (2004). Numerical modeling of interactions between a macro-crack and a cluster of micro-defects, *Engineering Fracture Mechanics*, 71(2), 193–217, <https://www.sciencedirect.com/science/article/pii/S0013794403000973>.
- [45] **Kumar, S. and Curtin, W.A.**, (2007), Crack interaction with microstructure, <https://www.sciencedirect.com/science/article/pii/S1369702107702079>.
- [46] **Gong, S.X.** (1994). Microcrack interaction with a finite main crack: An exact formulation, *International Journal of Fracture*, 66(3), R51–R56, <http://link.springer.com/10.1007/BF00042592>.
- [47] **Laures, J.P. and Kachanov, M.** (1991). Three-dimensional interactions of a crack front with arrays of penny-shaped microcracks, *International Journal of Fracture*, 48(4), 255–279, <http://link.springer.com/10.1007/BF00012916>.
- [48] **Tamuzs, V.P. and Petrova, V.E.** (2002). On macrocrack-microdefect interaction, *International Applied Mechanics*, 38(10), 1157–1177.
- [49] **Lorentz, E.** (2008). A mixed interface finite element for cohesive zone models, *Computer Methods in Applied Mechanics and Engineering*, 198(2), 302–317, <https://www.sciencedirect.com/science/article/pii/S0045782508002880>.
- [50] **Unosson, M., Olovsson, L. and Simonsson, K.** (2006). Failure modelling in finite element analyses: Element erosion with crack-tip enhancement, *Finite Elements in Analysis and Design*, 42(4), 283–297,

<https://www.sciencedirect.com/science/article/pii/S0168874X05000831>.

- [51] **Lancaster, I.M., Khalid, H.A. and Kougioumtzoglou, I.A.** (2013). Extended FEM modelling of crack propagation using the semi-circular bending test, *Construction and Building Materials*, 48, 270–277, <https://www.sciencedirect.com/science/article/pii/S0950061813005643>.
- [52] **Belytschko, T. and Black, T.** (1999). Elastic crack growth in finite elements with minimal remeshing, *International Journal for Numerical Methods in Engineering*, 45(5), 601–620.
- [53] **Song, J.H., Areias, P.M. and Belytschko, T.** (2006). A method for dynamic crack and shear band propagation with phantom nodes, *International Journal for Numerical Methods in Engineering*, 67(6), 868–893.
- [54] **Bobaru, F.** (2017). *Handbook of Peridynamic Modeling*, Chapman and Hall/CRC, <https://www.taylorfrancis.com/books/9781482230444>.
- [55] **Huynh, D.B. and Belytschko, T.** (2009). The extended finite element method for fracture in composite materials, *International Journal for Numerical Methods in Engineering*, 77(2), 214–239.
- [56] **Rabczuk, T.** (2013). Computational Methods for Fracture in Brittle and Quasi-Brittle Solids: State-of-the-Art Review and Future Perspectives, *ISRN Applied Mathematics*, 2013, 1–38.
- [57] **Moës, N., Dolbow, J. and Belytschko, T.** (1999). A finite element method for crack growth without remeshing, *International Journal for Numerical Methods in Engineering*, 46(1), 131–150.
- [58] **Belytschko, T., Chen, H., Xu, J. and Zi, G.** (2003). Dynamic crack propagation based on loss of hyperbolicity and a new discontinuous enrichment, *International Journal for Numerical Methods in Engineering*, 58(12), 1873–1905, <http://doi.wiley.com/10.1002/nme.941>.
- [59] **Budyn, É., Zi, G., Moës, N. and Belytschko, T.** (2004). A method for multiple crack growth in brittle materials without remeshing, *International Journal for Numerical Methods in Engineering*, 61(10), 1741–1770.
- [60] **Zhuang, Z. and Cheng, B.B.** (2011). Equilibrium state of mode-I sub-interfacial crack growth in bi-materials, *International Journal of Fracture*, 170(1), 27–36.
- [61] **Zhuang, Z. and Cheng, B.B.** (2011). Development of X-FEM methodology and study on mixed-mode crack propagation, *Acta Mechanica Sinica/Lixue Xuebao*, 27(3), 406–415.
- [62] **Zhuang, Z. and Cheng, B.B.** (2011). A novel enriched CB shell element method for simulating arbitrary crack growth in pipes, *Science China: Physics, Mechanics and Astronomy*, 54(8), 1520–1531.

- [63] **Wang, H., Liu, Z., Xu, D., Zeng, Q., Zhuang, Z. and Chen, Z.** (2016). Extended finite element method analysis for shielding and amplification effect of a main crack interacted with a group of nearby parallel microcracks, *International Journal of Damage Mechanics*, 25(1), 4–25.
- [64] **Huo, J., Zhang, Z., Meng, Z., Xue, L., Jia, G. and Chen, J.** (2019). A time-integral crack propagation model considering thickness effect, *IEEE Access*, 7, 41078–41089, <https://ieeexplore.ieee.org/document/8672119/>.
- [65] **Zhou, X., Wang, Y. and Qian, Q.** (2016). Numerical simulation of crack curving and branching in brittle materials under dynamic loads using the extended non-ordinary state-based peridynamics, *European Journal of Mechanics, A/Solids*, 60, 277–299, <https://www.sciencedirect.com/science/article/pii/S0997753816301875>.
- [66] **Bobaru, F. and Zhang, G.** (2015). Why do cracks branch? A peridynamic investigation of dynamic brittle fracture, *International Journal of Fracture*, 196(1-2), 59–98.
- [67] **Dugdale, D.S.** (1960). Yielding of steel sheets containing slits, *Journal of the Mechanics and Physics of Solids*, 8(2), 100–104.
- [68] **Barenblatt, G.I.** (1962). The Mathematical Theory of Equilibrium Cracks in Brittle Fracture, *Advances in Applied Mechanics*, 7(C), 55–129.
- [69] **Camacho, G.T. and Ortiz, M.** (1997). Adaptive Lagrangian modelling of ballistic penetration of metallic targets, *Computer Methods in Applied Mechanics and Engineering*, 142(3-4), 269–301.
- [70] **Xu, X.P. and Needleman, A.** (1994). Numerical simulations of fast crack growth in brittle solids, *Journal of the Mechanics and Physics of Solids*, 42(9), 1397–1434.
- [71] **Ha, Y.D. and Bobaru, F.** (2010). Studies of dynamic crack propagation and crack branching with peridynamics, *International Journal of Fracture*, 162(1-2), 229–244.
- [72] **Klein, P.A., Foulk, J.W., Chen, E.P., Wimmer, S.A. and Gao, H.J.** (2001). Physics-based modeling of brittle fracture: Cohesive formulations and the application of meshfree methods, *Theoretical and Applied Fracture Mechanics*, 37(1-3), 99–166.
- [73] **Ismail, J., Zaïri, F., Naït-Abdelaziz, M. and Azari, Z.** (2012). How cracks affect the contact characteristics during impact of solid particles on glass surfaces: A computational study using anisotropic continuum damage mechanics, *International Journal of Impact Engineering*, 40-41, 10–15, <http://dx.doi.org/10.1016/j.ijimpeng.2011.09.002>.
- [74] **Holmström, E., Samela, J. and Nordlund, K.** (2011). Atomistic simulations of fracture in silica glass through hypervelocity impact, *Epl*, 96(1).

- [75] **Rabczuk, T., Zi, G., Bordas, S. and Nguyen-Xuan, H.** (2010). A simple and robust three-dimensional cracking-particle method without enrichment, *Computer Methods in Applied Mechanics and Engineering*, 199(37-40), 2437–2455.
- [76] **Kosteski, L., Barrios D’Ambra, R. and Iturrioz, I.** (2012). Crack propagation in elastic solids using the truss-like discrete element method, *International Journal of Fracture*, 174(2), 139–161.
- [77] **Braun, M. and Fernández-Sáez, J.** (2014). A new 2D discrete model applied to dynamic crack propagation in brittle materials, *International Journal of Solids and Structures*, 51(21-22), 3787–3797.
- [78] **Ashurst, W.T. and Hoover, W.G.** (1976). Microscopic fracture studies in the two-dimensional triangular lattice, *Physical Review B*, 14(4), 1465–1473.
- [79] **Vashishta, P., Kalia, R.K. and Nakano, A.,** (2003), Multimillion atom molecular dynamics simulations of nanostructures on parallel computers.
- [80] **Sharma, A., Kalia, R.K., Nakano, A. and Vashishta, P.,** (2003), Large multidimensional data visualization for materials science.
- [81] **Zhou, S.J., Lomdahl, P.S., Thomson, R. and Holian, B.L.** (1996). Dynamic crack processes via molecular dynamics, *Physical Review Letters*, 76(13), 2318–2321.
- [82] **Fedelinski, P., Aliabadi, M.H. and Rooke, D.P.** (1997). The time-domain DBEM for rapidly growing cracks, *International Journal for Numerical Methods in Engineering*, 40(9), 1555–1572.
- [83] **Tada, T. and Yamashita, T.** (1997). Non-hypersingular boundary integral equations for two-dimensional non-planar crack analysis, *Geophysical Journal International*, 130(2), 269–282.
- [84] **Silling, S.A. and Askari, E.** (2005). A meshfree method based on the peridynamic model of solid mechanics, *Computers and Structures*, 83(17-18), 1526–1535, internal-pdf://101.237.163.103/Silling-2005-Ameshfreemethodbasedonthepe.pdf.
- [85] **Silling, S.A.** (2000). Reformulation of elasticity theory for discontinuities and long-range forces, *Journal of the Mechanics and Physics of Solids*, 48(1), 175–209.
- [86] **Javili, A., Morasata, R., Oterkus, E. and Oterkus, S.** (2019). Peridynamics review, *Mathematics and Mechanics of Solids*, 24(11), 3714–3739.
- [87] **Madenci, E. and Oterkus, E.** (2014). *Peridynamic theory and its applications*, volume 9781461484, Springer New York, New York, NY, <http://link.springer.com/10.1007/978-1-4614-8465-3>.
- [88] **Silling, S.A. and Lehoucq, R.B.** (2008). Convergence of peridynamics to classical elasticity theory, *Journal of Elasticity*, 93(1), 13–37.

- [89] **Silling, S.A. and Bobaru, F.** (2005). Peridynamic modeling of membranes and fibers, *International Journal of Non-Linear Mechanics*, 40(2-3), 395–409.
- [90] **Bobaru, F.** (2007). Influence of van der Waals forces on increasing the strength and toughness in dynamic fracture of nanofibre networks: A peridynamic approach, *Modelling and Simulation in Materials Science and Engineering*, 15(5), 397–417.
- [91] **Xu, J., Askari, A., Weckner, O. and Silling, S.** (2008). Peridynamic Analysis of Impact Damage in Composite Laminates, *Journal of Aerospace Engineering*, 21(3), 187–194.
- [92] **Kilic, B., Agwai, A. and Madenci, E.** (2009). Peridynamic theory for progressive damage prediction in center-cracked composite laminates, *Composite Structures*, 90(2), 141–151.
- [93] **Foster, J.T., Silling, S.A. and Chen, W.W.** (2010). Viscoplasticity using peridynamics, *International Journal for Numerical Methods in Engineering*, 81(10), 1242–1258.
- [94] **Foster, J.T., Silling, S.A. and Chen, W.** (2011). An energy based failure criterion for use with peridynamic states, *International Journal for Multiscale Computational Engineering*, 9(6), 675–687.
- [95] **Ha, Y.D. and Bobaru, F.** (2011). Characteristics of dynamic brittle fracture captured with peridynamics, *Engineering Fracture Mechanics*, 78(6), 1156–1168.
- [96] **Kilic, B. and Madenci, E.** (2010). Coupling of peridynamic theory and the finite element method, *Journal of Mechanics of Materials and Structures*, 5(5), 707–733.
- [97] **Oterkus, E., Madenci, E., Weckner, O., Silling, S., Bogert, P. and Tessler, A.** (2012). Combined finite element and peridynamic analyses for predicting failure in a stiffened composite curved panel with a central slot, *Composite Structures*, 94(3), 839–850, <https://www.sciencedirect.com/science/article/pii/S0263822311002741>.
- [98] **Bobaru, F., Ha, Y.D. and Hu, W.** (2012). Damage progression from impact in layered glass modeled with peridynamics, *Central European Journal of Engineering*, 2(4), 551–561.
- [99] **Ghajari, M., Iannucci, L. and Curtis, P.** (2014). A peridynamic material model for the analysis of dynamic crack propagation in orthotropic media, *Computer Methods in Applied Mechanics and Engineering*, 276, 431–452, <https://www.sciencedirect.com/science/article/pii/S004578251400111X>.
- [100] **Oterkus, S., Madenci, E. and Agwai, A.** (2014). Fully coupled peridynamic thermomechanics, *Journal of the Mechanics and Physics of Solids*, 64(1), 1–23.

- [101] **Oterkus, S., Madenci, E. and Agwai, A.** (2014). Peridynamic thermal diffusion, *Journal of Computational Physics*, 265, 71–96, <https://www.sciencedirect.com/science/article/pii/S0021999114000540>.
- [102] **De Meo, D., Russo, L. and Oterkus, E.** (2017). Modeling of the onset, propagation, and interaction of multiple cracks generated from corrosion pits by using peridynamics, *Journal of Engineering Materials and Technology, Transactions of the ASME*, 139(4), 1–9.
- [103] **Diyaroglu, C., Oterkus, E., Madenci, E., Rabczuk, T. and Siddiq, A.** (2016). Peridynamic modeling of composite laminates under explosive loading, *Composite Structures*, 144, 14–23, <http://dx.doi.org/10.1016/j.compstruct.2016.02.018>.
- [104] **Vazic, B., Wang, H., Diyaroglu, C., Oterkus, S. and Oterkus, E.** (2017). Dynamic propagation of a macrocrack interacting with parallel small cracks, *AIMS Materials Science*, 4(1), 118–136.
- [105] **Kalthoff, J.F. and Winkler, S.** (1987). Failure mode transition at high rates of loading, *Impact loading and dynamic behavior of materials*, 1, 185 – 195.
- [106] **Kalthoff, J.F.** (2000). Modes of dynamic shear failure in solids, *International Journal of Fracture*, 101(1-2), 1–31.
- [107] **Silling, S.A., Epton, M., Weckner, O., Xu, J. and Askari, E.** (2007). Peridynamic states and constitutive modeling, *Journal of Elasticity*, 88(2), 151–184.
- [108] **Ayatollahi, M.R. and Aliha, M.R.** (2009). Analysis of a new specimen for mixed mode fracture tests on brittle materials, *Engineering Fracture Mechanics*, 76(11), 1563–1573.
- [109] **Silling, S.A.** (2004). EMU user’s manual, Code Ver. 2.6d., **Technical Report**, Sandia National Laboratories, Albuquerque.
- [110] **Kilic, B. and Madenci, E.** (2010). An adaptive dynamic relaxation method for quasi-static simulations using the peridynamic theory, *Theoretical and Applied Fracture Mechanics*, 53(3), 194–204.
- [111] **Bobaru, F., Yang, M., Alves, L.F., Silling, S.A., Askari, E. and Xu, J.** (2009). Convergence, adaptive refinement, and scaling in 1D peridynamics, *International Journal for Numerical Methods in Engineering*, 77(6), 852–877.
- [112] **Silling, S.A.**, (2003). Dynamic fracture modeling with a meshfree peridynamic code, *Computational Fluid and Solid Mechanics 2003*, pp.641–644.
- [113] **Ren, H., Zhuang, X., Cai, Y. and Rabczuk, T.** (2016). Dual-horizon peridynamics, *International Journal for Numerical Methods in Engineering*, 108(12), 1451–1476, 1506.05146.

- [114] **Ren, H., Zhuang, X. and Rabczuk, T.** (2017). Dual-horizon peridynamics: A stable solution to varying horizons, *Computer Methods in Applied Mechanics and Engineering*, 318, 762–782, <http://dx.doi.org/10.1016/j.cma.2016.12.031>, 1703.05910.
- [115] **Amani, J., Oterkus, E., Areias, P., Zi, G., Nguyen-Thoi, T. and Rabczuk, T.** (2016). A non-ordinary state-based peridynamics formulation for thermoplastic fracture, *International Journal of Impact Engineering*, 87, 83–94, <https://www.sciencedirect.com/science/article/pii/S0734743X15001359>.
- [116] **Gu, X., Zhang, Q. and Xia, X.** (2017). Voronoi-based peridynamics and cracking analysis with adaptive refinement, *International Journal for Numerical Methods in Engineering*, 112(13), 2087–2109.
- [117] **Trask, N., You, H., Yu, Y. and Parks, M.L.** (2019). An asymptotically compatible meshfree quadrature rule for nonlocal problems with applications to peridynamics, *Computer Methods in Applied Mechanics and Engineering*, 343, 151–165, <https://doi.org/10.1016/j.cma.2018.08.016>, 1801.04488.
- [118] **Wang, H., Xu, Y. and Huang, D.** (2019). A non-ordinary state-based peridynamic formulation for thermo-visco-plastic deformation and impact fracture, *International Journal of Mechanical Sciences*, 159(May), 336–344, <https://doi.org/10.1016/j.ijmecsci.2019.06.008>.
- [119] **Candaş, A., Oterkus, E. and Imrak, C.E.** (2021). Dynamic crack propagation and its interaction with micro-cracks in an impact problem, *Journal of Engineering Materials and Technology, Transactions of the ASME*, 143(1), 1–10.
- [120] **Mahmoud, K.M.** (2007). Fracture strength for a high strength steel bridge cable wire with a surface crack, *Theoretical and Applied Fracture Mechanics*, 48(2), 152–160.
- [121] **Erdönmez, C.** (2010). Mathematical Modeling And Stress Analysis Of Wire Ropes Under Certain Loading Conditions, Phd thesis, Istanbul Technical University.
- [122] **Costello, G.A. and Miller, R.E.** (1977). Lay Effect of Wire Rope., *Ill Univ Dep Theor Appl Mech TAM Rep*, (422).
- [123] **Elata, D., Eshkenazy, R. and Weiss, M.P.** (2004). The mechanical behavior of a wire rope with an independent wire rope core, *International Journal of Solids and Structures*, 41(5-6), 1157–1172.
- [124] **Love, A.E.H.** (1944). *Treatise on mathematical theory of elasticity. 4th edition*, <https://archive.org/details/atreatiseonmath01lovegoog>.
- [125] **Timoshenko, S.** (1955). *Strength of Materials Vol. 2*, Van Nostrand, New York.

- [126] **Green, A. and Laws, N.** (1966). A general theory of rods, *Proceedings of the Royal Society of London. Series A. Mathematical and Physical Sciences*, 293(1433), 145–155.
- [127] **NAKAJIMA, K.** (1991). Calculation of stresses in In, *Journal of crystal growth*, 113(9), 477–484.
- [128] **Knapp, R.H.** (1979). Derivation of a new stiffness matrix for helically armoured cables considering tension and torsion, *International Journal for Numerical Methods in Engineering*, 14(4), 515–529.
- [129] **Velinsky, S.A.** (1985). General nonlinear theory for complex wire rope, *International Journal of Mechanical Sciences*, 27(7-8), 497–507.
- [130] **Hobbs, R.E. and Raouf, M.** (1983). Interwire Slippage and Fatigue Prediction in Standard Cables for Tlp Tethers., *Behaviour of Off-Shore Structures, Proceedings of the International Conference*, volume 2, pp.77–99.
- [131] **Raouf, M. and Kraincanic, I.** (1995). Analysis of Large Diameter Steel Ropes, *Journal of Engineering Mechanics*, 121(6), 667–675.
- [132] **Blouin, F. and Cardou, A.** (1989). A study of helically reinforced cylinders under axially symmetric loads and application to strand mathematical modelling, *International Journal of Solids and Structures*, 25(2), 189–200.
- [133] **Jolicoeur, C. and Cardou, A.** (1994). Analytical Solution for Bending of Coaxial Orthotropic Cylinders, *Journal of Engineering Mechanics*, 120(12), 2556–2574.
- [134] **Jolicoeur, C. and Cardou, A.** (1996). Semicontinuous Mathematical Model for Bending of Multilayered Wire Strands, *Journal of Engineering Mechanics*, 122(7), 643–650.
- [135] **Crossley, J.A., Spencer, A.J. and England, A.H.** (2003). Analytical solutions for bending and flexure of helically reinforced cylinders, *International Journal of Solids and Structures*, 40(4), 777–806.
- [136] **Crossley, J.A., England, A.H. and Spencer, A.J.** (2003). Bending and flexure of cylindrically monoclinic elastic cylinders, *International Journal of Solids and Structures*, 40(25), 6999–7013.
- [137] **Sathikh, S., Moorthy, M.B. and Krishnan, M.** (1996). Symmetric linear elastic model for helical wire strands under axisymmetric loads, *Journal of Strain Analysis for Engineering Design*, 31(5), 389–399.
- [138] **Sathikh, S., Rajasekaran, S., Jayakumar and Jebaraj, C.** (2000). General Thin Rod Model for Preslip Bending Response of Strand, *Journal of Engineering Mechanics*, 126(2), 132–139.
- [139] **Ramsey, H.** (1988). A theory of thin rods with application to helical constituent wires in cables, *International Journal of Mechanical Sciences*, 30(8), 559–570.

- [140] **Phillips, J.W. and Costello, G.A.** (1973). Contact Stresses in Twisted Wire Cables., *ASCE J Eng Mech Div*, 99(EM2), 331–341.
- [141] **Costello, G.A. and Phillips, J.W.** (1973). Contact stresses in thin twisted rods, *Journal of Applied Mechanics, Transactions ASME*, 40(2), 629–630.
- [142] **Costello, G.A.** (1977). Large Deflections of Helical Spring due to Bending, *Journal of the Engineering Mechanics Division*, 103(3), 481–487.
- [143] **Costello, G.A.** (1978). Analytical Investigation of Wire Rope, *Applied Mechanics Reviews*, 31(7), 897–900.
- [144] **Costello, G.A. and Butson, G.J.** (1982). Simplified Bending Theory for Wire Rope., *ASCE J Eng Mech Div*, 108(EM2), 219–227.
- [145] **Costello, G.A.** (1983). Stresses in multilayered cables, *Journal of Energy Resources Technology, Transactions of the ASME*, 105(3), 337–340.
- [146] **Velinsky, S.A., Anderson, G.L. and Costello, G.A.** (1984). Wire Rope with Complex Cross Sections, *Journal of Engineering Mechanics*, 110(3), 380–391.
- [147] **Costello, G.A. and Miller, R.E.** (1980). Static Response of Reduced Rotation Rope, *ASCE J Eng Mech Div*, 106(4), 623–631.
- [148] **Costello, G.A. and Phillips, J.W.** (1975). Effective Modulus of Twisted Wire Cables., *Ill Univ Dep Theor Appl Mech TAM Rep*, 102(398), 171–181.
- [149] **Costello, G.A. and Phillips, J.W.** (1974). A More Exact Theory for Twisted Wire Cables, *Journal of the Engineering Mechanics Division*, 100(5), 1096–1099.
- [150] **Phillips, J.W. and Costello, G.A.** (1977). Axial Impact of Twisted Wire Cables., *American Society of Mechanical Engineers (Paper)*, 44(77 -APM-2), 127–131.
- [151] **Conway, T.A. and Costello, G.A.** (1990). Bird-Caging in Wire Rope, *Journal of Engineering Mechanics*, 116(4), 822–831.
- [152] **Costello, G.A. and Sinha, S.K.** (1977). Torsional Stiffness of Twisted Wire Cables, *Journal of the Engineering Mechanics Division*, 103(4), 766–770.
- [153] **Conway, T.A. and Costello, G.A.** (1993). Viscoelastic response of a strand, *Journal of Applied Mechanics, Transactions ASME*, 60(2), 534–540.
- [154] **Chien, C. and Costello, G.A.** (1985). Effective Length of a Fractured Wire in Wire Rope, *Journal of Engineering Mechanics*, 111(7), 952–961.
- [155] **Phillips, J.W. and Costello, G.A.** (1985). Analysis of wire ropes with internal-wire-rope cores, *Journal of Applied Mechanics, Transactions ASME*, 52(3), 510–516, <http://appliedmechanics.asmedigitalcollection.asme.org/article.aspx?articleid=1408142>.

- [156] **Costello, G.A. and Bert, C.W.** (1992). *Theory of Wire Rope*, volume 59, Springer Publication, Berlin.
- [157] **Hruska, F.H.** (1952). Radial Forces in Wire Ropes, *Wire and Wire Products*, 27(5), 459–463, <http://ci.nii.ac.jp/naid/10003454658/en/>.
- [158] **Utting, W.S. and Jones, N.** (1987). The response of wire rope strands to axial tensile loads-Part I. Experimental results and theoretical predictions, *International Journal of Mechanical Sciences*, 29(9), 605–619.
- [159] **Utting, W.S. and Jones, N.** (1987). The response of wire rope strands to axial tensile loads-Part II. Comparison of experimental results and theoretical predictions, *International Journal of Mechanical Sciences*, 29(9), 621–636.
- [160] **Carlson, A., Kasper, R. and Tuccio, M.** (1973). A Structural Analysis of a Multiconductor Cable, **Technical Report**, Naval underwater systems center New London Conn New London Lab.
- [161] **Cutchins, M.A., Cochran, J.E., Guest, S., Fitz-Coy, N.G. and Tinker, M.L.** (1987). Investigation of the Damping Phenomena in Wire Rope Isolators., *American Society of Mechanical Engineers, Design Engineering Division (Publication) DE*, volume 5, pp.197–204.
- [162] **Chiang, Y.J.** (1996). Characterizing simple-stranded wire cables under axial loading, *Finite Elements in Analysis and Design*, 24(2), 49–66.
- [163] **Velinsky, S.A.** (1993). A stress based methodology for the design of wire rope systems, *Journal of Mechanical Design, Transactions of the ASME*, 115(1), 69–73.
- [164] **Velinsky, S.A. and Lembeck, M.F.** (1990). Designing wire-rope-based mechanical systems in an expert system environment, *Engineering with Computers*, 6(3), 167–176.
- [165] **Cardou, A. and Jolicoeur, C.** (1997). Mechanical models of helical strands, *Applied Mechanics Reviews*, 50(1), 1–14.
- [166] **Huang, N.C.** (1978). Finite extension of an elastic strand with a central core, *Journal of Applied Mechanics, Transactions ASME*, 45(4), 852–858.
- [167] **Shield, C.K. and Costello, G.A.** (1994). The effect of wire rope mechanics on the material properties of cord composites: An elasticity approach, *Journal of Applied Mechanics, Transactions ASME*, 61(1), 1–8.
- [168] **Shield, C.K. and Costello, G.A.** (1994). The effect of wire rope mechanics on the mechanical response of cord composite laminates: An energy approach, *Journal of Applied Mechanics, Transactions ASME*, 61(1), 9–15.
- [169] **Shield, C.K. and Costello, G.A.** (1994). Bending of Cord Composite Plates, *Journal of Engineering Mechanics*, 120(4), 876–892, [https://doi.org/10.1061/\(ASCE\)0733-9399\(1994\)120:4\(876\)](https://doi.org/10.1061/(ASCE)0733-9399(1994)120:4(876)).

- [170] **Paris, A.J. and Costello, G.A.** (2000). Bending of cord composite cylindrical shells, *Journal of Applied Mechanics, Transactions ASME*, 67(1), 117–127, <https://doi.org/10.1115/1.321156>.
- [171] **Paris, A.J. and Costello, G.A.** (2003). Bending of cord composite laminate cylindrical shells, *Journal of Applied Mechanics, Transactions ASME*, 70(3), 364–373, <https://doi.org/10.1115/1.1544541>.
- [172] **Velinsky, S.A.** (2004). Compressive loading of stiffened, wire-strand based structures, *Mechanics Based Design of Structures and Machines*, 32(1), 101–113.
- [173] **Kumar, K. and Botsis, J.** (2001). Contact stresses in multilayered strands under tension and torsion, *Journal of Applied Mechanics, Transactions ASME*, 68(3), 432–440.
- [174] **Jiang, W.G., Henshall, J.L. and Walton, J.M.** (2000). Concise finite element model for three-layered straight wire rope strand, *International Journal of Mechanical Sciences*, 42(1), 63–86.
- [175] **Nawrocki, A. and Labrosse, M.** (2000). Finite element model for simple straight wire rope strands, *Computers and Structures*, 77(4), 345–359.
- [176] **Machida, S. and Durelli, A.J.** (1973). Response of a Strand To Axial and Torsional Displacements., *J Mech Eng Sci*, 15(4), 241–251.
- [177] **Lanteigne, J.** (1985). Theoretical estimation of the response of helically armored cables to tension, torsion, and bending, *Journal of Applied Mechanics, Transactions ASME*, 52(2), 423–432.
- [178] **Kumar, K. and Cochran, J.E.** (1987). Closed-form analysis for elastic deformations of multilayered strands, *Journal of Applied Mechanics, Transactions ASME*, 54(4), 898–903.
- [179] **Velinsky, S.A.** (1988). Design and mechanics of multi-lay wire strands, *Journal of Mechanical Design, Transactions of the ASME*, 110(2), 152–160.
- [180] **Jiang, W.** (1995). A general formulation of the theory of wire ropes, *Journal of Applied Mechanics, Transactions ASME*, 62(3), 747–755.
- [181] **Jiang, W.G. and Henshall, J.L.** (1999). Analysis of termination effects in wire strand using the finite element method, *Journal of Strain Analysis for Engineering Design*, 34(1), 31–38.
- [182] **Yardibi, E.** (2000). Analysis of Wire Stresses of Axial Loaded and Bent Wire Rope, Msc. thesis, Istanbul Technical University.
- [183] **Şentürk, Ö.** (2007). Modelling and Analysis of Axial Loaded Wire Rope Strand Using The Finite Element Method, M.sc. thesis, Istanbul Technical University.
- [184] **Elata, D., Eshkenazy, R. and Weiss, M.P.** (2004). The mechanical behavior of a wire rope with an independent wire rope core, *International Journal of Solids and Structures*, 41(5-6), 1157–1172.

- [185] **Ghoreishi, S.R., Messenger, T., Cartraud, P. and Davies, P.** (2004). Assessment of cable models for synthetic mooring lines, *Proceedings of the International Offshore and Polar Engineering Conference*, pp.184–190.
- [186] **Ghoreishi, S.R., Cartraud, P., Davies, P. and Messenger, T.** (2007). Analytical modeling of synthetic fiber ropes subjected to axial loads. Part I: A new continuum model for multilayered fibrous structures, *International Journal of Solids and Structures*, 44(9), 2924–2942.
- [187] **Durelli, A.J., Machida, S. and Parks, V.J.** (1972). Strains and Displacements on a Steel Wire Strand., *Naval Engineers Journal*, 84(6), 85–93.
- [188] **Utting, W.S. and Jones, N.** (1985). Tensile testing of a wire rope strand, *The Journal of Strain Analysis for Engineering Design*, 20(3), 151–164.
- [189] **Raof, M. and Hobbs, R.E.** (1988). Torsion tests on large spiral strands, *The Journal of Strain Analysis for Engineering Design*, 23(2), 97–104.
- [190] **Bateman, M.B., Howard, I.C., Johnson, A.R. and Walton, J.M.** (2001). Computer simulation of the impact performance of a wire rope safety fence, *International Journal of Impact Engineering*, 25(1), 67–85.
- [191] **Onur, Y.A. and Imrak Erdem, C.** (2012). Experimental and theoretical investigation of bending over sheave fatigue life of stranded steel wire rope, *Indian Journal of Engineering and Materials Sciences*, 19(3), 189–195.
- [192] **Onur, Y.A.** (2016). Experimental and theoretical investigation of prestressing steel strand subjected to tensile load, *International Journal of Mechanical Sciences*, 118, 91–100.
- [193] **Hobbs, R.E. and Raof, M.** (1996). Behaviour of cables under dynamic or repeated loading, *Journal of Constructional Steel Research*, 39(1 SPEC. ISS.), 31–50.
- [194] **Foti, F. and de Luca di Roseto, A.** (2016). Analytical and finite element modelling of the elastic–plastic behaviour of metallic strands under axial–torsional loads, *International Journal of Mechanical Sciences*, 115-116, 202–214, <http://dx.doi.org/10.1016/j.ijmecsci.2016.06.016>.
- [195] **Jiang, W.G., Yao, M.S. and Walton, J.M.** (1999). A concise finite element model for simple straight wire rope strand, *International Journal of Mechanical Sciences*, 41(2), 143–161.
- [196] **Jiang, W.G., Warby, M.K. and Henshall, J.L.** (2008). Statically indeterminate contacts in axially loaded wire strand, *European Journal of Mechanics, A/Solids*, 27(1), 69–78.
- [197] **Jiang, W.G.** (2012). A concise finite element model for pure bending analysis of simple wire strand, *International Journal of Mechanical Sciences*, 54(1), 69–73.

- [198] **Argatov, I.I., Gómez, X., Tato, W. and Urchegui, M.A.** (2011). Wear evolution in a stranded rope under cyclic bending: Implications to fatigue life estimation, *Wear*, 271(11-12), 2857–2867, <http://dx.doi.org/10.1016/j.wear.2011.05.045>.
- [199] **Fontanari, V., Benedetti, M. and Monelli, B.D.** (2015). Elasto-plastic behavior of a Warrington-Seale rope: Experimental analysis and finite element modeling, *Engineering Structures*, 82, 113–120.
- [200] **Fontanari, V., Benedetti, M., Monelli, B.D. and Degasperi, F.** (2015). Fire behavior of steel wire ropes: Experimental investigation and numerical analysis, *Engineering Structures*, 84, 340–349.
- [201] **Bruski, D.** (2020). Determination of the bending properties of wire rope used in cable barrier systems, *Materials*, 13(17).
- [202] **Borrvall, T.** (2008). Mortar Contact Algorithm for Implicit Stamping Analyses in LS-DYNA®, *10th International LS-DYNA Users Conference*, 2, Detroit, MI, USA, pp.19–28, <https://www.dynalook.com/international-conf-2008/MetalForming2-3.pdf>.
- [203] **Huang, Q., Li, Z. and Xue, H.Q.** (2018). Multi-body dynamics co-simulation of hoisting wire rope, *Journal of Strain Analysis for Engineering Design*, 53(1), 36–45.
- [204] **Judge, R., Yang, Z., Jones, S.W. and Beattie, G.** (2012). Full 3D finite element modelling of spiral strand cables, *Construction and Building Materials*, 35, 452–459.
- [205] **Karathanasopoulos, N., Reda, H. and francois Ganghoffer, J.** (2017). Finite element modeling of the elastoplastic axial-torsional response of helical constructions to traction loads, *International Journal of Mechanical Sciences*, 133(July), 368–375.
- [206] **Erdem Imrak, C. and Erdönmez, C.** (2010). On the problem of wire rope model generation with axial loading, *Mathematical and Computational Applications*, 15(2), 259–268.
- [207] **Erdonmez, C. and Imrak, C.E.** (2011). A finite element model for independent wire rope core with double helical geometry subjected to axial loads, *Sadhana - Academy Proceedings in Engineering Sciences*, 36(6), 995–1008.
- [208] **Erdönmez, C. and Imrak, C.E.** (2011). Modeling techniques of nested helical structure based geometry for numerical analysis, *Strojniski Vestnik/Journal of Mechanical Engineering*, 57(4), 283–292.
- [209] **Erdönmez, C.** (2014). N-Tuple Complex Helical Geometry Modeling Using Parametric Equations, *Engineering with Computers*, 30(4), 715–726.
- [210] **Erdönmez, C.** (2019). Computational Design of the Compacted Wire Strand Model and Its Behavior Under Axial Elongation, *International Journal of Precision Engineering and Manufacturing*, 20(11), 1957–1968, <https://doi.org/10.1007/s12541-019-00204-y>.

- [211] **Erdönmez, C.** (2020). Analysis and design of compacted IWRC meshed model under axial strain, *International Journal of Mechanics and Materials in Design*, 16(3), 647–661.
- [212] **Kastratović, G., Vidanović, N., Grbović, A., Mirkov, N. and Rašuo, B.,** (2020). Numerical Simulation of Crack Propagation in Seven-Wire Strand, *Lecture Notes in Networks and Systems*, volume 90, pp.76–91.
- [213] **Madenci, E. and Oterkus, E.,** (2014), Fortran Codes, <https://extras.springer.com/2014/978-1-4614-8464-6.zip>.
- [214] **Stukowski, A.** (2010). Visualization and analysis of atomistic simulation data with OVITO-the Open Visualization Tool, *Modelling and Simulation in Materials Science and Engineering*, 18(1).
- [215] xyz file type, https://en.wikipedia.org/wiki/XYZ{_}file{_}format.
- [216] **Chaplin, C.R.** (1995). Failure mechanisms in wire ropes, *Engineering Failure Analysis*, 2(1), 45–57.

APPENDICES

APPENDIX A: A Matlab script for plotting output files from Fortran program.

APPENDIX B: A Matlab script for converting *.m file outputs to *.xyz files

APPENDIX C: A Fortran script for saving Fortran program as a time dependent *.xyz file

APPENDIX D: A Fortran script for micro-crack

APPENDIX D.1: The text file for micro-crack location

APPENDIX E: A Matlab script to create a wire section

APPENDIX F: The wave propagation of m-convergence test setups for $m = \{2, 3, 4, 5\}$ with constant $\delta = 0.003$ m. Times durations for each figure: Figure F.1: 0-13.1 μs ; Figure F.2: 17.4-30.5 μs ; Figure F.3: 34.8-47.9 μs ; Figure F.4: 52.2-60.9 μs .

APPENDIX G: The wave propagation of δ -convergence test setups for $\delta = \{0.0045, 0.003, 0.00225, 0.0015\}$ m with constant $m = 3$. Times durations for each figure: Figure G.1: 0-13.1 μs ; Figure G.2: 17.4-30.5 μs ; Figure G.3: 34.8-47.9 μs ; Figure G.4: 52.2-60.9 μs .

APPENDIX A

```
1 % A Matlab script for plotting output
2 % files of Fortran (for AC PhD)
3 clc
4 clear
5
6 %% Load coordinate files
7 % Name of x coordinate vector is: xcoord
8 cxcg;
9 % Name of y coordinate vector is: ycoord
10 cycg;
11 % Name of z coordinate vector is: zcoord
12 czcg;
13
14 %% Load displacement files
15 % Name of x displacement vector is: disp_x
16 uxcg;
17 % Name of y displacement vector is: dispy
18 uycg;
19 % Name of z displacement vector is: dispz
20 uzcg;
21
22 %% Load velocity files
23 % Name of x velocity vector is: velx
24 vxcg;
25 % Name of y velocity vector is: vely
26 vycg;
27 % Name of z velocity vector is: velz
28 vzcg;
29
30 %% Load damage file
31 % Name of damage vector is: dmg
32 dmgcg;
33
34 %% Pre-processing
35 % Assign dmg to a new dmg2 file.
36 dmg2=dmg;
37 % Clear the very small values that means nothing.
38 % They are produced from Fortran calculations.
39 dmg2 (dmg2<=0)=0;
40
41 %% Plotting
42 % Close figure windows to avoid overlapping
43 close all
44
45 %Figure 1: Damage
46 figure
47 % Scatter plot uses vectors for coordinates
48 % 20 is a scale for dimension of points
49 % 'filled' is for filled points
50 scatter3(xcoord,ycoord,zcoord,20,dmg2,'filled')
51 %Labeling axes.
```

```

52 xlabel('x-axis')
53 ylabel('y-axis')
54 zlabel('z-axis')
55 %Set view angle in 3D
56 view(20,75)
57 %Title of the graph
58 title('Figure 1: Damage in Kalthoff-Winkler')
59 % Add a colormap to see the limits
60 colormap jet
61 colorbar
62 % Saving figure as a Matlab file *.fig
63 savefig('Result-damage.fig')
64
65 % Figure 1_alternative: Damage
66 % Add displacement to coordinates
67 last_xcoord = xcoord + disp_x;
68 last_ycoord = ycoord + disp_y;
69 last_zcoord = zcoord + disp_z;
70 figure
71 scatter3(last_xcoord,last_ycoord,last_zcoord,20,dmg2,'filled')
72 %Labeling axes.
73 xlabel('x-axis')
74 ylabel('y-axis')
75 zlabel('z-axis')
76 %Set view angle in 3D
77 view(20,75)
78 %Title of the graph
79 title('Figure 2: Damage - with modified coords')
80 % Add a colormap to see the limits
81 colormap jet
82 colorbar
83 % Saving figure as a Matlab file *.fig
84 savefig('Result-modified-coords.fig')
85
86 %Figure 3: Displacement in y-axis
87 figure
88 scatter3(xcoord,ycoord,zcoord,20,dispy,'filled')
89 xlabel('x-axis')
90 ylabel('y-axis')
91 zlabel('z-axis')
92 view(20,75)
93 title('Figure 3: Displacement in y axis in Kalthoff-Winkler [m]')
94 colormap jet
95 colorbar
96 savefig('Result-dispy.fig')
97
98 %Figure 4: Velocities in y-axis
99 figure
100 scatter3(xcoord,ycoord,zcoord,20,vely,'filled')
101 xlabel('x-axis')
102 ylabel('y-axis')
103 zlabel('z-axis')
104 view(20,75)
105 title('Figure 4: Velocities in y axis in Kalthoff-Winkler [m/s]')
106 colormap jet
107 colorbar
108 savefig('Result-vely.fig')
109 %End of script

```

APPENDIX B

```
1 % A Matlab script for converting output
2 % to a *.xyz files (for AC PhD)
3 clc
4 clear
5
6 %% Load coordinate files
7 % Name of x coordinate vector is: xcoord
8 cxcg;
9 % Name of y coordinate vector is: ycoord
10 cycg;
11 % Name of z coordinate vector is: zcoord
12 czcg;
13
14 %% Load damage file
15 % Name of damage vector is: dmg
16 dmgcg;
17
18 %% Pre-processing
19 % Assign dmg to a new dmg2 file.
20 dmg2=dmg;
21 % Clear the very small values that means nothing.
22 % They are produced from Fortran calculations.
23 dmg2(dmg2==0)=NaN;
24
25 % Eliminate irrelevant particles.
26 xcoord(isnan(dmg2))=NaN;
27 ycoord(isnan(dmg2))=NaN;
28 zcoord(isnan(dmg2))=NaN;
29
30 % Total number of particles.
31 totnode=length(xcoord);
32 out = [xcoord(:),ycoord(:),zcoord(:),dmg2(:)];
33
34 % Open a *.xyz file
35 fid = fopen('output_dmg_ovito.xyz', 'w');
36 % Write data
37 fprintf(fid, '%d\n\n', totnode);
38 %Close the *.xyz file
39 fclose(fid);
40 % Save the *.xyz file
41 save('output_dmg_ovito.xyz','out','-append' ...
42     , '-nocompression', '-ascii')
43
44 %Name of *.xyz file is: output_dmg_ovito.xyz
45
46 %End of script
```


APPENDIX C

```
1 !This script can be inserted in the time
2 !iteration do loop in the Fortran program
3 !for Kalthoff-Winkler PD simulation provided
4 !in the book by Madenci and Oterkus
5
6 ! A script for saving results as xyz file
7 ! in Kalthoff-Winkler problem (for AC PhD)
8
9 !Calculate the last coords:
10 do i = 1,totnode
11 last_coord(i,1) = coord(i,1) + disp(i,1)
12 last_coord(i,2) = coord(i,2) + disp(i,2)
13 last_coord(i,3) = coord(i,3) + disp(i,3)
14 enddo
15
16 !Writing result files to result.xyz: coord(i,1)
17 ! coord(i,3) coord(i,3) disp(i,1) disp(i,1)
18 ! disp(i,1) vel(i,1) vel(i,1) vel(i,1) dmg(i,1)
19
20 !Writing initial values
21 if (tt.eq.1) then
22 write(*,*) "Saving data at time=0"
23 open(21,file = 'results.xyz')
24 write(21,821) totnode
25 write(21,822) 0
26 do i = 1,totnode
27 write(21,823) coord(i,1), coord(i,2), coord(i,3), disp(i,1)&
28             , disp(i,2), disp(i,3), vel(i,1), vel(i,2)&
29             , vel(i,3), dmg(i,1), last_coord(i,1)&
30             , last_coord(i,2), last_coord(i,3)
31 enddo
32 close(21)
33 endif
34
35 !Writing result files: coord(i,1) coord(i,3) coord(i,3) disp(i,1)
36 ! disp(i,1) disp(i,1) vel(i,1) vel(i,1) vel(i,1) dmg(i,1)
37
38 if ((tt.eq.36).or.(tt.eq.50).or.(tt.eq.100).or.(tt.eq.150)&
39     .or.(tt.eq.200).or.(tt.eq.250).or.(tt.eq.300)) then
40 write(*,*) 'Saving value at time=', tt
41 open(21,file = 'results.xyz',position='append')
42 write(21,821) totnode
43 write(21,822) tt
44     do i = 1,totnode
45 write(21,823) coord(i,1), coord(i,2), coord(i,3), disp(i,1)&
46             , disp(i,2), disp(i,3), vel(i,1), vel(i,2)&
47             , vel(i,3), dmg(i,1), last_coord(i,1)&
48             , last_coord(i,2), last_coord(i,3)
49     enddo
50 close(26)
51 endif
```

```

52
53 if ((tt.eq.350).or.(tt.eq.400).or.(tt.eq.450).or.(tt.eq.500)&
54     .or.(tt.eq.550).or.(tt.eq.600).or.(tt.eq.650)) then
55     write(*,*) 'Saving value at time=', tt
56     open(21,file = 'results.xyz',position='append')
57     write(21,821) totnode
58     write(21,822) tt
59     do i = 1,totnode
60 write(21,823) coord(i,1), coord(i,2), coord(i,3), disp(i,1)&
61             , disp(i,2), disp(i,3), vel(i,1), vel(i,2)&
62             , vel(i,3), dmg(i,1), last_coord(i,1)&
63             , last_coord(i,2), last_coord(i,3)
64     enddo
65     close(26)
66 endif
67
68 if ((tt.eq.700).or.(tt.eq.750).or.(tt.eq.800).or.(tt.eq.850)&
69     .or.(tt.eq.900).or.(tt.eq.950).or.(tt.eq.1000)) then
70     write(*,*) 'Saving value at time=', tt
71     open(21,file = 'results.xyz',position='append')
72     write(21,821) totnode
73     write(21,822) tt
74     do i = 1,totnode
75 write(21,823) coord(i,1), coord(i,2), coord(i,3), disp(i,1)&
76             , disp(i,2), disp(i,3), vel(i,1), vel(i,2)&
77             , vel(i,3), dmg(i,1), last_coord(i,1)&
78             , last_coord(i,2), last_coord(i,3)
79     enddo
80     close(26)
81 endif
82
83 if ((tt.eq.1050).or.(tt.eq.1100).or.(tt.eq.1150).or.(tt.eq.1200)&
84     .or.(tt.eq.1250).or.(tt.eq.1300).or.(tt.eq.nt)) then
85     write(*,*) 'Saving value at time=', tt
86     open(21,file = 'results.xyz',position='append')
87     write(21,821) totnode
88     write(21,822) tt
89     do i = 1,totnode
90 write(21,823) coord(i,1), coord(i,2), coord(i,3), disp(i,1)&
91             , disp(i,2), disp(i,3), vel(i,1), vel(i,2)&
92             , vel(i,3), dmg(i,1), last_coord(i,1)&
93             , last_coord(i,2), last_coord(i,3)
94     enddo
95     close(26)
96 endif
97
98 821 format (I6)
99 822 format ('Time=',I4)
100 823 format (e10.3,1x,e10.3,1x,e10.3,1x,e12.5,1x,e12.5,1x&
101             ,e12.5,1x,e12.5,1x,e12.5,1x,e12.5,1x,e12.5,1x&
102             ,e10.3,1x,e10.3,1x,e10.3)

```

APPENDIX D

```
1 ! This script can be inserted in the Fortran program
2 ! for Kalthoff-Winkler PD simulation provided
3 ! in the book by Madenci and Oterkus after line section,
4 ! "PD bonds penetrating through the crack surface are broken"
5
6 ! A script for creating micro-cracks
7 ! in Kalthoff-Winkler problem (for AC PhD)
8
9 !Microcrack integars
10 integer nmc, namc, zz, col
11 !Microcrack parameters
12 parameter(nmc = 200) !number of max micro crack
13 parameter(namc = 45) !number of actual micro crack on left side
14
15 !Microcrack reals
16 real *8 tol, pangle, crack_length, alpha_angle
17 real *8 perangle, pnormaly, pnormalx, ppery
18 real *8 pperx, slope, slopep, seg_int
19 real *8 DDD3, DDD2, DDD, NNN, DDD4, DDD5
20
21 !Microcrack matrices and vectors
22 real *8 ptcpm(nmc,5), ptcp(3), mcpn(3)
23 real *8 mcptpn(3), pmp(3), pmp3(3), P0(3)
24 real *8 uuu3(3), uuu2(3), P1(3)
25 real *8 uuu(3), www(3), ip(3), uuu4(3), uuu5(3)
26
27 !Start - Definition of the micro crack
28 write(*,*) "Definition of the micro crack surface"
29 tol = 1.0d-6
30
31 do zz = 1,nmc
32 ptcpm(nmc,1) = -99.000d0;
33 ptcpm(nmc,2) = -99.000d0;
34 ptcpm(nmc,3) = -99.000d0;
35 ptcpm(nmc,4) = -99.000d0;
36 ptcpm(nmc,5) = -99.000d0;
37 enddo
38
39 ! Open the crack file
40 ! 1st coloum: top point x
41 ! 2nd coloum: top point y
42 ! 3rd coloum: top point z
43 ! 4th coloum: angle
44 ! 5th coloum: lenght
45
46 open(1,file='points.txt')
47 read (1, *) ((ptcpm(i, j), j = 1, 5), i = 1, namc)
48 close(1)
49
50 ! Microcrack top point 1
51 ! For a single arbitrary crack
```

```

52 ! ptcpm(1,1) = -0.0277d0
53 ! ptcpm(1,2) = -0.0013d0
54 ! ptcpm(1,3) = 0.0d0
55 ! ptcpm(1,4) = 0.64000d2
56 ! ptcpm(1,5) = 3.0d0
57
58 do zz = 1, namc
59   ptcpm(zz+namc,1) = - ptcpm(zz,1);
60   ptcpm(zz+namc,2) =  ptcpm(zz,2);
61   ptcpm(zz+namc,3) =  ptcpm(zz,3);
62   ptcpm(zz+namc,4) = - ptcpm(zz,4);
63   ptcpm(zz+namc,5) =  ptcpm(zz,5);
64 enddo
65
66 do zz = 1, (2*namc) !integer +
67
68 !ENTER crack plane angle between
69 ! -0.89999d2 < pangle < +0.89999d2
70 ! if=0: 0 -1 0 direction CW
71 pangle = ptcpm(zz,4) !real +
72
73 ! !ENTER crack length
74 crack_length = ptcpm(zz,5) !real +
75
76 alpha_angle = -pangle !real +
77 perangle = 0.90000d2 + alpha_angle !real +
78
79 if (alpha_angle == 0.90000d2) then
80   pnormaly = 1.0d0 !real +
81   pnormalx = 0.0d0 !real +
82   ppery = 0.0d0 !real +
83   pperx = -1.0d0 !real +
84   else if (alpha_angle == 0.00000d2) then
85     pnormaly = 0.0d0
86     pnormalx = 1.0d0
87     ppery = 1.0d0
88     pperx = 0.0d0
89   else
90     slope = tan((alpha_angle*pi)/180) !real +
91     slopep = tan((perangle*pi)/180) !real +
92     pnormalx = ((1.0d0/(slope**2.0d0+1.0d0))*0.5d0)
93     pnormaly = ( pnormalx*slope )
94     ppery = ...
95     pperx = ((slopep**2.0d0)/((slopep**2.0d0)+1.0d0))*0.5d0
96   endif
97 !real !micro crack plane normal +
98 mcpn(1) = pnormalx
99 mcpn(2) = pnormaly
100 mcpn(3) = 0.0d0
101
102 !real !micro crack perpendicular plane normal +
103 mcptpn(1) = pperx
104 mcptpn(2) = ppery
105 mcptpn(3) = 0.0d0
106
107 !real + !real !top middle point on micro crack plane and perp ...
108 pmp(1) = ptcpm(zz,1)

```



```

109 pmp(2) = ptcpm(zz,2)
110 pmp(3) = ptcpm(zz,3)
111
112 !bottom middle point on micro crack plane +
113 pmp3(1) = ( pmp(1) - (mcptpn(1) * (crack_length*dx)) )
114 pmp3(2) = ( pmp(2) - (mcptpn(2) * (crack_length*dx)) )
115 pmp3(3) = ( pmp(3) - (mcptpn(3) * (crack_length*dx)) )
116
117 do i = 1, totnode
118 !limit i bottom top plane perpendicular to microcrack plane
119   P0(1) = coord(i,1) !real +
120   P0(2) = coord(i,2)
121   P0(3) = coord(i,3)
122
123   uuu3 = ( P0-(pmp3-(mcptpn*2.0d0*dx)) ) !real +
124   DDD3 = dot_product(uuu3,mcptpn) !real +
125   uuu2 = ( P0-(pmp+(mcptpn*2.0d0*dx)) ) !real +
126   DDD2 = dot_product(uuu2,mcptpn) !real +
127
128   if ( (DDD3>=0.0d0) .and. (DDD2<=0.0d0) ) then
129
130     do j = 1, numfam(i,1)
131       cnode = nodefam(pointfam(i,1)+j-1,1)
132
133       !limit cnode bottom top plane perpendicular to ...
134         microcrack plane
135       P1(1) = coord(cnode,1) !real +
136       P1(2) = coord(cnode,2)
137       P1(3) = coord(cnode,3)
138
139       uuu = ( P1-P0 ) !real +
140       www = ( P0-pmp ) !real +
141       DDD = dot_product(mcpn,uuu) !real +
142       NNN = -dot_product(mcpn,www) !real +
143       !compute the intersection parameter
144       seg_int = ( NNN / DDD ) !real +
145
146       if ( (seg_int < 0.0d0) .or. (seg_int > 1.0d0) ) then
147
148         else
149           ip = ( P0 + (seg_int*uuu) ) !real+
150           uuu4 = ( ip - pmp3 ) !real+
151           DDD4 = ( dot_product(uuu4,mcptpn) ) !real+
152           uuu5 = ( ip - pmp ) !real+
153           DDD5 = ( dot_product(uuu5,mcptpn) ) !real+
154
155           if ( ( (abs(DDD4))<tol) .or. (DDD4>0) ) &
156             .and. ( (abs(DDD5))<tol) .or. (DDD5<0) ) ) then
157             fail(i,j)=0
158           endif
159         endif
160       enddo
161     endif
162   enddo
163 !End - Definition of microcrack

```

APPENDIX D.1

```
1 ! Delete this information before proceeding.
2 ! 1. column: x-coordinate of the top of the crack.
3 ! 2. column: y-coordinate of the top of the crack.
4 ! 3. column: z-coordinate of the top of the crack.
5 ! 4. column: the angle between crack plane and -y axis.
6 ! 5. column: crack plane length in xy plane.
7 -0.0351 -0.0038 0.0000 66.0000 3.0000
8 -0.0345 -0.0002 0.0000 -9.0000 3.0000
9 -0.0343 0.0008 0.0000 64.0000 3.0000
10 -0.0341 -0.0053 0.0000 30.0000 3.0000
11 -0.0339 0.0064 0.0000 62.0000 3.0000
12 -0.0334 0.0106 0.0000 12.0000 3.0000
13 -0.0323 0.0134 0.0000 -63.0000 3.0000
14 -0.0322 -0.0101 0.0000 -29.0000 3.0000
15 -0.0275 -0.0098 0.0000 22.0000 3.0000
16 -0.0253 -0.0122 0.0000 -40.0000 3.0000
17 -0.0191 -0.0114 0.0000 38.0000 3.0000
18 -0.0351 0.0029 0.0000 72.0000 3.0000
19 -0.0354 0.0083 0.0000 38.0000 3.0000
20 -0.0206 -0.0099 0.0000 22.0000 3.0000
21 -0.0381 -0.0005 0.0000 -18.0000 3.0000
22 -0.0329 0.0118 0.0000 -50.0000 3.0000
23 -0.0251 -0.0098 0.0000 -65.0000 3.0000
24 -0.0331 -0.0066 0.0000 -66.0000 3.0000
```

APPENDIX E

```
1 % A Matlab script for create a wire
2 % cross section (for AC PhD)
3 clc
4 clear
5
6 %% Definitions
7 % Increment
8 nnum = 0;
9 % Cable box length
10 length_x = 0.09;
11 % Cable box height
12 height_y = 0.09;
13 % Cable box width
14 width_z = 0.003;
15 % Center cable diameter
16 diameter = 0.09;
17 % A tolerance value for avoid numeral erros.
18 tol=1e-6;
19
20 % Number of material points in x direction in box
21 ndivx = 121;
22 % Number of material points in y direction in box
23 ndivy = 121;
24 % Number of material points in z direction in box
25 ndivz = 6;
26 % Total node number
27 totnode = ndivx*ndivy*ndivz;
28 % Cordinates of material points matrix
29 coord=zeros(totnode,3);
30 % Distance between material points
31 dx=length_x/(ndivx-1);
32
33 for i = 1 : ndivx
34     for j = 1 : ndivy-1
35         for k = 1 : ndivz
36
37             coordx = -1.0e0 / 2.0e0 * length_x + (i - 1) * dx;
38             coordy = -1.0e0 / 2.0e0 * height_y + (j - 1) * dx;
39             coordz = -1.0e0 / 2.0e0 * width_z + (k - 1) * dx;
40
41             if ( (coordy^2 + coordx^2) ≤ ((diameter / 2 + ...
42                 tol)^2) )
43                 nnum=nnum+1;
44                 coord(nnum,1) = coordx;
45                 coord(nnum,2) = coordy;
46                 coord(nnum,3) = coordz;
47             end
48         end
49     end
50 end
```

```
51
52 %%
53 close all
54
55 scatter3(coord(:,1),coord(:,2),coord(:,3),20,'filled')
56 xlabel('x-axis')
57 ylabel('y-axis')
58 zlabel('z-axis')
59 view(0,90)
60 title('wire')
61
62 %End of script
```

APPENDIX F

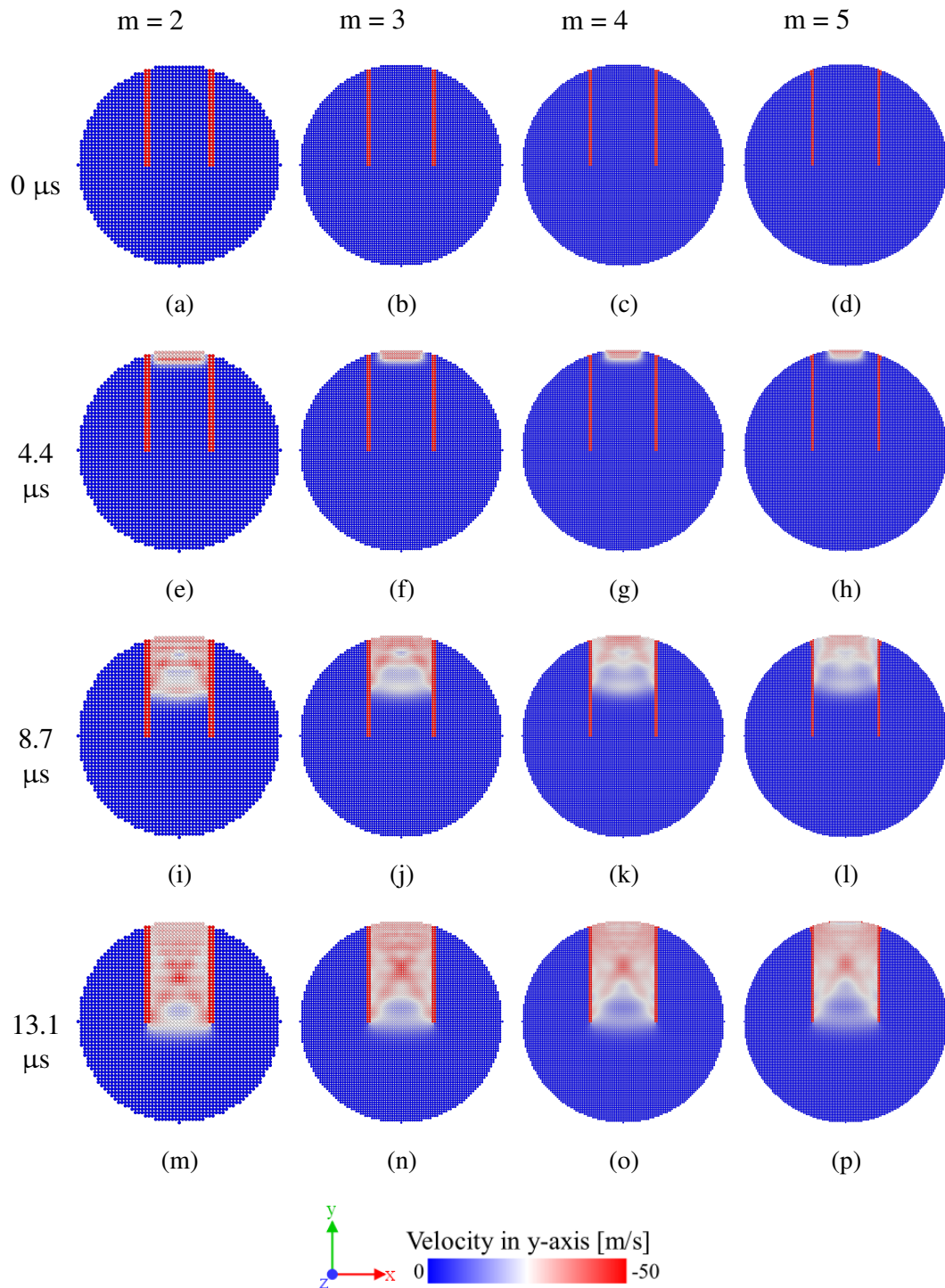


Figure F.1 : The wave propagation on m-convergence tests with $\delta = 0.003 \text{ m}$ during between 0-13.1 μs .

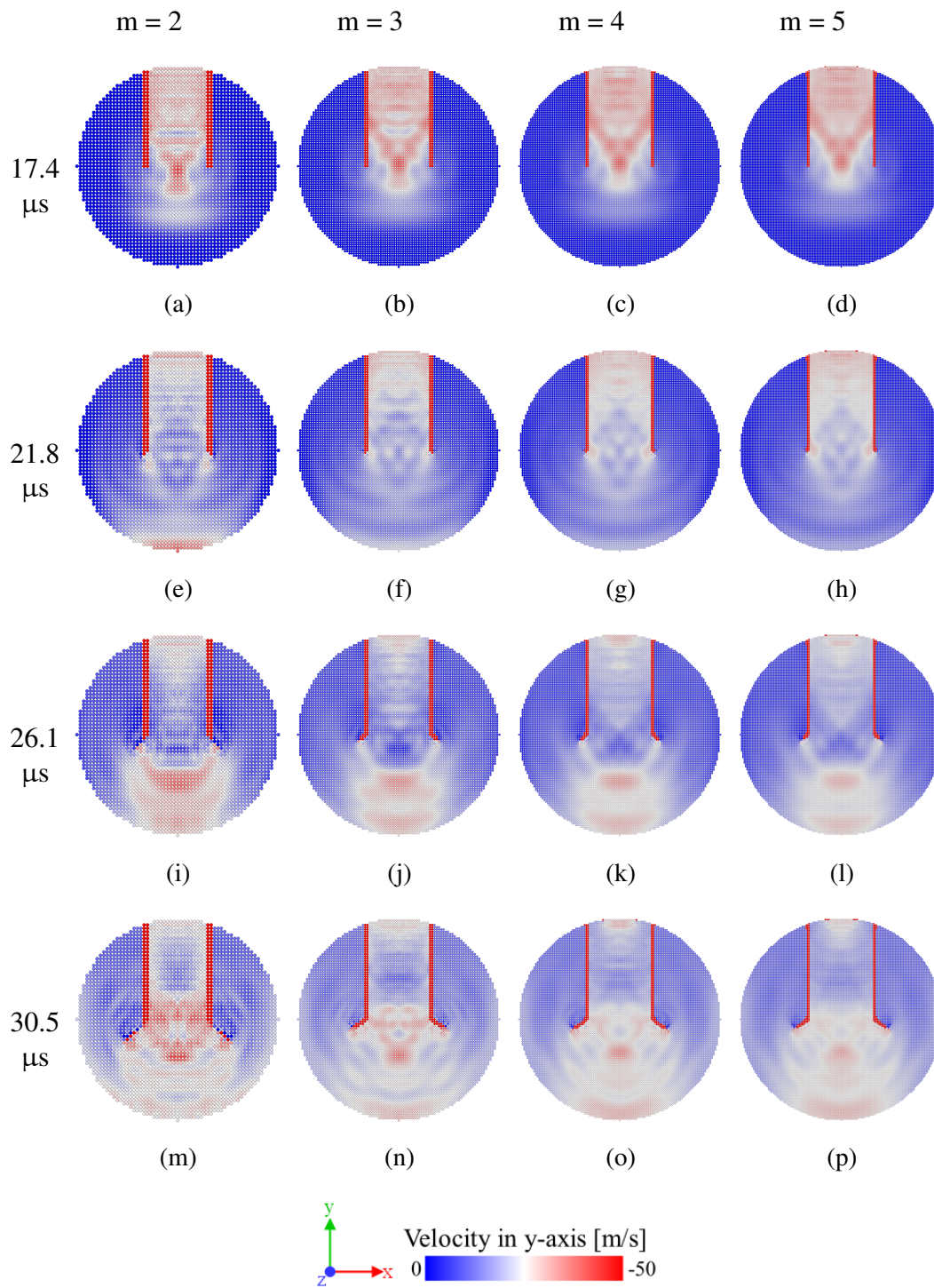


Figure F.2 : The wave propagation on m-convergence tests with $\delta = 0.003$ m during between 17.4 - $30.5 \mu\text{s}$.

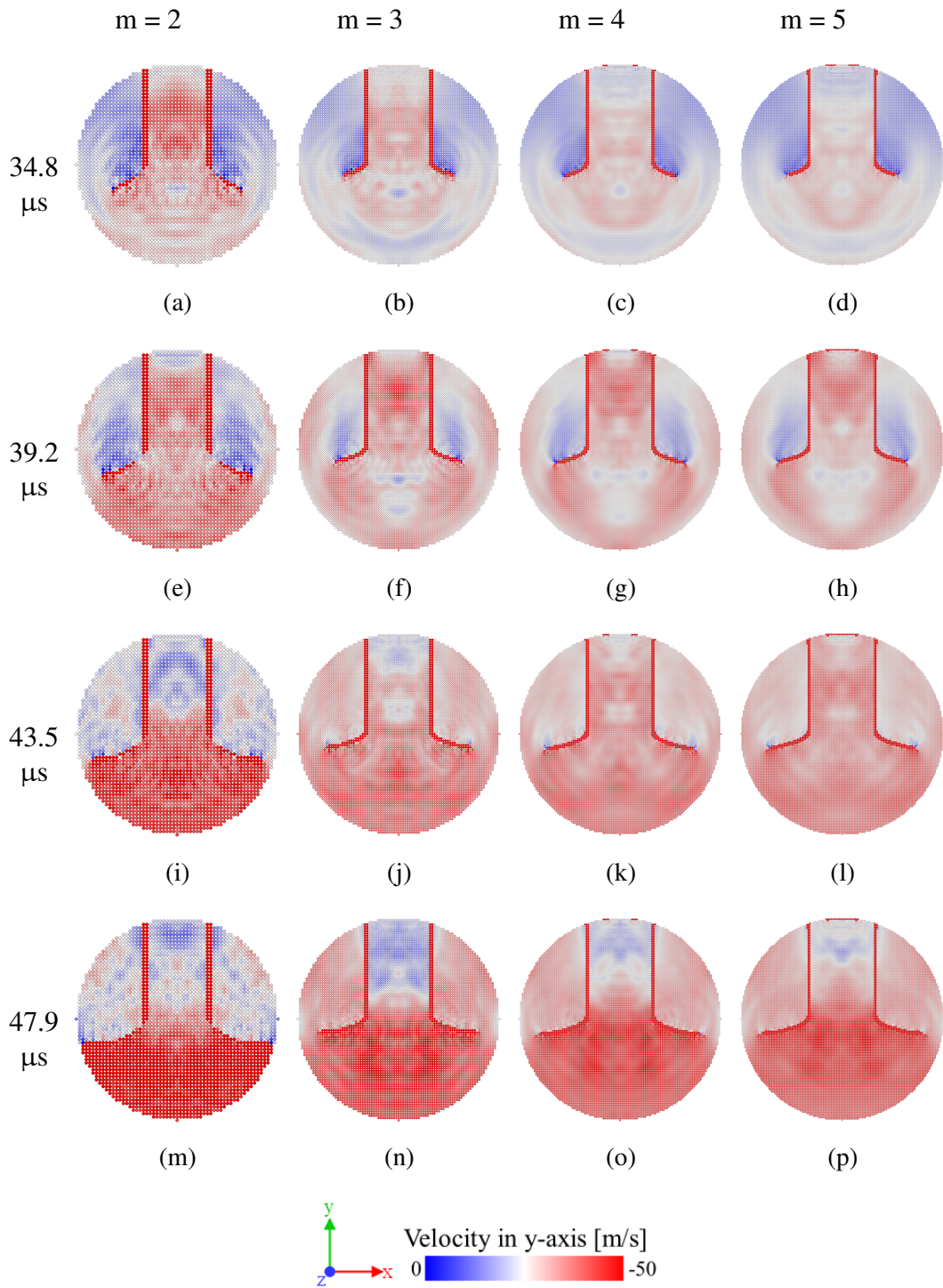


Figure F.3 : The wave propagation on m-convergence tests with $\delta = 0.003 \text{ m}$ during between $34.8\text{-}47.9 \mu\text{s}$.

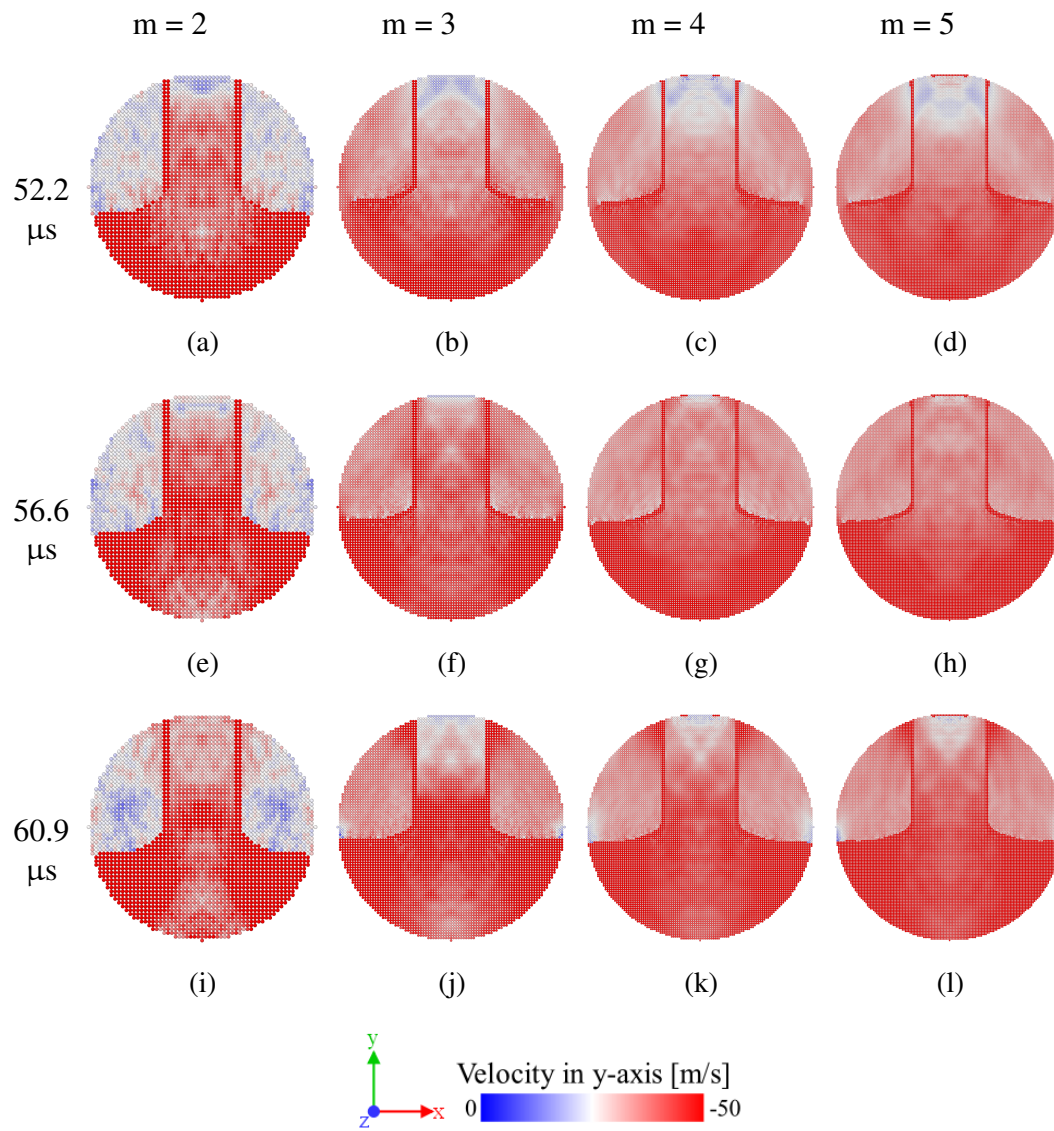


Figure E.4 : The wave propagation on m-convergence tests with $\delta = 0.003 \text{ m}$ during between $52.2\text{-}60.9 \mu\text{s}$.

APPENDIX G

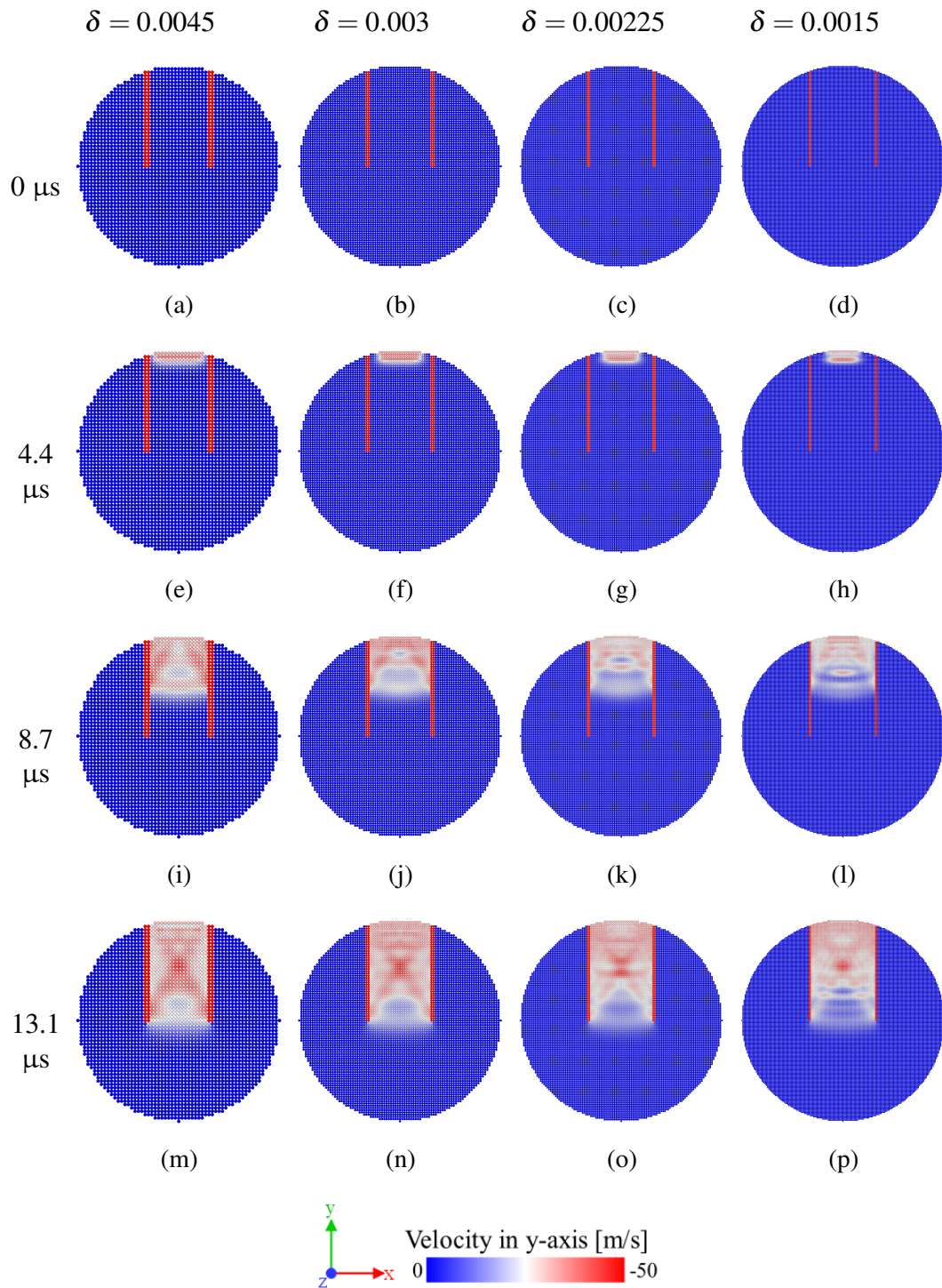


Figure G.1 : The wave propagation on δ -convergence tests with $m = 3$ during between 0-13.1 μs .

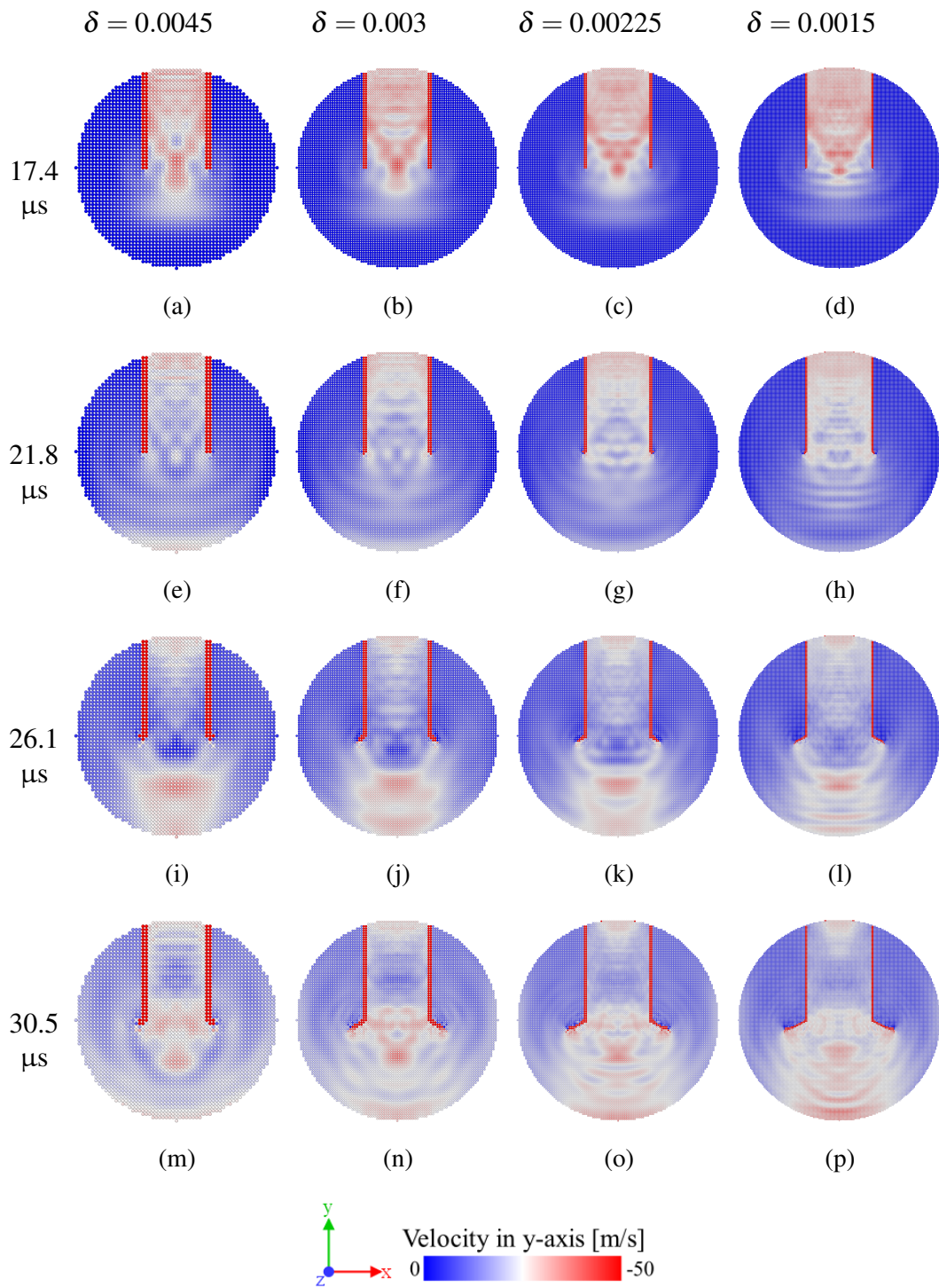


Figure G.2 : The wave propagation on δ -convergence tests with $m = 3$ during between 17.4-30.5 μs .

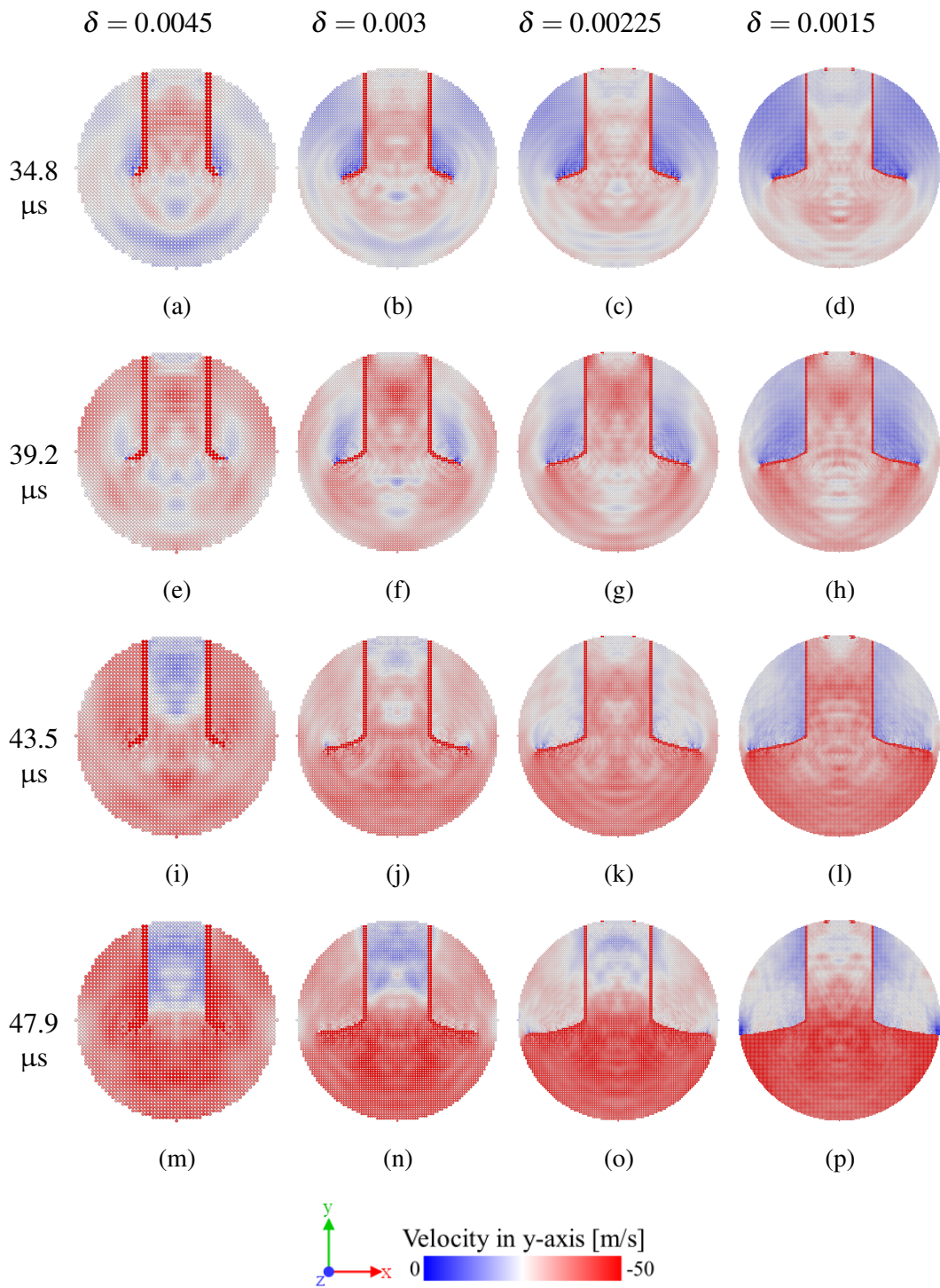


Figure G.3 : The wave propagation on δ -convergence tests with $m = 3$ during between 34.8-47.9 μs .

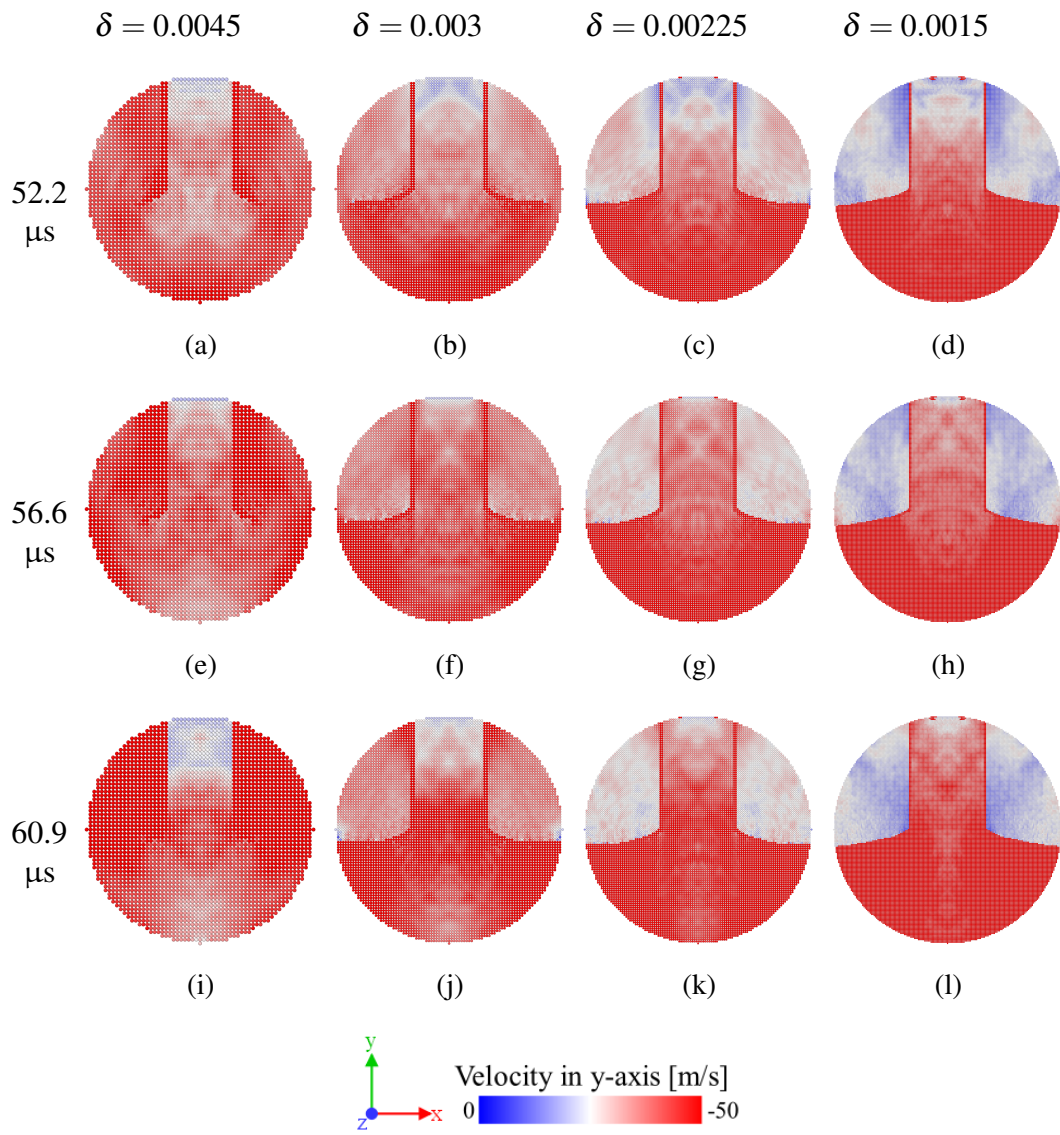


Figure G.4 : The wave propagation on δ -convergence tests with $m = 3$ during between 52.2-60.9 μs .

CURRICULUM VITAE



Name Surname: Adem Candaş

Place and Date of Birth: Dinar, 11 April 1988

E-Mail: candas@itu.edu.tr

EDUCATION:

- **Ph.D.:** 2021, Istanbul Technical University, Graduate School, Mechanical Engineering Programme.
- **M.Sc.:** 2017, Istanbul Technical University, Eurasia Institute of Earth Sciences, Geodynamics Programme.
- **M.Sc.:** 2013, Istanbul Technical University, Graduate School of Science Engineering and Technology, Mechanical Design Programme.
- **B.Sc.:** 2013, Anadolu University (Open Education), Public Administration.
- **B.Sc.:** 2010, Istanbul Technical University, Faculty of Mechanical Engineering, Mechanical Engineering Programme.

PROFESSIONAL EXPERIENCE:

- 2018-... Istanbul Technical University, Faculty of Mechanical Engineering. Lecturer.
- 2017 University of Strathclyde, Glasgow, UK, Naval Architecture, Ocean and Marine Engineering. Visiting Researcher (3 months).
- 2010-2018 Istanbul Technical University, Faculty of Mechanical Engineering. Research Assistant.
- 2009 TOFAŞ, Türk Otomobil Fabrikaları, Bursa, Turkey. Intern Engineer.

PUBLICATIONS, PRESENTATIONS AND PATENTS ON THE THESIS:

- **Candaş, A., Oterkus, E., İmrak, C.E.** (2021). Dynamic Crack Propagation and Its Interaction with Micro-Cracks in an Impact Problem. *Journal of Engineering Materials and Technology, Transactions of ASME, 143(1)*. doi.org/10.1115/1.4047746

OTHER PUBLICATIONS AND PRESENTATIONS:

Journal Papers

- **Candaş, A.**, Sarıkaya, M.A., Köse, O., Şen, Ö.L. Çiner, A. (2020). Modelling Last Glacial Maximum ice cap with Parallel Ice Sheet Model to infer palaeoclimate in south-west Turkey. *Journal of Quaternary Science*, 35(7): 935-950. doi.org/10.1002/jqs.3239
- Köse, O., Sarıkaya, M.A., Çiner, A., **Candaş, A.** (2019). Late Quaternary Glaciations and Cosmogenic ³⁶Cl Geochronology of Mount Dedegöl, South-West Turkey. *Journal of Quaternary Science*, 34(1), 51-63. doi.org/10.1002/jqs.3080

Other Papers - Web of Science Core Collection

- **Candaş, A.**, Kurt, S., Gerdemeli, S., Kayaolu, E. (2014). An experimental stress analysis of a jib crane. *Key Engineering Materials*, 572(1), 173–176. WOS: Book Citation Index. doi.org/10.4028/www.scientific.net/KEM.572.173
- **Candaş, A.**, Kayaoğlu, E. (2013). FEM and Experimental Stress Analysis of a Jib Crane. *Applied Mechanics and Materials*, 395–396, pp. 877–880. 3rd International Conference on Advanced Design and Manufacturing Engineering, ADME 2013, Anshan, China, 13-14 July 2013. WOS: Proceedings Citation Index. doi.org/10.4028/www.scientific.net/amm.395-396.877
- Gerdemeli, İ., Çotur, A.E., Kayaoglu, E., **Candaş, A.** (2011). Computer Aided Valve Design of Shock Absorbers Used in Vehicles. *Key Engineering Materials*, 486, 270-273. Advanced Design and Manufacture IV 2011. WOS: Book Citation Index. doi.org/10.4028/www.scientific.net/KEM.486.270
- Kayaoğlu, E., Salman, Ö., **Candaş, A.** (2011). Study on stress and deformation of an elevator safety gear brake block using experimental and FEA methods. *Advanced Materials Research*, 308-310, pp. 1513-1518, 1-3. International Conference on Advanced Design and Manufacturing Engineering, ADME 2011, Guangzhou, China, 16-18 Sept 2011. WOS: Conference Proceedings Citation Index. doi.org/10.4028/www.scientific.net/AMR.308-310.1513

Conference Papers (Full Papers)

- Kocabal, Y.Z., İmrak, C.E., **Candaş, A.** (2018). Asansörler ve Yürüyen Merdivenlerde Enerji Tüketimi ve Verimliliği. *IX. Asansör Sempozyumu Bildiriler Kitabı*, ISBN 978-605-01-1226-9, 18-20 Ekim, İzmir, Türkiye.
- Şahin, U., **Candaş, A.**, Boğoçlu M.E. (2018). Comparison of Analytical and Finite Element Analysis of a Tower Crane Boom. *21st International Research/Expert Conference “Trends in the Development of Machinery and Associated Technology”*, TMT 2018, 18th-22nd September, Karlovy Vary, Czech Republic.
- Şahin, T., **Candaş, A.**, İmrak, C.E. (2018). Analytical and Finite Element In-Plane Vibration Analysis of a Gantry Crane. *XXVI. International Scientific Conference on Transport, Road-Building, Agricultural, Hoisting - Hauling and Military Technics and Technologies, trans - MOTAUTO 2018*, Proceedings Volume 1, ISSN 1313-5031 (Print), ISSN 2535-0307 (Online), p. 45-47. Transport Techniques. Investigation of Elements. Vehicle Engines, Sofia, Bulgaria.

- Kayaođlu, E., **Candaş, A.**, Kocabal, Y.Z., İmrak, C.E. (2014). Early Application of Underground Funicular ‘Tunnel’ in Istanbul. *Elevator Technology 20*, ELEVCON 2014, Paris, France.
- Atay S., Kayaođlu E., **Candaş A.**, İmrak C.E. (2014). Determination of Loads Acting on Guide Rail Fixing Under Certain Loading Condition, *Elevator Technology 20*, ELEVCON 2014, Paris, France.
- Kayaođlu, E., **Candaş, A.**, Kocabal, Y.Z., İmrak, C.E. (2014). İstanbul’un Tarihi Füniküleri ‘TÜNEL’. VI. Asansör Sempozyumu Bildiriler Kitabı, ISBN: 978-605-01-0642-8, 25-27 Eylül, İzmir, Türkiye.
- Barlas, E., İmrak, C.E., Kayaođlu, E., **Candaş, A.**, Kocabal, Y.Z. (2012). The Street Called “Asansör” and Water Powered Elevator Installation in İzmir. *Elevator Technology 19*, ELEVCON 2012, Miami, USA.
- Elmalı, S., **Candaş, A.**, Kayaođlu, E., İmrak, C.E., Targıt, S. (2012). Modeling and Analysis of Guide Rail Brackets and Attaching Parts. *Elevator Technology 19*, ELEVCON 2012, Miami, USA.
- Kayaođlu, E., **Candaş, A.**, İmrak, C.E., Targıt, S. (2012). Ani tip Fren Bloklarının Modellenmesi, Testi ve Analizi, V. Asansör Sempozyumu Bildiriler Kitabı, ISBN: 978-605-01-0408-0, 4-6 Ekim, İzmir, Türkiye.
- Kocabal, Y.Z., **Candaş, A.**, Kayaođlu, E., İmrak, C.E. (2012). 19. Yüzyıl Hidrolik Asansör Teknolojisi ve Tarihi Asansör, V. Asansör Sempozyumu Bildiriler Kitabı, ISBN: 978-605-01-0408-0, 4-6 Ekim, İzmir, Türkiye.